Thèse de doctorat

Université de Limoges

ÉCOLE DOCTORALE 522 SI-MMEA

FACULTÉ DES SCIENCES ET TECHNIQUES

Année 2017 N° 2017LIMO0011

Thèse

Pour obtenir le grade de

DOCTEUR DE L'UNIVERSITÉ DE LIMOGES

Discipline: Matériaux Céramiques et Traitements de Surface

Présentée par **Jess GAMBE**

le 31 janvier 2017

Synthèse non-hydrolytique et structure de nanoparticules de ZrO_2

Thèse dirigée par Olivier MASSON, Fabien REMONDIERE et Jenny JOUIN

JURY:

Rapporteurs

Guido BALDINOZZI	Directeur de Recherche CNRS, SPMS, Paris (France)
Hubert MUTIN	Directeur de Recherche CNRS, ICG, Montpellier (France)

Examinateurs

Olivier MASSON	Professeur, SPCTS, Limoges (France)
Fabien REMONDIERE	Maître de Conférences, SPCTS, Limoges (France)
Jenny JOUIN	Chargée de Recherche, SPCTS, Limoges (France)
Reynaldo VEQUIZO	Professeur, MSU-IIT, Iligan (Philippines)

Invités

Abid BERGHOUT	Maître de Conférences, SPCTS, Limoges (France)
Philippe THOMAS	Directeur de Recherche CNRS, SPCTS, Limoges (France)

Thèse de doctorat

Université de Limoges

ECOLE DOCTORAL 522 SI-MMEA

FACULTE DES SCIENCES ET TECHNIQUES

Year 2017 N° 2017LIMO0011

Thesis

Submitted for the degree of

DOCTOR OF PHILOSPHY OF THE UNIVERSITY OF LIMOGES

Discipline: Ceramic Materials and Surface Treatment

Presented by **Jess GAMBE**

31 January 2017

Non-hydrolytic synthesis and structure of ZrO_2 nanoparticles

Supervisors: Olivier MASSON, Fabien REMONDIERE and Jenny JOUIN

JURY:

Reviewers

Guido BALDINOZZI	Directeur de Recherche CNRS, SPMS, Paris (France)
Hubert MUTIN	Directeur de Recherche CNRS, ICG, Montpellier (France)

Examiners

Olivier MASSON	Professeur, SPCTS, Limoges (France)
Fabien REMONDIERE	Maître de Conférences, SPCTS, Limoges (France)
Jenny JOUIN	Chargée de Recherche, SPCTS, Limoges (France)
Reynaldo VEQUIZO	Professor, MSU-IIT, Iligan (Philippines)

Guest

Abid BERGHOUT	Maître de Conférences, SPCTS, Limoges (France)
Philippe THOMAS	Directeur de Recherche CNRS, SPCTS, Limoges (France)

“We will cross the bridge when we get there”

Acknowledgement

I, Jess Gambe, am grateful to the Ceramics Processes and Surface Treatments (SPCTS) in Limoges headed by Dr. Thierry Chartier for having welcomed be into the laboratory. Above all, warm thanks to Dr. Olivier Masson, Dr. Fabien Remondiere and Dr. Jenny Jouin, who impressively performed their role as advisers. Their fervor for knowledge, patience, understanding, and enthusiasm for the thesis work were a strong motivation during its development.

To the thesis committee members; Dr. Guido Baldinozzi, Dr. Hubert Mutin, Dr. Reynaldo Vequizo, Dr. Abid Berghout, and Dr. Philippe Thomas for sharing their time and knowledge. Their diligent and constructive discussions and criticism have improved greatly the thesis work.

Appreciative acknowledgement is made to everyone who has made my stay a memorable one and this includes; Julie Cornette, Jean Rene Duclere, Richard Mayet, Pierre Carles, Olivier Noguera, Pamela Bathias, Virginie Reytier, Helene Memy, Calve Nicolas, Florence Delautier, Etienne Laborde, Yann Launay, Sebastien Chenu, Romain Lucas, Lech Pawloski, Anastasia Gulenko, Anthony Betrand, Salyani Mahmod, Jayan Channagiri, Pawel Sokolowski, Catalin Constantine Scu, Robert Kaczmarek, Irmina Gutkoski, Joanna Krowka, Aenor Marty, Kasia Krupa, Aleksandea Malachowska, Arish Dasan, Florean Rejasse, Fabien Bouzat, Moustapha Coulibaly, Imane El Younsi, Camille Ortali, Laura Guironnet, Khaoula Lebdioua, Nadia El-Felss, Miriana Munoz, Vanessa Orozco, Rolando Candidato Jr., Alex Lemarchand, Lyna Torzuoli, Angel Prato, Jonathan Raynaud, Morgane Dolhen, Romain Trihan, Andrej Warchal, Karolina Kozak, Wisley Truong, Masayuki Tanaka, Kenichiro Ueno, Mohammed Reda Zaki, Dimitrii Ivachenko, Ivan David Correa, Alberto Jose Fernandez Carrion, and Rodion Zhukovskii.

A big thanks to those who have added value to my life by being a good friend and a sincerely apology if I have forgotten to mention you.

Finally, a big thanks to my much loved-family, Artemio Gambe and Anita Gambe, for the love and support; to my beloved sisters, Dr. Engr. Arni Gambe and Dr. Zeny Gambe, who are always there for me; and to God almighty, the great provider, for all His blessings.

Contents

General introduction

Nanocrystalline materials have become the corner stone of several technological advancements because of their intrinsic properties that are different compared to their conventional micrometric counterparts. These properties are mainly caused by quantum confinement effects brought about by the reduction of the particles' size which are widely studied and relatively well understood [1] [2] [3] [4].

The particles' size also has a strong effect on their unusual structure that is non-identical to the so-called perfect monocrystalline structure [5]. Moreover, understanding the properties of such materials is quite limited because of the current complexity in synthesizing and characterizing stable objects that are less than 5 nm [6].

Hence, this work is devoted to the determination of a reproducible way to synthesize nanoparticles with selectable phase and tunable size. Then, having control over these parameters, we investigated their structural features in relation to their scale which is consequential for a better understanding of these materials, including their properties.

One of the typical procedure used in synthesizing nano-sized particles belongs to the chemical solution routes. Indeed, these routes offer a versatile way to form particles by following a "bottom-up" approach. In principle, this type of approach removes the lower limit of size that can be formed. However, stabilization of such small particles with acceptable crystallinity and chemical purity requires a more complete understanding on the chemical behavior of the individual precursors during the synthesis. Generally, these routes can be divided in two categories: the hydrolytic and non-hydrolytic processes. Each process offers the opportunity to form nano-sized particles with a wide variety of designable properties but also with its corresponding limitations. For example, we can cite the hydrolytic sol-gel synthesis of ZrO_2 which is able to produce nanoparticles with sizes under 2 nm. Unfortunately, they possess a wide-size distribution and present large quantities of carbonaceous impurities at their surface [7]. In contrast, non-hydrolytic sol-gel synthesis of ZrO_2 conducted by solvothermal routes also produced nano-sized particles but with a more satisfactory features in terms of size distribution and absence of impurities [8]. It is clear that for this particular work the decision to follow a non-hydrolytic procedure offers a better strategy in obtaining minute size objects.

The choice of ZrO_2 as the material to be studied was dictated by its remarkable intrinsic properties and its potential for great technological advancement such as in catalysis [9] [10], gas sensing [11] [12], fuel cell technology [13] [14], and ceramics [15]. Moreover, it has a complex polymorphism and has the particularity of being stabilized at the nanometric scale in crystalline forms which are not stable at standard pressure and ambient temperature.

In this work, solvothermal strategy was used and served as an experimental basis for the synthesis of the zirconia nanoparticles. The main selected reagents were zirconium isopropoxide-isopropanol adduct, benzyl alcohol and sodium hydroxide as the zirconium, solvent and alkali sources, respectively. The preparations for all the synthesis were realized inside a glove box containing dry air to ensure minimal exposure to moisture.

For the chemical, morphological and structural characterizations, we combined different techniques in order to obtain a better insight into the nature of these particles. The structural characterization was given a particular attention and was realized by using X-ray total scattering (TS) and the atomic pair distribution function analysis (PDF). This tool specializes in analyzing the medium-range and short-range regions of the nanoparticles structure which gives invaluable information in identifying the kind of polymorph. Selected samples with peculiar structural features were investigated and allowed a much better understanding on the nature of its crystallization and stabilization.

The manuscript is divided into five chapters.

In the first chapter which is the state of the art we briefly discuss the relevant works done in synthesizing and characterizing nanocrystals. Here, we tackle more on the current issues related to the stabilization of metal oxide using a non-hydrolytic sol-gel route.

The details of the synthesis and characterization techniques are presented in the chapter 2. As mentioned earlier, the characterizations are categorized into three types: chemical (thermogravimetric analysis, inductive-coupled plasma mass spectrometry, X-ray photoelectron spectroscopy, proton nuclear magnetic resonance spectroscopy, and Fourier transform infrared spectroscopy), morphological (Transmission Electron Microscopy) and structural (X-ray diffraction and X-ray total scattering). In this section we briefly discuss the principles and mechanisms behind the mentioned characterization tools.

The chapter 3 presents the initial results on the synthesis of nano-size zirconia in a non-hydrolytic sol-gel route using two types of zirconium precursors. From successfully producing zirconia nanoparticles, we then demonstrate the fine tuning of the particles' size and phase purity by varying its operating temperature, amount of alcohol content and dual stage synthesis. Here, we selected some samples that have some interesting characteristics for in-depth characterization which proved to be indispensable in understanding their structural characteristics.

In the chapter 4, we focused more on the structural properties of the samples exhibiting interesting structural features and compared them to the four polymorphs of zirconia having a fluorite-derived structure. This was done by generating theoretical models of these polymorphs and comparing them with the experimental results. Out of these selected zirconia samples, we have chosen one of them which had a finite size inferior to 2 nm and a good crystallinity and conducted two kinds of experiments: the first was the investigation of the effects of thermally assisted ageing and the second was the effects of *ex-situ* water on the structural characteristics of the sample.

Finally, in the fifth and last chapter, we performed complementary experiments to investigate the effects of both cationic and anionic counterparts of sodium hydroxide and other inert or acid-base salts and solvent-type by substituting benzyl alcohol with other alcohols or ethers. Combined with the results obtained from other chapters, we proposed schemes that describe the formation of various types of zirconia nanoparticles and future recommendations derived from the experimental works.

Chapter 1: State of the art

1 State of the Art

1.1 Introduction

Nanotechnology plays a vital role in the technological advancement of various fields in science and engineering. Often, nanotechnology is considered as the foundation of the 20th century and beyond. But it has also played roles in the ancient times such as the manipulation of gold and silver nanoparticles to create changing color effects in the Lycurgus cup (Figure 1) or create various colors in medieval stained glass windows in churches in the 4th and 6th century, respectively [16].

Figure 1: Lycurgus cup photographed (a) front-lit with flash, the cup appears in the green color it has without light coming through the cup and (b) appearance when back-lit.

Despite such achievements in early periods, the mechanisms remained unknown to the artisans and craftsmen who made such intricate designs using such tiny particles. It was not until 1959 when the ideas and concepts about nanotechnology were given much interest in the form of a lecture by the physicist Richard Feynman at the California Institute of Technology [17]. His lecture posed several questions and proposed answers in dealing with general manipulation of matter on the atomic scale and catalyzed several researches. A decade later (1974), Professor Norio Taniguchi coined the term “nano-technology” to describe semiconductor processes such as thin film deposition and ion beam milling in the nanometer scale (10^{-9} m) [18]. But only in the advent of the scanning tunneling microscope in the year 1981 when we were able to “see” individual atoms for the first time which awarded the inventors Gerd Binnig and Heinrich Rohrer the Nobel Prize in

Physics in 1986 [19]. From then on the number of publications related to nanotechnology and nanoscience has increased significantly (see Figure 2 and Figure 3).

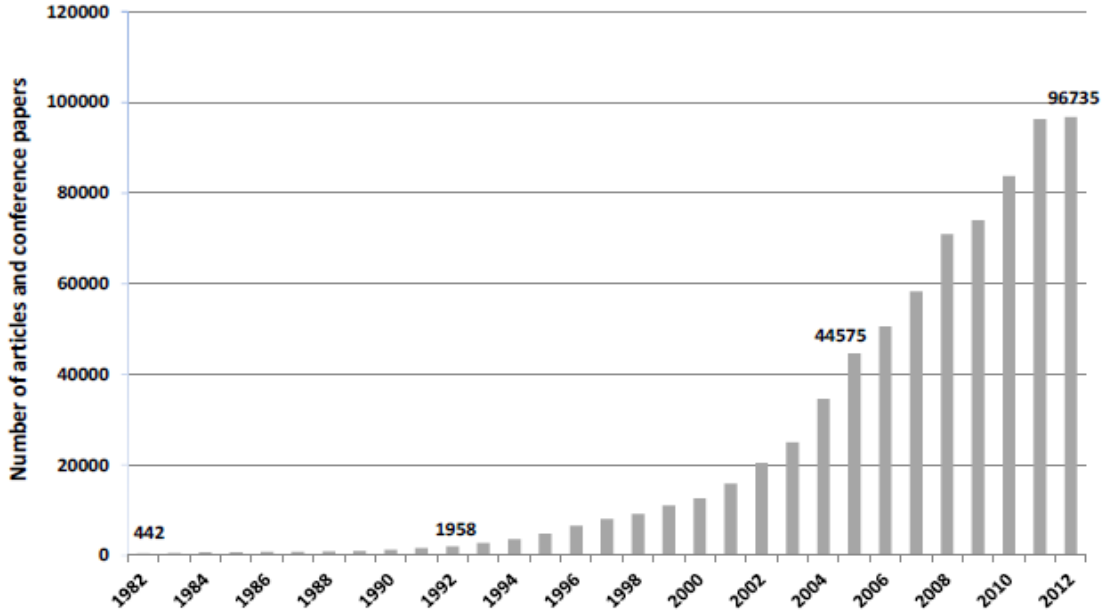

Figure 2: Evolution of the number of articles and conference papers in nanotechnology: 1982-2012 [20].

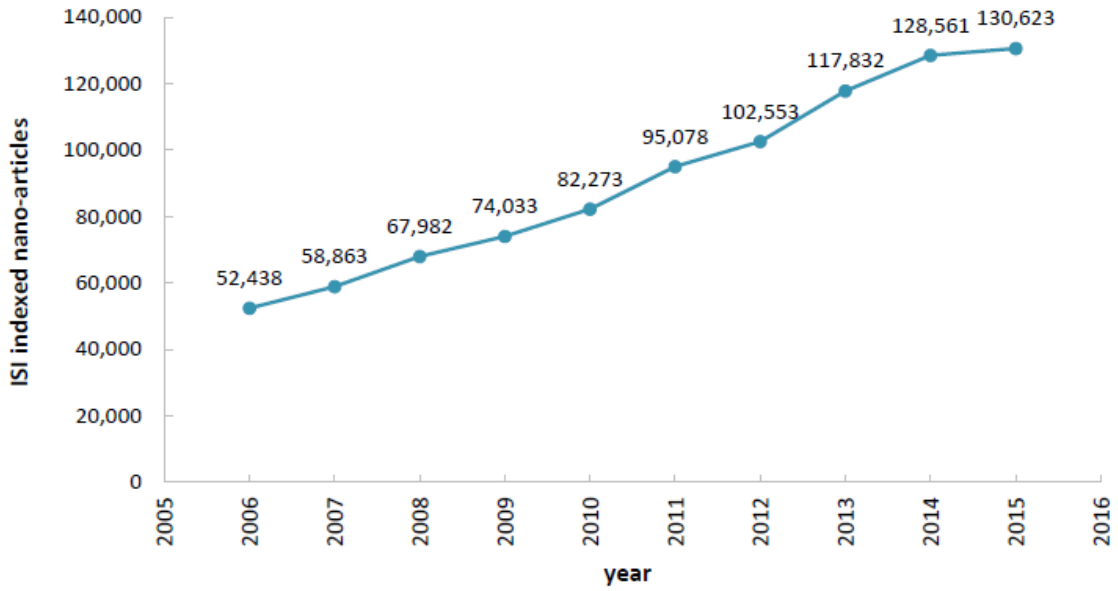

Figure 3: Number of ISI indexed Nano®-articles in 2006-2015 [21].

Generally, the scale of nanomaterials is within the range of 10^{-10} to 10^{-7} m or 0.1 nm to 100 nm as shown in Figure 4. This range consists of particles that the normal or naked eye can no longer see since it is way below our detection limit which is around 100 μm unaided by any tool.

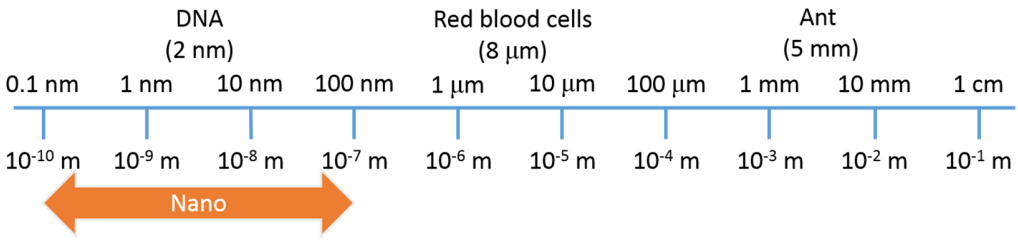

Figure 4: General scale of nano-materials.

For inorganic crystals, the nanoparticles can be considered simply as the miniature version of their large counterpart thus exhibiting similar structural and electronic properties. However, there have been much interest on the nanoparticles with less than 10 nm in size which properties are ruled by quantum confinement effects caused by the finite size of the particles [4]. Nanosize is also presumed to have substantial effect on the structure of the material that also modifies their properties which are neither that of the atomic nor bulk characteristics [22]. For example, semiconductor nanocrystals are small crystalline particles which are typically synthesized with dimensions ranging from 1 to 100 nm. Since the discovery of nanocrystals embedded in glasses in the early 1980s, they have attracted considerable attention as a new category of materials for electronics. Semiconductor materials are characterized by their band structures (direct or indirect) and a band gap energy (E_{gap}) that falls within a range of between $0 < E_{gap} < 4\ eV$, and can be thought of as the minimum energy required to excite an electron from the valence band (VB) to the conduction band (CB). Furthermore, if one dimension of a semiconductor is smaller than the Bohr exciton radius of the material, the band structure will be modified and blue shifted to higher energy by the quantum confinement effect. In the case of very small particle size, the so-called strong confinement regime, quantized levels appear which is distinct with the continuous band of bulk counterparts and shows characteristics of the discrete molecular semiconductors as illustrated in Figure 5.

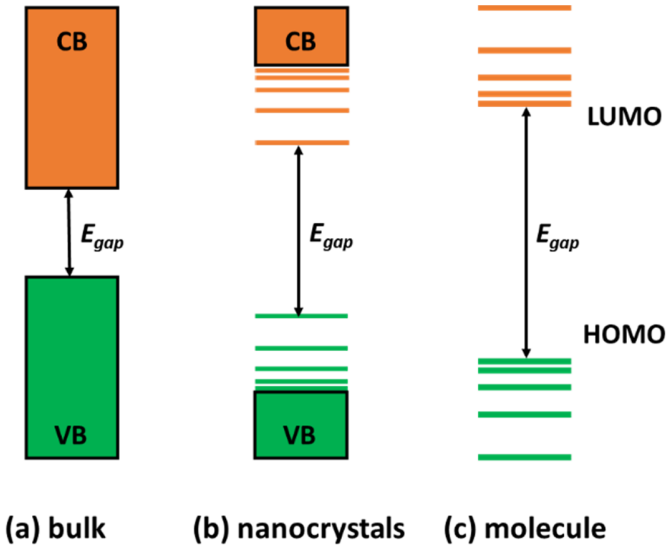

Figure 5: Schematic illustration of the electronic energy states of semiconductor materials as (a) bulk material, as (b) nanocrystals and (c) molecular state.

These quantum confinement effects vary depending on the shape or dimensions of the nanomaterial as shown in Figure 6. Despite the difference in shape of the three types of dimensions (0D, 1D and 2D) of nanoparticles, they can all be characterized by the following qualities: they can be amorphous or crystalline, can be single crystalline or polycrystalline, can be composed of single or multi-chemical elements, can exist individually or incorporated in a matrix, and can be metallic, ceramic, molecular, or polymeric in nature. For 0-Dimension nanomaterials, the electron is confined in a 3-dimensional space and no electron delocalization occurs. For 1-Dimension nanomaterials, the electron is confined in a 2-dimensional space where the delocalization takes place along the long axis of a nanowire, rod or tube. And for the 2-dimension nanomaterials, the electrons are confined across the thickness but delocalized in the plane of the sheet. These confinement effects can be calculated by quantum mechanics as the “particle in a box problem” where the energy levels are in discrete arrangement closer to the energy levels of the atomic state.

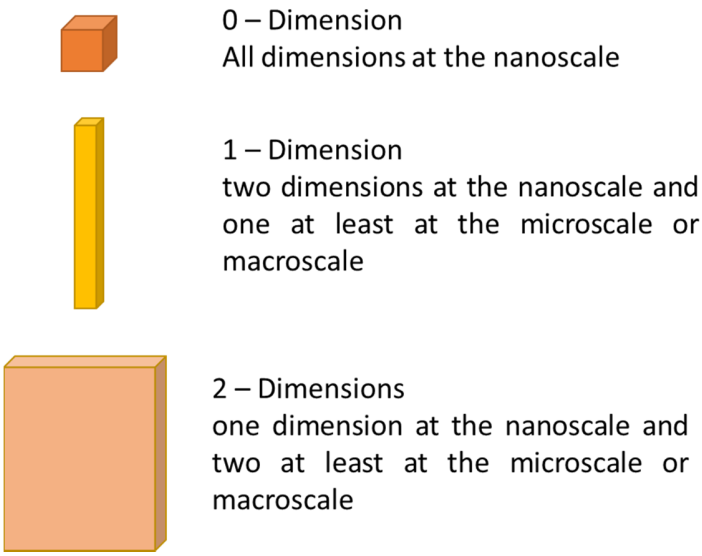

Figure 6: Various possible dimensions of nanoparticles.

The smallness in size of the inorganic particles would entail that they are composed of very few atoms and would suggest an influence in their structural arrangement where the fraction of atoms on the surface would be larger as compared to the atoms in the core. This also suggests that the chemical characteristics of these tiny particles will be enhanced or altered as a subsequent effect of the alteration of size. Hence, aside from the quantum confinement effects, the particles may exhibit changes in phase transition pressure or temperature, melting & boiling points, optical, optoelectronic, catalytic, magnetic and electric properties which are different to that of their bulk versions or to that of their molecular species precursors [23] [24] [25] [26] [27] [28] [29]. From such novel properties, various potential fields in science and engineering for nanotechnology has sprung up and created new materials as shown in Figure 7 [30].

Although there are several types of nanomaterials that can be produced for different applications, in this work we focus on the synthesis and characterization of nanosize metal oxide of the d^0-transition metal oxide, namely TiO_2 or ZrO_2. Transition metals are defined as elements whose electrons have partially filled subshell *d* and they are located at the *d*-block of the periodic table within the groups 3 to 12. In some cases the *f*-block lanthanide and actinide series are also considered as transition metals and are called the “inner transition metals” [31]. The electronic characteristics observed for transition metals provide unique properties for the transition-metal

oxide such as high dielectric constants [32] [33], reactive electronic transitions [34] [35], good electrical characteristics [36] [37] and modified band gap [38] [39]. These features induce a new state of matter having altered properties such as ferromagnetic state, ferrimagnetic state and semiconductive state. Despite the current knowledge of the properties of nanosize transition-metal oxides it is still at its infancy and requires a deeper understanding.

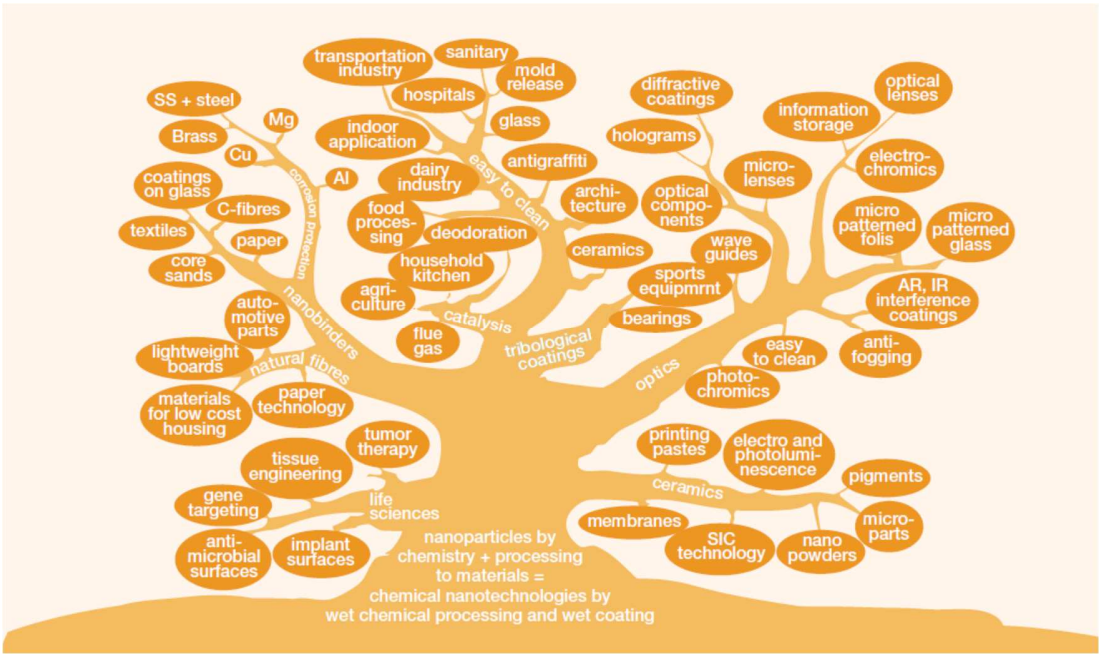

Figure 7: Various potential application areas for nanotechnology [30].

There are various ways of synthesizing nanosize materials but generally it can be categorized into two types of approaches: the top-down approach and the bottom-up approach as shown in Figure 8. The top-down approach is initiated by a bulk material which is reduced to powder size around the microscale. The powder is then reduced further to the nanoscale by some processes which can either be mechanical or chemical. However, the size that can be achieved via top-down approach is very limited (200 to 50 nm) in comparison to the bottom-up approach. Although it is possible to rectify this problem in order to reach smaller sizes, the cost would rise significantly [40]. Another alternative to this is the bottom-up approach which is governed mostly by chemical principles. The bottom-up approach solves the problem of size limitation of top-down approach by starting at the metalorganic reagents. Then a “crystal embryo” having similar characteristics to that of an inorganic molecular clusters is formed and then transformed into the stable seed *nuclei*. Finally

nanocrystals having sizes inferior to 5 nm can be obtained. This type of approach is invaluable if we want to understand the formation mechanisms of such tiny oxidic materials that exhibit unique properties and states.

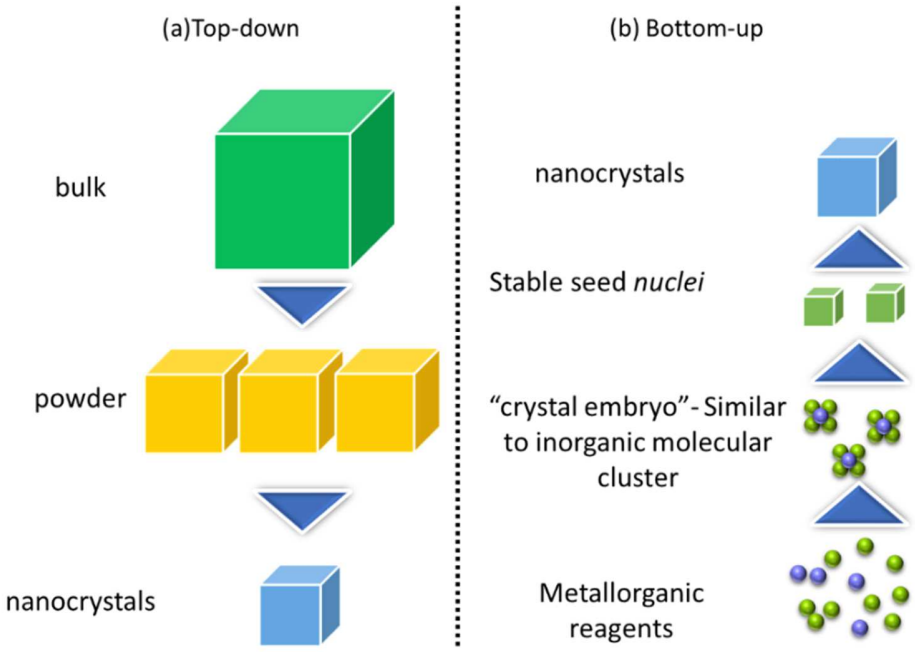

Figure 8: (a) top-down and (b) bottom-up approaches for the synthesis of nanomaterials.

There are various types of synthesis that follow the principles of bottom-up approach such as chemical vapor deposition, plasma or flame spraying synthesis, laser pyrolysis, atomic or molecular condensation, and sol-gel chemistry. Sol-gel chemistry offers several advantages due to its simplicity in preparation and relatively low-cost in comparison to the other mentioned methods. There are various products that can be obtained using sol-gel chemistry as summarized in Figure 9. By manipulating the process steps they can be obtained and tailored to fit any design, which suggests the versatility of the sol-gel route [41]. In this dissertation, we denote any process as "sol-gel", as long as the transformation of the molecular precursor into the final oxide compound involves chemical condensation reactions in liquid medium under mild conditions. Before to speak about the basics of the crystallization occurring during the chemical procedure, it is necessary to recall the details of the sol-gel chemistry.

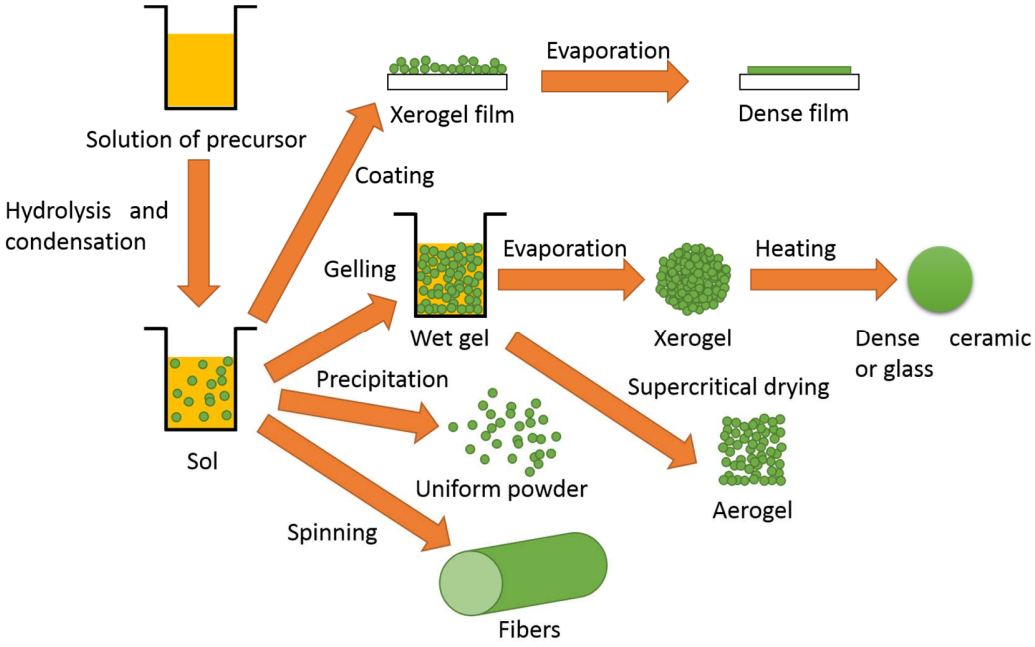

Figure 9: Steps in the sol-gel chemistry producing various products [42].

1.2 Sol-gel processing for nanoparticles synthesis

Sol-gel processing, as one category of the so-called soft chemistry and based on the use of metal precursors (alkoxide, salt, and halide), is widely utilized because of its favorable qualities in regard to the particle size and sample characteristic manipulation. The sol-gel synthesis implies the production of monomers which are then turned into colloidal suspension or sol which is constituted by solid particles in a liquid with sizes varying from 1 nm to few hundreds nm. The size of these particles is quite small and gravitational effects can be ignored into the sol. It means that the interactions are dominated by short-range forces such as van der Waals interactions and surface charges [42].

Typically, the precursor used for sol-gel synthesis consists of a metal or metalloid element center surrounded by ligands such as alkoxides and/or inorganic anions. One of the most studied example of metal alkoxide is the silicon tetraethoxide ($Si(OC_2H_5)_4$) which permits to synthesize silica at moderate temperature in a hydrous solvent medium. Figure 10 shows the evolution of the silicon precursor under acidic, neutral or basic condition but this view is analogous for other materials.

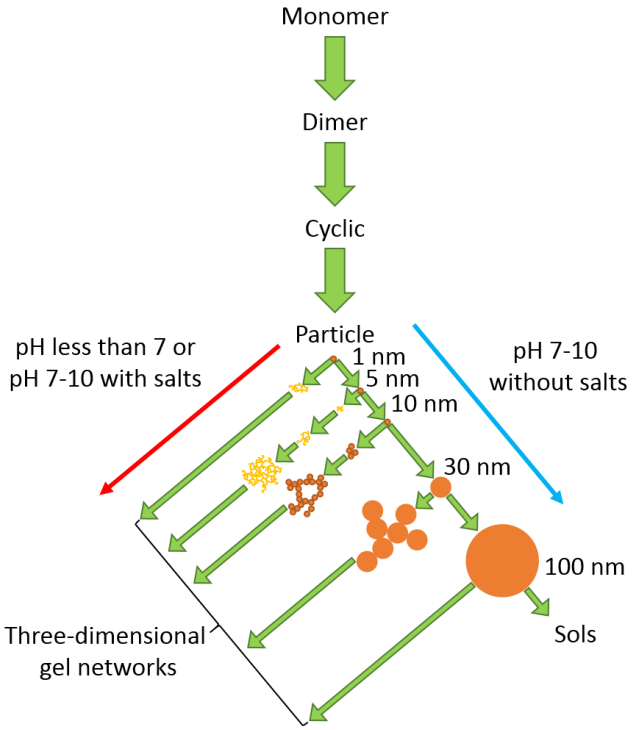

Figure 10: Inorganic polymerization of aqueous silica under acidic and basic condition [43].

In this model the sol-gel processing occurs in three distinct stages. The first step is the formation of oligomeric species by hydrolysis and condensation reactions, *i.e.*, the polymerization of the molecular precursors into a highly crosslinked cluster. This cluster will serve as a seed *nuclei*. Second, the *nuclei* reaching the critical radius begins to increase in size by progressive addition of monomers and/or Ostwald ripening mechanism and lead to a sol, a dispersion of colloidal particles in a liquid. And third, the linking of particles into chain and further condensation result in a network that extends through the liquid medium as a gel [42]. The easy agglomeration or aggregation of fine clusters or particles (sol particles) is caused by attractive van der Waals forces and/or minimization of the total surface or interfacial energy of the system. Evidently, the adsorption of an organic layer (steric "barrier" or hindrance) and the presence of electrostatic repulsion between particles can prevent the aggregation by opposing repulsive forces and stabilize the sol.

At this stage of the manuscript, we should distinguish two main sol-gel chemistry using metal alkoxide as precursor namely the "hydrolytic sol-gel chemistry" and the "non-hydrolytic sol-gel chemistry" which refers respectively to the synthesis of metal oxides in presence of water (aqueous

medium, *e.g.* aqueous alcohol) and in organic solvents. In some cases, when a hydrated metal oxide precursor is used or when water is produced *in-situ*, it is no more possible to exclude a hydrolytic reaction pathway and some researchers prefer to use the terminology "non-aqueous sol-gel chemistry". This implies that water is not only implicitly added but the product of a side-reaction.

1.2.1 Hydrolytic sol-gel processing

Sol-gel polymerization and sol-gel transition were discovered and studied by Ebelmen in 1845-47 who worked on the glass conversion of silicic acid under the action of moisture, but the first sol-gel patent (patent DE736411C) was only deposited in 1939 by the *Schott-Glaswerke* German firm, almost one century after the first experimental evidence of the effective process [44].

Chemical aspects play an important role in studying and controlling the sol-gel process in order to obtain an aerogel, a glass or some nanoparticles. The reactivity of the metal precursor in aqueous medium depends mainly on the electronegativity of the metal atom, its ability to increase or not the coordination number, the steric hindrance of the alkoxy groups, and on the molecular complexity of the initial precursor and all the intermediate products.

1.2.1.1 Hydrolysis and condensation

1.2.1.1.1 Hydrolysis

Hydrolytic or aqueous sol-gel processing using a metal alkoxide precursor is achieved by the combination of the hydrolysis and condensation of the metal alkoxide in water or rather in water-based solvents due to the immiscibility of the organic compounds. The hydrolysis reaction (and reverse reesterification of the metal hydroxide bond) is shown in Equation (1) for one group only.

$$\equiv M - OR + H_2O \rightleftarrows \equiv M - OH + ROH \qquad (1)$$

As observed, the alkoxy group (*OR*) was exchanged by a hydroxyl one via a nucleophilic attack of the oxygen atom of a water molecule and followed by the release of alcohol (*ROH*). The amount of added water, the pH of the mixture and the way how this water was delivered determined whether the alkoxide groups were completely hydrolyzed or not, and which intermediate oligomeric species were formed.

1.2.1.1.2 Condensation by oxolation, alcoxolation and olation

Immediately after the hydrolysis was initiated and largely before it was completed, the condensation step started. There are three possible competitive ways to form the metal-oxide bridge, *i.e.* oxolation, alcoxolation and olation and they are given by Equations (2) and (3).

The former equation is the condensation between two partially hydroxylated metal alkoxides which produces water as the final product (oxolation, and reverse hydrolysis of metal oxide bond). This water can also be used for further hydroxylation following Equation (2). The latter Equation (3) is the condensation between a partially hydroxylated metal alkoxide with a metal alkoxide which leads to the release of alcohol (alcoxolation and reverse alcoholysis of metal oxide bond). Both can act in combination in order to connect more molecules forming a large inorganic network.

$$\equiv M - OH + HO - M \equiv \rightleftarrows \equiv M - O - M \equiv + H_2O \quad (2)$$

$$\equiv M - OR + HO - M \equiv \rightleftarrows \equiv M - O - M \equiv + ROH \quad (3)$$

In a nonpolar solvent, an alcolation reaction proceeding by an olation-like mechanism will result in the formation of an alkoxy bridge as shown in Equation (4).

$$2(M - OR) \rightleftarrows \quad \begin{matrix} & OR & \\ M & & M \\ & OR & \end{matrix} \quad (4)$$

As seen in Table 1, compared to silicon which is less electropositive and possesses a smaller partial positive charge, the large partial charge of titanium and zirconium makes the transition metals excessively susceptible to nucleophilic reagents. This causes the kinetics of hydrolysis and condensation to be much faster than what was observed for silica.

Moreover, unlike silicon alkoxides, transition metal alkoxides exhibit several possible coordination numbers larger than their valence. When they are coordinatively unsaturated, they are able to expand their coordination by using their vacant d-orbitals to accept Lewis base solvents lone pair.

Table 1: Cationic size, stable coordination, Pauling's electronegativity and partial charge distribution for metal cation in metal ethoxides

Metal ethoxide $M(OEt)_4$	**Cation size**	**Stable coordination**	**Pauling's EN**	**δ_M**
$Si(OEt)_4$ (TEOS)	0.41 Å	4	1.8	+ 0.32
$Ti(OEt)_4$	0.68 Å	6	1.5	+ 0.63
$Zr(OEt)_4$	0.80 Å	7 or 8	1.4	+ 0.65

Indeed, according to Livage *et al.*, the hydrolysis rate of $Ti(OR)_4$ is about 10^5 times faster than the case of $Si(OR)_4$ with the same alkoxide substituents. The reactivity of some tetravalent isopropoxides in hydrolysis reactions increases in the following order:

$$Si(O^iPr)_4 <<< Sn(O^iPr)_4, Ti(O^iPr)_4 < Zr(O^iPr)_4 < Ce(O^iPr)_4$$

It results from this feature that the degree of oligomerization is important to consider in the sol-gel processing of such metal alkoxides. Coordination expansion occurs via OR bridges. The degree of oligomerization influences not only the solubility of the metal alkoxides but also the reaction kinetics. For example, monomeric $Zr(O^nPr)_4$ is hydrolyzed more rapidly than polymeric $Zr(OEt)_4$ despite the larger alkoxo ligands. Indeed, metal alkoxides can associate μ_2- or μ_3-OR bridges (the label 2 or 3 denotes the number of metal atoms coordinated to the bridging ligand). The degree of association depends on the size of the metal and on the size of the organic chain due to steric hindrance favoring a lower degree for larger alkyl group.

Another way to increase the coordination number can occur when the alkoxide is dissolved in polar solvents and forms a solvate (adduct). Then, addition of solvent can occur and compete with association. Upon hydrolysis, the coordinated solvent is more easily cleaved than the alkoxide bridge. $[Zr(O^iPr_4)\bullet HO^iPr]_2$ which is the widely used zirconium precursor in this work is an example of molecular specie obtained by both association via O^iPr bridge and HO^iPr coordinated solvate.

Finally, olation can occur when the full coordination of a metal is not achieved. It is generally the case for titanium and zirconium under the form of $M(OR)_4$ and able to reach respectively a [6]-fold and [8]-fold coordination. Bridging hydroxo groups can be formed through the elimination of a

solvent molecule. The latter is either H_2O or ROH depending on the water content of the medium as shown in Equations (5) and (6):

$$\equiv M - OH \; + \{\equiv M \longleftrightarrow (ROH)\} \rightleftarrows \equiv M - (OH) - M \equiv + ROH \qquad (5)$$

$$\equiv M - OH \; + \{\equiv M \longleftrightarrow (OH_2)\} \rightleftarrows \equiv M - (OH) - M \equiv \; + H_2O \qquad (6)$$

The kinetics of such nucleophilic substitution is governed by the global charge distribution. The reaction is strongly favored when the nucleophilic character of the entering group and the electrophilic strength of the metal are high. Moreover, since no proton transfer is involved within the transition state, the reaction rate is usually quite fast when possible.

1.2.1.2 Influent factors on hydrolysis and condensation kinetics

1.2.1.2.1 Acid- or base-catalyzed processing

The rapid kinetics of nucleophilic reactions causes the fundamental studies of the hydrolysis and condensation of transition metal alkoxides to be more complex. Nevertheless, the relative slow rates of hydrolysis and condensation of silicon alkoxides facilitated the emergence of studies related to the catalytic role of acids, bases, and solvents. The use of catalysts such as mineral acids, ammonia, acetic acid, alkaline hydroxide, alkaline fluoride and hydrofluoric acid is widespread in literature and the general consensus of opinion is that mineral acids are more effective as catalysts than an equivalent amount of base. However, the changing properties of the intermediate products and the retro-reactions generating unhydrolyzed species via base-catalyzed alcoholic or hydrolytic depolymerization processes would need to be considered. Hydrolysis using silicon alkoxide seems to be *first order* with respect to acid or base concentration but as the concentration of TEOS was increased, the reaction no longer followed a simple order and became complicated by secondary reactions. Nevertheless, the hydrolysis mechanism can be presented as follows:

- The first step is a nucleophilic addition of a water molecule to the positively charged metal atom M. This leads to a transition state where the coordination number of M has been increased by one.
- The second step involves a proton transfer within the intermediate leading to the next transition state. A proton from the entering water molecule is transferred to the negatively charged oxygen of an adjacent OR group.

- The third step is the departure of the better leaving group, which should be the most positively charged species within the second transition state as shown in Figure 11.

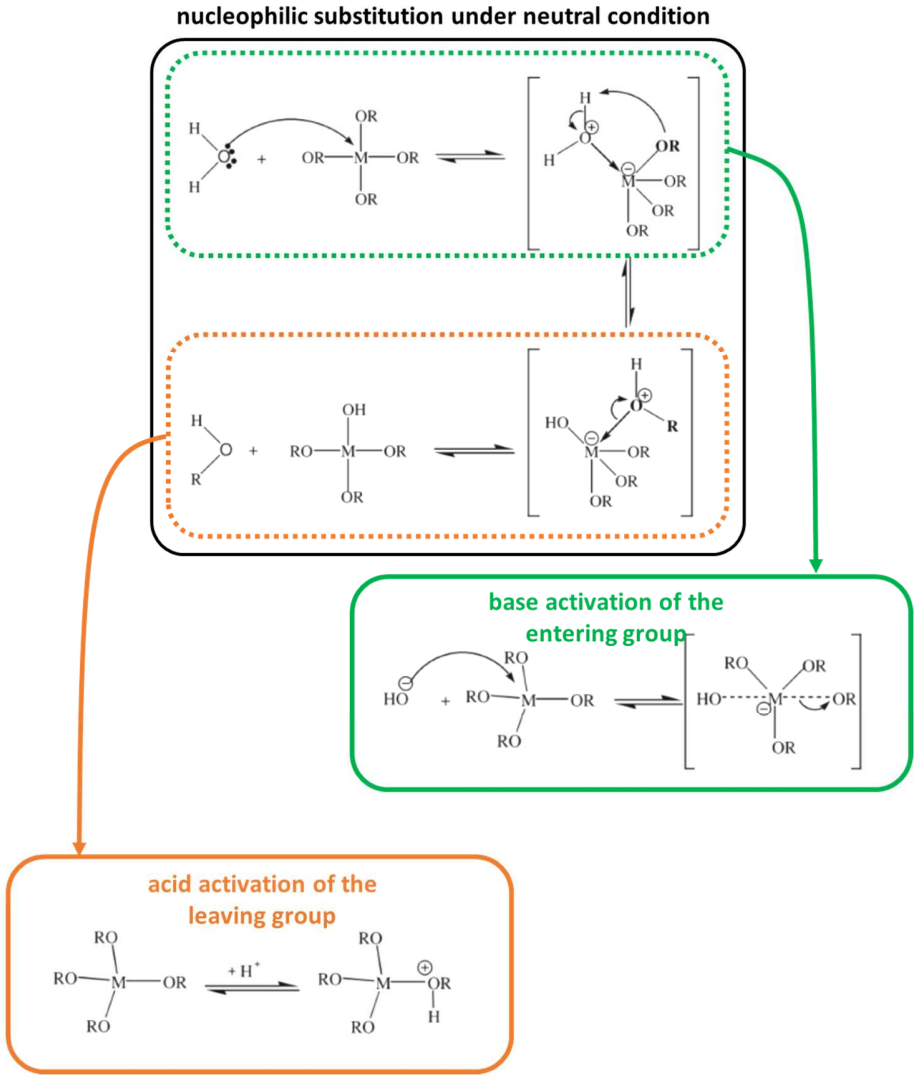

Figure 11: Hydrolysis mechanism under neutral condition and corresponding acid or base activation

The following parameters determine the kinetics of the reaction:

(1) The electrophilic character of the metal center as mentioned in Table 1,

(2) The nucleophilic character of the entering molecule,

(3) The nucleofugal character of the leaving group,

(4) The coordination state of the precursor: the more unsaturated the coordination, the lower the activation energy associated with the nucleophilic addition,

(5) The ability to transfer a proton: the more acidic the proton, the lower the activation energy associated with the proton transfer.

If the synthesis is performed for example under acidic conditions, steps 3 and 5 are no longer rate-limiting in the global hydrolysis pathway. The global mechanisms are given in Figure 12.

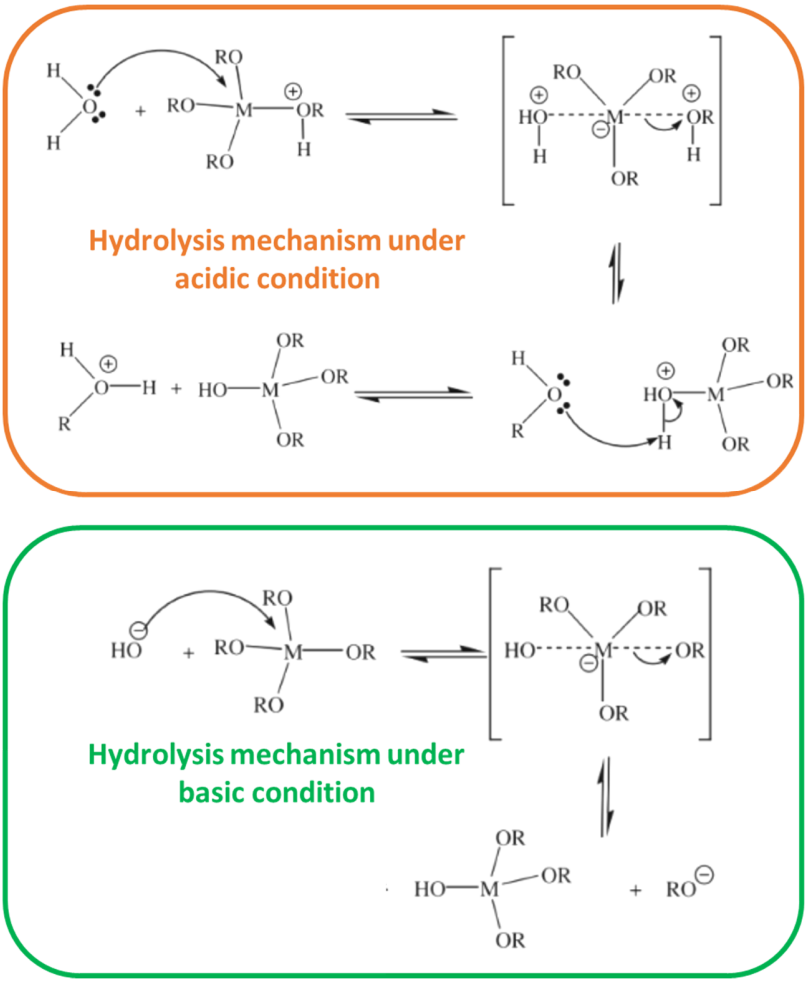

Figure 12: Hydrolysis mechanism under acidic or basic conditions.

The mechanisms for oxolation and alcoxolation are basically the same as in the hydrolysis; so globally the acid- or base-activation, of respectively, the leaving group (protonation) or the entering group $(RO)_3M\text{-}O^-$ obtained by deprotonation of an hydroxyl group is effective in condensation reactions. Figure 13 summarizes the mechanisms of oxolation and alcoxolation.

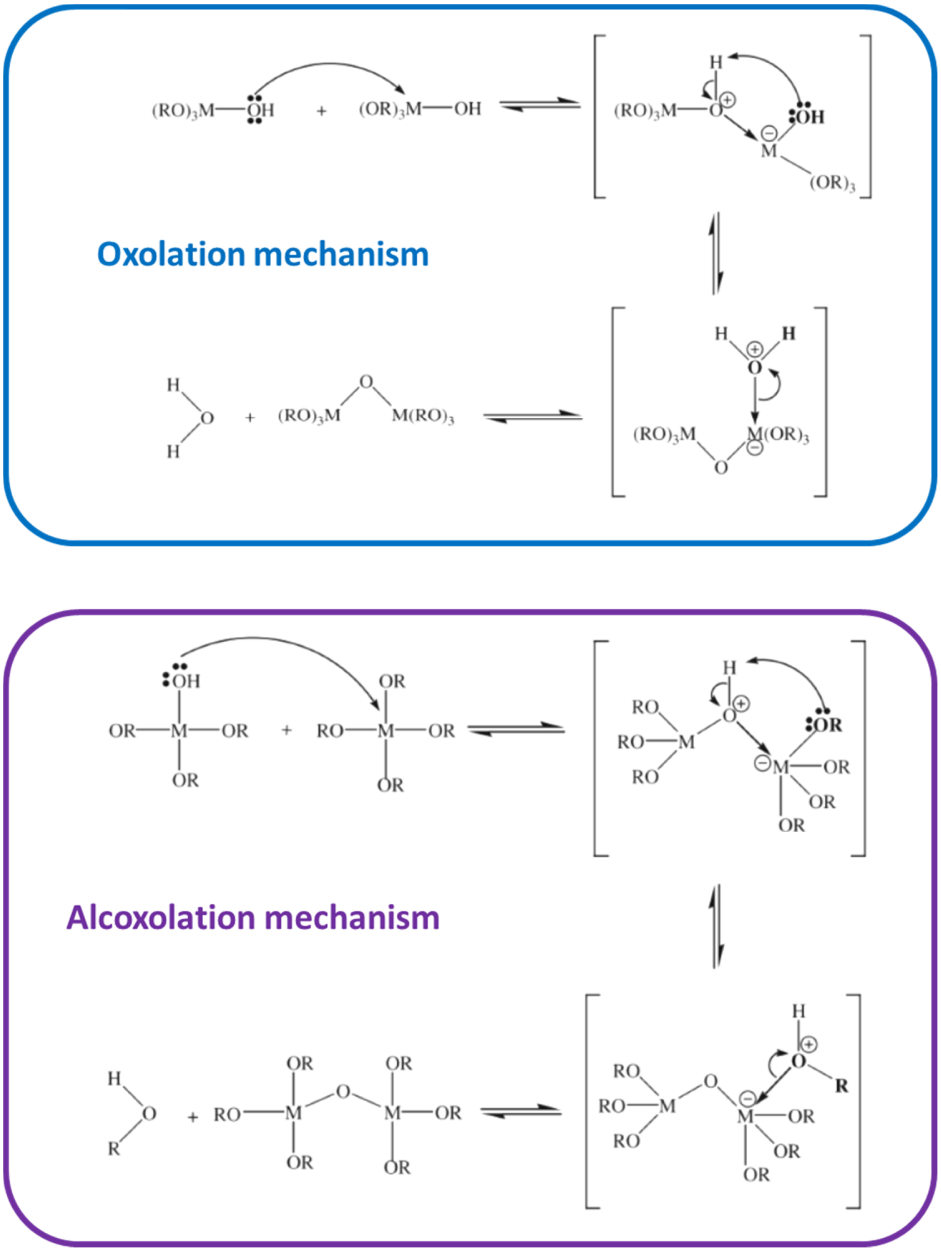

Figure 13: Oxolation and alcoxolation mechanisms for condensation step.

1.2.1.2.2 *Steric hindrance and inductive effects*

Another influent factors are the steric and inductive effects that have a large influence on the hydrolytic stability of the species. Any branching or extension of the alkyl chain length, or the presence of aromatic ring reduce the rate of hydrolysis. Inductive effects result in alterations of the hydrolysis rate too. Under acidic conditions the rate of hydrolysis decreases with each subsequent

hydrolysis step (electron withdrawing), but under basic conditions, the increased electron withdrawing capabilities of OH compared to OR may result in a favorable condition in which each subsequent hydrolysis step makes the hydrolysis faster.

Since the reactions in acidic conditions are favored due to the large electronic density on the metal center able to stabilize the positively-charged transition state, electron-providing goups improve the reaction rate by reinforcing the pH-dependence of the condensation mechanism. Conversely in basic medium, electron-withdrawing groups able to decrease the electronic density of the metal center accelerate the reaction as it is shown in Figure 14.

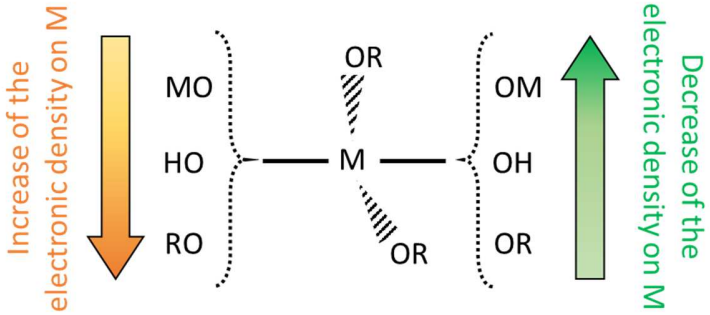

Figure 14: Schematic illustration of the inductive effects of alkoxide, hydroxide or metal oxide groups on the electronic density of the metal center.

1.2.1.2.3 Solvent role and effects

The solvent in sol-gel processing was initially used to prevent phase separation to occur during the early stages of hydrolysis and to control the relative concentrations of metal alkoxide and water that influence the gelation kinetics. However, the choice of the solvent is also of importance due to its potential solvating ability that influences the chemical activity of the species, solutes, monomers, transient intermediates etc. The main features of the solvent that we have to take in account are: its polarity, solvating ability and presence of labile protons:

- Polarity of the solvent is important in determining its solvating ability for polar or nonpolar solutes. Solvents such as water or alcohols which are polar are used to solvate polar species used in sol-gel processing. Less polar solvents can be used to limit an extensive hydrolysis for example.

- The lability of protic solvent determines the strength of solvation of cations and anions through hydrogen bonding. If solvent molecules bond to hydroxyl or hydronium ions then the catalytic activity of these ions is reduced. Moreover, such solvents influence the extent of the reverse reactions, namely reesterification (reverse of hydrolysis) or the metal oxide hydrolysis or alcoholysis. Aprotic solvent do not participate in reverse reactions like reesterification of M-OH or hydrolysis of M-O-M since they do not possess any sufficiently electrophilic protons nor the ability to be deprotonated to form the strong nucleophiles required for these reactions.
- Protic solvents form hydrogen bond with nucleophilic deprotonated species, *i.e.* alcoholate, whereas aprotic solvents bond to electrophilic protonated ones. As a consequence, protic solvents slow down base-catalyzed condensation and increase the rate of acid-catalyzed condensation, whereas aprotic solvent has the reverse effect.
- Solvents used in sol-gel processing also have the ability to promote depolymerization of the metal oxide network. Nucleophiles, such as HO^-, are involved in the base-catalyzed hydrolysis of metal oxide bonds (reverse oxolation), while aprotic solvents cannot hydrogen bond to HO^- thus making it a stronger nucleophile. This promotes restructuring and results in a greater condensed species.

1.2.1.2.4 Consequences

The acidic or basic conditions in selected solvents or co-solvents have a profound effect on the way the polymeric clusters grow. In acidic condition, it appears to favor the long chained networks which is in contrast with the basic condition that favors compact formation. As an illustration, different partially-hydrolyzed and condensed titanium polymers are shown in Figure 15.

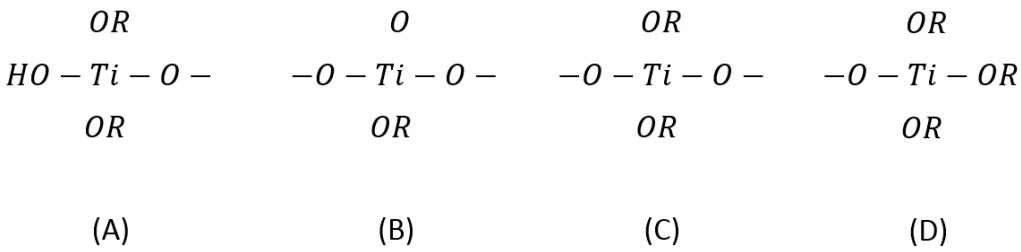

Figure 15: Different types of partially hydrolyzed titanium polymers.

Charge calculations were performed by Livage *et al.* on different moieties of this polymer identified as (A, B, C and D) and gathered in Table 2:

Table 2: Various charges of the different types of polymers

Site	δ (OR)	δ (M)
A	-0.01	+0.70
B	+0.22	+0.76
C	+0.04	+0.71
D	-0.08	+0.68

For acid-catalyzed condensation, the ease of protonation decreases as D >> A > C >> B which reflects on the electron-providing power of the type of ligands (alkoxy > hydroxo > oxo) [42]. This promotes in a chain-like growth since the condensation occurs preferentially on the ends rather than in the middle of the chain.

In contrast, the base-catalyzed condensation shows that the order of reactivity follows the decrease from B >> C ≈ A > D which is correlated to the decrease of the positive charge of the titanium atom when nucleophilic addition of HO^- occurs. Using NH_3 or NaOH, condensation is always activated through the formation of highly nucleophilic species such as $M-O^-$:

$$M-OH+B \rightleftarrows M-O^- + BH^+$$

This reactive condensation precursor will attack the more positively charged metal atom. This condensation favors the middle rather than the ends of the chain thus resulting in a more compact and highly branched species [42]. Figure 16 shows a schematic representation of the products obtained for the acid- or base-catalyzed reaction.

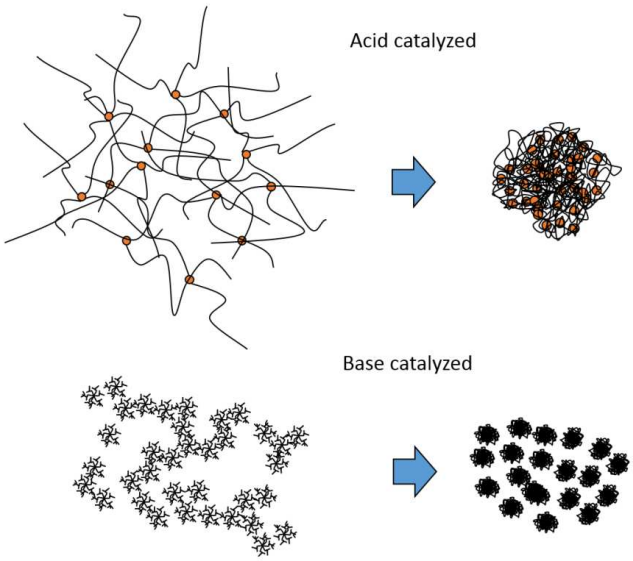

Figure 16: Schematic representations of the products obtained by either an acid- or a base-catalyzed reaction.

1.2.1.3 Hydrolytic route to metal oxide nanoparticles

We could retain from the few last paragraphs that these four reactions (hydrolysis, alcoxolation, oxolation, olation) may be involved in the transformation of a molecular precursor into an oxide network. The structure and the morphology of the resulting oxide strongly depend on the relative contribution of each reaction. These contributions can be optimized by carefully adjusting the experimental conditions which are related to both *internal* (nature of the metal atom and alkyl groups, structure of the molecular precursor) and *external* (water-to-alkoxide ratio, catalyst, concentration, solvent and temperature) parameters.

Nevertheless, the quite high reactivity of the metal oxide precursor (except for silicon alkoxide) and the double role of water as a ligand and solvent which allows the hydrolysis, condensation and aggregation to occur almost simultaneously make it difficult to have an effective control over the size and the phase purity if the target product is to get nanoparticles. Indeed, the aqueous sol-gel process leads frequently to some amorphous precipitates and the required post-synthetic annealing step to induce crystallization ruins any chance to get a good control over the crystal size and the shape especially if the issue of the synthesis is to obtain isolated nanoparticles.

One possibility to decrease and to adjust the reactivity of the metal precursor is the use of organic β-diketones which act as chelating ligands and moderate the reactivity of the precursor. Two

methodologies were used to obtain crystalline material at the nanosize as shown in Figure 17 and Figure 18.

- Moderate heat treatment of a zirconia aerogel obtained by gelation and supercritic evaporation of an acidic mixture of 2,4-pentanedione, water and zirconium n-propoxide in HO^{n}Pr [45],

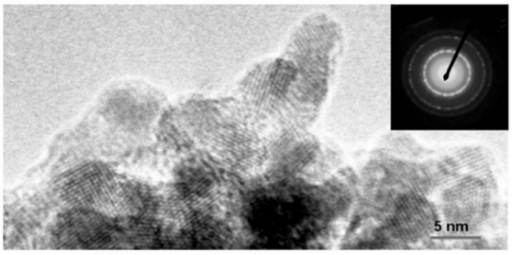

Sample	Av. nanocrystals size
Aerogel at 1000°C	> 20 nm
Aerogel at 650°C	5-6 nm
Aerogel at 350°C	2-3 nm
Raw aerogel (270°C/5,5GPa)	< 2 nm

Figure 17: TEM micrograph of a zirconia aerogel heat-treated at 350°C, corresponding SAED pattern and average nanocrystals size at different annealing temperature.

- Displacement of the keto-enolic tautomerism and *in-situ* crystallization of zirconia from a 2,4-pentanedione-modified zirconium n-propoxide precursor in a mixture of water and HO^{n}Pr by the use of a strong organic acid, namely tosylic acid (PTSA), at 80°C [46].

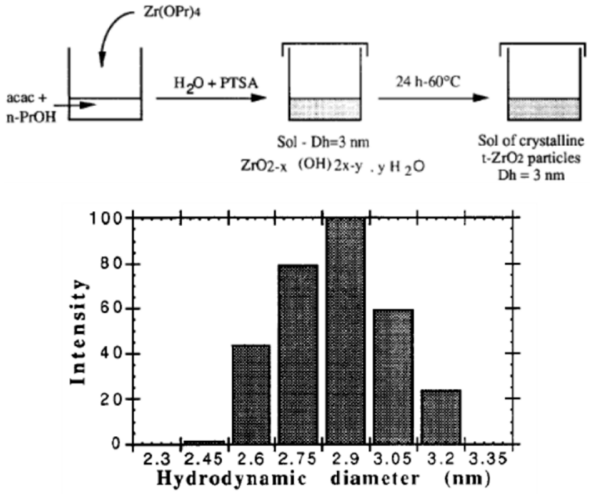

Figure 18: Experimental protocol for the synthesis of t-ZrO_2 colloidal nanocrystals.

1.2.2 Non-aqueous sol-gel processing

In non-aqueous sol-gel chemistry, the synthesis of nanomaterial is relatively sophisticated and essentially based on the direct aprotic condensation (strictly non-hydrolytic process) or on the non-aqueous hydroxylation of the metallic precursor, followed by the condensation of the hydroxylated

precursor. Aprotic condensation typically results in an ether elimination of (R_2O) (and reverse, etherolysis) shown in Equation (7).

$$\equiv M - OR + RO - M \equiv \rightleftarrows \equiv M - O - M \equiv + R_2O \qquad (7)$$

This reaction is known to be more difficult to occur in comparison to those of the aqueous sol-gel chemistry due to the organic nature of the solvent and ligands and to the high activation barrier that offers a kind of control over the morphology and the *in-situ* crystallization of the oxidic material. Moreover, non-aqueous sol-gel chemistry is far more favorable in the synthesis of metal oxide nanoparticles due to its ability to produce nanoparticles with good homogeneity, crystallinity, phase purity and size control [47]. Similarly, non-aqueous procedures can be classified further into surfactant- or solvent-controlled strategies. In the next sections, we will discuss the advantages and disadvantages of the two strategies.

1.2.2.1 Surfactant-controlled syntheses

Surfactant-controlled non-aqueous sol-gel synthesis is commonly used to synthesize monodispersed nanoparticles by a strong surface stabilization. Generally nanoparticles have a high surface area to volume ratio (specific surface area, SSA) which favors agglomeration. This behavior is driven by the need to reduce the large surface energy of the particles and the introduction of surfactant reduces efficiently the agglomeration of the particles by coating its surface. The surfactant molecules that cap the surface create a steric hindrance between nanoparticles.

1.2.2.1.1 Hot-injection synthesis

This process which was developed by Murray *et al.* in 1993 for the synthesis of monodisperse cadmium chalcogenide nanocrystals consists in injecting the cold metal precursor solution directly in pre-heated of molten surfactants or mixture of solvent and surfactant [48]. The fast injection of the precursor induces a large degree of supersaturation, resulting in a brief but intense burst of nucleation. In consequence of the nucleation effect, the precursor concentration will reduce abruptly and because of the temperature difference between the “hot” solution and “cold” reactants, combined with the already low concentration of the unreacted precursor, any further nucleation events is prevented. Then the temperature is increased slowly to allow further growth of the *nuclei* into larger nanoparticles. The process principle is presented in Figure 19.

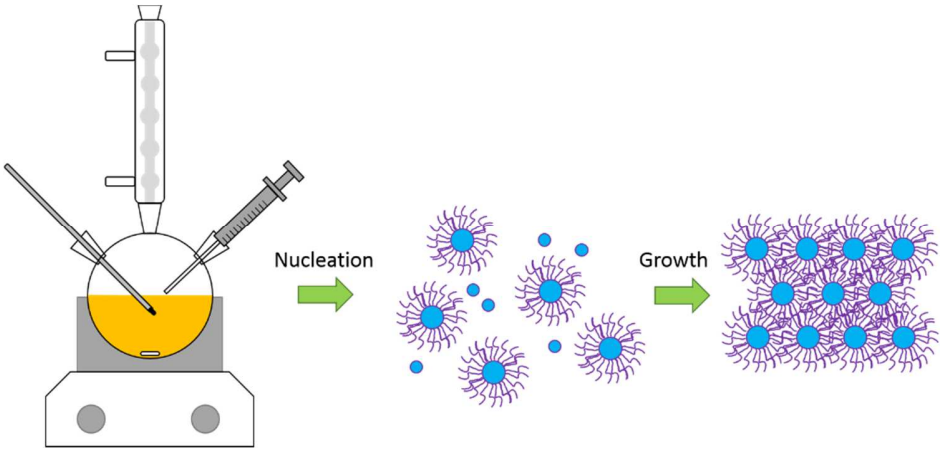

Figure 19: Hot-injection set-up and reaction scheme for controlled-size nanocrystals synthesis

This strategy proved to be particularly versatile for preparing numerous semiconductor nanocrystals, however it has been extended to the synthesis of other materials such as metals and metal oxides. This is perfectly illustrated for zirconia and titania nanocrystals obtained respectively by Joo *et al.* and Trentler *et al.* and shown in Figure 20.

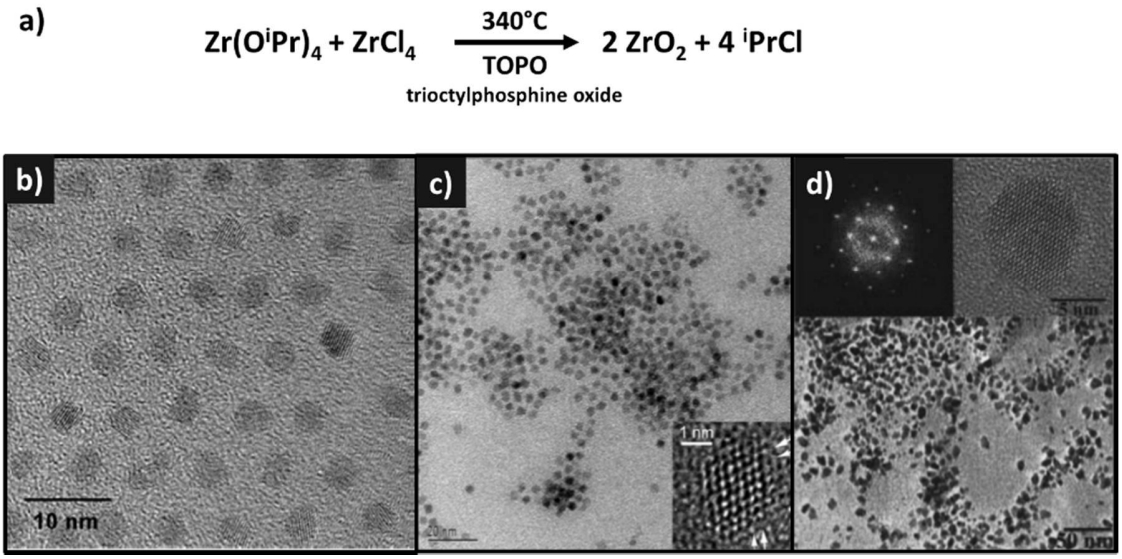

Figure 20: (a) reaction of the zirconia synthesis in TOPO, (b-c) TEM micrographs of zirconia nanoparticles prepared by Joo *et al.* [49] and (c) TEM micrographs of titania nanoparticles obtained by Trentler *et al* [50].

The choice of different type of surfactants allows a thermally dynamic adsorption and desorption of the molecules on the particles' surface which permits the control over the particle size and morphology. However, this technique results in severe limitations, *i.e.* a reduced chemical purity, high toxicity and reduced accessibility of the surface for catalytic and sensing applications [51].

1.2.2.1.2 Two-phase synthesis of colloidal nanocrystals

In 2006, Zhao *et al.* has developed a two-phase approach for the synthesis of shape-controlled colloidal zirconia nanocrystals, including spherical-, teardrop-, rod-, and rice grain-shaped particles. They found that the key factors for controlling the shape were the reaction time, the nature of the capping agent, and the monomer concentration [52]. The two-phase approach was combined with an autoclave, for the synthesis of crystalline ZrO_2 nanocrystals within a narrow size distribution. In this approach, they used zirconium n-propoxide and oleic acid in toluene and *tert*-butylamine in water and then heated the mixture without stirring. The nanoparticles obtained are shown in Figure 21.

This method exhibits a number of interesting features:

(i) The reaction temperature was less than 180°C; that is much lower than the temperature required for the thermal decomposition hot-injection process.

(ii) Nucleation and growth appeared to take place continuously without a clear boundary.

(iii) The reaction occurred under a certain pressure at the interface between the two phases; this process probably facilitates the preparation of shape-controlled nanocrystals.

(iv) The resulting nanocrystals were capped with alkyl chains, and thus they were soluble in nonpolar solvents.

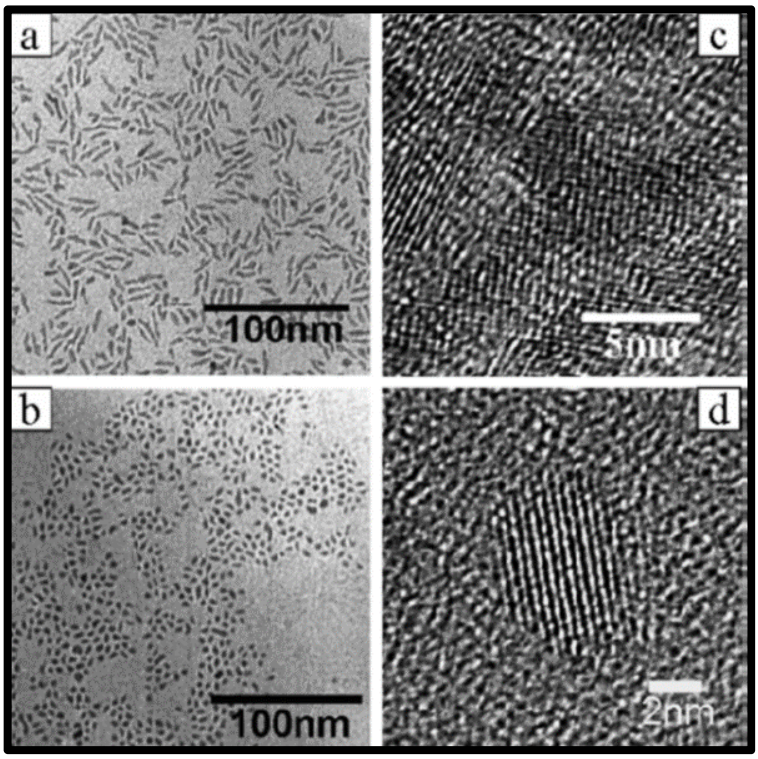

Figure 21: (a-b) TEM micrographs of ZrO_2 nanocrystals prepared over 72h at 180°C and [Zr] monomer concentration of (a) 0.07 mol.L^{-1} and (b) 0.4 mol.L^{-1}. (c-d) corresponding HRTEM for 0.07 mol.L^{-1} (c) and 0.4 mol.L^{-1} (d) according Zhao *et al.*

Despite the very satisfying shape-control promoted by this methodology, a strong limitation remains. Indeed, there was a coexistence of monoclinic and tetragonal nanocrystals whatever the experimental parameters used.

1.2.2.1.3 Heating-up solvothermal synthesis

In 2009, Xu *et al.* has published a new method enabling the fine tuning of the sizes and phases of ZrO_2 nanocrystals. Indeed, monodisperse and pure phase zirconia (tetragonal or monoclinic) nanocrystals with finely tuned sizes as well as ultrathin t-ZrO_2 nanowires have been selectively synthesized by a facile solvothermal method in the presence of oleate ligands as shown in Figure 22 [53].

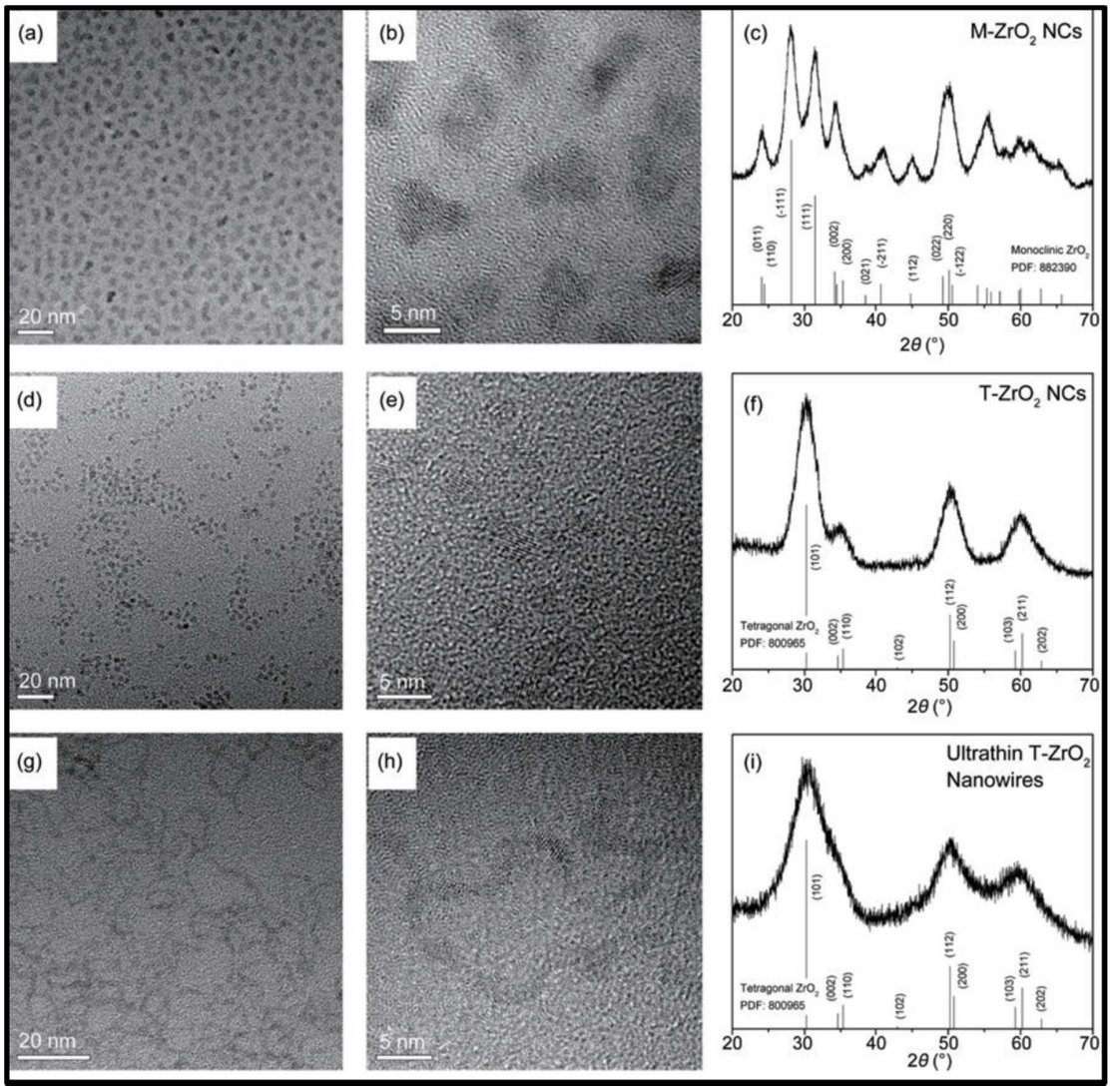

Figure 22: TEM, HRTEM and XRD images of m-ZrO_2 nanocrystals (a-c); t-ZrO_2 nanocrystals (d-f); and t-ZrO_2 ultrathin nanowires (g-i), respectively according Xu *et al.*

The first step of the synthesis consisted in the preparation of the zirconyl oleate complex, then followed by its solvothermal treatment in various experimental medium:

(i) In order to produce m-ZrO_2, zirconyl oleate is dissolved in the presence of oleic acid, oleylamine and ethanol and solvothermally treated at 200°C for 2 days. The sizes of the nanocrystals could be tuned from 8.0 nm to 2.8 nm by shortening the reaction time from 2 days to 4 h. When n-butanol was used in place of ethanol, flower-like m-ZrO_2 nanocrystals were obtained.

(ii) In order to produce t-ZrO_2, zirconyl oleate was dissolved in the presence of oleic acid, oleylamine and n-octane and solvothermally treated at 200°C for 2 days. The sizes of

the nanocrystals could be tuned from 3.0 nm to 0.8 nm by shortening the reaction time from 2 days to 4 h. The replacement of ethanol by n-hexanol also yielded t-ZrO_2 nanocrystals.

(iii) In order to produce t-ZrO_2 ultrathin nanowires, zirconyl oleate was dissolved in the presence of oleylamine and cyclohexane and solvothermally treated at 200°C for 3 days.

From the effect of alcohols with different chain length, they have found that the use of a longer chain alcohol (n-hexanol) yielded to pure tetragonal phase whereas ethanol or n-butanol yielded to the monoclinic polymorph. They concluded that the formation of either a monoclinic or a tetragonal phase was achieved by different reaction kinetic processes. Moreover, the solvolysis of zirconyl oleate yielded t-ZrO_2, whereas m-ZrO_2 was obtained when the alcohol-induced esterification and hydrolysis reactions prevail.

This methodology is extremely promising in terms of size and shape control for both polymorphs of zirconia but it does not allow to obtain a good yield when the temperature or duration of the synthesis are lowered.

1.2.2.2 Solvent-controlled non-aqueous sol-gel synthesis

In solvent-controlled strategy, the choice of the solvent dictates the size, distribution and dispersibility of the crystals. They can be grouped into chemically inert organic solvents or chemically active ones such as the oxygen-donor type (alcohols, aldehydes, ketones or ethers).

Such methodology offers a much simpler path in the formation of the nanoparticles but sometimes results in some agglomeration. This agglomeration of particles can be remedied by adding a post-synthesis functionalization process. To summarize the difference between the surfactant-controlled and solvent controlled Table 3 is presented and it shows the pros and cons of the two strategies according to the review of Niederberger and Pinna [41].

Table 3: advantages and disadvantages of surfactant-controlled and solvent controlled non-aqueous liquid-phase routes to metal oxide nanoparticles [41]

	Surfactant-controlled	Solvent-controlled
Advantages	Excellent control over size	Low amount of organic impurities
	Narrow size distribution	Non-toxic solvents
	Good shape control	Simple, robust and widely applicable synthesis protocols
	Low agglomeration	
	Good redispersibility	Good accessibility of the surface
Disadvantages	Presence of impurities	Less control over crystallite size and shape
	Toxicity of surfactants	Broader size distributions
	Poor accessibility of the surface	Formation of agglomerates
	Complex reaction mixtures	Limited redispersibility

1.2.2.2.1 Non-hydrolytic condensation

There are a couple of condensation mechanisms that lead to the formation of M-O-M bridges under a non-aqueous solvent-controlled route and they are the ether elimination (X = OR), the alkyl halide elimination (X = Cl, Br, I), and the ester elimination (X = OOCR') (Equation (8)) [41].

$$\equiv M - X + R - O - M \equiv \rightleftarrows \equiv M - O - M \equiv + R - X \quad (8)$$

There are also more complex mechanisms towards the synthesis of metal oxides such as the C-C bond formation, namely coupling of benzylic alcohols and alkoxide precursors or aldol/ketamine condensation (not developed in this thesis).

1.2.2.2.2 Benzyl alcohol route based on C-C coupling

In alkaline conditions, Niederberger, Garnweitner and Pinna have shown that conjointly to the formation of oxidic nanoparticles a C-C bond formation analogous to Guerbet condensation of benzyl alcohol on isopropoxide ligand was possible during the formation of the alkaline earth zirconate $BaZrO_3$, titanate $BaTiO_3$, and lithium niobate $LiNbO_3$ nanoparticles [54] [55]. Figure 23 and Figure 24 show respectively the formation of Ti-O-Ti bridge, and the TEM and HRTEM micrographs of the $BaTiO_3$ synthesis.

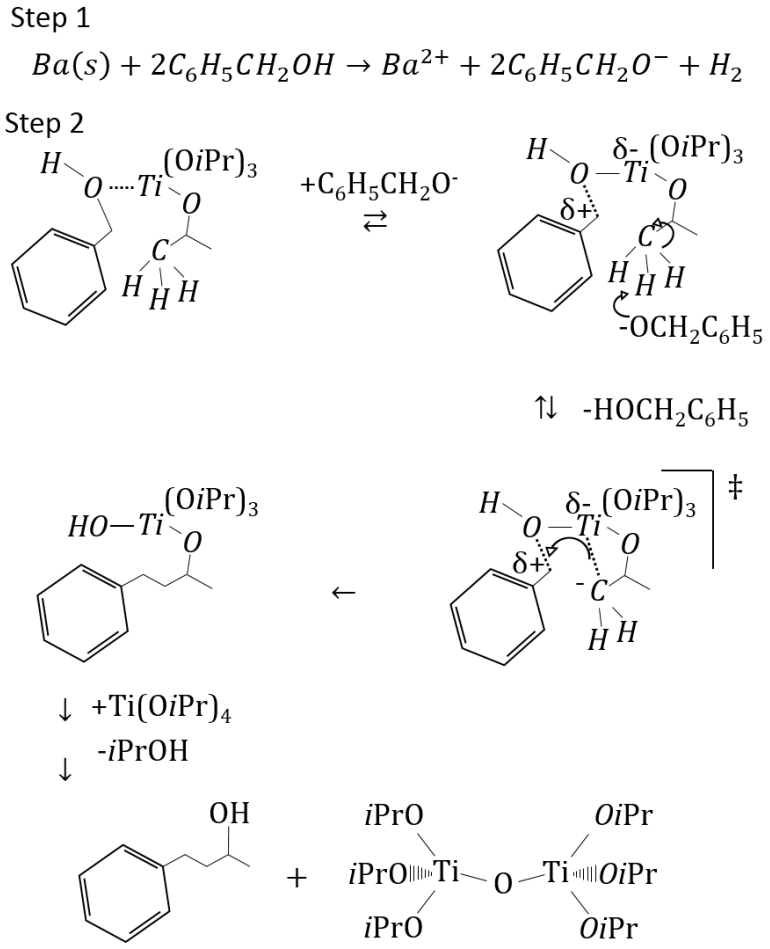

Figure 23: Proposed mechanism for the synthesis of Ti-O-Ti bridge via C-C bond coupling or Guerbet-like condensation.

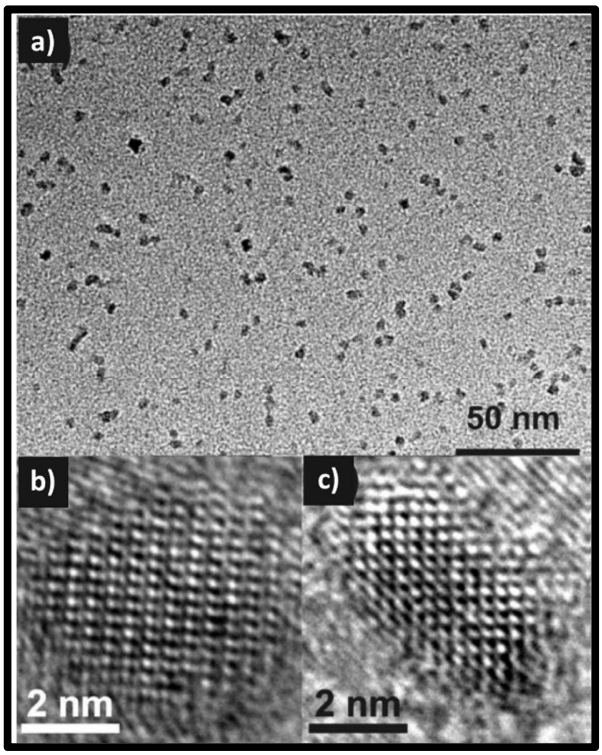

Figure 24: TEM micrographs of as-synthesized $BaTiO_3$ nanoparticles: (a) an overview image and (b-c) HRTEM images of isolated $BaTiO_3$ nanocrystals according to Niederberger *et al.*

The reaction is initiated by the dissolution of metallic barium in benzyl alcohol prior to the addition of the metal alkoxide shown in step 1. The presence of benzyl alcoholate induces a different chemical pathway shown in step 2. This chemical pathway involves the formation of the C-C bond between the isopropoxy ligand of titanium isopropoxide and benzyl alcohol. This is then followed by the release of a hydroxyl group from benzyl alcohol. Finally, the hydroxylated titanium (*Ti-OH*) promotes condensation with another metal alkoxide forming the Ti-O-Ti with formal release of 4-phenyl-2-butanol.

1.2.2.2.3 Benzyl alcohol route based on ether elimination

One of the frequently used alcohol solvent is the benzyl alcohol which is commonly known as benzyl alcohol route [56] [54]. Benzyl alcohol belongs to the family of the benzylic alcohols and readily reacts with metal alkoxides by alcohol interchange and then form metal aryloxides:

$$M(OR)_Z + x\ BnOH \ \rightleftarrows\ M(OR)_{z-x}(OBn)_x + x\ ROH$$

Metal aryloxides are more resistant toward hydrolysis than aliphatic alkoxides due to the (+E) mesomeric effect of the aromatic ring which increases the π-donor ability of aryloxo groups and decreases the positive charge on M. Such effect will strongly depend on the availability of the metal d-orbitals but also on the (-I) inductive effect which inversely increases the positive charge on metal. Moreover, benzyl alcohol has been demonstrated to favor ether-elimination pathway.

The benzyl alcohol route combined with solvothermal treatment produced zirconia nanoparticles (2.8 nm) [57] and has been successfully used to prepare other oxides such as TiO_2 (4 nm) [58] and SnO_2 (3.5nm) [59].

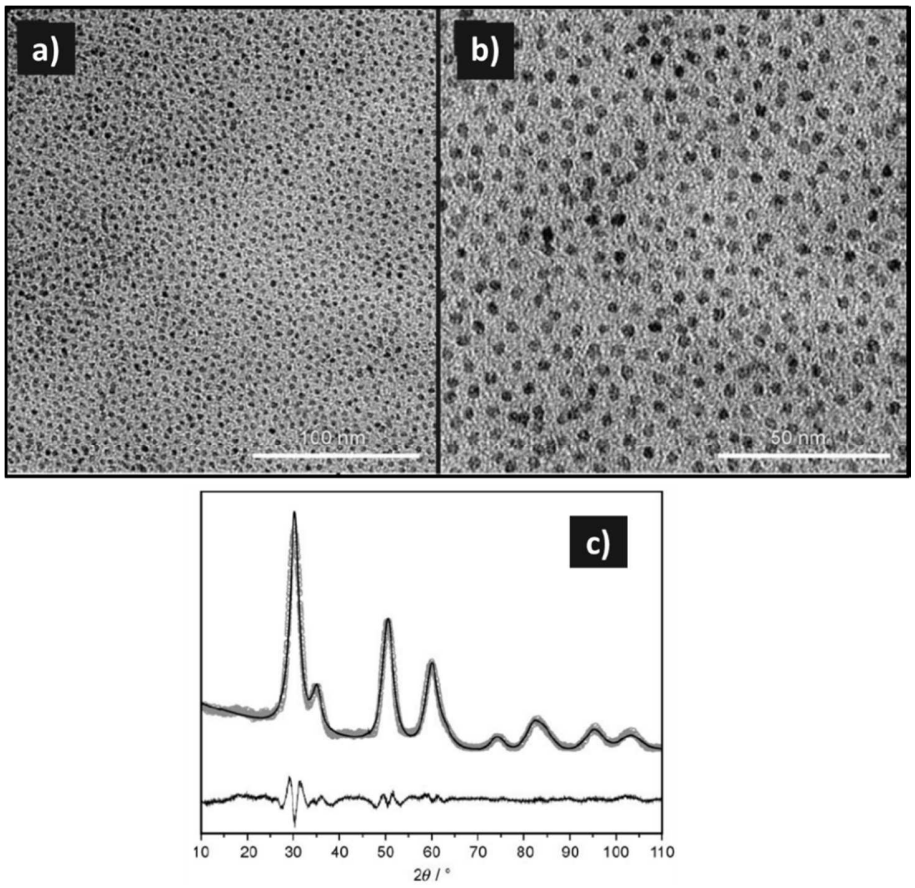

Figure 25: TEM images of ZrO_2 nanoparticles after post-functionalization with octadecanoic acid (a-b) and XRD diffraction pattern of as-prepared ZrO_2 nanoparticles (c) according to Garnweitner *et al.*

This route usually proceeds by the reaction of a metal alkoxide and/or halide source and alcohol to form M-O-M bonds via ether elimination and/or alkyl halide elimination in case of a halide precursor. It is also possible that the alcohol is oxidized in direct or as side-reaction which could interfere and create a cascade of complex reactions that could result in the difficulty in the

identification of their role in the formation of the oxidic nanoparticles. In the case of zirconia, Garnweitner *et al.* have shown that zirconia nanoparticles were produced via an ether-elimination pathway following a two-step mechanism. First by the exchange of ligand between the isopropoxide with the benzyl alcohol molecule and second by the condensation of the alkoxide species to form the metal-oxygen-metal bonds with the release of organic ethers [57] (see Figure 25).

Moreover, Cheema *et al.* has evidenced that the use of zirconium n-propoxide in n-propanol and benzyl alcohol in place to zirconium isopropoxide-isopropanol adduct would lead to a mixture of t-ZrO_2 and m-ZrO_2 at 220°C and gradually to almost pure t-ZrO_2 by increasing the temperature up to 270°C as shown in Figure 26 and Table 4.

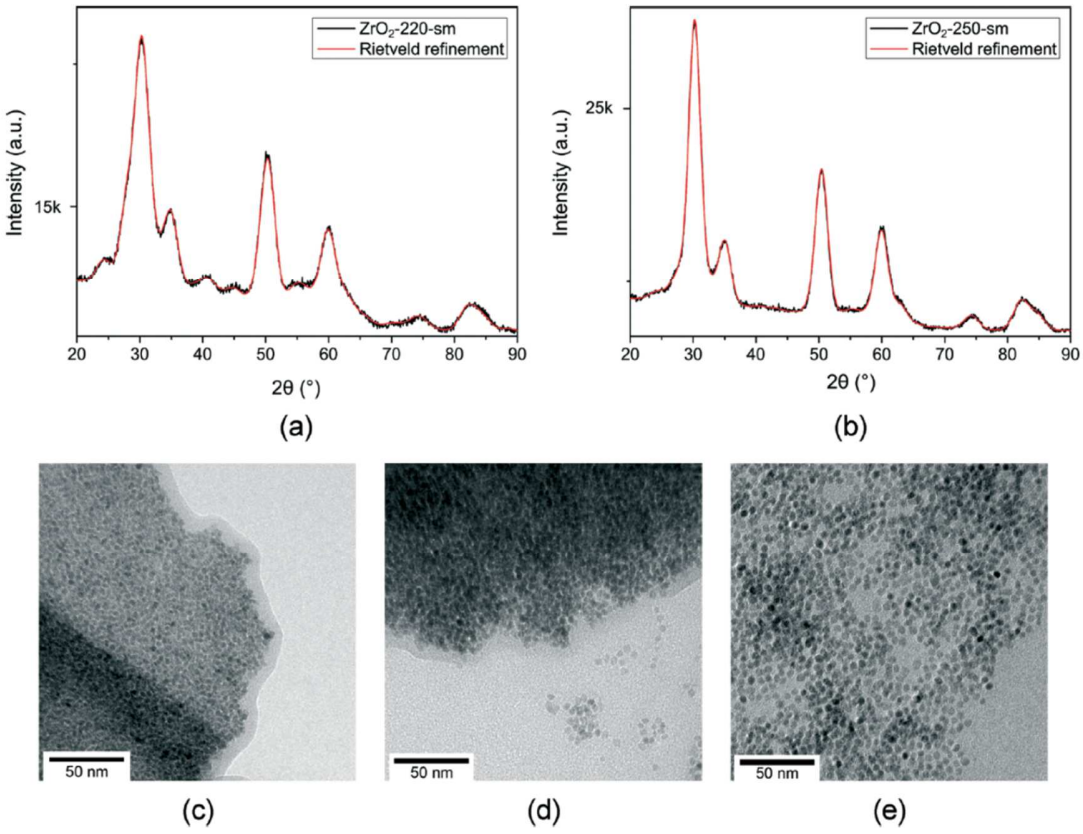

Figure 26: XRD patterns of ZrO_2 nanoparticles synthesized at 220°C (a) and 250°C (b) at small scale along with its Rietveld refinement (red); at bottom, TEM micrographs of ZrO_2 synthesized at 220°C (c), 250°C (d) and 270°C (e).

Table 4: Crystal properties of the ZrO_2 synthesized in small scale for 72 hours at different temperatures determined by PXRD and TEM (rounded to the nearest 5):

Sample	m-ZrO_2 fraction[a] (wt%)	Crystallite size		GOF	Tem particles size (nm)
		m-ZrO_2 (nm)	t-ZrO_2 (nm)		
ZrO_2-220-sm	45	3.5	3.7	1.28	4.4
ZrO_2-230-sm	40	3.4	4.4	1.99	-
ZrO_2-240-sm	30	3.1	4.0	1.65	-
ZrO_2-250-sm	25	2.9	4.3	1.81	4.5
ZrO_2-260-sm	15	3.4	4.7	1.87	-
ZrO_2-270-sm	<10	5.8	5.3	2.98	4.6

Recently, Keukeleere *et al.* has shown that it was possible to drastically reduce the solvothermal duration of the global treatment from 48 h to only 6 h by monitoring the reaction in a microwave reactor at 230°C. Several zirconium precursors, *i.e.* zirconium propoxide, chloride, ethoxide or acetate have been used and lead to different zirconia nanocrystals exhibiting pure t-ZrO_2, pure m-ZrO_2 or mixture of both polymorphs as shown in Figure 27.

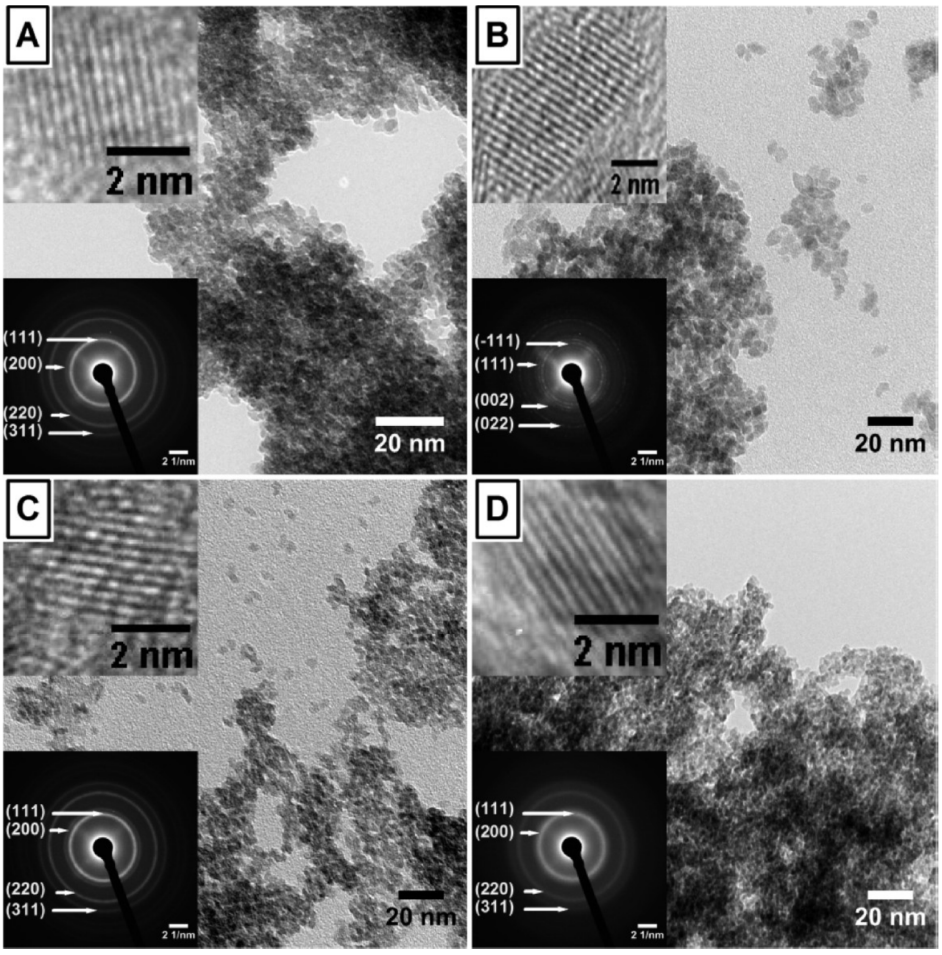

Figure 27: TEM and HRTEM micrographs of zirconia using (A) zirconium propoxide, (B) zirconium chloride, (C) zirconium ethoxide, and (D) zirconium acetate precursors according to Keukeleere *et al.* [60].

Finally, Portal *et al.* evidenced that the presence of water produced by the dehydration of isopropanol was detrimental to the phase purity of t-ZrO_2 nanocrystals. They have proposed to remediate to this inconvenient by dissolving sodium metal in benzyl alcohol before the addition of zirconium isopropoxide-isopropanol adduct in order to promote a strong base activation of the global process. The pure as-produced nanoparticles are shown in Figure 28 and correspond to t-ZrO_2. Portal et al. postulated a NaOBn desiccating effect coupled with a C-C coupling Guerbet-like mechanism.

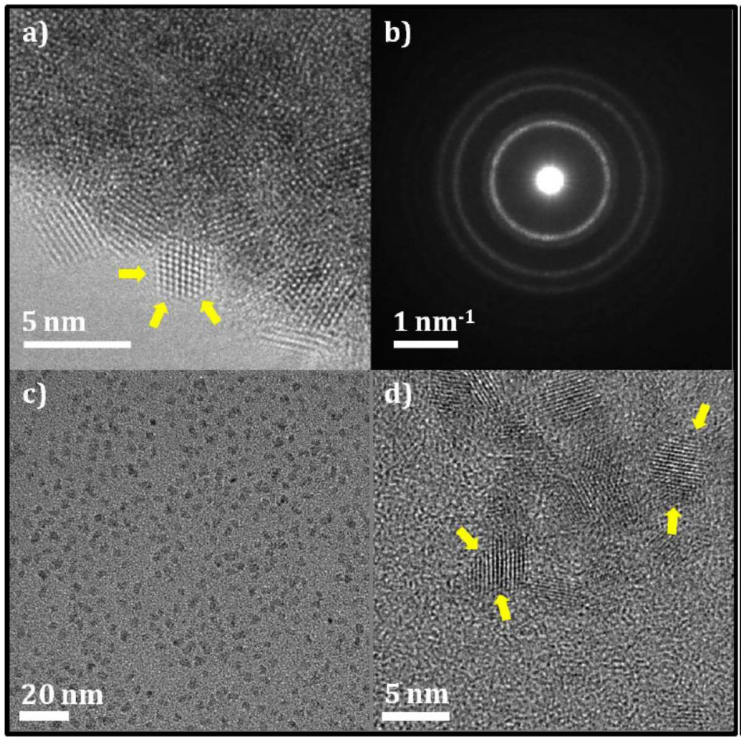

Figure 28: TEM and HRTEM micrographs of zirconia nanoparticles obtained by a strong base activation of the benzyl alcohol route initially developed by Garnweitner (according to Portal *et al.*).

1.3 Formation of a solid phase by chemical solution synthesis

In this section we will briefly discuss the classical and non-classical nucleation and growth mechanisms. The information that can be obtained from an independent study of the nucleation and growth mechanism will be invaluable in understanding the nanomaterial's texture and its intrinsic properties. In dealing with soft-chemistry experiments, whether it is aqueous or non-aqueous chemistry, the problem of isolating the nucleation and growth mechanism is very persistent where the nucleation step is coupled with coarsening and agglomeration growth steps. The main difficulty consists to find a connection between the crystal and its monomeric building units, and especially, the intermediate structures between molecules and solids. The classical view considers the different stages of crystallization to proceed via attachment of the basic monomers, which (depending on the crystal) can be atoms, ions or molecules and we will distinguish the case of non-classical crystallization in which the building units of solids are no more atoms or ions but possibly clusters and even nanoparticles themselves. In solution, there are three possible nucleation models: classical nucleation, spinodal decomposition and non-classical nucleation. In the classical nucleation theory, homogeneous nucleation has a high thermodynamic energy barrier that originates from the high surface-to-volume ratio of the *nucleus*. By contrast, spinodal decomposition has practically no energy barrier. In this model, the surface energy of the *nuclei* is negligible compared with their bulk free energy, thus spinodal decomposition can spontaneously occur and a phase separation takes place all over the medium. The energetics of non-classical nucleation are somewhere in between those two extremes of high energy barrier and no barrier at all.

1.3.1 Classical nucleation

The most fundamental step in crystallization is nucleation, *i.e.* the formation of the first *nuclei* in a system that has become supersaturated. Control of crystallization, in principle, requires nucleation control. Classical nucleation assumes that the bulk energy of a nascent *nucleus* drives nucleation, where its structure is that of the macroscopic bulk material. However, the generation of a phase interface, and with it, of interfacial tension, impedes *nucleus* growth. The first important assumption made in this simple model is to use the interfacial tension of the bulk material at the nanoscale. Because the total volume and surface energies of the native particle scale with the cube

and the square of the radius of the *nuclei*, respectively, the bulk energy begins to balance the energetic cost due to the generation of a phase interface at the so-called critical size.

Mathematically and for spherically-shaped objects (constant shape and inner structure of the *nuclei* identical to the final crystal), the stability of the *nuclei* or small clusters can be written as function of the radius as shown in Equation (9) where ΔG is the Gibbs free energy of the growing *nuleus*, ΔG_v is the free energy of phase formation, γ is the surface energy per unit area, and r is the sphere radius of the *nucleus* or particle [61] [62].

$$\Delta G = -\frac{4}{3}\pi r^3 \cdot \Delta G_v + 4\pi r^2 \cdot \gamma \tag{9}$$

The Gibbs free energy (Equation (9)) is graphically represented in Figure 29 to aid the understanding the classical nucleation theory. To calculate the minimum size for a stable *nucleus*, it is necessary to differentiate the Equation (9) with respect to r and setting it to zero. Result is given in Equation (10) where r_{crit} is the critical size to balance the surface and bulk energies.

$$r_{crit} = -\frac{2\gamma}{\Delta G_v} \tag{10}$$

ΔG_v is defined in Equation (11) and is dependent upon the temperature, the Boltzmann's constant k_B, the supersaturation s, and its molar volume V:

$$\Delta G_v = -\frac{k_B T \cdot \ln(s)}{V} \tag{11}$$

To obtain the critical energy the critical size formula is substituted back to Equation (9) and obtain Equation (12) where ΔG_{crit}^{homo} is the critical energy for $r = r_{crit}$.

$$\Delta G_{crit}^{homo} = \frac{16\pi \cdot \gamma^3}{3 \cdot \Delta G_v^3} \tag{12}$$

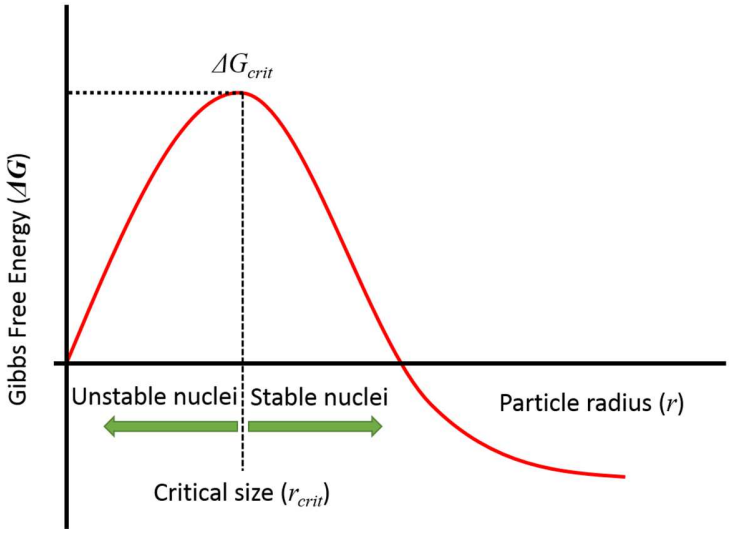

Figure 29: Graphical representation of the Gibbs free energy for homogeneous nucleation [62].

As observed in Figure 29, the r_{crit} value corresponds to the minimum size at which a *nucleus* survives in solution without being redissolved. The change in free enthalpy for the formation of precritical *nuclei* ($r < r_{crit}$) is positive, hence, their formation is thermodynamically improbable, and can only occur through random density fluctuations on sub-microscopic lengthscales and exhibits similarity with the notion of activated complexes in chemical kinetics. In consequence, for a highly supersaturated system, classical pre- or sub-critical *nuclei* are rather rare species and the cluster size distribution is characterized by an exponentially decaying function with an average of size of monomers or dimers of the underlying molecular units.

A rate of nucleation of N *nuclei* during time t can be described using an Arrhenius-type equation where A_0 is a pre-exponential factor representing the frequency of collides between monomers and E_A the activation energy barrier related to the chemical reaction giving birth to the monomer (*eg.* oxolation, olation, alkoxolation) (Equation (13)):

$$\frac{dN}{dt} = A_0 \cdot exp\left(-\frac{\Delta G_{crit}^{homo} \cdot E_A}{k_B T}\right) \tag{13}$$

In the presence of active centers (impurities, walls, bubbles, etc.) the barrier to overcome for nucleation to occur is globally decreased. Unlike homogeneous nucleation, the *nuclei* are formed

on the first surface of a foreign body. Germs no longer have spherical shape but exhibit a contact angle θ with the support as shown in Figure 30. The critical energy for heterogeneous nucleation is now obtained using Equation (14).

$$\Delta G_{crit}^{hetero} = \frac{(2 + cos\theta)(1 - cos\theta)^2}{4} \cdot \Delta G_{crit}^{homo} \quad (14)$$

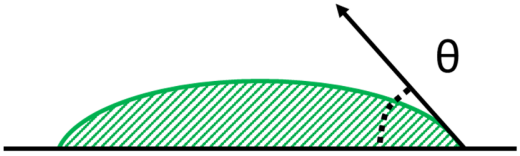

Figure 30: Illustration of the contact angle θ for the heterogeneous nucleation.

1.3.2 Non-classical nucleation

Recently, the classical nucleation theory has been reinvestigated due to an increasing number of cases which do not fit to the model. Indeed, numerous studies of solute solutions reported so-called non-classical pathways of nucleation, which involve the aggregation of either pre-nucleation clusters of monomers or primary particles. An evidence for non-classical behavior brought a clarifying insight in the case of magnetite. Indeed, Baumgartner *et al.* used cryogenic transmission electron microscopy to visualize magnetite formation and found that nucleation proceeds by aggregation of metastable primary particles, approximately 2 nm in size, consisting of an amorphous iron oxide phase as shown in Figure 31 [63].

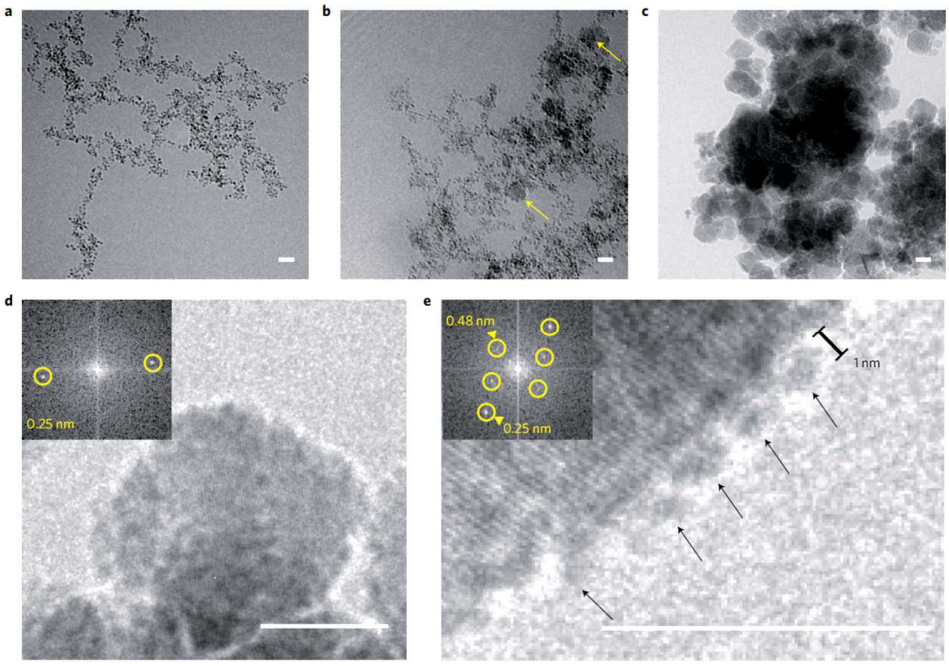

Figure 31: Cryo-TEM images for the nucleation and growth process of co-precipitated magnetite. Time series of the evolving primary particles and magnetite-nanoparticle aggregates after 2 min (a), 6 min (b) and 82 min (c). Yellow arrows in (b) indicate the early formed crystalline magnetite nanoparticles. Image of a magnetite nanoparticle (d). Image of non-crystalline primary particles attaching to the surface of a magnetite nanoparticle (e). Scale bars, 10 nm.

Lately, research activities go to understand the impact of prenucleation clusters and primary particles on the rate equations of classical nucleation theory by developing a general analysis of aggregation-based nucleation that preserves important classical concepts. In doing so, they provide a framework for predicting whether pathways of nucleation are direct or rather stepwise, and whether they occur through monomer-by-monomer addition or indirectly through cluster aggregation whatever the level of supersaturation or even sometimes in undersaturated solution. The different possibilities that have been observed in various systems belong to one the pathways presented in Figure 32.

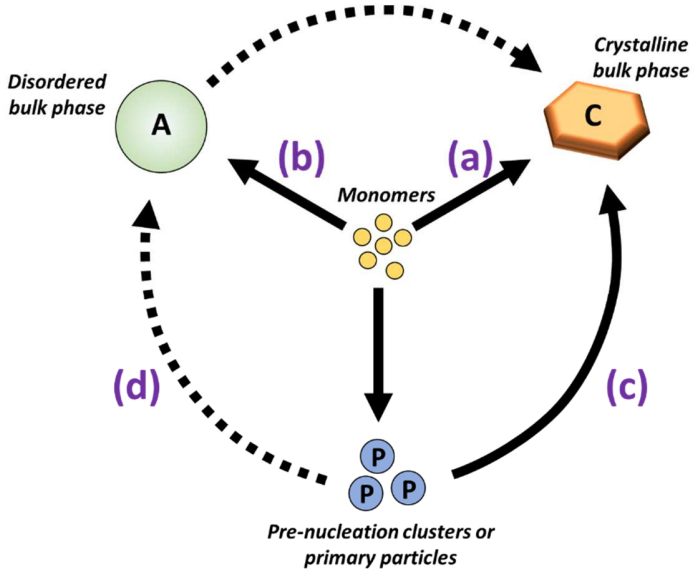

Figure 32: Nucleation pathways from monomers to the bulk crystal. Both monomers and clusters can nucleate the crystalline bulk phase either directly (a) and (c) or through an amorphous or disordered precursor phase ((b) and (d).

1.3.2.1 Stepwise nucleation

A drastic factor resulting in a decrease of the classical nucleation energy barrier relates to the structural variances, namely amorphism and polymorphism. Indeed, under low supersaturation conditions, two-step nucleation through an amorphous-to-crystalline transition is energetically favored over direct crystallization foreseen by classical nucleation. Such a phenomenon has been observed from multi-scale and various systems, i.e. proteins, metallic clusters, metal chalcogenides, minerals like calcium carbonate, calcium phosphate, iron oxide and silica and is perfectly illustrated by the optical microscope study of the crystallization of colloidal polystyrene particles as shown in Figure 33.

In the first step, amorphous *nuclei* are formed – their surface energy is lower than that of the crystalline nuclei as a consequence of their disordered interfaces with the solution. In the second step, an amorphous-to-crystalline transition takes place in the middle of the amorphous phase; this transition has to overcome a much lower free energy barrier as compared to the direct crystallization from solution. In other words, the amorphous phase can mediate the nucleation of the crystalline phase by buffering the large entropy difference between solution and crystal.

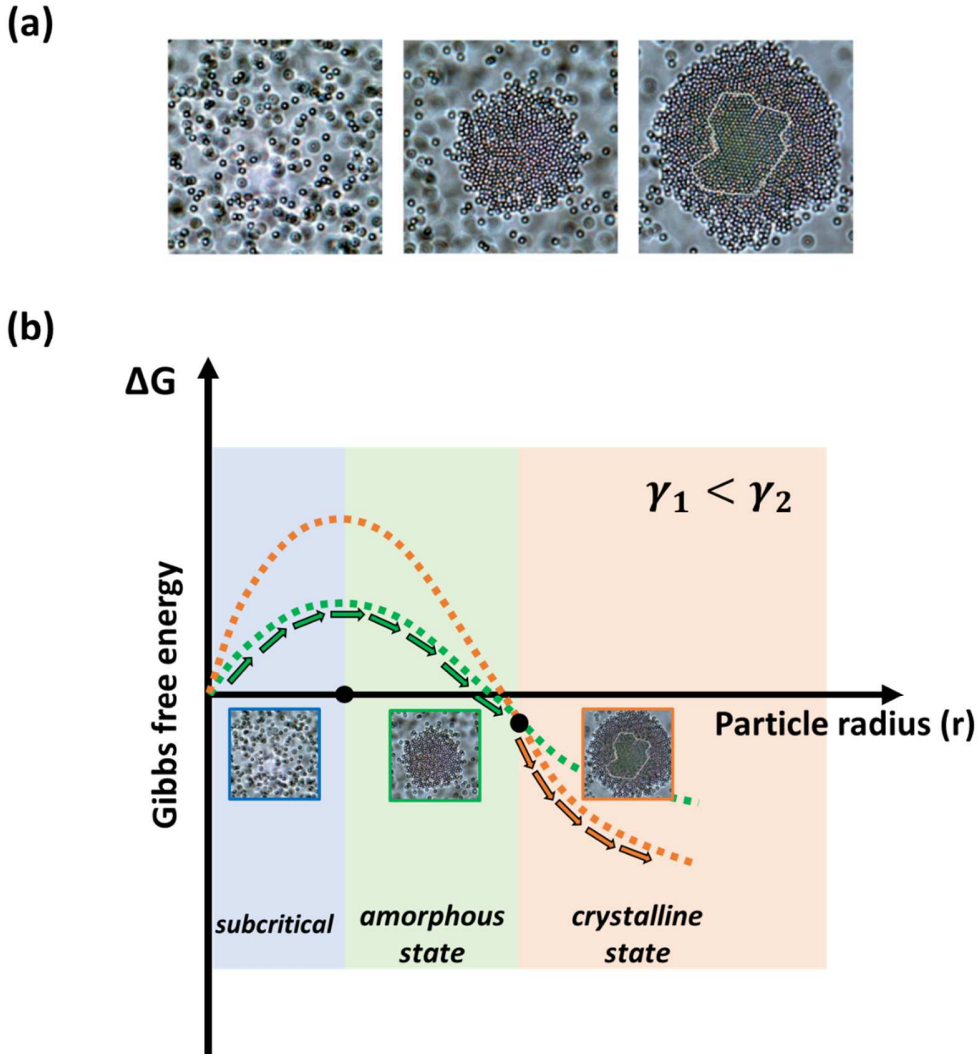

Figure 33: (a) optical microscopy study of colloidal polystyrene particles self-assemblies according to Zhang *et al*. and (b) energetic interpretation of the process [64].

Stepwise phase transitions in the crystallization of polymorphic solids can also induce non-classical nucleation. Indeed, when the particle is ultra-small, its free energy is dominated by the surface energy term and finally when the particle grows, its thermodynamic stability becomes more dependent on the bulk free energy term. As a consequence, in the early stages, the *nucleus* tends to have the structure with the lowest surface energy but is transformed to the structure with the lowest bulk energy as it grows, as conjectured in the Ostwald step rule. For example, ZrO_2 nanoparticles have a tetragonal structure, whereas bulk ZrO_2 is monoclinic under ambient conditions. A stepwise

phase transition occurring because of the difference between the surface and bulk energies of the two phases is illustrated in Figure 34.

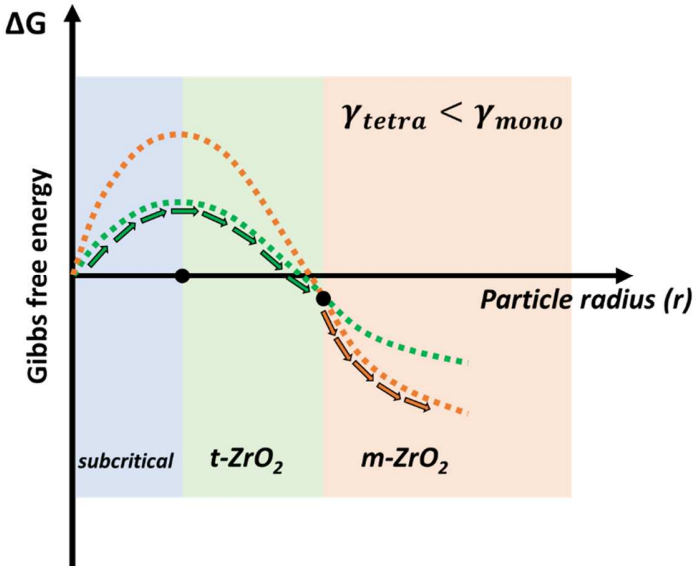

Figure 34: Energetic interpretation of the 2-step nucleation process for metastable tetragonal zirconia and size-dependent *tetra-mono* phase transition.

1.3.2.2 Pre-nucleation clusters and aggregation principle

Nanoclusters with discrete sizes and structures form during the subcritical period of the synthesis of nanoparticles of various systems (metals, semi-conductors and metal oxides). The formation of these nanoclusters reveals the presence of local minima in the energy landscape, which can effectively lower the energy barrier for nucleation, so that it can take place at a level of supersaturation lower than that estimated by classical nucleation theory. An example referring to this prenucleation clusters is magic-sized metallic clusters whose stability is related to the geometric full-shell and electronic superatom configurations.

Other nanoclusters could form transiently before growing into nanoparticles due to non-constant bulk and surface energy terms leading to local minima in the energy profile and giving rise to metastable clusters or even stable prenucleation clusters as shown in Figure 35. Compared to monomers, those species are relatively favorable, yet thermodynamically unstable, intermediates to crystal nucleation.

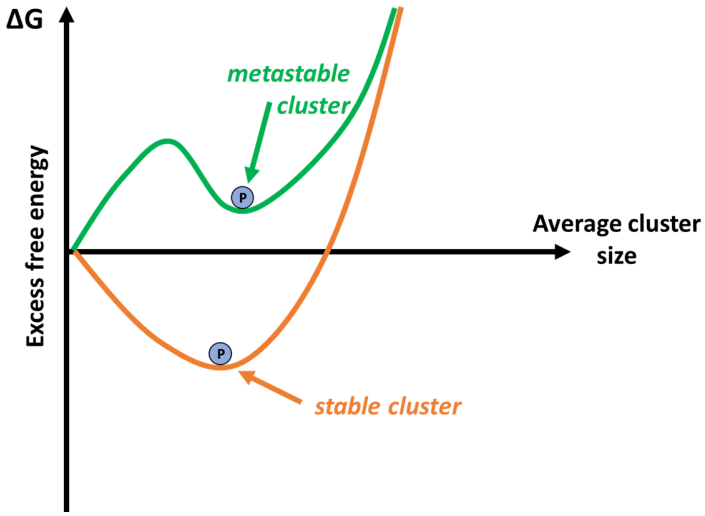

Figure 35: Excess free energy profile relative to the free ions in solution and normalized to the bulk surface energy for metastable and stable prenucleation cluster as a function of the average cluster size.

A new proposition for the crystal nucleation sequence via prenucleation clusters would consist then in two steps as it was confirmed for iron oxide-hydroxide by Baumgartner *et al.* [63]:

- (i) first, the agglomeration of prenucleation clusters and formation of partially organized structures comparable to a disordered mesocrystals,
- (ii) and second, the ripening of the agglomerates into the final crystal structure.

As thermodynamic rationale, many authors suggest to compare the classical nucleation and the cluster energy profiles in order to exhibit an effective lowering of the nucleation barriers. Nucleation from particularly favorable clusters could be delayed or just impossible due to an increase in the free energy barrier as compared with the dispersed solute solution. The three schemes using the superposition of the classical nucleation energy profile and those proposed previously for either metastable or stable clusters are illustrated in Figure 36.

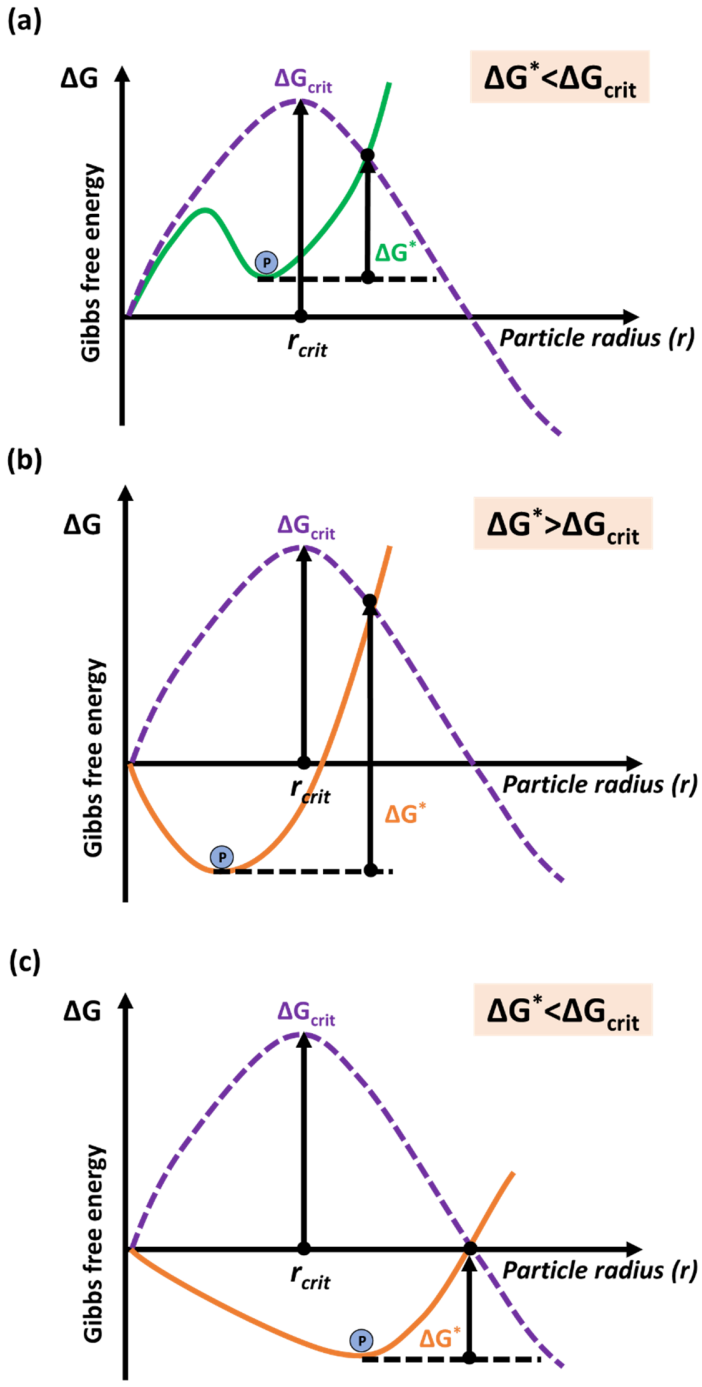

Figure 36: Thermodynamical rational for (a) metastable and subcritical prenucleation cluster as relatively favorable intermediates to crystal nucleation, (b) small and stable cluster exhibiting a considerable increase in the energy barrier for the cluster-to-nucleus transition and favoring nucleation from bulk solution, (c) large and stable prenucleation clusters as a favorable building blocks to crystal formation.

The three possible scenarios correspond to different degree of thermodynamic stability:

(a) In the first case, metastable and subcritical prenucleation clusters may be interpreted as relatively favorable intermediates to crystal nucleation and are thus well-suited as building blocks to non-classical crystal nucleation.

(b) In the case of clusters that are thermodynamically preferred over solutions of dispersed solutes, the picture is more complex. The example of small and stable clusters exhibits a considerable increase in the energy barrier for the cluster-to-nucleus transition and even larger than the barrier to nucleation from bulk solution. The nucleation will finally take place from the bulk solution in coexistence with the prenucleation clusters. The stable clusters could then either dissociate to compensate the abrupt decrease in solute concentration arising from the onset of classical nucleation or collide with an emerging *nucleus* and merge into it.

(c) The example of large and stable prenucleation clusters illustrates a favorable case of low effective barrier to crystal nucleation, thus qualifying the clusters as building blocks to crystal formation. This model represents a rough estimation of the transition barrier which does not take into account the energy barrier arising from cluster reorganization.

1.3.2.3 Aggregation principle

Another important nucleation pathway is aggregation. Compared to 2-step nucleation, which involves thermodynamic stabilization via structural change, the role of aggregation in the nucleation process has a more kinetic origin. Subcritical *nuclei* are supposed to be unstable and to dissolve until the critical size is reached but if their dissolution rate is much slower than their collision rate, it is possible two or more subcritical *nuclei* bind together to form a stable postcritical *nucleus* ($r > r_{crit}$). This phenomenon induces a large deviation from the classical nucleation theory. It is important to recall that nucleation is a self-limiting process because the formation of particles lowers the supersaturation and, as the supersaturation level decreases, part of the *nuclei* disappears by a ripening process. Aggregation can stabilize the *nuclei* under ripening by abruptly increasing their size, which is equivalent to a “tunneling” effect through the free energy barrier. More interestingly, this effect can occur even at lower supersaturation in which monomer-by-monomer, or atom-by-atom, addition is not possible.

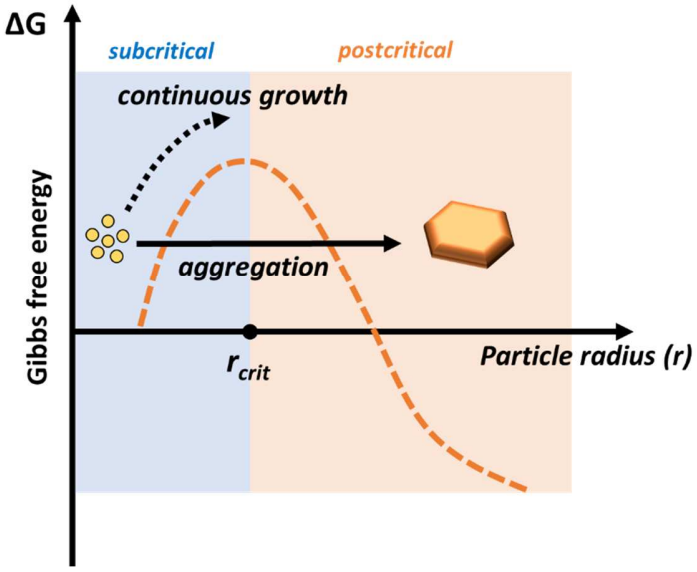

Figure 37: Nucleation by aggregation of prenucleation clusters.

In many cases, stepwise nucleation and aggregation work together in a complementary way. Easy formation of amorphous or disordered nanoparticles leads to a high concentration and to more frequent collisions among them. Upon aggregation and sudden size increase, the small disordered nanoparticles reach the postcritical domain and the amorphous- or disordered-to-crystalline phase transition takes place. The Figure 37 depicts the possible combinations and pathways that have been reviewed briefly in the previous paragraphs.

1.3.3 Growth mechanisms

After the formation of *nuclei* from the solution they then become larger by molecular addition from the dissolved species or unreacted species. The growth process continues as long as there are available monomers. This growth is essentially dependent on two mechanisms: the surface reaction and the monomer's diffusion to the surface. The growth can be modeled by the Fick's first law of diffusion where the driving force for the process is the concentration gradient namely the difference of concentration between the bulk solute solution and the nanoparticle surface. Equation (15) is based on the r, J, D, and C parameters where they represent respectively the particle radius, the total flux of monomers passing through a spherical plane with radius x, the diffusion coefficient and the concentration of monomers at the distance x as it is shown in Figure 38.

$$J = 4\pi x^2 \cdot D \cdot \frac{dC}{dx} \tag{15}$$

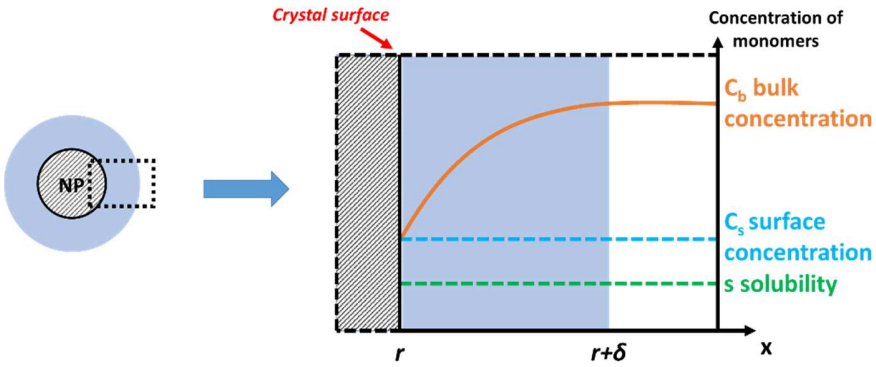

Figure 38: Schematic illustration of diffusion layer (δ) near the surface of a nanocrystal (left) and plot of the monomer concentration as a function of the distance x (right) according Kwon *et al.* [65].

According to Thanh *et al.* [66] the combination of both rate-determining mechanisms leads to the following Equation (16):

$$\frac{dr}{dt} = \frac{D.V.(C_b - s)}{r + {}^{D}/_{k}} \tag{16}$$

In that expression, D is the diffusion coefficient and k the rate of surface reaction whereas C_b and s are respectively the concentration of the bulk solute solution and the solubility of the particle. Strictly speaking, the solubility of nanoparticles is not independent of particle's size and according to Gibbs-Thomson relation we could use the Equation (17) dedicated for a spherical shape particle:

$$s = C_b . exp\left(\frac{2\gamma . V}{r . k_B T}\right) \tag{17}$$

1.3.3.1 La Mer mechanism

The first mechanism is the La Mer's model which has the conceptual separation of the nucleation and the growth as shown in Figure 39 [67]. The plot is divided into three regions as indicated by the roman numerals *I*, *II* and *III*:

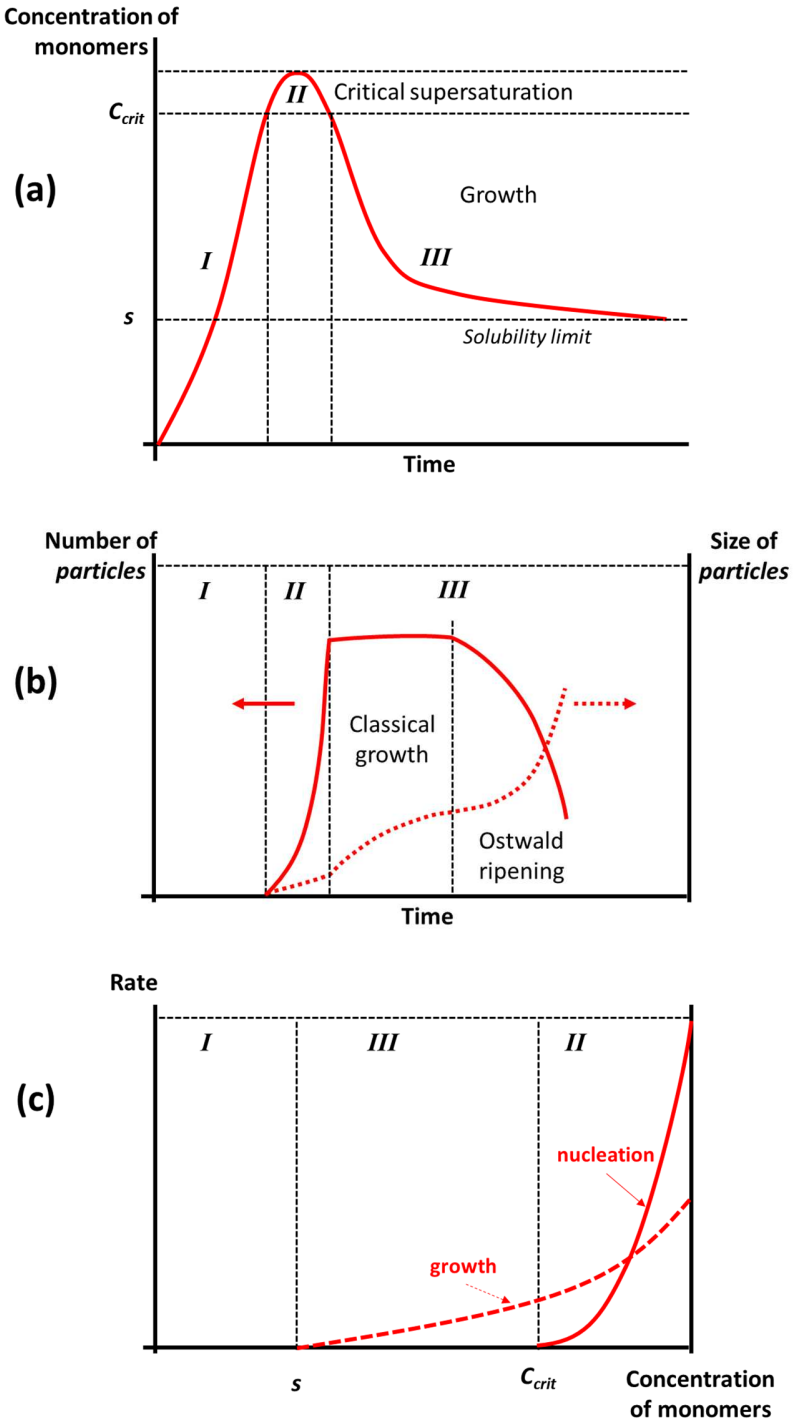

Figure 39: Diagrams of La Mer's model. Schematic evolution of the concentration of monomers (a) and the number and size of the particles (b) during the precipitation of the solid phase. (c) Rates of nucleation and growth as a function of the concentration of monomers. S represents the solubility limit and C_{crit} the minimal supersaturation allowing the nucleation rate to increase drastically [67].

- Stage *I* corresponds to the subcritical region where no formation of *nuclei* is possible but a large increase in the concentration of free monomers due to continuous redissolution of subcritical clusters.
- For the stage *II*, the system is now largely supersaturated and the formation of metastable *nuclei* is promoted as long as the concentration of monomers exceeds the critical concentration allowing the classical nucleation. Once the *nuclei* formed, growth occurs by addition of monomers parallel to a continuous nucleation event. The rate of nucleation is proportional to the supersaturation level (effectively infinite when $C > C_{crit}$) and the consumption of monomers in this "burst-nucleation" jointly to the growth of the formed *nuclei* will abruptly reduce the concentration of monomers under the critical concentration value inhibiting then the continuous nucleation process.
- The stage III represents the last region where pure growth is observed under the diffusion of the monomers through the solution until the concentration reaches the solubility value of the solid phase. Eventually, the concentration of monomers could be depleted or insufficient and other mechanisms come into play in the growth process such as Ostwald ripening where larger nanoparticles grow at the expense of smaller ones [68].

Both the number and the primary particles size are related to the relative rates of nucleation and growth. To obtain a homogeneous dispersion of particles' size, it is necessary to clearly separate the nucleation and growth events. Such a separation is only possible if the rate of nucleation is quite larger than the rate giving birth to the monomer - in that conditions, the burst-nucleation is strong enough to effectively split from the growth mechanism. Shown in Figure 40 is the schematic representation of the (a) independent and (b) dependent nucleation and growth mechanism. The independent scheme shows an ideal condition of the synthesis where there is a clear distinction of the nucleation curve and growth curve. The parameters that are typically involve in such synthesis are the temperature, concentration and pH [62]. However, in actual experiments the separation of the nucleation and growth curves are not that apparent and sometimes it is indistinguishable and the presence of large overlapping region exists which suggests that the nucleation and growth mechanism occur simultaneously which leads to poor control over the size distribution, crystallinity and phase purity.

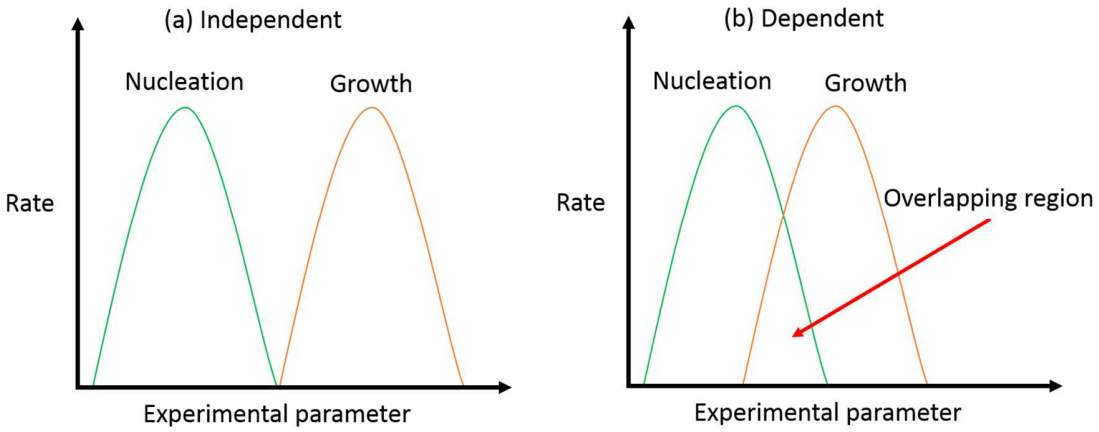

Figure 40: Schematic representations of (a) independent and (b) dependent nucleation and growth mechanism [62].

1.3.3.2 Ostwald ripening

Ostwald ripening (OR) is a growth mechanism caused by the change in solubility of the nanoparticles dependening on their size. Due to the higher solubility and the surface energy of smaller particles within the solution, the smallest crystals or sol particles are dissolved and redeposited onto larger crystals or sol particles as shown in Figure 41.

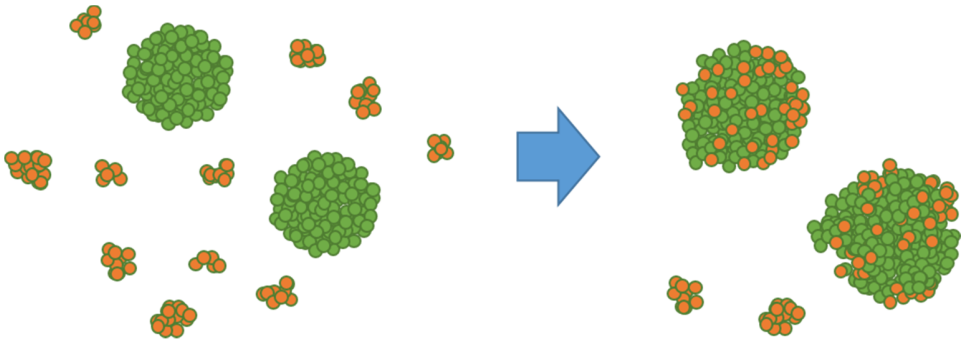

Figure 41: Scheme for Ostwald ripening for nanoparticles (diameter ~10 nm).

A kinetic model for the OR mechanism was developed by Lifshitz, Slyozov and Wagner and is known as the LSW model [69]. The LSW model predicts that the mean particle radius $\bar{r}$ should evolve as a function of time according to the following Equation (18) where n is dependent of the type of limiting step to the growth:

$$\bar{r}^n - \bar{r_0}^n \propto t \quad (18)$$

The power law coefficient n = 3 is obtained by considering dilute conditions, where diffusion of monomers in solution is the limiting step. In concentrated conditions (*e.g.*, solids, or nucleation in melts), the coefficient may be equivalent to 2 or 4, depending on the limiting step involved in the interfacial reactions (*i.e.*, dissolution or reprecipitation).

1.3.3.3 Growth by coalescence (aggregation and oriented attachment)

Classical growth and Ostwald ripening are somewhat very well-accepted mechanisms in explaining the growth for systems in reactional equilibrium or growth phenomenon occurring after the reactants are consumed but dependent on diffusional parameters and on the particles' relative mobility [62]. Nanoparticle growth can proceed not only by monomer-to-monomer addition, but also by assembly and merging of smaller primary particles into larger ones. This concept complements the classic theory by extending the definition of the building units from monomers to clusters and nanoparticles.

If nanoparticles are attached together to each other but their relative crystallographic orientations are not perfectly aligned parallel to each other, defects such as grain boundaries, twinning, or misfit dislocations are formed at the interface. However, in many nanostructures formed by the attachment of primary particles, it was observed that the primary particles are oriented so that they share the same crystal lattice and constitute a single domain.

This phenomenon has been observed for example as shown in Figure 42 in the case of titania 5 nm nanoparticles under hydrothermal conditions (100-250°C, 15-40 bars), where rapid growth occurs along [001], driven in part by the relatively high surface energy of (001) and in part by a kinetic effect involving a cyclic generation of highly reactive adsorption sites. The second major coarsening mechanism significantly reduces the surface energy, especially under acidic conditions. This mechanism involves topotactic attachment of primary particles at high energy surfaces (most commonly (112), less commonly (001)) and can result in elongated single crystals.

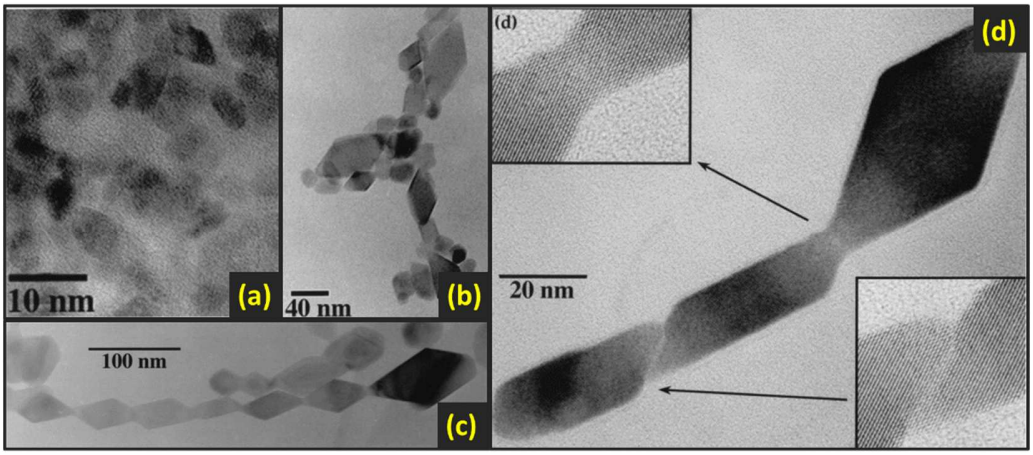

Figure 42: TEM micrograph of titania particles hydrothermally retreated in dionized water at 250°C for 2.2 h (a), 183 h (b), or hydrothermally coarsened in diluted hydrochloric acid (c) and single crystal with magnified inset of the attachment interfaces (d).

Recently, the development of *in-situ* liquid-cell TEM has enabled the direct real-time observation of the aggregation of nanoparticles in solution as shown in Figure 43 and Figure 44.

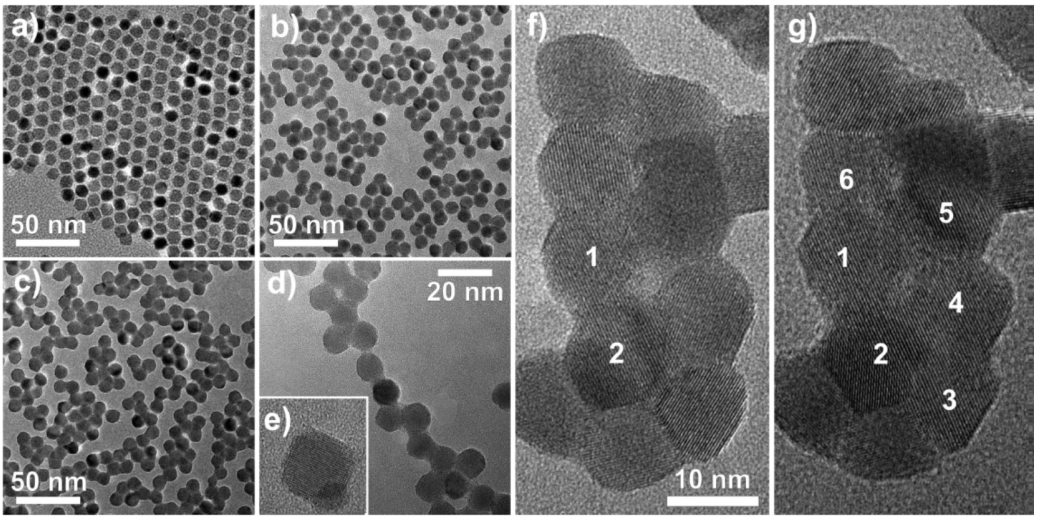

Figure 43: TEM images displaying the attachment and merging process of PbSe quantum dots (QDs). (a) Starting configuration: 2D array of 10 nm sized PbSe nanoclusters on a SiN substrate. The array shows hexagonal ordering. (b,c) Upon gentle annealing at a temperature of 100 °C, the QDs become mobile. Coalescence and initial attachment takes place. (d) In low-density areas, strings of QDs are formed. (e) Isolated QDs tend to adopt a truncated cubic morphology. (f,g) Continued annealing at 130 and 150 °C leads to crystal unification. (f) Agglomeration of some 11 connected QDs. Dots no. 1 and no. 2 have fused into a two-dot single crystal. (g) The same agglomeration 10 min later. Dots nos. 3-6 have fused with dots nos. 1-2 into a six-dot single crystal according van Huis *et al.* [70]

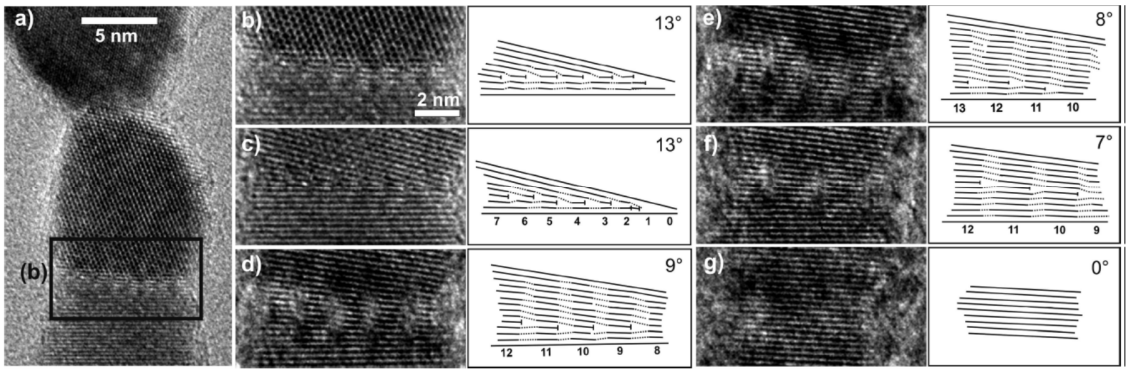

Figure 44: Rotations followed by interface relaxation, imaged during heating of 10 nm sized PbSe QDs at a temperature of 170 °C, increasing to 200 °C, over a time span of 23 min. (a) Triplet of attached quantum dots with interfaces. The two dots at the bottom fuse into a single crystal. (b-g) Details of the bottom interface. Lattice planes drawn from the images are shown on the right-hand side. (b) The dots are not aligned. (c) The top QD has rotated, so that both crystals now display the same line pattern with a mistilt of φ=13°. The interface is very sharp and involves only a few atomic layers, in which 7 interface dislocations can be identified (displayed schematically on the right-hand side of the image). (d) The mistilt has decreased to φ=9° through a reduction of the number of interface dislocations to 4. Also the interface area broadens as the dislocations evolve and produce strain fields also in atomic layers further away from the interface. (e,f) Further decrease of the mistilt to 8 and 7° accompanied by a decrease of the number of dislocations. (g) There are no dislocations left; the crystals have fused into a single crystal according van Huis *et al.* [70].

Two underlying mechanisms are revealed in the assembly and merging processes as shown in Figure 45:

(1) If two nanoparticles are in close proximity before collision, there is a strong interaction between them favoring the alignment of their crystallographic orientations. The strength of the interaction is large enough to help in the rotational and translational motions required to align the nanoparticles before collision. Once the alignment is complete, the nanoparticles immediately merge together by an attractive force. For semiconductors, the mutual alignment was proposed to be induced by a dipole-dipole Keesom interaction. To date, no rationale was found for other systems.

(2) If two misaligned particles are attached, spontaneous reconstruction of the imperfect lattice takes place during the merging process to remove the defects. Even after partial attachment, the nanoparticles can undergo multiple rotational motions to minimize the misalignment of their lattices.

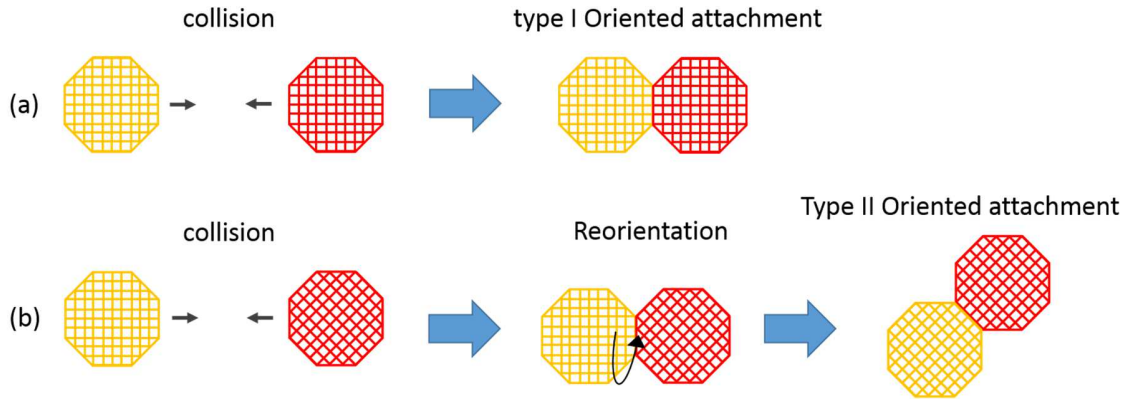

Figure 45: Oriented attachment mechanisms (a) type I OA and (b) type II OA [62].

One has to keep in mind that the behaviors of the nanoparticles in their reaction medium are not yet elucidated and specially, various effects as the solvent molecules, non-van der Waals interactions and particles' shape-dependent potentials become preponderant at the nanoscale.

1.4 Zirconium dioxide

Zirconium oxide (ZrO_2) or zirconia is a versatile refractory ceramic with high mechanical strength, fracture toughness, hardness, resistance to wear and thermal-shock. It is extensively used in many applications including automobile engine, cutting tools and abrasives [71]. Its low thermal expansion coefficient, as well as excellent chemical resistance, makes it a good candidate for thermal-barrier coatings in harsh environment. Furthermore, zirconia is a particularly good oxygen ion conductor. Consequently, yttrium-stabilized zirconia (YSZ) has been chosen as the standard solid electrolyte for sold-oxide fuel cell (SOFC) [72] [73] and gas sensor [74] [75].

New interests have also emerged in recent years on the luminescent properties of rare-earth-doped zirconia and on the catalytic behavior of zirconia [76] [77] [78]. Indeed, zirconia has been studied and employed as catalyst and support in many organic reactions [79] [80]. On the zirconia surface, zirconium atoms form the Lewis acid sites whereas oxygen atoms become Lewis base sites. Consequently, the surface of zirconia can exhibit both acidic and basic, as well as oxidizing and reducing, properties [81] [82] [83]. In an aqueous environment, the surface oxygen becomes negatively charged hydroxyl, which serves also as Brønsted base. All of these sites may be catalytic active in one or the other reaction. Furthermore, the multifunctional surface of zirconia tends to bind any available molecule that matches these sites. Therefore, zirconia is a very effective chromatographic stationary phase for biotechnology purification [84]. For these reasons, the surface properties in solvent, as well as the relative affinity of different ligands, have been studied [85].

Finally, an important emerging application of zirconia nanocrystals is the fabrication of nanocomposite with high refractive index since it finds market in a wide range of optic devices, including, the coating of brightness enhancement film for LCD display (Olson D., B., US patent US7547467, 2009), the encapsulation of LED [86], and holographic grating [57]. Such nanocomposite is typically obtained by the incorporation of nanocrystals into a transparent resin matrix. To maintain a certain level of transparency, the particles must be less than 10 nm in size and non-agglomerated. These drastic specifications and the prospects for technological integration have greatly stimulated the research on zirconia nanomaterials over the last two decades. The intrinsic properties of zirconia are governed by its atomic and bulk characteristics. In the following section we will discuss some of the properties of zirconia.

1.4.1 Polymorphism of zirconia

ZrO_2 has three known polymorphic phases at atmospheric pressure or 1 atm. When it is heated up to 1270ºC, the zirconia exists as a monoclinic phase also known as the baddeleyite [87]. It is in the tetragonal phase when it is between 1270°C and 2370°C [88] and finally, it crystallizes in a cubic system at temperatures above 2370°C [89]. Also, at higher pressure, zirconia can exist into two types of orthorhombic species: orthorhombic I [90] and II [91], appearing around 3 to 11 GPa and 9 to 15 GPa, respectively. Except for orthorhombic II, all of the phases of zirconia exhibit a fluorite-derived structure. Shown in Figure 46 are the structural models of the fluorite-derived structures. In the following sections, we discuss various ways in stabilizing the tetragonal phase zirconia.

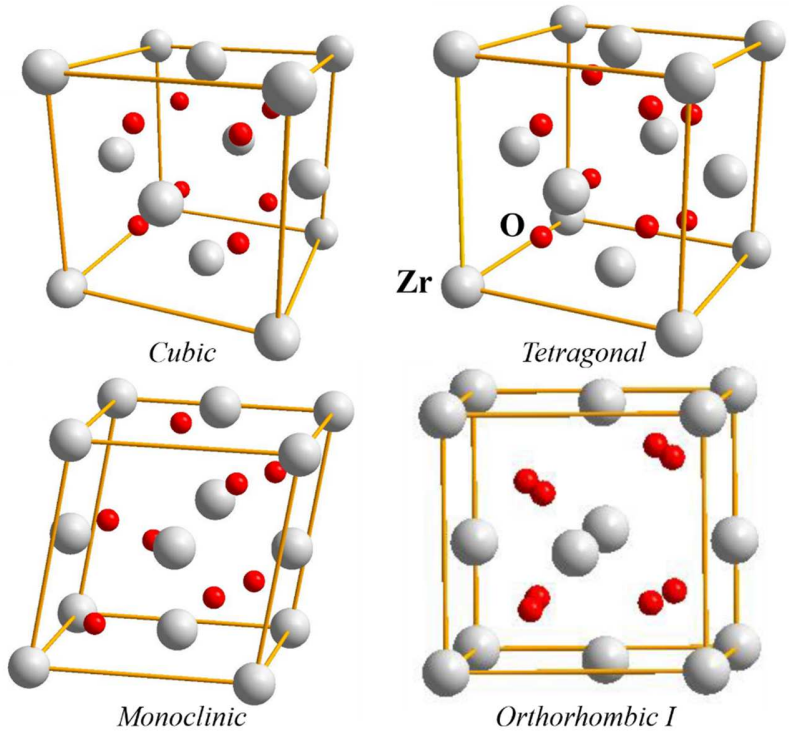

Figure 46: Graphical representation of fluorite-derived structures of zirconia.

1.4.2 Stabilization of bulk tetragonal phase zirconia particles

Stabilization of tetragonal phase zirconia for bulk material is popularly done via calcinations at high temperatures in order to favor a higher coordination of zirconia over oxygen (for this case an 8 fold coordination) by forming oxygen ion vacancies [92] [93]. There are other ways to obtain vacancies at lower temperatures such as altering the oxygen partial pressure by setting it in low

oxygen condition [94]. Lastly, the presence of oxygen ion vacancies can be achieved by doping with trivalent, and/or pentavalent cations which allows the stabilization of bulk tetragonal phase zirconia [95] [96] [97].

1.4.3 Stabilization of metastable tetragonal phase by various models

For the stabilization of nano-sized metastable tetragonal phase zirconia, various models exist involving surface energy, strain energy, internal and external hydrostatic pressure, structural similarities, foreign surface oxides, water vapour, anionic impurities, and lattice defects (oxygen ion vacancies). They will be briefly discussed in the following sections.

1.4.3.1 Stabilization of metastable tetragonal phase via surface energy

For very small particles with sizes less than 100 nm the surface properties tend to be more active in the stabilization of a particle. In the work done by Garvie [98], he demonstrated that the specific surface energy of nanocrystalline zirconia is enhanced for very small particles. He proposed a theoretical model for the relation of the size and specific surface area as expressed in Equation (19) where S is the specific surface area of the particle, M is the molecular weight, ρ is the volumetric mass density and D is the nanocrystallite size. The theoretical variation of excess energy as a function of crystallite size can be presented by Equation (20) where ΔE is the excess energy, N is the Avogadro's number, d is diameter of the particle, K is the factor to convert ergs to kilocalories, and γ is the surface energy.

$$S = \frac{6M}{\rho D} \tag{19}$$

$$\Delta E = 12N(n-1)^2 d^2 K\gamma n^{-3} \tag{20}$$

Garvie claimed that the stabilization of the metastable phase is due to both the improved specific surface area and excess energy [98]. The size below which the tetragonal phase zirconia is maintained is called the critical size and for aggregated particles it is around 30 nm [98]. For non-aggregated and strain free, the critical size is around 10 nm on the basis of thermodynamic consideration [99].

1.4.3.2 Stabilization of metastable tetragonal phase via strain energy

Surface energy imposes that the critical size should be around 10 nm for non-aggregated and 30 nm for aggregated metastable tetragonal phase zirconia. But in the work done by Mitsuhashi et al., they were able to produce tetragonal ZrO_2 particles larger than 30 nm and monoclinic particles of zirconia smaller than 10 nm [100]. Similar results were obtained by Wang and Lin [101] and Ramamoorthy *et al.* [102]. Mitsuhashi et al. suggested to introduce strain energy term in the thermodynamic analysis of the monoclinic to tetragonal phase transformation. Garvie later modified the surface energy equation in order to compensate for the strain energy [103].

1.4.3.3 Stabilization of metastable tetragonal phase via external and internal hydrostatic pressure

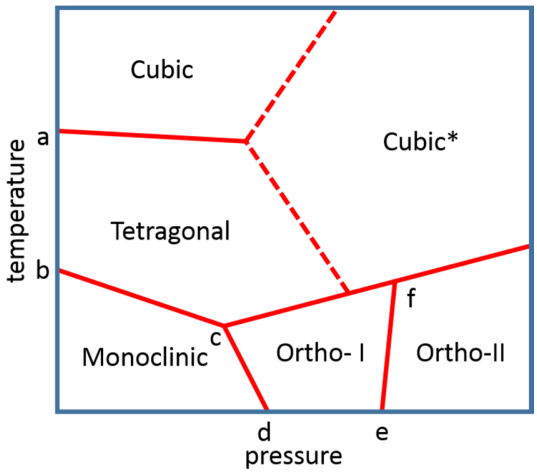

Figure 47: schematic representation of temperature against pressure diagram for bulk zirconia; (a) 1 atm at 2300°C,(b) 1 atm at 1175°C, (c) 2.2 GPa at 600°C ,(d) 4GPa at 25°C, (e) 13GPa at 25°C, and (f) 15 GPa at 25°C [104] (* hypothetical phase)

Figure 47 shows the schematic representation of temperature versus pressure phase diagram for bulk zirconia [104]. As observed the monoclinic phase can be transformed to orthorhombic I and II at lower temperatures but with high pressure. The role of external and internal hydrostatic pressure can account for the stabilization of metastable tetragonal phase zirconia at lower temperatures but brought about by the presence of external pressure and internal hydrostatic pressure for sizes greater than 30 nm and less than 10 nm, respectively [105] [106] [107].

1.4.3.4 Stabilization of metastable tetragonal phase via structural similarities

Another way of stabilizing the metastable tetragonal phase zirconia is by understanding the structural similarities of the amorphous phase zirconia with the tetragonal or monoclinic phase calcined zirconia [108] [109] [110] [111] [112] [113] [114] [115]. Using electron density and neutron diffraction measurements, Livage *et al.* observed that the Zr-Zr distances have the following values 0.22, 0.33, 0.37, 0.47, and 0.60 nm. They are exactly the same as the Zr-Zr interatomic distances of 0.33, 0.37 and 0.60 nm in the $(111)_{\underline{T}}$ plane of the tetragonal phase zirconia [108]. Therefore, due to structural similarities of the amorphous and tetragonal phase zirconia this transformation is also favored. However, other works suggests that the similarities of monoclinic phase zirconia and amorphous phase zirconia would favor the transformation process from amorphous phase to monoclinic phase zirconia [112] [113] [114]. Both results suggest that the transformation from the amorphous phase remains inconclusive and requires further analysis and experimentations.

1.4.3.5 Stabilization of metastable tetragonal phase via the presence of water vapor

The atmospheric condition appears to alter the interfacial energies as observed by the works done by Murase and Kato [116]. In this work, the presence of moisture during the synthesis was avoided by using argon gas. The absence of moisture during the ball-milling process inhibited the transformation from monoclinic to tetragonal phase which suggests that the presence of moisture promotes the transformation of zirconia.

1.4.3.6 Stabilization of metastable tetragonal phase via the presence of anions

The presence of various anions such as OH^- [117] [118], Cl^- [111] [119] [120], CH_3COO^- [118] [120] [121], CO_3^{2-} [122], SO_4^{2-} [119] [120] [121] [122] [123] [124], and PO_4^{3-} [125] within or over the surface of zirconia lattice appear to aid in the stabilization of the tetragonal phase at room temperature. The anions appear to increase the room temperature stability of tetragonal phase zirconia by either trapping the lattice dislocations or avoiding the ingress of oxygen ions onto the zirconia lattice. Thermodynamically, when these anions are present on the particles' surface, it is able to promote the tetragonal phase stability by increasing the interfacial difference between the phases. In contrast, when these anions are present internally, the stabilization of tetragonal phase at room temperature may be due to the reduction of the heat of phase transformation or bulk crystals

and/ or the generation of hydrostatic strains within the tetragonal lattice. However, there appears to be a limited understanding in the precise mechanism for the room temperature stabilization of tetragonal phase zirconia [126].

1.4.3.7 Stabilization of metastable tetragonal phase via the presence of oxygen ion vacancies

The presence of oxygen ion vacancies have been used to explain the stabilization of the bulk tetragonal phase zirconia and are believed to be generated at high temperature calcination, vacuum condition, or by doping with a trivalent species. For the nano-sized zirconia, the presence of oxygen ion vacancies are believed to be generated due to the "nanoparticle size effect" which allows the stabilization of metastable tetragonal phase zirconia. In the works done by Igawa *et al.* and similar works by Chraska *et al.*, they were able to compare the lattice parameters of the nanosized metastable tetragonal phase zirconia at room temperature with that of doped zirconia at room temperature and undoped zirconia at high temperatures [127] [99]. The results show that they are quite identical suggesting that similar phenomenon of oxygen vacancy may be attributed to such effect. This is further supported by the works done by Liu *et al.*, they were able to demonstrate the "nanoparticle size effect" by electron spin resonance (ESR) analysis of nanocrystalline zirconia powder synthesized in the absence of any impurities or atmosphere with low oxygen partial pressure [128]. Their results show that the number of oxygen ion vacancies with trapped electrons which is proportional to the F-center ESR signal intensity is observed to increase with decreasing nanocrystallite size. Sizes that are quite small appearing to favor the tetragonal or cubic phase suggest a strong correlation of the presence of oxygen ion vacancy to tetragonal phase stability.

Chapter 2: Synthesis and Characterization

2. Synthesis and Characterization

2.1. Introduction

In this section we will present the details of the syntheses and the characterization tools devoted to the study of nano-sized zirconia particles. As a guide, the flowchart of the synthesis and characterization steps is shown in Figure 48.

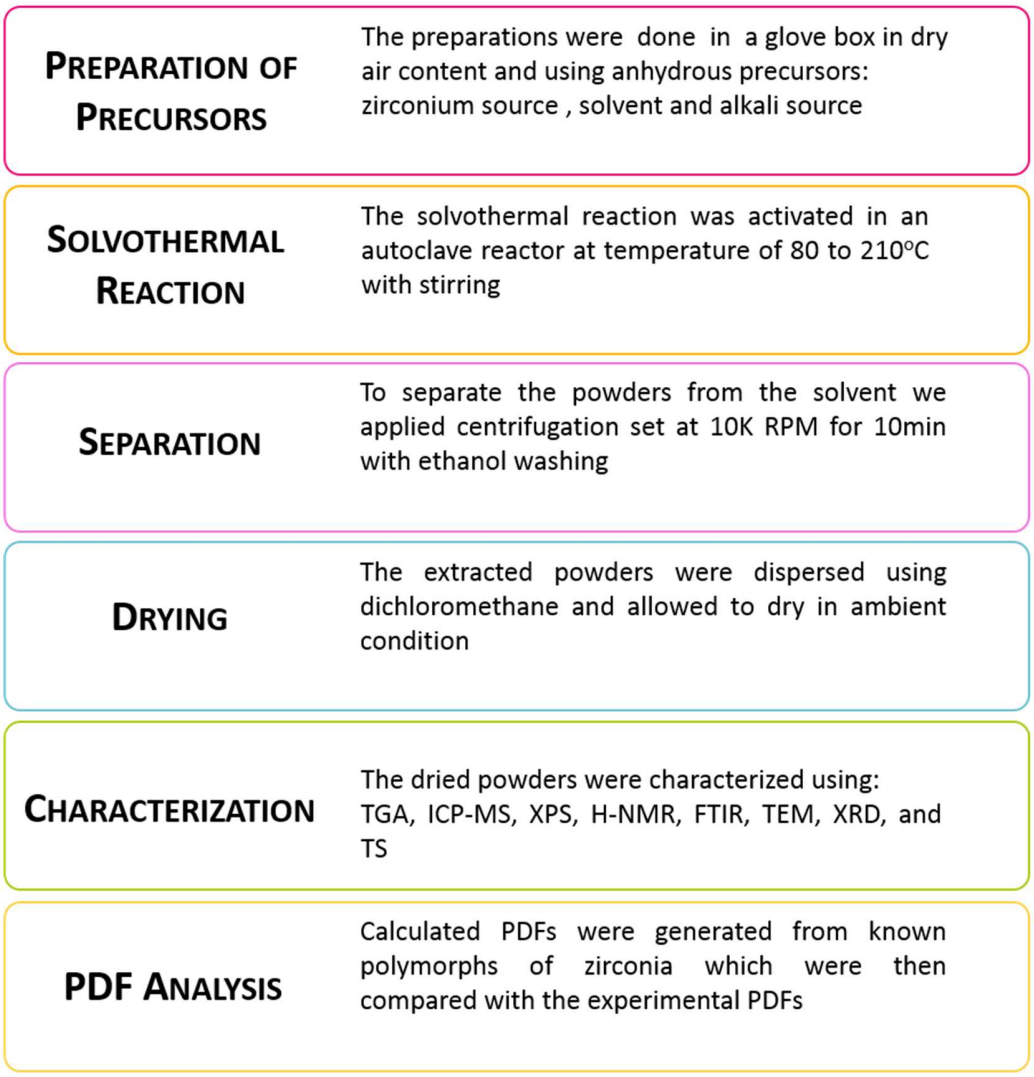

Figure 48: Experimental flowchart for the synthesis and characterization of zirconia nanoparticles using solvothermal method in a non-hydrolytic sol-gel route.

2.2. Sample preparation and synthesis

2.2.1. Preparation of precursors

Table 5: Chemical precursors for the synthesis of zirconia nanoparticles via non-hydrolytic sol-gel solvothermal treatment

Metallic precursors				
Chemical compound	**Chemical formula**	**Brand**	**Purity**	**CAS No.**
Zirconium isopropoxide with isopropanol adduct	$Zr(OiPr)_4(HOiPr)_2$	STREM	99.9%	14717-56-7
Zirconium chloride	$ZrCl_4$	Alfa Aesar	99.5%	10026-11-6
Solvents				
Benzyl alcohol	$C_6H_5CH_2OH$	Sigma Aldrich	99.8%	100-51-6
Isopropyl alcohol	$(CH_3)_2CHOH$	Sigma Aldrich	99.7%	67-63-0
Ethanol	CH_3CH_2OH	Alfa Aesar	96%	64-17-5
Diisopropyl ether	$((CH_3)_2CH)_2O$	Sigma Aldrich	99%	108-20-3
Dibenzyl ether	$(C_6H_5CH_2)_2O$	Sigma Aldrich	98%	103-50-4
Anisole	$CH_3OC_6H_5$	Alfa Aesar	99%	100-66-3
Benzaldehyde	C_6H_5CHO	Alfa Aesar	99%	100-52-7
Acetone	$(CH_3)_2CO$	Labogros	99%	67-64-1
Alkali sources				
Sodium hydroxide	NaOH	Alfa Aesar	97%	1310-73-2
Lithium hydroxide	LiOH	Alfa Aesar	99.9%	1310-65-2
Potassium hydroxide	KOH	Alfa Aesar	99.9%	1310-58-3
Sodium fluoride	NaF	Alfa Aesar	99.99%	7681-49-4
Sodium chloride	NaCl	Prolabo	99%	7647-14-5
Sodium bromide	NaBr	Alfa Aesar		7647-15-6
Sodium ethoxide	$NaOC_2H_5$	Alfa Aesar	96%	141-52-6
Sodium methoxide	$NaOCH_3$	Alfa Aesar	98%	124-41-4
Sodium isopropoxide	$NaOCH(CH_3)_2$	Alfa Aesar		683-60-3
Sodium Amide	$NaNH_2$	Sigma Aldrich	95%	7782-92-5
Tetra-butyl ammonium methoxide	$C_{17}H_{39}NO$	Sigma Aldrich	20% in methanol	34851-41-7
Sodium nitrate	$NaNO_3$	Interchim	99.999%	7631-99-4
Sodium sulfate	Na_2SO_4	Alfa Aesar	99%	7757-82-6
Drying agents				
Dichloromethane	CH_2Cl_2	Alfa Aesar	99.5%	75-09-2
Oleic acid	$C_{18}H_{34}O_2$	Sigma Aldrich	90%	112-80-1
Dissolving agents				
Hydrofluoric acid	HF	Normapur	40%	7664-39-3
Sulfuric acid	H_2SO_4	Normapur	95%	7664-93-9
Nitric acid	HNO_3	Sigma Aldrich	70%	7697-37-2

The syntheses of zirconia nanoparticles were performed using different combination of reagents which are categorized into three classes; (i) the type of zirconium precursor, (ii) the type of solvent and (iii) the option of adding an alkali source. Listed in Table 3 are the chemicals used for the experimental work devoted to the synthesis and characterization of zirconia samples. Because of the nature and the sensitivity of the sol-gel chemistry, the experiments were conducted in the absence of moisture and inside a glovebox under a continuous flow of dry-air. In addition, the reagents utilized in the synthesis are all anhydrous.

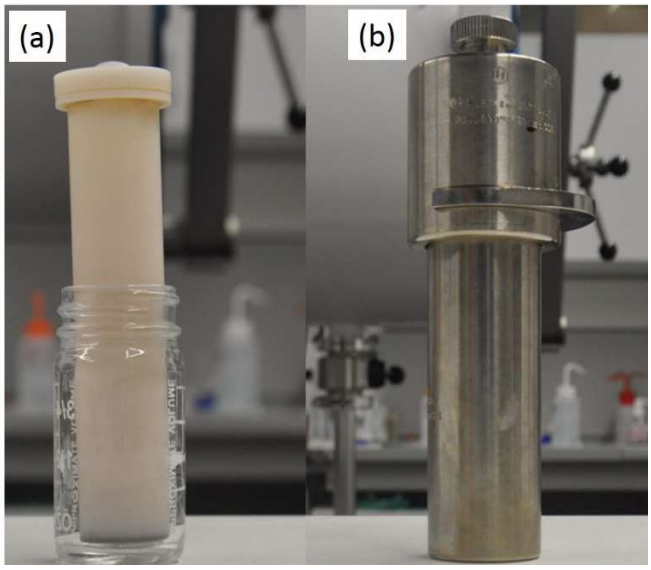

Figure 49: (a) Teflon® insert and (b) Parr acid digestion bomb typically used for solvothermal treatment of reaction mixture (upper pressure limit of the used equipment ≈ 124 bar).

The selected reagents were added into a Teflon® insert shown in Figure 49 (a) together with the reactor Figure 49 (b) and accessories used for the autoclave thermal treatment. The capacity of this type of insert is up to 25 mL. The content of the different reagents vary depending on the desired characteristics of zirconia particles but typically the total volume of the suspension was approximately around 15 mL. This amount of suspension would leave a vacant volume space in the insert of about 10 mL. No additional pressure was applied and all syntheses were carried out under autogenous pressure, *i.e.* the pressure generated by the content of the autoclave upon heating in an airtight vessel. One can assume that the pressure will be primarily due to the evaporation of the solvent used, even though the metal oxide or reaction byproducts may also contribute to this

pressure, especially in experiments where a high concentration of reactants was used. Nevertheless, a 60% filling of the reactor will not give rise to any critical autogenous pressure. After the preparation of the reaction mixture, we proceeded to the solvothermal treatment for at least 3 days with temperatures ranging from 80 to 210ºC.

2.2.2. Solvothermal reaction

The autoclave bomb (Figure 49 (b)) was placed inside a pre-heated isothermal box on a hot plate as shown in Figure 50. The temperature was then raised over the boiling point of the solvent but the autoclave bomb allows various reactions to occur in liquid solution due to the autogenous pressure. It is very important to perform the non-hydrolytic sol-gel route under solvothermal conditions due to the lower reactivity of metal alkoxides in the absence of water.

Figure 50: Autoclave reactors placed inside a pre-heated isothermal device on a hotplate

Figure 51: Synthesized suspension of zirconia after solvothermal reaction.

The synthesis temperature was adjusted (typically around 80 to 210°C and depending on the type of synthesis) and the magnetic stirrer placed inside the insert was set at 350 revolutions per minute. Right after adding the reactor on the hotplate device, one could notice a sudden temperature drop of the isothermal box but within a couple of minutes the temperature was normalized back to the selected temperature. The entire set-up was kept inside a chemical fume hood to help regulate the changes in temperature due to outside environment during the 3 days solvothermal treatment. After 3 days, the synthesized suspensions were then collected. They would typically appear in various colors (white to brown) but mostly they were white and have a turbid appearance as shown in Figure 51. Finally, the collected suspensions were placed inside a polypropylene centrifuge tube for the separation of the solid and the supernatant parts.

2.2.3. Separation process of the synthesized suspension

The tubes containing the synthesized suspension were placed inside a centrifuge to separate the powder from the liquid part which contains mostly initial solvent and organic byproducts. Shown in Figure 52 is the diagram for the separation process.

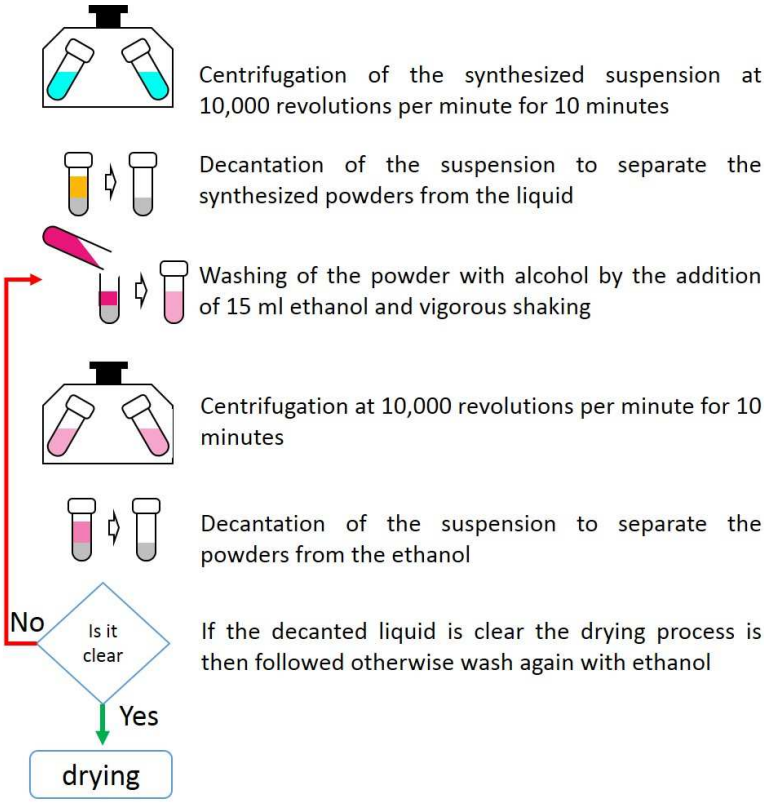

Figure 52: Flow chart for the separation process.

After the first centrifugation the remaining powder was washed with alcohol by adding 15mL of ethanol and vigorously shaken to homogenize the alcoholic suspension. Centrifugation was then applied to enhance the ethanol washing and aid in the removal of synthesized organics that were not removed in the initial centrifugation step. After the second centrifugation, the liquid was then decanted from the washed powders and the turbidity or clarity of the liquid was inspected. When the liquid remained turbid or not clear then further ethanol washing was done. After a clear liquid was obtained, the powders were dried.

2.2.4. Drying in ambient condition

For the drying process of the zirconia powders, 20 mL of dichloromethane was added to the centrifuge tube and shaken vigorously in order to remove the precipitate from the wall of the tube. The samples appearance before and after drying process is shown in Figure 53. The drying process was performed inside a fume hood which allowed the evaporation of the liquid phase containing mostly dichloromethane and traces of ethanol. The sample appeared to be white after the drying process, although some samples appeared to be greyish or yellowish due to the presence of residual organics.

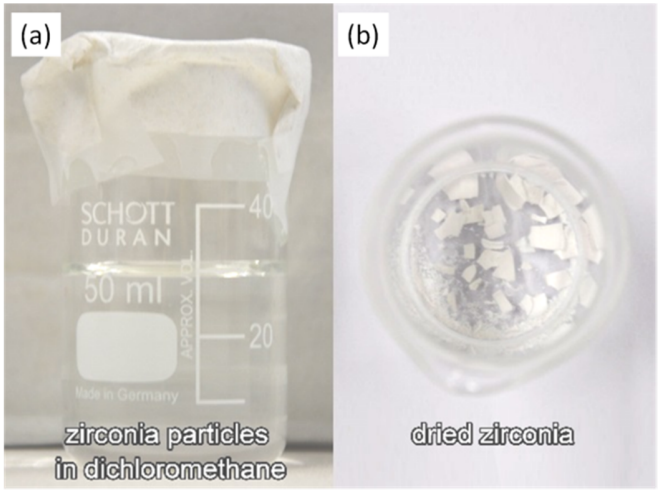

Figure 53: Zirconia particles in (a) readily dispersed in dichloromethane and (b) finally recovered after evaporation of dichloromethane.

2.3. Chemical, morphological and structural characterization

The dried zirconia powders were then prepared for various characterizations to extract information regarding their chemical, morphological and structural properties. The characterization tools, described in the following sections, used here were Thermogravimetric analysis (TGA), Inductive coupled plasma mass spectrometry (ICP-MS), X-ray photoelectron spectroscopy (XPS), proton nuclear magnetic resonance (H-NMR), Fourier transform infrared spectroscopy (FTIR), transmission electron microscopy (TEM), X-ray diffraction (XRD), and total scattering and pair distribution function (PDF) analysis.

2.3.1. Thermogravimetric (TGA) analysis

TGA is the analysis of the mass variations of a sample with respect to time or temperature in a controlled atmosphere. The mass losses give several informations regarding the drying, desorption, reduction or degradation processes with respect to the atmospheric condition. The mass gain are linked to phenomenon such as wetting, oxidation or adsorption processes. Thermogravimetric analyses using TGA NETZSCH STA 449 F3 Jupiter (see Figure 54) were performed on the synthesized powders placed in an alumina crucible with a heating rate of 10°C per minute over the range of 30 to 1000°C in an argon environment with 20 ml/min flow rate. The powders' weight were recorded during the heating and cooling step to determine the weight lost.

Figure 54: TGA device used for characterization (TGA NETZSCH STA 449 F3 Jupiter)

2.3.2. Inductive coupled plasma with mass spectrometry (ICP-MS) analysis

Inductive coupled plasma mass spectrometry (ICP-MS) is an analytic technique that determines the elemental composition of a sample. ICP-MS converts the atoms of the dissolved samples into ions that are then separated and detected by a mass spectrometer that is coupled with the device [129]. The principles of the measurement is represented in Figure 55.

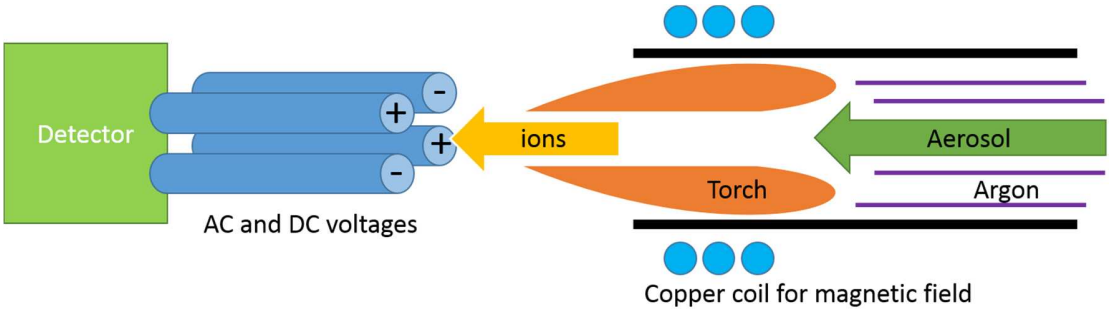

Figure 55: Principles of the ICP-MS anaylsis

The ions are then analyzed by a mass spectrometer where they are separated by their mass-to-charge ratio which allows the identification of the ions that composes the sample [129]. The most commonly used type of mass spectrometer is the quadrupole mass filter. This type of filter has 4 rods with an approximate size of 1 cm in diameter and 15 to 20 cm in length. Alternating current and direct current are supplied to opposite rods alternately and are synchronized with the radio frequency field or magnetic field. This creates an electrostatic filter that allows ions of single mass-to-charge ratio to pass through the rods to the detector at any given time. By changing the setting, this set-up allows the detection of specific mass-to-charge ratio. Also, the supplied voltages on the rods can be switched rapidly, thus enabling the filter to separate up to 2,400 atomic mass unit per second. The zirconia powder samples were mixed with acids (nitric acid (HNO_3), hydrofluoric acid (HF) and sulfuric acid (H_2SO_4)) and then dissolved in a microwave oven. They dissolved powders were placed into the device. The advantages of ICP-MS are low signal detection (ppm to ppt range), a wide element coverage and a fast analysis.

2.3.3. X-ray photoelectron spectroscopy (XPS) analysis

The chemical composition of the powder was then analyzed via X-ray photoelectron spectroscopy (XPS). XPS is a surface-sensitive analytical technique using the kinetic energy of the low energy electrons that are emitted in the sample due to different excitation processes. The strong interaction

between the sample and the low-energy electrons allows near surface electrons to escape inelastically. The mechanism is initiated by the absorption of X-rays which drives the emission of electrons or photoelectrons as shown in Figure 56. The Fermi levels for solid sample are the same as for the spectrometer but their vacuum levels are shifted. This induces the incorporation of the work function in the calculation of the binding energy by using Equation (21), which is based on the works of Ernest Rutherford [129], the binding energy is then used to determine the composition of the surface. The electrons ejected are analyzed by the detector by measuring its kinetic energy which provides information as to the type of elements present on the sample. Note that the thickness of penetration varies for different types of samples but typically for metals it is approximately 2.5 nm and for organic it is about 10 nm.

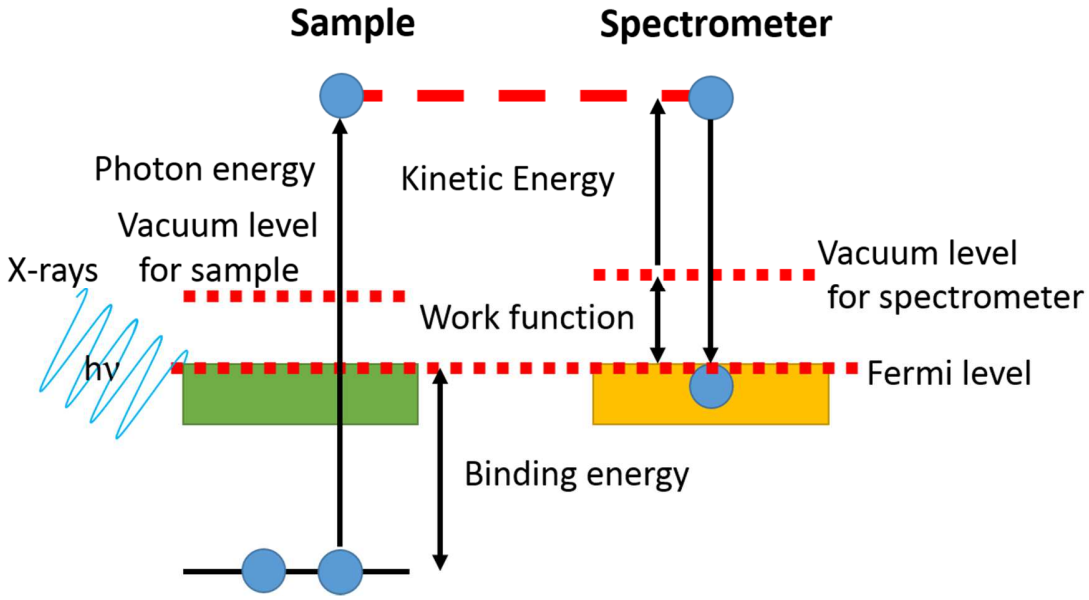

Figure 56: Photoelectron generation for XPS

$$E_{binding} = E_{hv} - (E_{kinetic} + \varphi) \quad (21)$$

Where $E_{binding}$ is the binding energy,

E_{hv} is the photon energy from X-ray,

$E_{kinetic}$ is the kinetic energy determined by the machine,

And φ is the work function for the spectrometer

A tiny amount of the powder was placed inside the device for spectroscopic analysis. The device used for the XPS characterization was an AXIS Ultra DLD spectrometer, Kratos Analytical Ltd, with a monochromated X-ray Source ($Al_{K\alpha}$, 1486.6 eV) and a spot size of 300 by 700 µm. The hemispherical analyzer was operated in CAE (Constant Analyzer Energy) mode, with pass energy of 160 eV and a step of 0.5 eV for the acquisition of surveys spectra, and pass energy of 20 eV and a step of 0.1 eV for the acquisition of high resolution spectra.

2.3.4. Proton nuclear magnetic resonance spectroscopy (H-NMR) analysis

H-NMR analysis was done in order to obtain the chemical compounds present in the synthesized solution. NMR is a technique used to identify carbon-hydrogen framework of an organic compound by taking advantage of the magnetic properties of the atomic nucleus. A spinning charge generates a magnetic field and the resulting spin produces a magnetic moment that is proportional to the spin. In the absence of external magnetic field, the nuclear spins are randomly oriented but align themselves when an external magnetic field is applied (see Figure 57). There are two alignments with respect to the direction of the external magnetic field which are called α (+1/2) and β (-1/2) spin state for protons that align and against the direction of the external magnetic field.

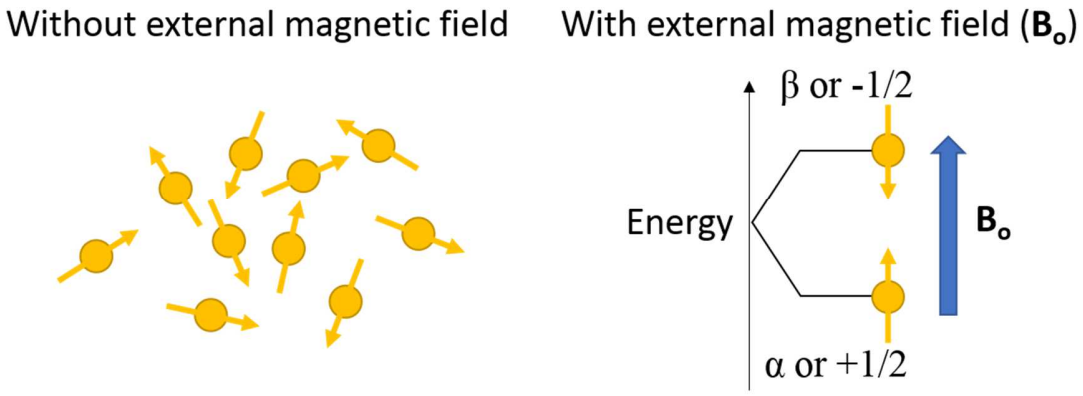

Figure 57: Principles of nuclear magnetic resonance spectroscopy.

The energy difference between the two spin states is dependent on the strength of the applied magnetic field. Irradiation of the sample with radio frequency energy equal to the energy difference between spin states causes spin excitation moving α state and β state. When the nuclei undergo relaxation, they emit electromagnetic frequencies that can be interpreted as the signature of the compound. After the solvothermal treatment, 15 to 30 mg of the liquid sample were extracted and

mixed with chloroform solvent. The mixed solution were poured into a tube (~1 cm diameter) until it reached a height of about 5 cm. The NMR characterization where done at the NMR Faculty of Pharmacy of the University of Limoges and the device for characterization was Bruker Avance DPX 400 MHz.

2.3.5. Fourier transform infrared spectroscopy (FTIR) analysis

The FTIR analysis was carried out using a Thermo Fisher Nicolet 6700, shown in Figure 58, to determine the infrared spectrum of the samples over the wavelength range of 400 to 4000 cm^{-1} with a resolution of 4.0 cm^{-1}. A minute amount (about a pinch) of the zirconia powders were mixed with some potassium bromide to mold pellets that were then placed inside the machine.

Figure 58: FTIR device used for characterization (Thermo Fischer Nicolet 6700)

The sample was irradiated by a broadband of IR source and the resulting spectrum or the transmitted spectrum was measured by an IR spectrometer as shown in Figure 59. The relation of these intensities is given by the Bouguer-Lambert-Beer law (see Equation (22)).

$$T = \frac{I}{I_o} \tag{22}$$

Where T is the transmittance,

I is the measured intensity,

And I_o is the incident intensity.

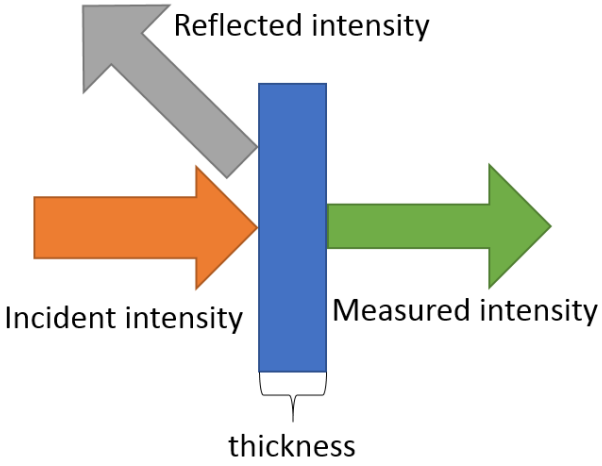

Figure 59: IR transmission and signals observed

The absorbance of the sample can also be obtained from the transmittance information given by Equation (23).

$$A = \log\frac{1}{T} = -\log\frac{I_o}{I} \tag{23}$$

Where A is the absorbance.

Infrared (IR) region is situated at wave numbers from 13000 cm^{-1} to 33 cm^{-1}. Infrared region can be categorized into three parts which are called the near, mid and far infrared regions. The region that is most beneficial in terms of vibrational modes of a compound is the mid infrared region ranging from 4000 cm^{-1} to 400 cm^{-1}. When the IR radiation is absorbed by the sample, it will produce a signal with its frequency matching a particular vibration that is inherent to a particular atom to atom bond. These molecular vibrations can range from a simple coupled motion of two atoms (diatomic) or a much larger network containing several atoms (polyatomic) and act as a large polyfunctional molecule.

2.3.6. Transmission electron microscopy (TEM)

The morphological characteristics of the samples were analyzed via TEM analysis. A high resolution TEM was used (JEOL JEM 2100f shown in Figure 60). The samples were prepared by diluting first one drop of the washed suspension into 20 mL of dichloromethane and 2 drops of oleic acid and finally adding one drop of this diluted solution onto an ultrathin carbon-A holey 400 mesh copper grid. The sample grid was then placed inside the machine under vacuum condition.

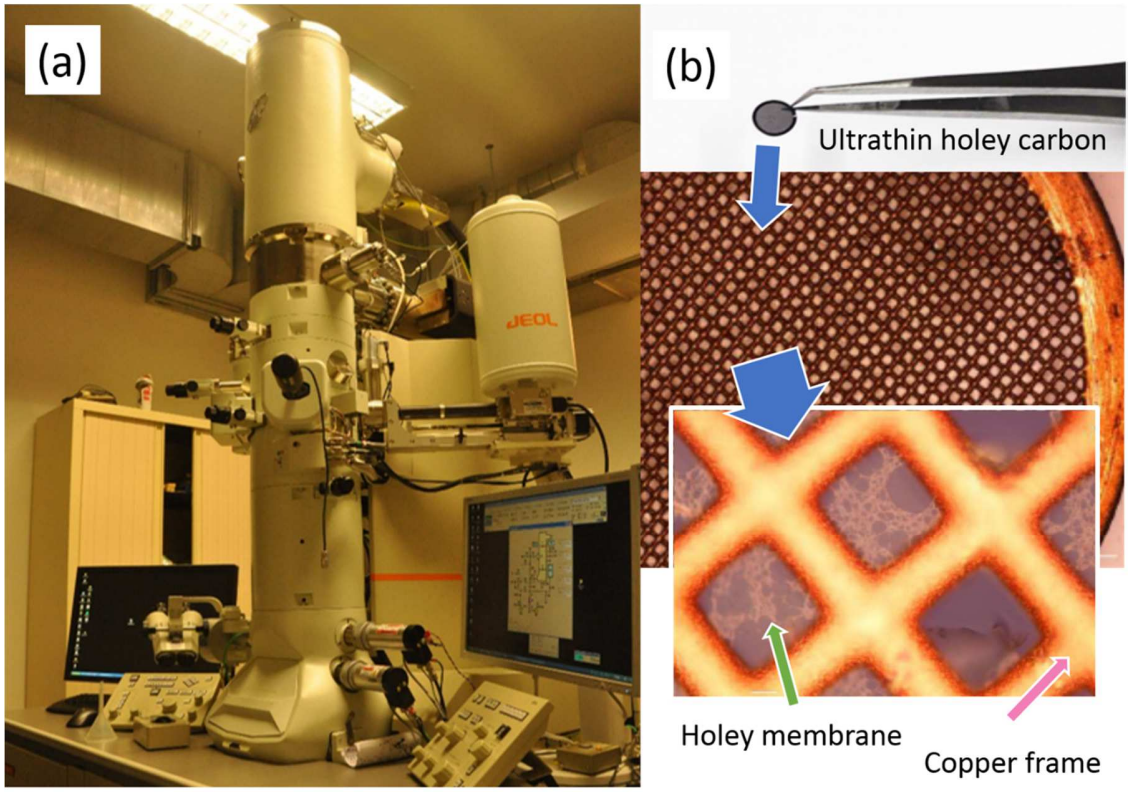

Figure 60: (a) TEM device used for characterization with the (b) ultrathin mesh copper grid

The TEM configuration is generally the same as those of a classic light microscope with similar physical principles involve but at a much higher resolution (see Figure 61). Instead of using a visible light as a source, electrons are used which are produced via thermionic emission and accelerated using electromagnetic fields in vacuum condition.

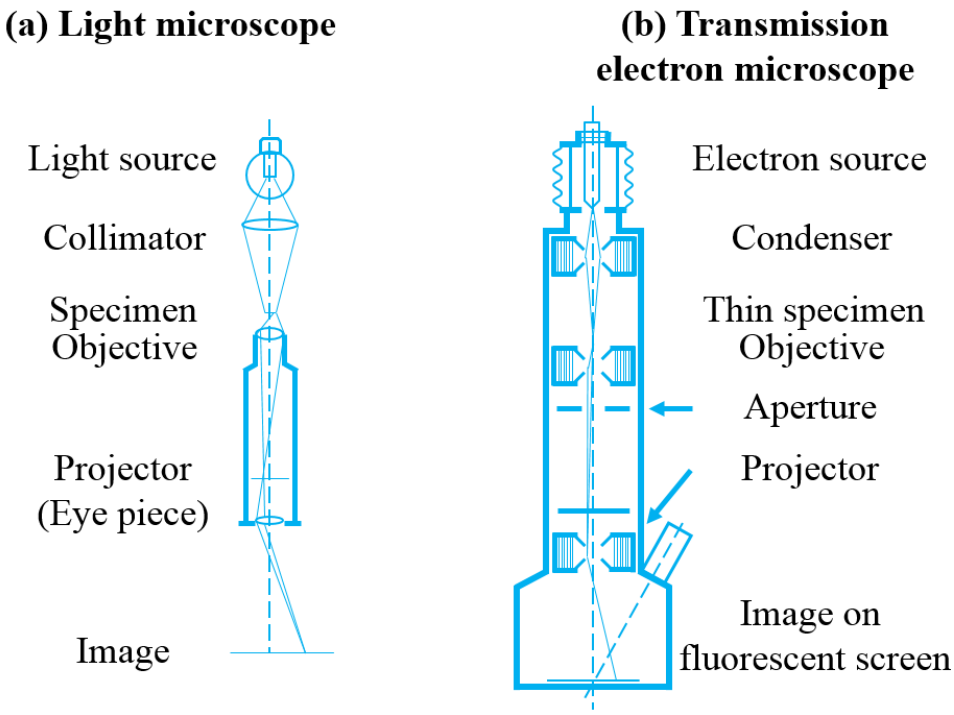

Figure 61: Comparison of a (a) light microscope and (b) transmission electron microscope

The wave-particle duality of electrons allows the calculation of their wavelength given by the de Broglie equation (see Equation (24)). For electrons moving at high speeds, a relativistic correction is added to the de Broglie equation given in Equation (25). By varying the supplied voltage, the electron wavelength can be tuned to desired value. An acceleration voltage of 1kV can then produce a wavelength of 40 pm while 1MV can have a 0.9 pm [129]. This allows the production of a huge variety of wavelengths that can be used for analyzing the specimen.

$$\lambda = \frac{h}{mv} \tag{24}$$

Where h is the Planck's constant,
m is mass of the particle,
and v is the velocity of the particle.

$$\lambda = \frac{h}{m_o v\sqrt{1-\frac{v^2}{c^2}}} = \frac{h}{\sqrt{2m_o eV(1+\frac{eV}{2m_o c^2})}} \quad (25)$$

Where m_o is the mass of electron equal to $9.1\text{x}10^{-31}$kg,

c is the speed of light equal to $3\text{x}10^{8}$ m/s,

e is the electronic charge equal to $1.6\text{x}10^{-19}$ C,

and V is the voltage applied.

The interaction between electron and matter produces a variety of responses as shown in Figure 62. These responses can be used and analyzed by different characterization techniques but for this work we will focus on the morphological information which is obtained from the transmitted beam.

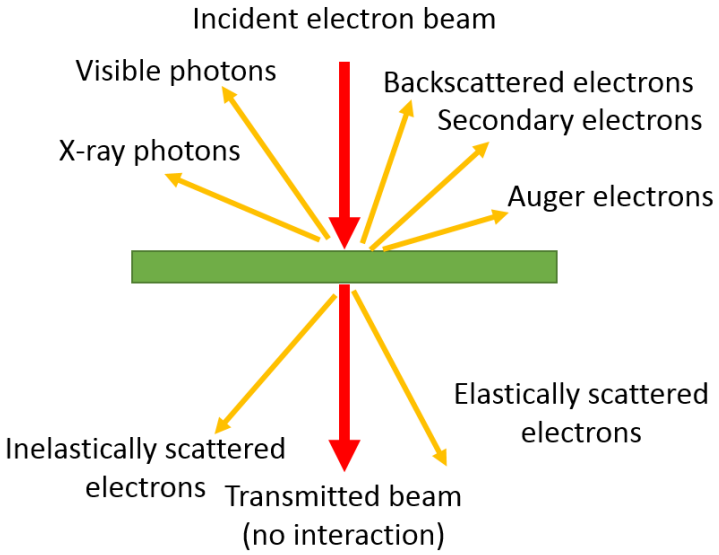

Figure 62: Main signals generated by an electron beam–specimen interaction in TEM

There are two basic operating functions of TEM which are the diffraction and imaging. The objective lens plays a vital role in both operations. When the electrons propagate towards the image plane of the objective lens, they recombine giving a real space image of the specimen which is its two dimensional projection. The nature of patterns observed will depend on the structural characteristics of the specimen. The electrons that are travelling along parallel trajectories emerge

from the specimen or those electrons that are scattered from a set of crystalline planes at Bragg condition with the beam produces diffraction patterns which is inherent to the specimen and observed in the focal plane of the objective lens. This pattern represents the reciprocal space or Fourier space representation. By fine tuning the electron beam into a finer probe, we can extract the diffraction pattern for nanometer size particles. This mode is done through selected area electron diffraction (SAED). For thin single crystals the diffraction pattern appears as an array of spots, for nano or polycrystalline materials the pattern appears as a fine nested rings and for amorphous materials it has a pattern of diffused nested rings. Also, for thicker single crystals, the appearance of Kikuchi bands is observed [129].

2.3.7. X-ray diffraction analysis (XRD)

The average structure of the samples were characterized by X-ray powders diffraction (XRD) using a Bruker D8 Advance diffractometer equipped with a Lynxeye rapid detector. The wavelength of the monochromated primary beam was $\lambda_{CuK\alpha1}$ = 1.5406 Å and de angular measuring range was 10 to 110º with step size of 0.02º and an equivalent time step of 1567 seconds. The dried powders were placed on a silicon flat plate sample holder. Shown in Figure 63 is the X-ray diffractometer utilized.

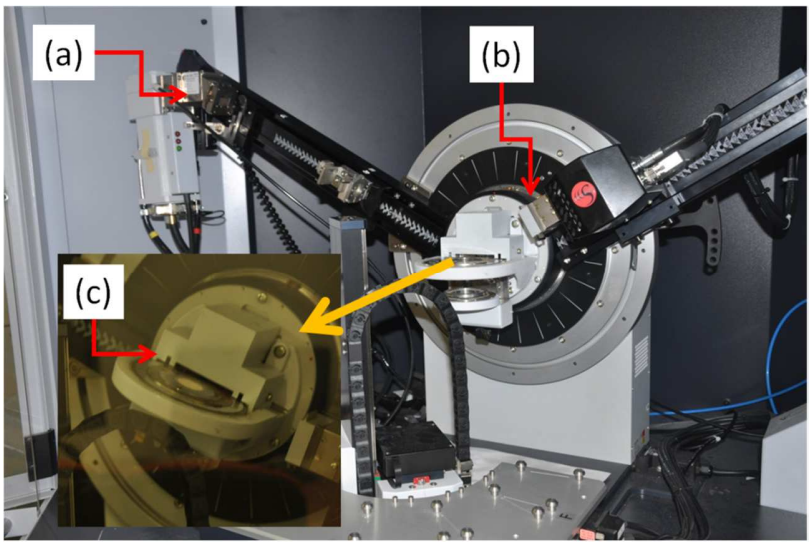

Figure 63: Bruker D8 Advance X-ray diffractometer for XRD characterization (a) source, (b) detector and (c) mounted sample

XRD is a non-destructive method widely used to identify a crystalline material and determine its structural and microstructural features, *i.e.* size, strain, crystallite size, preferred orientation and

defects. This method is also ideal for *in-situ* characterization and can use both laboratory and synchrotron X-ray sources, the latter being also ideal for thin samples [130].

2.3.7.1. Basics of XRD

2.3.7.1.1. Bragg's law

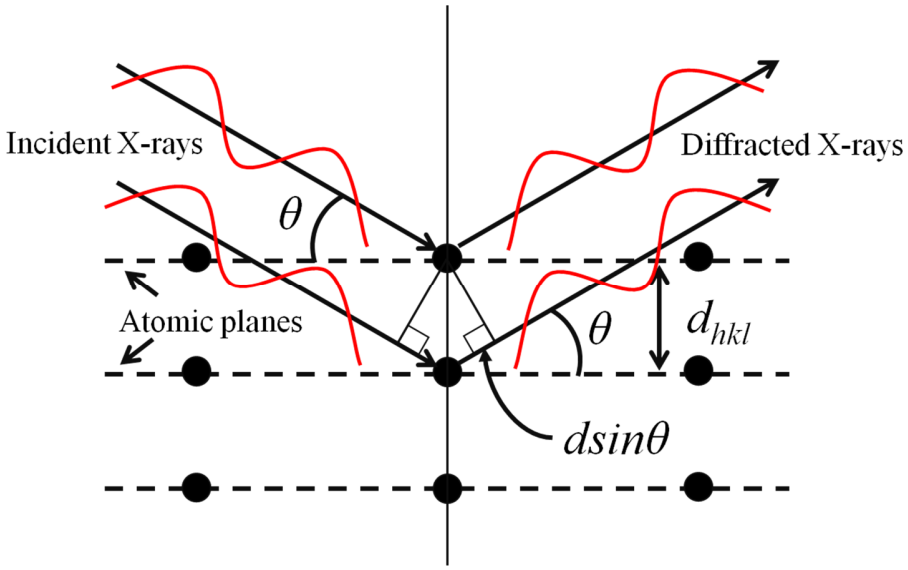

Figure 64: Diffraction of X-rays from a crystalline material

Solids can be classified into two main categories; crystalline and amorphous solids. Crystalline solids are composed of arrays of atoms arranged in a three dimensional regular repetition while amorphous solids are disordered [131]. The reflection of the X-rays from the lattice planes produces wave interferences that are either constructive or destructive. Figure 64 represents a crystalline material under X-ray beam. If the angle (θ) and the distance (d) is positioned in such a way that a constructive interference is formed then an intensity can be measured. This constructive interference condition is given by the Bragg's law (see Equation (26)).

$$2d_{hkl}sin\theta = n\lambda \tag{26}$$

Where, h, k and l are the Miller indices of the observed plane,

d_{hkl} is the interplanar spacing, θ is the incident angle,

n is an integer representing the order of reflection,

and λ is the wavelength of the source.

XRD pattern serves as a “fingerprint” of the material allowing the phase identification of its phase by search and match method. This method is a simple and rapid way of comparing the experimental data obtained to a known standard on databases such as International Centre for Diffraction Data (ICDD) [132] and Cambridge structural database (CDS) [133].

2.3.7.1.2. Size effect

There are several factors that may affect the width of the diffraction peaks: instrument, crystal size, microstrains, inhomogeneity, and temperature factors. Luckily, the instrumental contribution can be measured and the inhomogeneity and temperature variation can be controlled in an XRD experiments. To measure the average size values of a crystalline material, Scherrer’s equation (see Equation (27)) relates the crystal size to the broadening of the Bragg’s peak [134]. This expression shows that the peak width is inversely proportional to the size of the crystallites which suggests that if they become smaller the peaks will become broader.

$$B(2\theta) = \frac{K\lambda}{Lcos\theta} \tag{27}$$

Where, B is the peak width or line broadening at full width at half maximum (FWHM),
K is the Scherrer’s constant, generally close to unity,
λ is the X-ray wavelength,
L is a characteristic size of the crystallite,
and θ is the Bragg angle.

Scherrer’s equation is best for measuring the size from single peak’s width between (2θ) 30^o and 50^o where they are well pronounced, highly symmetric and where the contribution of the strain effects is low. It is interesting to note that the Scherrer’s constant K actually depends on crystallite shape and Miller indices. The values typically are close to unity but can vary from 0.62 to 2.08 [135].

A more efficient way of characterizing the size from the diffraction peaks is via the use of the integral breadth (β) which is the ratio of the peak area to peak maximum. The apparent size (T) of the crystallite is related to the integral breadth as defined in Equation (28).

$$\beta(2\theta) = \frac{\lambda}{T cos\theta} \tag{28}$$

Where λ is the X-ray wavelength, θ is the Bragg angle, and

T is the apparent size of the crystallite.

The advantage of the use of the integral breadth over the Scherrer's formulation is that the apparent size is perfectly defined with respect to crystallite shape and size and there is no need to calculate the value of the constant *K*. For example, when the crystallites have shape, the apparent size relates to the particle diameter (D) through Equation (29) [136]:

$$T = \frac{3D}{4} \tag{29}$$

2.3.7.1.3. Strain effect

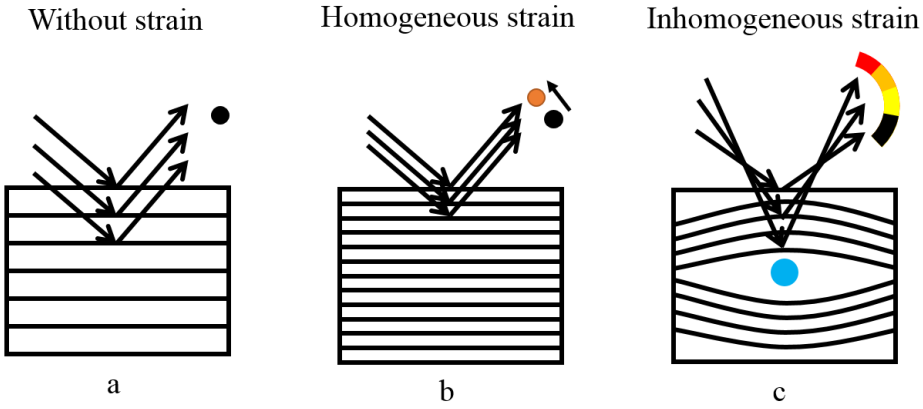

Figure 65: Homogenous and inhomogeneous strain effects for macro and micro sizes; a) unconstrained crystallite, b) homogenously strained crystallite leads to shifting of the position, and c) inhomogenously strained crystallite leads to the broadening of the position.

The next thing to consider in dealing with nanocrystals is the strain effect. There are generally two types of strains which are the macrostrains (i.e. homogeneous strains) and the microstrains (i.e. inhomogeneous strains). As shown in Figure 65, macrostrains shift the position of the peak (cell parameter change) while microstrains broaden the peak Warren [137]. Both kind of strains can occur simultaneously. When dealing with nanoparticles, microstrains information are valuable because they reflect the structural disorder within the particles. The effect of the microstrains on the broadening is given by Equation (30).

$$B(2\theta) = \eta tan\theta \quad (30)$$

Where, B is peak broadening brought about by strain effect,

θ is the Bragg angle, and η is the apparent microstrains.

2.3.7.1.4. The Rietveld method

When there is an extensive overlapping of peaks, individual peak analysis becomes less reliable. Whole profile analysis offers an alternative to this problem which is very common for nanomaterials. It is a way to simulate all the peaks of the XRD diagram at once and extract the needed information regarding their positions, intensities and broadness. Examples of full profile analysis are Le Bail, Pawley and Rietveld methods with each having their own advantages and disadvantages. In this work we will focus on the Rietveld method for which peak intensities are calculated thanks to a structural model, which makes it more efficient to obtain information from very broad profiles.

The XRD diagrams obtained were analyzed using the Rietveld method to obtain the structural properties (average apparent size, apparent microstrains, and lattice parameters) of the samples. The calculations were conducted by using FullProf suite program version 3.00 which is a versatile program designed for structural characterization [138].

The typical refinement procedure begun with the selection of an appropriate model as close as possible to the sample. The scale of the calculated diagram was then adjusted followed by the background and cell parameters refinement. Once reasonable values for these parameters were obtained, the peak shapes were then refined to calculate the size and strain of the sample. Further improvement on the refinement was done to include the atomic positions and thermal displacements. Lastly, we inspected the R-factors and the model generated and compared it to the experimental data and assessed the goodness of the fit. The refinement flowchart is summarized in Figure 66.

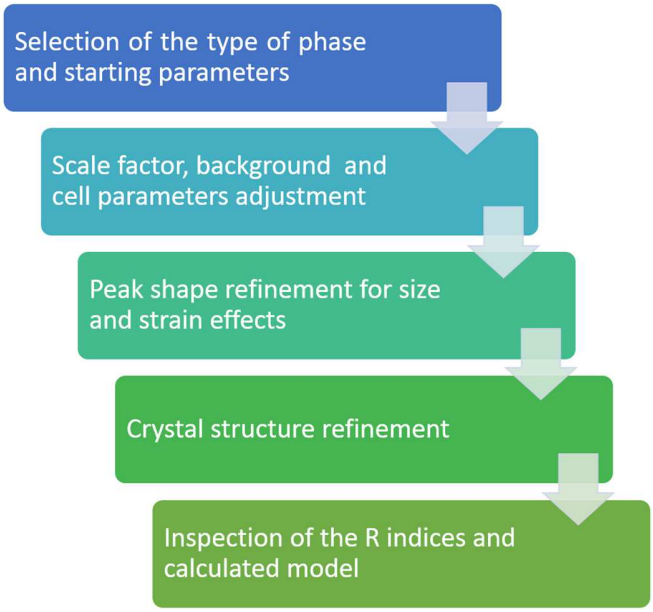

Figure 66: Refinement flow chart

2.3.7.1.5. *Principle of the Rietveld Method*

The Rietveld method is based on the diminishing of the difference between measured intensity and the calculated intensity from a model. The classical least-squared criterion used in this method is given in Equation (31) where S_y should be minimized.

$$S_y = \sum_i w_i \, (y_i - y_{ci})^2 \tag{31}$$

Where, S_y is the least-square residue,

$w_i = 1/y_i$ is the weight for observation y_i

y_i observed intensity at the i^{th} step,

and y_{ci} is the calculated intensity at the i^{th} step.

The calculated intensity is then the main concern of the method and how it can be best obtained. Classical intensity equation gives us a function that will serve as the basis for our calculated intensity (see Equation (32)).

$$y_{ci} = s \sum_{K} L_K |F_K|^2 \Phi(2\theta_i - 2\theta_K) P_K A + y_{bi} \quad (32)$$

Where, s is the scale factor,

K is the miller indices , h, k, and l, for a brag reflection,

L_K contains the Lorentz, polarization, and multiplicity factors,

Φ is the reflection profile function,

P_K is the preferred orientation,

A is the absorption factor,

F_K is the structure factor for the K^{th} Bragg reflection,

And y_{bi} is the background intensity at the i^{th} step.

The calculated intensity depends on the phase properties, instrumental geometry characteristics and sample condition. Though each of the parameters can be refined, some factors can be set to a constant such as the absorption factor. Others, such as Lorentz-polarization factor are dependent on the diffractometer and are not refined. Absorption factor (A) depends on the type of instrument geometry but it is usually taken to be a constant for most XRD experiments with a typical configuration of the sample lying flat while its surface is maintained normal to the diffraction vector. The wide array of parameters presented by the model allows the refinement of various characteristics such as atomic position, thermal displacement, site-occupancy, background, lattice parameters, instrumental geometrical-optical features, specimen aberrations, amorphous components, and sample reflection-profile-broadening agents such as crystallite size and microstrain [139]. The following sections will describe the different refinable parameters of the calculated intensity.

2.3.7.1.6. Background contribution

The measurement of an XRD displays the Braggs peak but also a diffuse scattering which is often referred as the background. In our case, the background is modeled with the polynomial function of the 6th order. Equation (33) is the general formulation for the polynomial function used to represent the background intensity.

$$y_{bi} = \sum_{m=0}^{5} a_m (2\theta_i)^m \quad (33)$$

Where, a_m is a refinable polynomial coefficient,

m is the order of polynomial,

and y_{bi} represents the background intensity function.

However, there are cases, especially when the peaks are very broad, when the background is very difficult to tell from the reflections and an automatic refinement is not successful. This can be rectified by carefully inspecting the XRD diagram and manually setting the background profile.

2.3.7.1.7. Peak profile function

To represent the effects of both the instrumental features and the specimen-caused broadening of the reflection profiles, the reflection profile function $\Phi(2\theta_i - 2\theta_K)P_K$ is employed. There are several profile shape functions which are mostly based on the Gaussian and Lorentzian functions. In this work we utilized the modified Thompson-Cox-Hastings pseudo-Voigt (TCHZ) function given in Equation (34) [139]. The linear combination function enhances the fitting of the XRD diagram and allows the refinement of peaks having non pure Gaussian or non-pure Lorentzian shapes.

$$TCHZ = \eta L - (1 - \eta)G \quad (34)$$

Where L is a Lorenztian function,

G is a Gaussian function,

η = *1.36603q- 0.47719q*^{2} *+0.1116q*^{2} ,

$q = \Gamma_L / \Gamma$,

$\Gamma = \left(\Gamma_G^5 + A\Gamma_G^4\Gamma_L + B\Gamma_G^3\Gamma_L^2 + C\Gamma_G^2\Gamma_L^3 + D\Gamma_G\,\Gamma_L^4 + \Gamma_L^5\right)^{0.2}$,

A, B, C and *D* are constants,

$\Gamma_G = (U\tan^2\theta + V\tan\theta + W + Z\cos^2\theta)^{1/2}$ where (U, V, W and Z are refineable parameters),

And $\Gamma_L = X\tan\theta + Y/\cos\theta$ where *X* and *Y* are refineable parameters.

2.3.7.1.8. The structure Factor

The structure factor represents and calculates the constructive interference created inside a crystal. This factor is sensitive to the type and position of each atom in the structure, with each of them producing scattering of X-rays under the beam. The structure factor given by Equation (35) also includes the thermal parameter. Though solids remain fairly stable, the atoms still experience thermal motion in the form of vibration and rotation.

$$F_K = \sum_j N_j f_j e^{[2\pi i(hx_j+ky_j+lz_j)]} e^{-8\pi^2 u^2 (\frac{sin^2\theta}{\lambda^2})} \quad (35)$$

Where, N_j is equal to the site occupancy multiplier for the j^{th} atom site,

f_j is the scattering factor of the j^{th} atom,

x_j, y_j and z_j, are the position parameters of the j^{th} atom in the unit cell,

And u^2 [137] is the root-mean-square thermal displacement of the j^{th} atom parallel to the diffraction vector.

2.3.7.1.9. Quality of the refinement

In Rietveld method, R-factors are used to analyze the calculated model and they are weighted pattern index (R_p), pattern index (R_{wp}), expected index (R_{exp}), and goodness of fit *(GofF)* which are based on the least-squared fit refinement (Equation (31)) and are given by Equations (36), (37), (38), and (39).

$$R_p = \frac{\sum_i |y_i - y_{ci}|}{\sum_i y_i} \quad (36)$$

Where y_i is observed intensity at the i^{th} step and

y_{ci} is the calculated intensity at the i^{th} step.

$$R_{wp} = \sqrt{\frac{\sum_{i=1}^{N} w_i (y_i - y_{ci})^2}{\sum_{i=1}^{N} w_i y_i^2}} \quad (37)$$

Where $w_i = 1/y_i$.

$$R_{exp} = \sqrt{\frac{(N-P)}{\sum_{i=1}^{N} w_i \, y_i^2}} \tag{38}$$

Where N is the number of points,

And P is the number of refined parameters.

$$GoF = \frac{R_{wp}}{R_{exp}} \tag{39}$$

Among these factors, R_{wp} is probably the most important in a mathematical point of view, since its value does not depend on the absolute value of the intensities but rather on the contribution from all the peaks of the diagram. A good indication that the fitting made is adequate is to look at the *GoF* or also known as the χ^2 factor. If its value is close to 1.0 then it is considered an adequate fit. However, when its value is higher than 1.5 then it is considered as an inadequate model or a false minimum. However, R_{wp} can be reduced significantly if there is a high background contribution fitted with a relatively crude background function. Thus, GoF factor should not be the only basis in determining the quality of the refinement but also qualitatively inspecting the fit and the acquired data.

2.3.8. Pair distribution function analysis by total X-ray scattering

Total scattering (TS) and pair distribution function (PDF) analysis were also performed to determine the medium-range and short-range order of the nanoparticle structure. Total scattering experiments are very similar to that of XRD experiments with the major difference is its ability to measure precisely both Bragg and diffuse scattering. For disordered structures, diffuse scattering contains valuable information regarding the short and medium range order which is needed when dealing with particles of nanometer size. Structures are generally described using three ranges of structural order which are the long-range order, the medium-range order and the short-range order. Ultrasmall particles lack long-range order but have medium- and short-range orders which makes the measurement of diffuse scattering particularly valuable.

For elastic scattering, the scattering vector Q is defined by the relationship between the initial (k_{init}) and final (k_{final}) wave vectors as shown in Figure 67 and Equation (40).

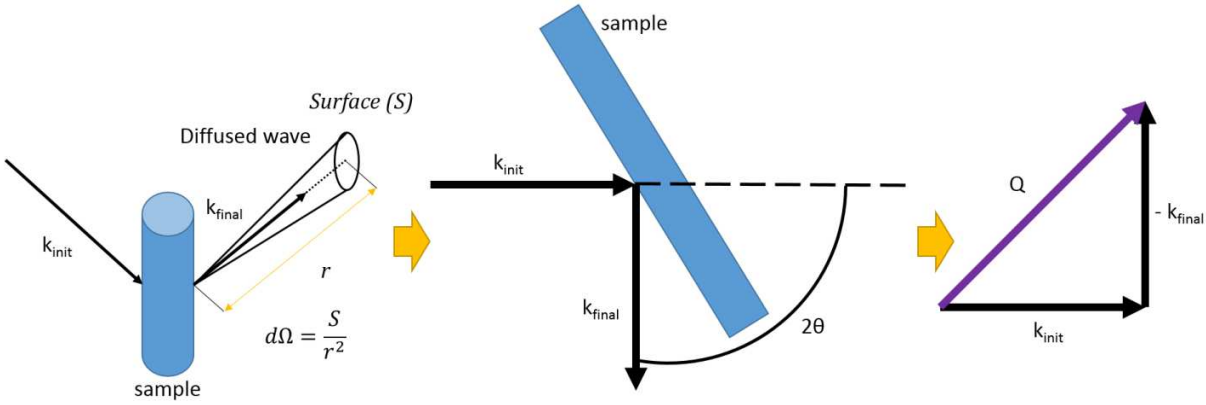

$$|Q| = \frac{4\pi sin\theta}{\lambda} \tag{40}$$

Where λ is the wavelength of the beam,

And 2θ is the angle between the incident and diffracted beams.

Figure 67: Geometry of interaction in the total scattering measurement as defined by the scattering vector

The measured scattered data is then corrected and normalized to get the structure function which is then Fourier transformed to obtain the atomic pair distribution function *G(r)* given by Equation (41). With this Fourier transformation, this technique allows us to work directly in real-space instead of the reciprocal-space [6].

$$G(r) = 4\pi[\rho(r) - \rho_o] = \frac{2}{\pi}\int_0^\infty Q[S(Q) - 1]\sin(Qr)dQ \tag{41}$$

Where $\rho(r)$ is the microscopic pair density,

$\rho 0$ is the average number density,

r is distance between two atoms,

And *S(Q)* is the structure function. (Note that *S(Q)* is not the same as the crystallographic $F_{hkl}(Q)$, which represents the amplitude scattered by crystalline unit cell)

The PDF *G(r)* represents the probability to find a pair of atoms separated by a distance *r* in the structure. It is a one dimensional function which presents peaks at the *r* values corresponding to interatomic distances. Figure 68 illustrates the construction of such a function.

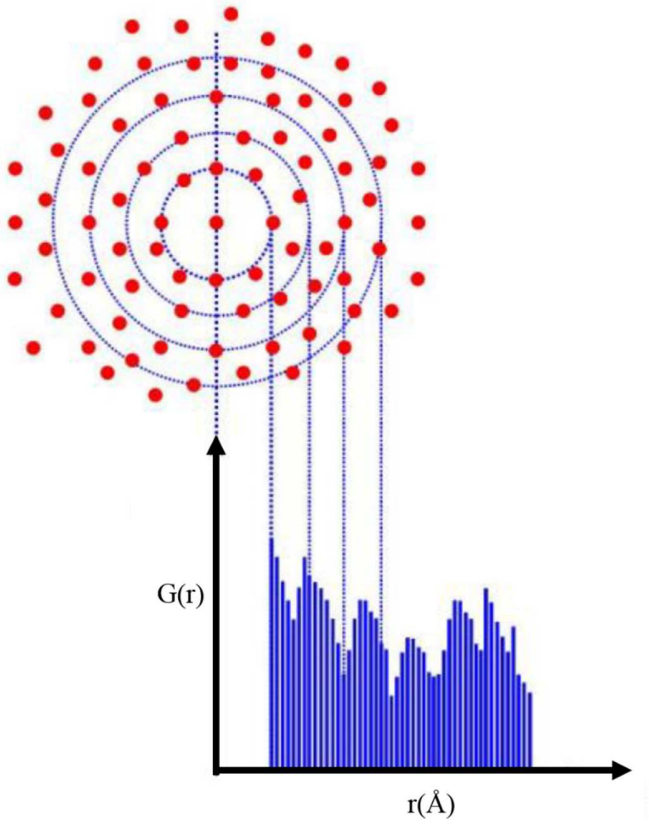

Figure 68: Scheme representing the pair distribution function G(r).

Note that when the distances are smaller than a minimum r-value, the function is equal to zero. This distance characterizes the shortest interatomic distance present in the structure. We can also point out that *G(r)* converges to 1 (oscillating around this value) for great *r* values. Thus each peak of the PDF is directly associated with pairs of atoms present in the material and the peak area is proportional to the probability of the presence of the pair. The PDF is very intuitive and permits a simple description of the short- and medium-range order in studied materials.

2.3.8.1. Experimental details

The diffractometer used in this work was developed in 2008 in SPCTS laboratory in collaboration with Pierre Lecante from CEMES in Toulouse. The setup use a molybdenum (Mo) source having a wavelength of about 0.709 Å, which gives a scattering vector length up to 17 $Å^{-1}$. It can be compared with the conventional X-ray source which is the copper K-alpha ($\lambda_{K\alpha 1} = 1.5406$ Å) which gives a much smaller scattering vector up to 8 $Å^{-1}$. This difference translates to the detail of information that can be obtained within the short range order. The details of the experimental apparatus are described elsewhere [45]. The zirconia powders were inserted into a 0.7 mm glass capillary and then carefully sealed by melting the top opening with a torch. The filled capillary was then placed on the goniometric head and adjusted in such a way that it will remain fixed in the center of the incident beam during its rotation. For this purpose we adjusted the angles and the translations of the goniometric head with the help of a microscope. The acquisitions of the diagrams were performed using the XTSScan software developed in the laboratory [140]. The scattered intensity of the sample was collected by a sodium iodide scintillator type detector mounted on the 2θ holder. The parameters of the experiment were set so that the magnitude of scattering vector (Q) range from 0 to 17 $Å^{-1}$ (2θ = 0 to 147.29°), the step was ΔQ = 0.02 $Å^{-1}$, and counting time was t = 240 s.

The fundamental parts of the diffractometer are shown in Figure 69. It consists of the following:

(1) a molybdenum sealed X-ray tube;
(2) a graphite monochromator cut along the planes (002) that allows the selection of the molybdenum doublet ($K_{\alpha 1}$, $K_{\alpha 2}$) wavelength ($\lambda_{K\alpha 1} = \lambda_{K\alpha 2}$= 0.7093 Å);
(3) a goniometric head, which supports the capillary containing the powder and which should be adjusted so that the axis of the capillary coincide with the rotational axis of the goniometer;
(4) a front collimator to define a quasi-parallel incident beam;
(5) a back collimator to define the direction of 2θ; And
(6) a scintillation detector to count the photons scattered by the sample.

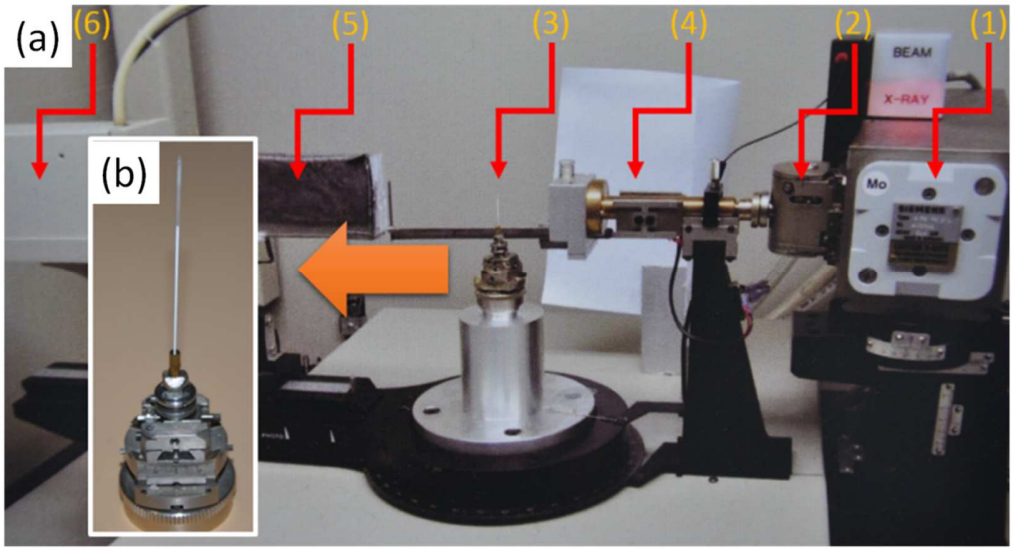

Figure 69: (a) Total scattering device used for characterization and (b) goniometric head with a mounted sample

The raw data obtained from the scattering experiment requires corrections in order to extract only the elastic scattering from the sample. Typical corrections include Compton scattering, empty capillary and air scattering, fluorescence and absorption. Corrections were performed using the software pyReduWaxs developed in the laboratory [141] and are described elsewhere [8]. In the following section, we describe the choice of the capillary diameter for minimizing absorption corrections.

The X-ray actually passes through different materials (ambient air and glass capillary) before hitting the sample. To estimate the absorption of the incident X-ray beam by the sample alone and to minimize the absorption corrections, it is necessary to determine the linear attenuation coefficients μ for each component in order to foresee an adequate capillary diameter. Therefore to this end, we calculate the mass attenuation coefficient μ/ρ for the sample following the Equation (42). X_i represents the mass fraction and $(\mu/\rho)_i$ the mass attenuation coefficient of each element i. The latter can be found in the international tables for crystallography. The density ρ is calculated considering that the compactness of the powder inside the capillary is about 40%.

$$\left(\frac{\mu}{\rho}\right)_{total} = \sum_i X_i \left(\frac{\mu}{\rho}\right)_i \quad (42)$$

Where μ is the linear attenuation,

ρ is the density of the sample,

$(\mu/\rho)_i$ is the mass attenuation coefficient for each element i,

and X_i is the mass fraction of the element.

Typically, the radius of the capillary r is set so that $\mu r \approx 1$. However, it is difficult to get a capillary of the exact obtained value, so we chose a greater diameter than calculated one in order to avoid practical difficulties when filling the capillary, which can lead to a decrease of the local compactness. In this work we used capillaries with a diameter of 0.7 mm for all the samples.

Chapter 3: Synthesis of Zirconia Samples

3 Synthesis of zirconia samples

3.1 Introduction

This chapter is devoted to the synthesis of zirconia nanocrystals following a non-aqueous procedure based on a solvent-controlled strategy. In the first part of the chapter, we will show how the type of zirconium (IV) precursors and the properties of the oxygen-donor solvent affect the nature of the final oxide material. We propose to study the oxidic conversion of two different zirconium precursors, namely the zirconium (IV) chloride and the zirconium (IV) isopropoxide-isopropanol adduct in the presence of various solvents: diisopropyl ether ($^{i}Pr_2O$) and benzyl alcohol (BnOH) for the former, then, BnOH or benzaldehyde with or without the presence of sodium hydroxide for the latter.

The effect of the alkali addition on the formation of the zirconia nanocrystals will be illustrated and discussed in terms of phase purity and particle size. The careful choice of the reagents and the operating conditions plays a valuable role in obtaining a pure and crystallized product; the study will emphasize the detrimental role of some specific side reactions.

Once the best effective synthesis conditions determined and adjusted, we will present three different strategies in order to promote a size-controlled effect on the particle size. These promising methodologies consist in balancing the thermal energy by an increase of the chemical reactivity of the initial mixture, limiting the chemical pathway of nanoparticle formation by varying the benzyl alcohol content and finally adding a second solvothermal process with some altered synthesis conditions.

Among the most promising results that we have obtained, only some selected samples are subjected to further analyses and various characterization techniques specifically to TEM, FTIR, TG, ICP and XPS. The selection process of these samples is simply based on purity, crystallinity and size; and those selected samples will be the object of the fine structural analysis developed in chapter 4.

3.2 From zirconium (IV) precursors to zirconia dioxide material

Largely inspired by the extended study of titanium dioxide TiO_2-based system [142] [55], we decided first to explore the potentiality for oxidic conversion of two families of zirconium source that are frequently used in the synthesis area of zirconium dioxide. The conversion process generally follows a chemical reaction that can be halide elimination and possibly ether elimination [143] [144] [60]. The zirconium sources used in this study are zirconium (IV) chloride and zirconium (IV) isopropoxide-isopropanol adduct.

3.2.1 Zirconium (IV) chloride

In the early 1950's the non-hydrolytic condensation involving an alkyl halide elimination from the reaction between metal alkoxides and metal halides was introduced in sol-gel chemistry by Gerrard *et al.* and reinvestigated by Corriu *et al.* in the 1990's [145] [146] [147]. Generally, the choice of a halide precursor coupled with a good oxygen-donor solvent allows a large conversion yield of the precursor into metal oxide at moderate temperatures from room temperature up to 150°C. Such a low processing temperatures permit to drastically limit the grain growth and offers a perspective of size control. In the work published by Arnal *et al.*, the effectiveness of halide precursor conversion in terms of yield is demonstrated in the synthesis of titanium oxide (TiO_2). The use of titanium chloride precursor and diisopropyl ether ($^{i}Pr_2O$) as a solvent produced TiO_2 nanocrystals at a moderate temperatures with an excellent 95% yield [142]. Also, when titanium chloride reacted with another class of oxygen-donor solvents like benzyl alcohol, the sizes obtained ranged from 4 to 8 nm. The nanoparticles' size appeared to be strongly influenced by the operating temperatures as shown by Niederberger *et al.* [148]. Indeed, the $TiCl_4$-to-solvent ratio and the reaction temperature influenced the crystallite size and the adjustment of these parameters allowed the tailoring of the size of the nanocrystals in small increment. From the experimental works using a halide source such as chloride, the reaction at the origin of the metal oxide bridge in a non-hydrolytic pathway is given by Equation (43).

$$\text{M-Cl} + \text{M-OR} \rightleftarrows \text{M-O-M} + \text{R-Cl} \qquad \text{Alkyl halide elimination} \qquad (43)$$

The alkoxide groups needed for the condensation to occur can be obtained by the direct reaction of a metallic halide with an ether or an alcohol accompanied by the release of an alkyl halide or

hydrochloric acid, respectively (see Equations (44) and (45)). Vioux *et al.* underlined the catalytic effect promoted by the presence of hydrochloric acid in condensation and many side-reactions [149].

$$M\text{-}Cl + ROR \rightleftarrows M\text{-}OR + R\text{-}Cl \qquad \text{Etherolysis} \qquad (44)$$

$$M\text{-}Cl + ROH \rightleftarrows M\text{-}OR + H\text{-}Cl \qquad \text{Alcoholysis} \qquad (45)$$

Zirconium chloride is a white inorganic, corrosive and high-melting point compound which hydrolyzes rapidly with moisture. The compound adopts a polymeric structure which degrades easily under the effect of a Lewis base. Theoretically, the reaction between zirconium chloride and diisopropyl ether or benzyl alcohol would proceed in a similar manner that for titanium chloride and result in a ligand exchange equilibrium as shown in Equations (46) and (47), respectively.

$$Zr\text{-}Cl + {}^{i}Pr_2O \rightleftarrows Zr\text{-}O{}^{i}Pr + {}^{i}Pr\text{-}Cl \qquad \text{Etherolysis} \qquad (46)$$

$$Zr\text{-}Cl + BnOH \rightleftarrows Zr\text{-}OBn + H\text{-}Cl \qquad \text{Alcoholysis} \qquad (47)$$

After the formation of the zirconium chloro-alkoxide, the reaction can then proceed towards the formation of zirconium oxide bridges as shown in Equation (48).

$$Zr\text{-}Cl + Zr\text{-}OX \rightleftarrows Zr\text{-}O\text{-}Zr + X\text{-}Cl \qquad \text{Alkyl halide elimination} \qquad (48)$$

where X is either an isopropyl or a benzyl group

3.2.2 Zirconium (IV) isopropoxide-isopropanol adduct

The reaction of metal halides with an oxygen-donor solvent almost always results in the formation of metal oxide nanoparticles with halide impurities. To avoid this contamination, some researchers have investigated the use of metalorganic precursors as metal acetates, metal acetylacetonates or metal alkoxides [150] [60]. The other type of zirconium precursor used in the study was the zirconium isopropoxide-isopropanol adduct $[Zr(O{}^{i}Pr)_4 \cdot (HO{}^{i}Pr)]_2$. This compound possesses an oligomeric structure that partially stabilizes the metallic center in an octahedral coordination but this structure is rarely maintained in the solvent upon dissolution.

The absence of a halide consequently alters the non-aqueous pathway. This was observed in the work done by Garnweitner *et al.* and Keukeleere *et al.* where the authors proposed that the formation of the zirconium oxide bridges was initiated by the partial ligand exchange of the isopropoxide groups with the benzoxide ones, accompanied by an alcohol elimination as shown in

Equation (49). The benzoxide-modified zirconium precursor could then proceed with the condensation reaction forming the zirconium oxide bridge accompanied by the release of various ethers (diisopropylether, dibenzyl ether or mixed ether) as shown in Equation (50) [55] [150] [60].

$Zr\text{-}(O^{i}Pr) + BnOH \rightleftarrows Zr\text{-}OBn + HO^{i}Pr$ Ligand exchange (49)

$Zr\text{-}OR + R'O\text{-}Zr \rightleftarrows Zr\text{-}O\text{-}Zr + R\text{-}O\text{-}R'$ Ether elimination (50)

where R and R' represent isopropyl or benzyl group

3.2.3 Choice of solvents

In solvent-controlled synthesis the type of solvent plays a fundamental role in determining the properties of the metal oxide such as phase purity and size distribution of the nanocrystals. It has been observed how the solvent affects the route towards the formation of the metal oxide bridge when the solvent is also used as the source of oxygen needed during the condensation reaction [149].

In this section, the choice of solvents were set in order to follow a non-hydrolytic route and to avoid problems that are brought about by aqueous-based or common hydrolytic routes. The solvents studied here are diisopropyl ether, benzyl alcohol and benzaldehyde:

- The justification for the use of diisopropyl ether and benzyl alcohol with zirconium chloride or zirconium isopropoxide-isopropanol adduct is presented in the earlier paragraphs.
- The use of benzaldehyde is expected to offer an alternative reaction pathway for the formation of zirconium oxide bridges. In the case of titania, for a synthesis performed at room temperature, well-defined titanium oxo-clusters were obtained, whereas the solvothermal treatment of $Ti(O^{i}Pr)_4$ in ketones and aldehydes extended the size of the products beyond clusters and led to the formation of nanocrystalline anatase in the size range of 7 to 20 nm, depending on the solvent. The mechanism would be initiated by a Meerwein-Ponndorf-Verley-like (MPV) reaction as it was determined and proposed by Garnweitner *et al.* for TiO_2 nanocrystals synthesis [55]. The MPV-like reaction of the titanium isopropoxide and benzaldehyde led to the formation of benzyl alcohol and acetone. This reaction was then followed by two possible reaction pathways. First, the benzyl alcohol could react with the isopropoxide ligand via the C-C coupling reaction. And second,

the aldol-addition of the acetone to the aldehyde occurred. Both reactions would then lead towards the formation of the titanium oxide bridges but the potential stabilization of an intermediate carbocation due to the mesomeric effect of the phenyl ring mainly favored the C-C coupling [55].

Finally, although that many research groups investigate the catalytic effect of acidic medium onto the formation mechanism of nanoparticles, we decided to investigate the effect of an alkaline catalyst, namely sodium hydroxide (NaOH), in order to pursue the investigation based on the use of sodium benzoxide studied by Portal *et al.* during her PhD study [8].

Evidently, the alkaline conditions will alter the benzaldehyde-based synthesis since the Cannizzaro reaction, *i.e.* a disproportionation reaction of benzaldehyde lacking a hydrogen atom in the alpha position, will modify drastically the reaction mixture (see Figure 70). The products of the disproportionation are benzyl alcohol and benzoate base which are known to be a strong capping ligand especially since it was reported for a few reaction systems as Y_2O_3, Gd_2O_3, Sm_2O_3 or $W_{18}O_{49}$ [151]. The benzoate species in our case are expected to bind strongly to the growing inorganic zirconia fulfilling several potential functions: selective capping of specific crystal faces leading to anisotropic shape, stabilizers avoiding agglomeration limiting the final size of the particles and possibly, assemble the nanocrystals into larger superstructures forming a stable hybrid material.

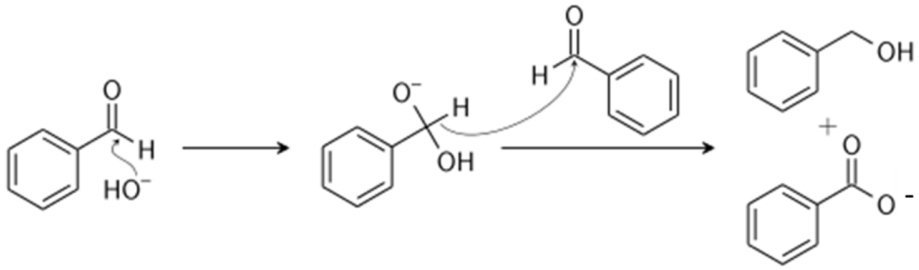

Figure 70: Chemical equation for the disproportionation of benzaldehyde in alkaline medium namely Cannizzaro reaction.

3.2.4 Synthesis details

The synthesis procedure is described in Chapter 2 while the details for concentrations and parameters used in this work are given in Table 1. The manipulation of chemicals is carried out in a dry-air glovebox to rule out the possibility of moisture influence. In the first step, a volume of solvents were measured and solid precursors were weighed. They were then transferred into an autoclave which was sealed and heated at the operating temperature for at least 3 days. Note that

some of the experiments were performed below the boiling point of the solvent and the reaction actually took place under sub-solvothermal conditions. Therefore, if the reaction was performed in a non-pressurized vessel but in an open reaction flask at the same temperature under ambient pressure, only a white precipitate mainly amorphous in nature would be obtained instead of the expected crystalline metal oxide [55].

Table 6: Synthesis details for the chemical content and solvothermal treatment

Zirconium chloride			
concentration	**solvent (100% volume)**	**Temp (ºC)**	**Time (days)**
0.25 mol.L^{-1}	benzyl alcohol	150	3.0
0.25 mol.L^{-1}	diisopropyl ether	150	3.0
Zirconium isopropoxide - isopropanol adduct			
concentration	**solvent (100% volume)**	**Temp (ºC)**	**Time (days)**
0.3 mol.L^{-1}	benzyl alcohol without NaOH	210	3.0
0.3 mol.L^{-1}	benzyl alcohol with 0.2 mol.L^{-1} NaOH	210	3.0
0.3 mol.L^{-1}	benzaldehyde with 0.2 mol.L^{-1} NaOH	210	3.0

The samples prepared using zirconium chloride were analyzed by XRD and exhibit significant differences from one another despite that both solvents act as oxygen donors as shown in the powder diffractograms in Figure 71 (a).

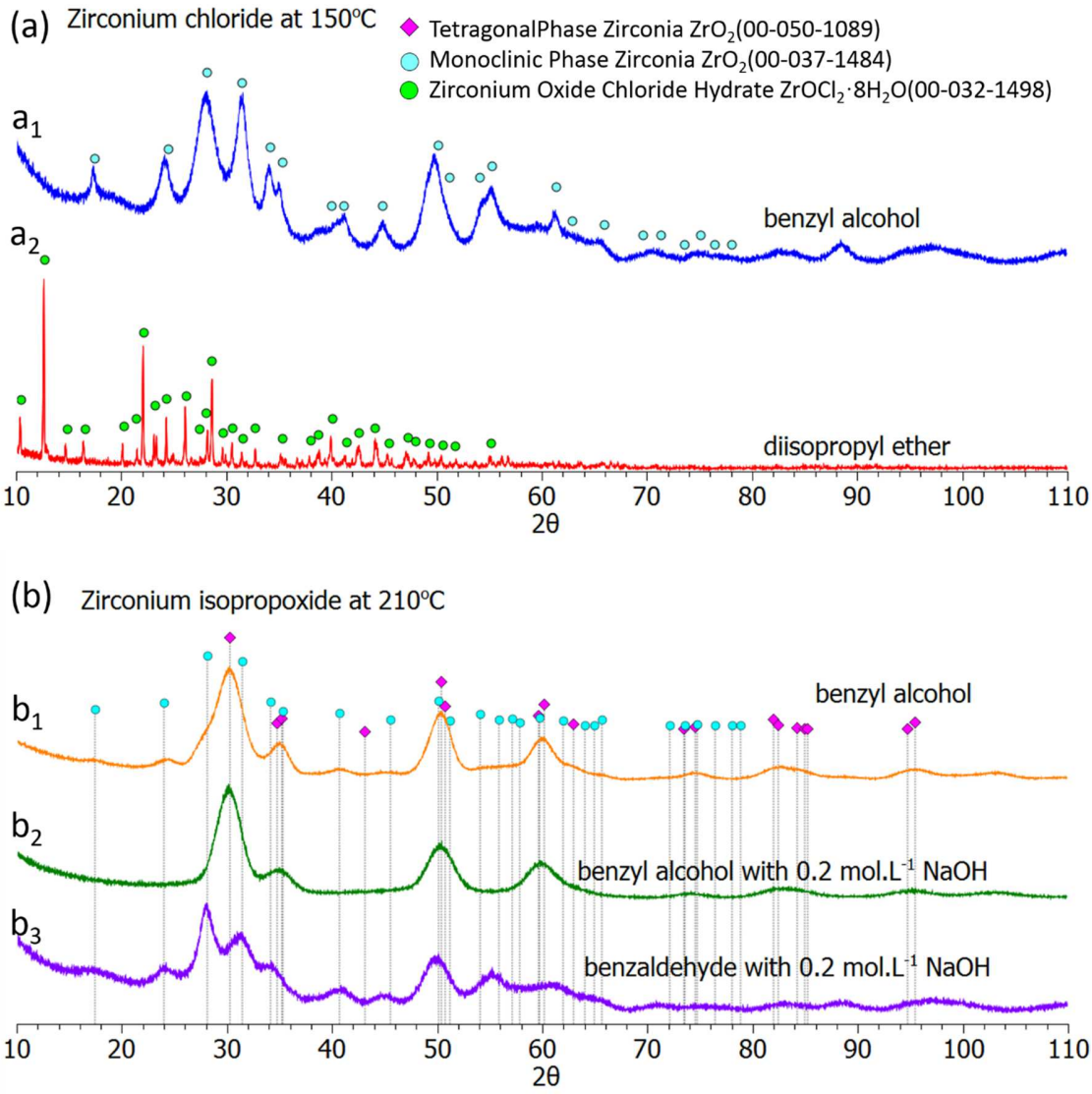

Figure 71: XRD patterns of samples obtained using $ZrCl_4$ precursor (a) and $[Zr(O^iPr)_4 \cdot HO^iPr]_2$ (b) under varied solvents coupled or not with the presence of sodium hydroxide and solvothermal technique for 3 days at 150°C (a) or 210°C (b).

In the case of the precipitate prepared by reaction of $ZrCl_4$ with benzyl alcohol (BnOH), the reaction led to the formation of a single crystalline phase which coincides to monoclinic zirconia m-ZrO_2 (Figure 71 (a_1)). Monoclinic phase is one of the known polymorphs of zirconia that has a fluorite-derived structure. Size calculation of the crystallite size reveals that the average apparent size is about 3.6 nm and measurements suggest that the particles have anisotropy. This can be seen if we consider the first two most intense peaks at approximately $2\theta = 27.9^o$ and 31.5^o which corresponds to the (-111) and (111) planes, respectively. Indeed, these peaks have a different broadening. This anisotropic characteristic could be due to the growth mechanism of the crystals which favors one

crystallographic direction over the others in several cases, *i.e.* intrinsic anisotropy of the unit cell, oriented attachment of the crystals, Ostwald ripening, or preferential binding of organic molecules on specific crystallographic faces.

An interesting fact emphasized by this sample is that the zirconia crystal structure is not following the grain size effect prediction of Garvie. Indeed, below the critical size value of 10 nm, the metastable tetragonal phase is normally thermodynamically favored over the monoclinic one due to some surface energy considerations. Nevertheless as a matter of fact, we observe in our case that the precipitate adopts preferentially the monoclinic rather than the metastable tetragonal phase despite an apparent grain size of 3.6 nm. Two interpretations could be given to explain this atypical result; *(i) either the reaction pathway mediates the direct growth of monoclinic zirconia nanocrystals from nuclei presenting the crystallographic feature of the monoclinic phase or (ii) the room-temperature metastable tetragonal nanocrystals foreseen by Garvie undergo a phase transformation during the ageing period of the solvothermal processing.*

This second option is mainly supported in the literature by many authors but interpreted differently:

- *Murase et al.* [116] *evidenced the transformation of metastable tetragonal zirconia into monoclinic one upon thermal treatment or contact with water vapor.*
- *Such effect has also been evidenced by Li et al.* [152] *upon methanothermal treatment of zirconyl nitrate dihydrate where crystal water from the precursor was suspected to be responsible for the appearance of a small amount of monoclinic crystals. Li et al. showed that with the increasing addition of urea, the crystal water was consumed in the hydrolysis of urea shown in Equation* (51) *and consequently only the metastable tetragonal phase was formed.*

$$(NH_2)_2CO + H_2O \rightarrow 2\ NH_3 + CO_2 \qquad \text{Hydrolysis of urea} \qquad (51)$$

- *The formation of monoclinic phase zirconia is often related to the possible formation of in-situ HCl. In the works conducted by Li et al., the effect of HCl induced the etherification of the alcohols which produced an ether and in-situ water (Equation (*52*))* [153]. *The water was thought to promote the formation of monoclinic phase type zirconia via hydrolysis and condensation as shown in Equations (*53*) and (*54*), respectively* [154] [152]. *Indeed, the solubility of the formed zirconia precipitate increased in presence of water which allowed the dissolution and precipitation process leading to the thermodynamically stable type of*

zirconia which is the monoclinic phase [152] [155] [156]. *The monoclinic sizes observed by Li, et al. was 9.1 nm and 12.0 nm for Taguchi, et al. We could argue that since these values are close to the critical size defined by Garvie, et al. they were most likely driven by critical size effect.*

Bn-OH + BnO-H ⇄ Bn_2O + H_2O	Etherification of alcohol	(52)
Zr-Cl + H_2O ⇄ Zr-(OH) + HCl	Hydrolysis reaction	(53)
Zr-Cl + Zr-OH ⇄ Zr-O-Zr + HCl	Condensation reaction	(54)

- *Another explanation on the formation of monoclinic phase zirconia was presented by Keukeleere et al.* [60] *where in-situ water was effectively detected after the microwave treatment of the chloride precursor but not directly accused to be responsible for the formation of monoclinic zirconia. According to their XRD and GC-MS analyses, the intentional addition of water did not led to the formation of monoclinic phase zirconia and there was no evidence of hydrolysis of their zirconium alkoxide whereas the addition of trifluoroacetic acid, a strong acid like HCl, led to the production of monoclinic zirconia. Keukeleere et al. asserted that the release of a strong acid, such as HCl, from the reaction of the chloride precursor, mediated the mechanism behind the control over crystal phase formation.*

In most of the syntheses, scientists from different groups have found at the same time the presence of an aqueous phase and m-ZrO_2. No consensus is clearly accepted and the experimental arguments are not relevant enough since the modification of one synthetic parameter, *i.e.* the addition of an *ex-situ* organic strong acid or the change in metallic precursors, has several levels of impacts in terms of chemical pathway, side-reaction, etc. The question of the presence of m-ZrO_2 whether due to a phase conversion under the effect of water or directly produced as a result of the choice of the reagents and possible intermediate products is addressed in the Chapter 5 of this dissertation.

Anyway, in order to avoid any *in-situ* water production, a true non-hydrolytic strategy was proposed in the literature by Mutin *et al.* in the form of reacting $ZrCl_4$ with diisopropyl ether ($(^iPr)_2O$), a polar aprotic solvent. In our case, the reaction appears to lead exclusively to the formation of crystalline zirconium oxide chloride hydrate (Figure 71 (a_2)). The narrower peaks indicate that the size of these particles are quite large. The chemical conversion yield of the initial

precursor could then be evaluated to a 50%-ratio since just the zirconyl form is observed. Further analysis of the sample was not pursued since this type of complex compound is not covered in this work.

Changing the zirconium source from zirconium chloride to zirconium isopropoxide-isopropanol adduct requires an increase of the synthesis temperature up to 210°C to guaranty the production of a crystalline compound with a good conversion yield whatever the type of selected solvent, namely benzyl alcohol, NaOH-benzyl alcohol mixture or NaOH-benzaldehyde.

According to the XRD patterns presented in the Figure 71(b), the three reactional mixtures led to the formation of zirconia. The diffraction peaks are rather broad in comparison with the case of the more reactive chloride precursor. The peaks are perfectly identified to different polymorphs of zirconia: a mixture of polymorphs, t-ZrO_2 and m-ZrO_2, is detected in the case of pure benzyl alcohol (Figure 71 (b_1)) whereas pure t-ZrO_2 is observed in the presence of sodium hydroxide and benzyl alcohol (Figure 71 (b_2)) and pure m-ZrO_2 is detected in the presence of sodium hydroxide and benzaldehyde (Figure 71 (b_3)). The particle size was calculated from the XRD patterns using a Rietveld refinement methodology and summarized in the Figure 72. The refinement confirms the limited apparent size of the nanoparticles which is below 4 nm for all the cases and largely below the critical size estimated by Garvie [157] [103] [158].

Firstly, the alkoxide route seems to be more effective than the chloride one in offering a crystalline oxide compound with limited size and simultaneously exhibiting a strong dependence on the synthesis parameters, *i.e.* solvent type and mixture alkalinity. Secondly, two main effects can be extracted from these initial experiments: the alkalinity of the alcoholic medium favors the metastable t-ZrO_2 and permits the inhibition of the monoclinic presence that is detected in the experiment (Figure 71 (b_1)) whereas the alkalinity coupled with the use of benzaldehyde favors the monoclinic polymorph over the metastable one below the critical size. These promising results need to be investigated in detail in order to understand the reasons leading to such prominent differences. In particular, we want to examine the fine structural properties of the samples and determine the relation between the synthesis background and the intimate structure of the particles.

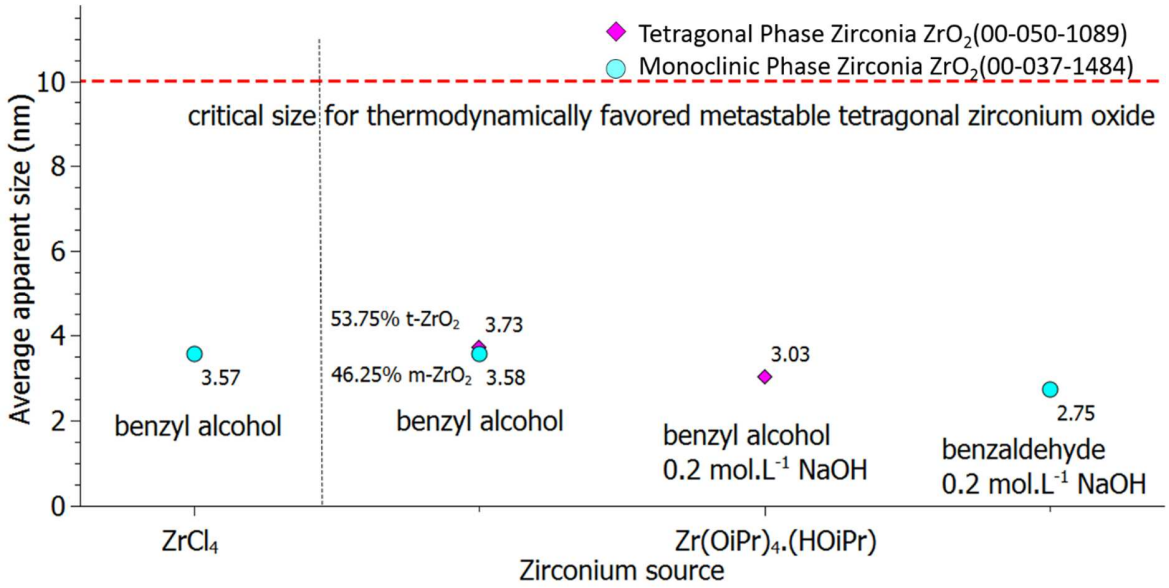

Figure 72: Average apparent size of the zirconia particles obtained using zirconium chloride ($ZrCl_4$) precursor and zirconium isopropoxide-isopropanol adduct $[Zr(O^iPr)_4 \cdot HO^iPr]_2$ with or without the presence of sodium hydroxide under varied solvents prepared using solvothermal technique at 150°C and 210°C for 3 days.

According to the ^{1}H-NMR analyses of the three different supernatant, water was detected together with organics in the case of Figure 71 (b_1) and Figure 71 (b_3). No water was detected in the case of the metastable t-ZrO_2 sample (Figure 71 (b_2)) prepared in 0.2 mol.L^{-1} NaOH benzyl alcohol medium.

Water was already detected in syntheses by Portal *et al.* in cases similar to Figure 71 (b_1) and attributed to a dehydration of isopropanol occurring onto the catalytic amphoteric surface of the zirconia nanoparticles. The result is more surprising in the third case (Figure 71 (b_3)) due to the alkaline condition and must be interpreted carefully. In the case of aldehydes or ketones, the release of oxygen generally involves an aldol condensation reaction under elimination of water and formation of α,β-unsaturated carbonyl compounds. Such aldol elimination processes are known to be catalyzed by the metal oxide precursors. The eliminated water is then normally consumed for the formation of the oxide, thus driving the equilibrium to the side of the condensation products. We know now that a second source of *in-situ* water production is possible and the Cannizzaro disproportionation will disturb the reaction mixture by converting progressively benzaldehyde into benzyl alcohol and benzoate species. The formation and stabilization of monoclinic ZrO_2 nanoparticles in such case is probably due to several conjugated effects like (i) isopropanol dehydration and aldol-condensation producing water, (ii) water conversion of t-ZrO_2 into m-ZrO_2,

(iii) capping of the particles surface by benzoate enhancing the steric hindrance and then a limiting growth of the particles, and (iv) possibly parallel to the point (i) to (iii), a large decrease of the surface energy of the monoclinic polymorph compared to the metastable one due to the strong capping of benzoate species allowing the nucleation and growth of the unusual polymorph of zirconia, *i.e.* m-ZrO_2 at the nanoscale largely below the critical size of 10 nm.

From the point of view of the oxidic conversion of the metallic precursor, the use of a metallic alkoxide seems to be more beneficial in the case of the zirconium system than the use of a halide one since the former permits to form zirconia under the action of a large panel of solvents and conditions. In addition, the use of halide source also increases the risk of halide impurities into the final sample. The rest of the study will focus on the use of the zirconium isopropoxide-isopropanol adduct and will investigate the causes for the phase selection revealed by the use of an alkaline alcohol medium.

3.3 Study of the phase selection

The method developed by Garnweitner *et al.* which is based on the use of zirconium isopropoxide-isopropanol adduct and benzyl alcohol as the solvent was expected to produce metastable “cubic” zirconia. In our case with only minor modification in terms of concentration and heating mode as it was already shown by Portal *et al.*, the presence of the monoclinic phase zirconia made the sample problematic for fine structural characterization due to phase impurity. However the problem was addressed by adding an alkali source such as sodium hydroxide to control the phase of the zirconia. In this chapter we present the results obtained by varying the concentration of the alkali source. The synthesis details for the chemical syntheses are listed in Table 7.

Table 7: Synthesis details for the chemical content and solvothermal treatment "study of the effect of the NaOH concentration"

NaOH content ($mol.L^{-1}$)	**Zirconium concentration ($mol.L^{-1}$)**	**Solvent Benzyl alcohol (% volume)**	**Solvothermal treatment (T°C/days)**
0.0	0.3	100%	210°C/3.0
0.05	0.3	100%	210°C/3.0
0.1	0.3	100%	210°C/3.0
0.2	0.3	100%	210°C/3.0
0.5	0.3	100%	210°C/3.0
1.0	0.3	100%	210°C/3.0
2.0	0.3	100%	210°C/3.0

According to Figure 73, the addition of sodium hydroxide (NaOH) led to various effects on the phase purity of the sample depending on the introduced amount. Minimal content of sodium hydroxide (below 0.1 $mol.L^{-1}$) does not seem to influence the phase purity of the sample which retains its dual phases feature. However, increasing the amount of sodium hydroxide beyond 1.0 $mol.L^{-1}$ led to the formation of sodium carbonate and finally extra unidentified organic compounds. The formation of sodium carbonate can be explained by the reaction of residual sodium hydroxide and carbon dioxide during the drying process and the storing of the powder in ambient atmospheric condition (see Equation (55)).

$$2NaOH + CO_2 \rightleftarrows Na_2CO_3 + H_2O \qquad \text{carbonation} \qquad (55)$$

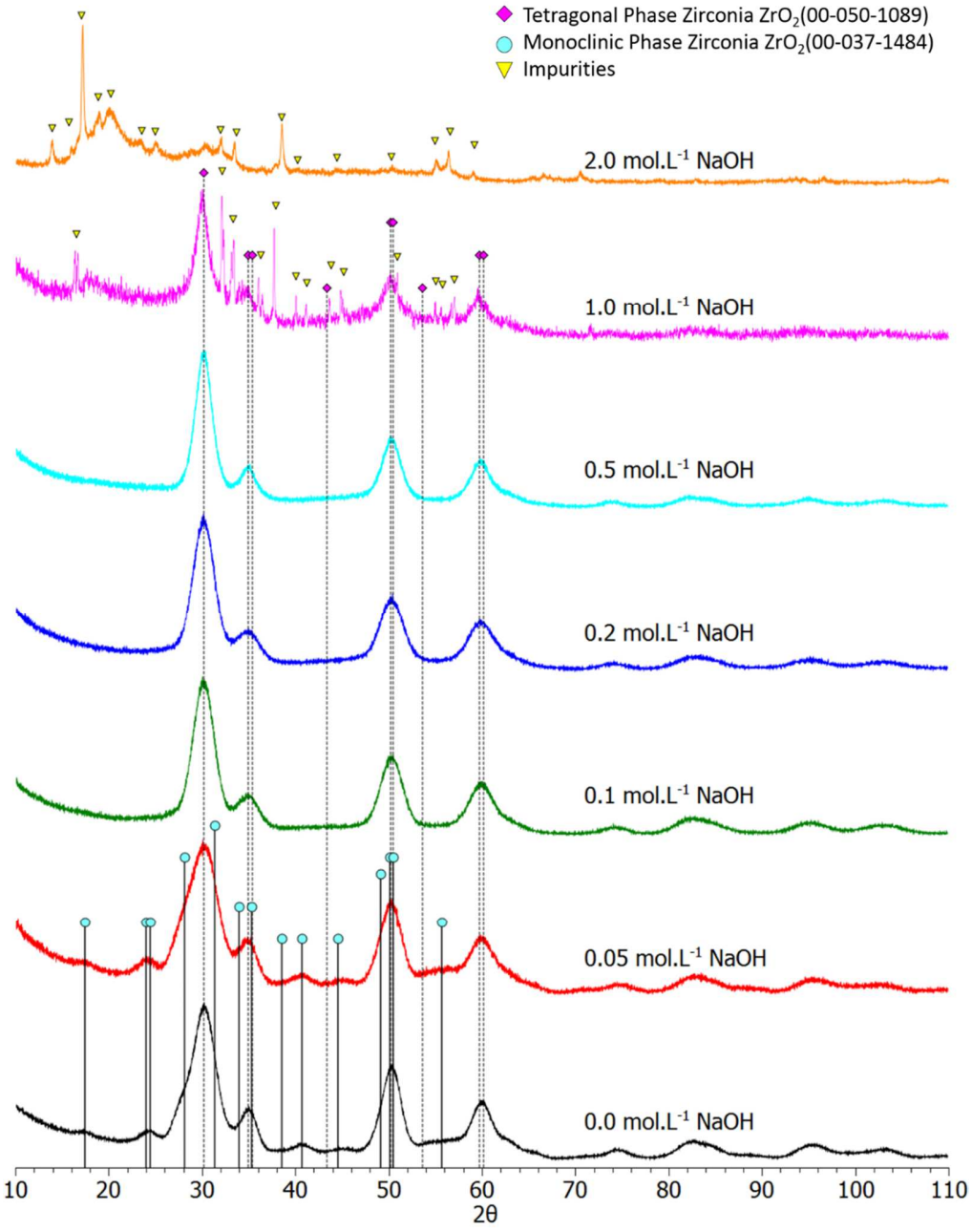

Figure 73: XRD patterns of samples obtained via a solvothermal technique at 210°C for 3 days using $[Zr(O^iPr)_4 \cdot HO^iPr]_2$ in benzyl alcohol with different amounts of NaOH.

Finally when we added sodium hydroxide from 0.1 up to 0.5 mol.L^{-1} the reaction mixture led to the formation of a single phased tetragonal zirconia t-ZrO_2. These results show that there is a specific narrow window in which the formation of single phase t-ZrO_2 is possible. Moreover, the addition of any amount of NaOH influenced the average apparent size of both the monoclinic phase and tetragonal phase zirconia as shown in Figure 74. For the single phased samples, the data clearly

indicate an increase of the apparent size of 2.8 nm, 3.0 nm to 3.5 nm for NaOH amount of respectively 0.1 mol.L^{-1}, 0.2 mol.L^{-1} and 0.5 mol.L^{-1}. Comparing the three t-ZrO_2 in terms of phase purity and moderate grain growth, the sample prepared with 0.2 mol.L^{-1} of NaOH appears to be the best compromise to insure the inhibition of the monoclinic impurity while keeping its apparent size lower than 4 nm.

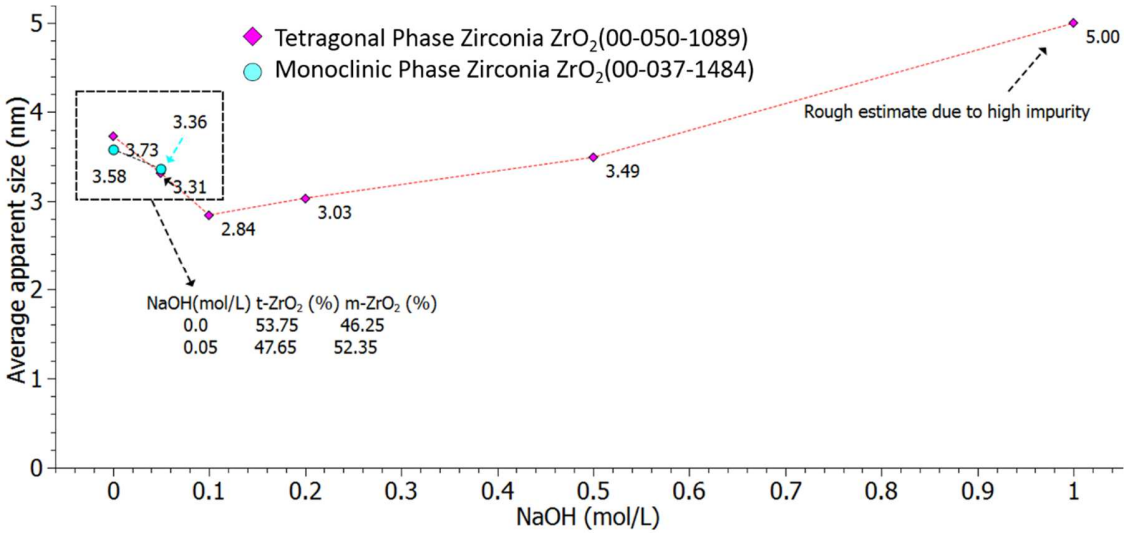

Figure 74: Average apparent size of the samples obtained via a solvothermal technique at 210°C for 3 days using $[Zr(O^iPr)_4 \cdot HO^iPr]_2$ in benzyl alcohol with different amounts of NaOH.

In her PhD work, Portal *et al.* defended the idea that the presence of m-ZrO_2 in the sample prepared using a protocol close to Garnweitner's one was due to a phase conversion process activated by the detrimental presence of *in-situ* water [8]. The water phase detected in the supernatant was attributed to the isopropanol dehydration mediated by the catalytic properties of the growing surface of the nanocrystals of zirconia. The appearance of an aqueous phase is not surprising in non-aqueous sol-gel route when the solvent used for the reaction to occur is a protic alcohol and such an aqueous phase was detected at the end of the synthesis of different transition-metal niobate nanocrystals [159] [160]. Only the reactions dealing with the use of a metal halide and organic ether or organic anhydride are classified by Mutin *et al.* as exclusively and strictly non-hydrolytic sol-gel routes.

In the works done by Aramendia, et al. [82] *and Kostestkyy, et al.* [83], *they reinvestigated the acid-base amphoteric nature of zirconia for dehydration-dehydrogenation of several alcohols like propan-1-ol (HO^nPr) and propan-2-ol (HO^iPr). The reaction mechanism for the conversion of isopropanol has been reviewed by Aramendia, et al. and some of the proposed mechanisms account for both the dehydrogenation and dehydration processes:*

- *The E_1 mechanism is a two-step process in which the rate-determining step is ionization of the substrate to a carbenium ion (by release of a leaving group such as HO^-) that rapidly loses a β-proton. This mechanism normally operates without a base.*
- *In the E_2 mechanism, both the leaving group and the proton depart simultaneously, the proton being pulled off by a base. The mechanism thus takes place in a single step.*
- *In the third possibility, the proton leaves firs and then followed by the leaving group. This is a two-step process called the E_{1cB} mechanism. The intermediate is a negatively charged species (the conjugate base of the substrate). Mechanisms E_1 and E_{1cB} take place over an acid-base couple.*

The three mentioned mechanisms show more similarities than differences. In each case there is a leaving group that departs with its electron pair and another (usually hydrogen) that comes off without it. The only difference is the order in which they leave. It is now generally accepted that there is a spectrum of mechanisms ranging from one extreme, in which the leaving group departs well before the proton (pure E_1), to the other extreme, in which the proton comes off first and then, after some time, the leaving group follows (pure E_{1cB}). The pure E_2 mechanisms would be somewhere in between, with both groups leaving simultaneously. However, most E_2 reactions do not lie exactly in the middle of the two extremes. Propene could be formed from any of the three mechanisms, but acetone (product of dehydrogenation) only with the E_{1cB}.

In summary, catalysts with a large number of acid sites lead predominantly to dehydration (which takes place via an E_1 mechanism). However, dehydrogenation takes place to a limited extent only via an E_{1cB} mechanism. In solids with a large number of basic sites, both dehydrogenation and dehydration take place via an E_{1cB} mechanism, with the former predominating over the latter. Over solids of acid-base character like zirconia, the dehydration may take place via a concerted E_2 mechanism. The simultaneous interaction of an acid-base couple with the –OH group and the proton of the carbon in propan-2-ol would cause both groups to be released and propene to be produced. (However, dehydrogenation takes place via an E_{1cB} mechanism. The interaction between a basic site and an alcohol molecule causes a proton to be abstracted from the alcoholic group, thus producing an adsorbed alkoxide species. The release, in a subsequent step, of a hydride from the alkoxide carbon atom leads to the formation of acetone).

More recently [83], *the Lewis-acid catalyzed dehydration of simple alcohols on various simple metal oxide like TiO_2, ZrO_2, and γ-Al_2O_3 has been investigated by combining ab-initio calculations with temperature programmed desorption (TPD) experiments. Both theoretical and experimental results demonstrate that the dehydration reaction occurs through an E_2-elimination mechanism involving surface oxide groups of the catalyst as we can see in the scheme of the* Figure 75.

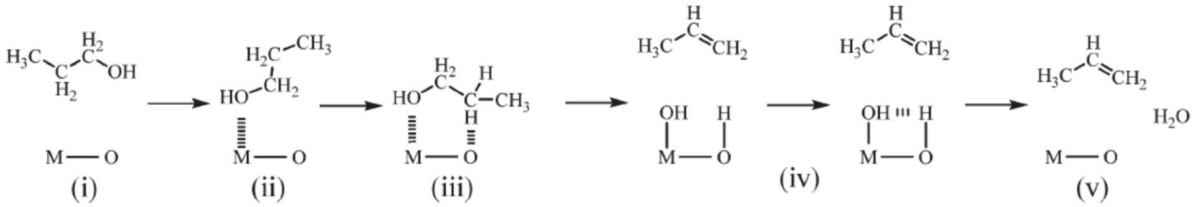

Figure 75: Schematic representation of the concerted E_2 elimination dehydration reaction involving surface oxygen (a) of the oxides. The steps are: alcohol adsorption on the Lewis acid site M ((i) → (ii)), β-hydrogen transfer to a surface O (a (iii)), alkene formation and desorption (iv), water formation, desorption and catalyst regeneration (iv) → (v).

One remedy proposed by Portal, *et al.* to eliminate any presence of water was to use sodium metal in addition to the other reactants in order to dehydrate the medium and to avoid the formation of *in-situ* water. The sodium benzoxide produced by the redox dissolution of sodium metal in benzyl alcohol was thought to react at high temperature:

- (i) with isopropanol to produce 4-phenyl-2-butanol and sodium hydroxide likely to initiate a non-hydrolytic hydroxylation and the condensation of the alkoxide,
- (ii) with zirconium isopropoxide-isopropanol adduct to produce 4-phenyl-2-butanol and zirconium hydroxide groups to initiate alcoxolation and/or oxolation,
- (iii) finally a third possible acid-base reaction occurs in the case of appearance of water:

$$BnONa + H_2O \rightleftarrows BnOH + NaOH$$

Among the three levels of interaction of benzoxide species, the reaction (i) consumes isopropanol and reaction (iii) uses the formed water; both limit the risk to form an aqueous phase. Whereas the reaction (ii) activates the condensation and crystallization. The faceted nanoparticles obtained in the alkaline conditions were pure and monodisperse t-ZrO_2 illustrating the strong entanglement between inorganic and organic products appearing during synthesis.

In this work, we have shown that it is possible to obtain similar results in terms of phase purity and apparent particle size without the use of sodium benzoxide but with the use of sodium hydroxide.

These experimental data complement the work of Portal while highlighting new perspectives: the disappearance of the aqueous phase would not be due to the consumption of isopropanol, as we get the same effect without metallic sodium and no opportunity to consider the Guerbet reaction. Surely, the sodium hydroxide that we introduce in our synthesis plays an important role in the initiation and the propagation of the sol-gel process. However, we have to consider a new perspective regarding the absence of water production.

An alternative explanation appeared on reading carefully the work from Kozlowski *et al.* [161]concerning the study of condensation mechanisms of short chain alcohols catalyzed by heterogeneous amphoteric oxides such as micrometric ZrO_2 or basic ones such as MgO. In particular, the influences of adding sodium to zirconia on the acid-base properties of the surface and on the catalytic conversion of ethanol and acetone were investigated. They found that the addition of 1.0 wt.% Na to ZrO_2 (by a wet impregnation process) decreased the rate of ethanol dehydration by more than an order of magnitude, which was consistent with a neutralization of acid sites evaluated by ammonia adsorption microcalorimetry. Although the rate of ethanol coupling was not increased by the addition of Na, the overall selectivity of ethanol to butanol was improved over the 1.0 wt.% Na/ZrO_2 sample because of the significant inhibition of ethanol dehydration side-reaction. This important observation could be the missing link in explaining the secondary effective role of NaOH and more specifically the Na^+ cations as surface inhibitors of the acidic surface site responsible for the dehydration of isopropanol. Some complementary experiments will be presented in Chapter 5 of the manuscript.

We have shown that the phase control to obtain a sample exclusively composed by tetragonal nanocrystals was successfully obtained over a specific content of alkaline source. The use of NaOH has been effective in inhibiting the production of water and mediating the synthesis of a pure t-ZrO_2 samples.

In parallel, we have shown that the average apparent size was highly dependent on the chosen concentration content of NaOH. In the following sections we will deal with influencing the size of the zirconia particles by adjusting the synthesis temperature, the alcohol content, and by splitting the global solvothermal treatment in two separate stages.

3.4 Size control

In this section we tackle on how to influence and control the size of the zirconia particles. Here we present three possible routes to fine tune the size by essentially varying the synthesis temperature, alcohol content and adding a second solvothermal stage in order to achieve the smallest crystalline nanoparticles that it is possible to produce for the fine structural study which is the heart of this thesis.

3.4.1 Temperature and alkalinity interplay on average apparent size

We have seen previously that the presence of sodium hydroxide inhibited the formation of monoclinic crystals jointly with the tetragonal metastable ones, but it also promoted the grain growth of the crystals. The goal of this section is to illustrate how the chemical budget (the mixture reactivity) can balance the decrease of the thermal budget and offer a control over the size of the particle while ensuring a good reaction yield. Table 8 shows the summary of the experiments performed to illustrate this effect:

Table 8: Solvothermal synthesis details for the chemical treatment exhibiting the interplay of NaOH content and temperature

NaOH ($mol.L^{-1}$)	**Zirconium ($mol.L^{-1}$)**	**Benzyl alcohol (% volume)**	**ageing period (days)**	**Temperature (°C)**
0.2	0.3	100%	3.0	210
0.2	0.3	100%	3.0	150
0.5	0.3	100%	3.0	210
0.5	0.3	100%	3.0	150
0.5	0.3	100%	3.0	125
0.5	0.3	100%	3.0	100
1.0	0.3	100%	3.0	210
1.0	0.3	100%	3.0	150
1.0	0.3	100%	3.0	125
1.0	0.3	100%	3.0	100
1.0	0.3	100%	3.0	80
1.0	0.3	100%	3.0	60

The peaks of the XRD patterns presented in Figure 76 are all identified to coincide with the tetragonal polymorph of zirconia whatever the sodium hydroxide content or the operating temperature used for the synthesis, except for the XRD diagram with T = 210ºC (Figure 76 c) where extra-peaks are visible. A strong alkaline and alcohol medium at high temperature (210°C) seem to promote extra organic and inorganic side-reactions whose crystalline products are no longer observed below 150°C.

The first thing that we observed from these series was the rapid limitation for decreasing the operating temperature due to the absence of precipitate at the end of the solvothermal treatment. Indeed, with the NaOH concentration at 0.2 $mol.L^{-1}$, no precipitate was formed when the temperature was decreased from 210°C to 150°C. Interestingly, the increase of sodium hydroxide in the reaction mixture shifts this limiting factor to lower temperatures and we succeeded to form precipitate at 150°C with a molar concentration of NaOH of 0.5 $mol.L^{-1}$ and even lower than 100°C when the molar concentration of NaOH is raised up to 1.0 $mol.L^{-1}$. Among the samples, only the sample synthesized at 80°C with NaOH concentration at 1.0 $mol.L^{-1}$ is drastically different from the others. It exhibits a large broadening of the diffraction peaks at positions 2θ = 30.3°, 49.9°, and 58.5° which corresponds to the main peaks of a tetragonal zirconia (JCPDS 00-050-1089).

A Rietveld refinement method was conducted for all the XRD patterns and the data are summarized in Figure 77. The main effect in the concentration content of NaOH on the apparent crystallite size is clearly demonstrated for the higher operating temperature namely 210°C. Generally, the decrease in temperature induces a decrease in the apparent size of the crystallites in accordance with the classic results obtained with a thermoactivated grain growth mechanism.

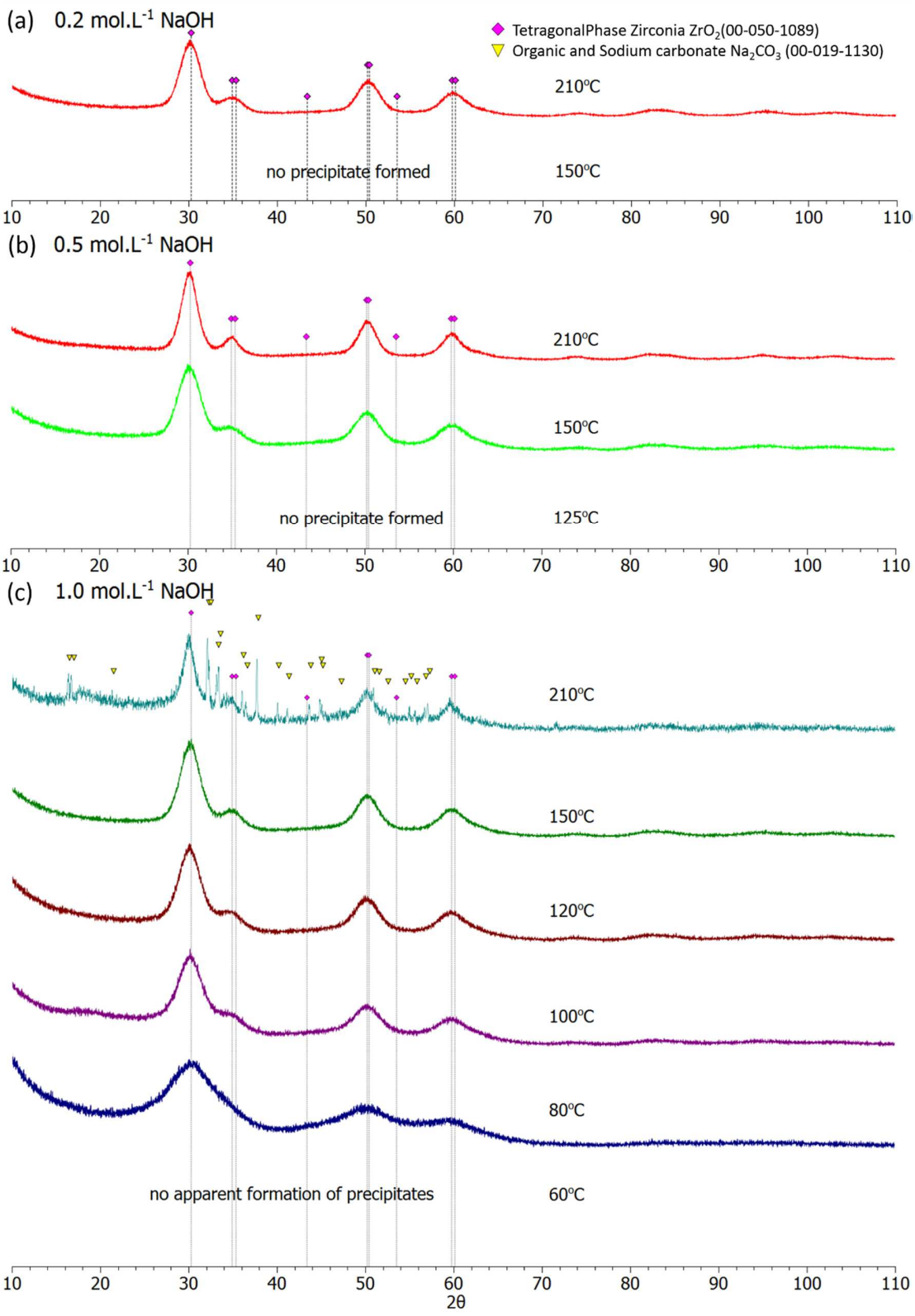

Figure 76: XRD patterns of samples obtained via a solvothermal technique under varied synthesis temperature for 3 days using $[Zr(O^iPr)_4 \cdot HO^iPr]_2$ in benzyl alcohol with (a) 0.2, (b) 0.5 and (c) 1.0 mol.L^{-1} NaOH.

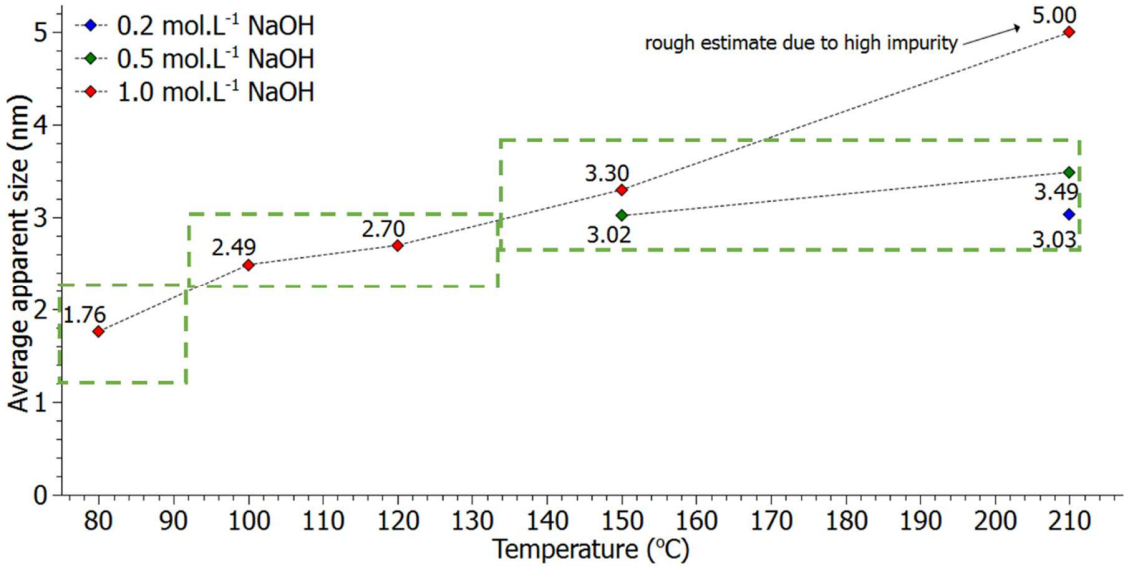

Figure 77: Average apparent size of the samples obtained via a solvothermal technique under varied synthesis temperature for 3 days using $[Zr(O^iPr)_4 \cdot HO^iPr]_2$ in benzyl alcohol with (a) 0.2, (b) 0.5 and (c) 1.0 mol.L^{-1} NaOH.

Certainly the tunability of the apparent size which is observed in the case of a highly alkaline synthesis is interesting in terms of technological parameter to achieve a controlled grain size. Here we observed that the decrease in size is not linearly correlated with the decrease in temperature but appears to behave in a step like manner with a sudden decrease at the lowest temperature. We note that the highest concentration content (1 mol.L^{-1}) of NaOH was able to achieve sizes that are less than 2.0 nm at lower temperatures. Indeed, the sample prepared in the richest alkaline environment and with the lowest operating temperature shows a drastic broadening of the Bragg diffraction peaks, indicating an extremely small crystallite size roughly estimated to 1.76 nm. This provokes a sudden rupture in the global trend for diminishing the crystallite size.

All these results illustrate perfectly the technological potential offered by the use of NaOH as a phase selection agent and efficient chemical energy supplier permitting to decrease the operating temperature as low as 80°C while keeping a good reaction yield and guaranteeing a crystalline zirconia.

3.4.2 Influence of alcohol content on the average apparent size

The previous section suggests that lowering the operating temperature and conjointly increasing the alkalinity of the reaction mixture allows an efficient control on the size of the zirconia crystallites. However, the abundant concentration of alkaline species may pose a problem in terms

of chemical purity and possible formation of other impurities, like sodium carbonate. Hence in this section we investigate the effects of lowering the benzyl alcohol content of the synthesis solution while keeping constant the NaOH concentration at 0.2 mol.L^{-1}, 0.5 mol.L^{-1}, 1.0 mol.L^{-1}, and 2.0 mol.L^{-1}. The total volume is maintained at 15 mL by complementing benzyl alcohol with a known inert solvent which is anisole [149] in order to keep the zirconium concentration at 0.3 mol.L^{-1}. The experimental details of the syntheses for size control via alcohol reduction are shown in Table 9.

According to the XRD diagrams shown in Figure 78 (a), dilution of benzyl alcohol in anisole keeping constant the NaOH concentration at 0.2 mol.L^{-1} does not induce drastic changes in the diffraction patterns from 100 vol.% to 13 vol.% of BnOH. Nevertheless, below this dilution state, *i.e.* for 10 vol.% of BnOH or also full absence of benzyl alcohol, a drastic broadening comparable to that was already seen in the previous section is observed. Moreover, one can note by comparing the series with 0.2 mol.L^{-1}(Figure 78 (a)) and 0.5 mol.L^{-1} (Figure 78 (b)) NaOH concentration, that the abrupt change or more precisely the borderline separating the two types of broadening is sensitive to the alkalinity of the mixture. Indeed, a large increase in alkalinity from 0.2 mol.L^{-1} up to 0.5 mol.L^{-1} leads in a slight but observable decrease of the borderline toward the lowest values of BnOH content.

Table 9: Synthesis details for the chemical treatment with varied benzyl alcohol content

NaOH content ($mol.L^{-1}$)	**Zirconium concentration ($mol.L^{-1}$)**	**Benzyl alcohol volume fraction (% volume)**	**Solvothermal ageing period (days)**
0.2	0.3	100%	3.0
0.2	0.3	50%	3.0
0.2	0.3	20%	3.0
0.2	0.3	15%	3.0
0.2	0.3	13%	3.0
0.2	0.3	10%	3.0
0.2	0.3	0%	3.0
0.5	0.3	100%	3.0
0.5	0.3	10%	3.0
0.5	0.3	0%	3.0
1.0	0.3	100%	3.0
1.0	0.3	0%	3.0
2.0	0.3	100%	3.0
2.0	0.3	0%	3.0

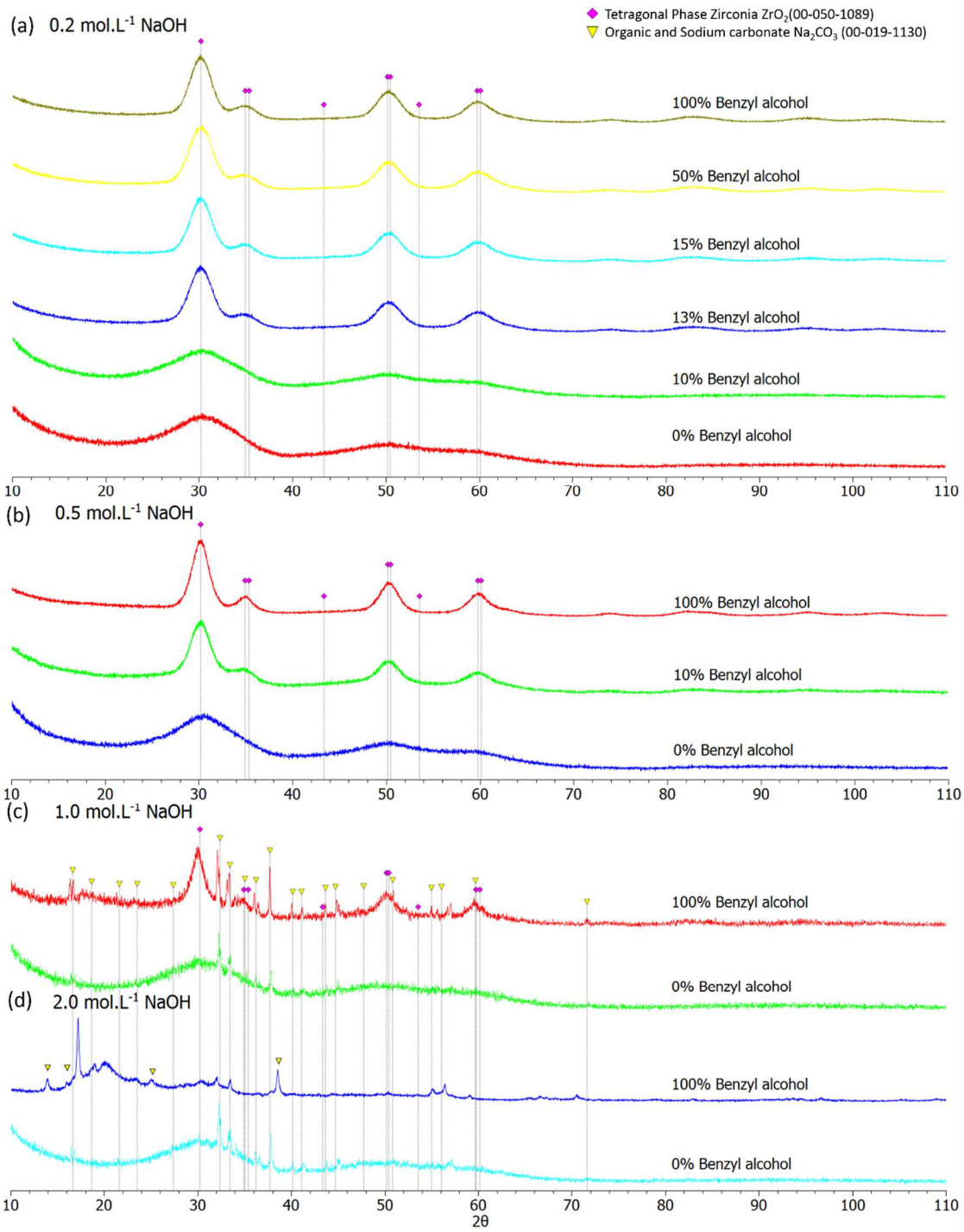

Figure 78: XRD patterns of samples obtained via a solvothermal technique at 210°C for 3 days using $[Zr(O^iPr)_4 \cdot HO^iPr]_2$ under varied amounts of benzyl alcohol with (a) 0.2, (b) 0.5, (c) 1.0 and (d) 2.0 $mol.L^{-1}$ NaOH.

One interesting aspect lies in the fact that all the diagrams obtained for extremely low volume content of BnOH exhibit the same state of broadening. Indeed, when the alkalinity is raised from 0.5 mol.L^{-1} up to 1.0 mol.L^{-1} (Figure 78 (c)) and even more up to 2.0 mol.L^{-1} (Figure 78 (d)), no evolution of the sample is observed concerning the broad envelop whose maxima are exactly located at the same positions (*i.e.* 2θ = 30.3°, 49.9° and 58.5°) that those of the dominant peaks of t-ZrO_2. The presence of extra phases that is observed in the diagram can be interpreted as possible organic by-products or/and sodium carbonate impurities.

The alkalinity of the solution which seemed to play an important role on the growth of the particles in a BnOH-rich environment looks to be ineffective in the present situation when the content of BnOH was largely reduced below 10 vol.%. A series of samples were prepared in anisole with varied amounts of NaOH (0.0, 0.2, 0.5, and 1.0 mol.L^{-1}) added into the reaction mixture. All the samples appear to have broad peaks with the sample without NaOH as the broadest as shown in Figure 79. However, subtle difference is observed when NaOH is added as indicated by the slight narrowing of the peaks.

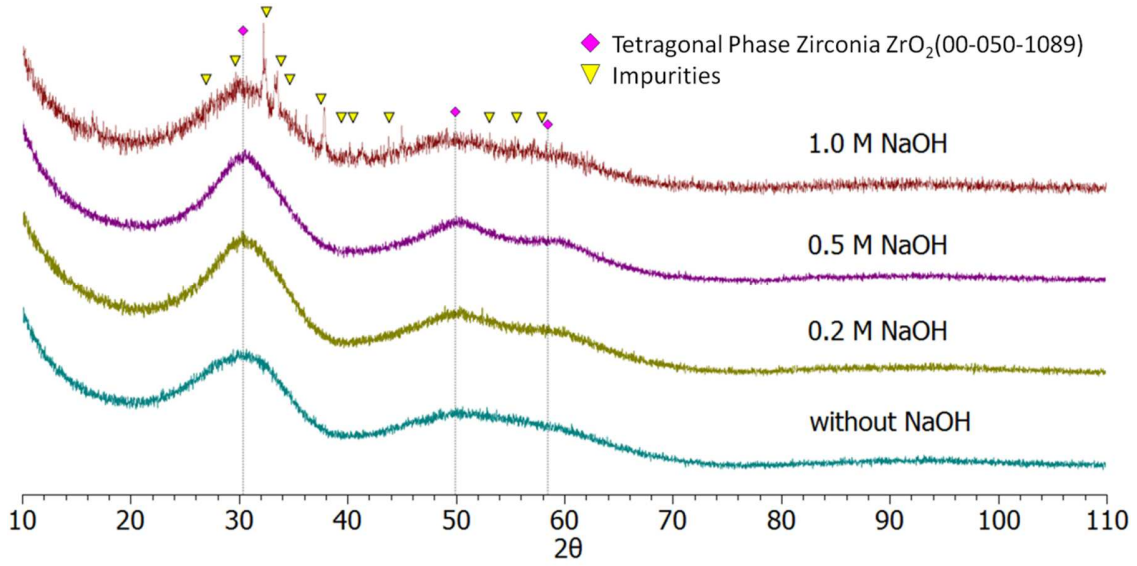

Figure 79: XRD patterns of samples obtained via a solvothermal technique at 210°C for 3 days using $[Zr(O^iPr)_4 \cdot HO^iPr]_2$ and anisole under varied amounts of NaOH (0.0, 0.2, 0.5, and 1.0 mol.L^{-1})

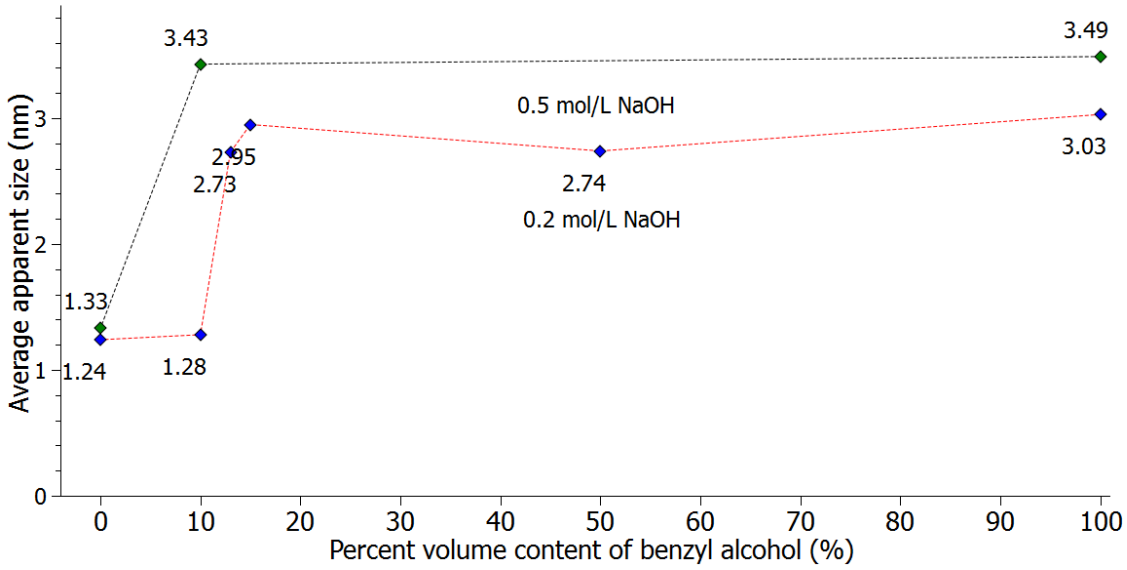

Figure 80: Average apparent size of the samples obtained via a solvothermal technique at 210°C for 3 days using $[Zr(O^iPr)_4 \cdot HO^iPr]_2$ and varied amounts of benzyl alcohol with 0.2 and 0.5 mol.L^{-1} of NaOH.

The quantitative refinements performed on the XRD diagrams issued from the series (a) and (b) are summarized in Figure 80. The size does not appear to decrease monotonously but rather drops immediately below a certain percentage of benzyl alcohol. This sudden drop in size also slightly varies with the amount of alkali source. For a BnOH-rich environment, whatever the concentration of sodium hydroxide used, the crystallite size seems to "saturate" at the same average value of BnOH content for all the samples and depends exclusively on the alkalinity of the reaction mixture: an apparent size of about 2.7 to 3.0 nm for an alkalinity of 0.2 mol.L^{-1} and 3.4 to 3.5 nm for an alkalinity of 0.5 mol.L^{-1}. For a BnOH-poor environment, the crystallite size seems to converge to the same level of broadening (largely below the sensitivity of the Rietveld method applied to such a large broadened pattern) whatever the alkalinity and no progressive evolution between these two extreme states seems to rule the abrupt transition.

In summary, by diluting the benzyl alcohol content with an inert ether, we have shown that it was necessary to apply at least a 1/10 dilution to observe a drastic effect on the final sample product. The isolation of a crystalline sample characterized by an extreme broadening of the Bragg diffraction pattern was possible but further analyses are needed to attribute properly the broadening to the presumed small crystallite size. Finally, these series of experiment have shown that the benzyl alcohol is directly involved in the formation mechanism of the nanocrystals, i.e. the

direct condensation of zirconium isopropoxide-isopropanol adduct is largely limited in an alcohol-poor medium.

3.4.3 Influence of dual stage solvothermal synthesis on the average apparent size

Based on the previous experiments, it appears that both the temperature and alcohol content plays a significant role in the phase selection and size control when combined with the alkali source NaOH. Hence, in this section we introduce the dual stage solvothermal synthesis where we exploit the previous findings in order to orchestrate a crystallite size control. The dual stage solvothermal synthesis consists in applying to the product obtained after stage 1 a second solvothermal treatment with a different operating temperature and reaction medium, namely type of solvent and presence of alkali precursor. The different synthesis preparations via dual stage solvothermal synthesis are listed in Table 10.

Table 10: Synthesis details for the dual stage sovothermal synthesis strategy

	NaOH content ($mol.L^{-1}$)	**Zirconium concentration ($mol.L^{-1}$)**	**Benzyl alcohol volume content (% volume)**	**Solvothermal ageing period (days)**	**Temperature (°C)**
Stage 1	0.2	0.3	100	3	210
Stage 2	0.0	0.0	100	3	210
	0.2	0.0	100	3	210
Stage 1	0.2	0.3	0	3	210
Stage 2	0.0	0.0	100	3	210
	0.0	0.0	100	3	150
	0.2	0.0	100	3	150

Applying a second solvothermal step to a previously formed zirconia sample showed some susceptibility to changes as observed in their XRD patterns (Figure 81). It also modifies their crystallite apparent sizes as shown Figure 82. Two main series of experiments were conducted in

this section: the first one is based on the retreatment of a tetragonal zirconia sample obtained in benzyl alcohol while the second one is based on the retreatment of a zirconia sample obtained in anisole (both stage1-samples are obtained in the presence of 0.2 mol.L^{-1} NaOH). Two different solvothermal second steps were proposed for the sample initially prepared in benzyl alcohol: a solvothermal treatment either at 150°C or 210°C for 3 days more and the regeneration of the supernatant with fresh benzyl alcohol with and without 0.2 mol.L^{-1} concentration of NaOH.

No effect is visible in the absence of NaOH; indeed, the sample (a_1) remains tetragonal in nature and the apparent crystallite size is still about 3.06 nm after the second solvothermal step while it was 3.03 nm after the first one. In order to induce a change in the sample, the reaction mixture of the second step needs to include a regenerated fraction of NaOH; in that case, the diffraction peaks of the sample (a_2) appear to be narrower and the apparent size jumps up to 3.66 nm. The absence of any change in the case of a second solvothermal step performed in benzyl alcohol indicates the robust feature of the synthesis achieved in the initial solvothermal step whereas the joint presence of benzyl alcohol and NaOH enhances the grain growth of the crystallites under the effect of a powerful mineralizing mixture. Fortunately, such a reactional mixture does not allow the sample to undergo a phase conversion from the tetragonal state to the monoclinic one.

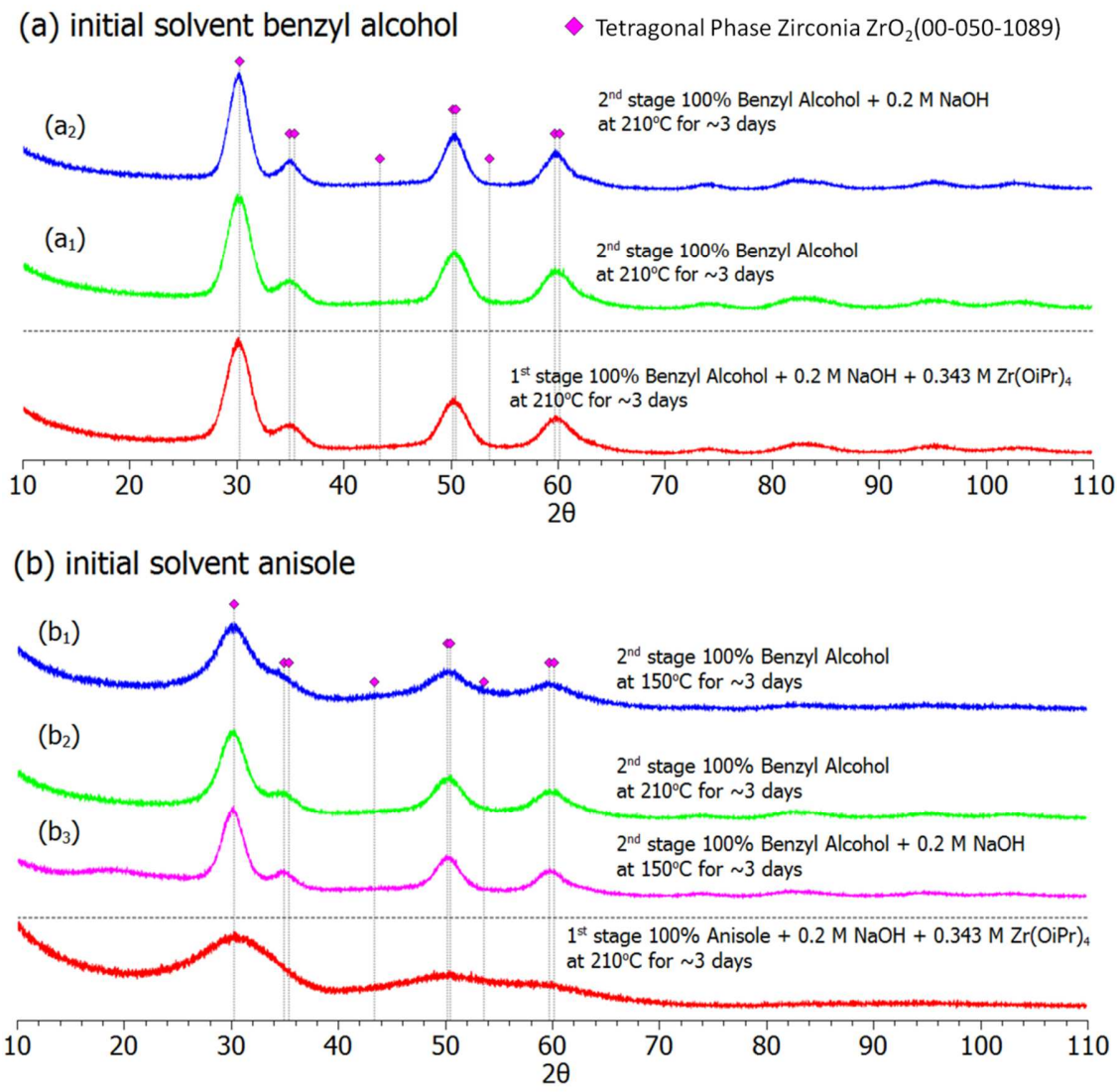

Figure 81: XRD patterns of samples prepared by dual stage synthesis using $[Zr(O^iPr)_4 \cdot HO^iPr]_2$ with 0.2 mol.L^{-1} NaOH in (a) benzyl alcohol and (b) anisole at 210°C for 3 days for the first step and then, secondly in benzyl alcohol with or without 0.2 mol.L^{-1} NaOH for the second step.

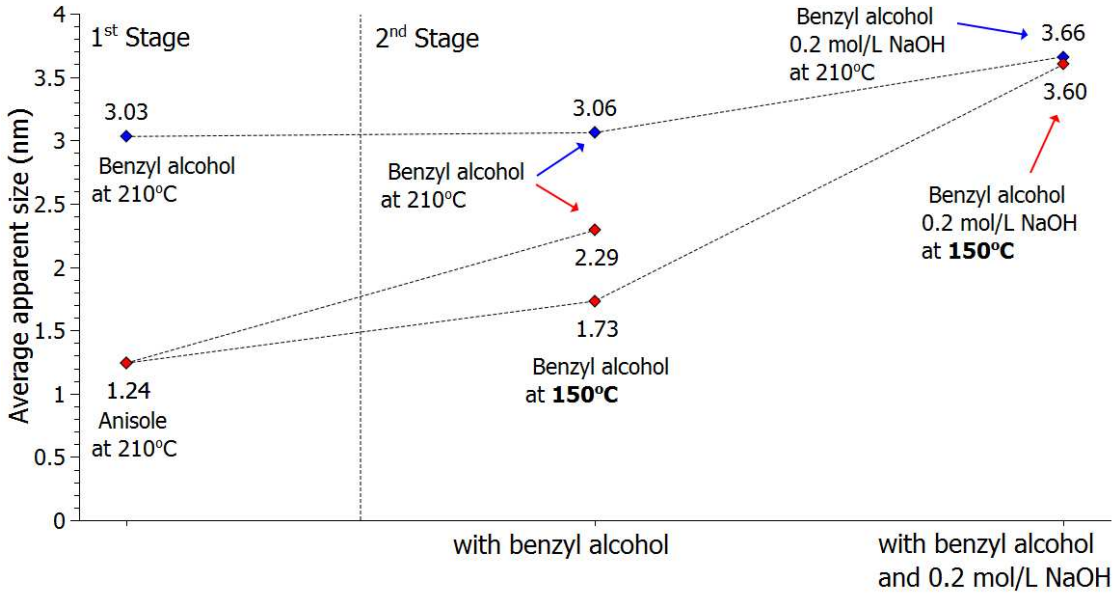

Figure 82: Average apparent size of the samples prepared by dual stage synthesis using $[Zr(O^iPr)_4 \cdot HO^iPr]_2$ with 0.2 mol.L^{-1} NaOH in (a) benzyl alcohol and (b) anisole at 210°C for 3 days for the first step and then, secondly in benzyl alcohol with or without 0.2 mol.L^{-1} NaOH for the second step. (Lines are only used as a guide for the eyes)

The final samples (b_1) and (b_2) using the anisole-based zirconia sample as starting material were obtained by retreatment in pure regenerated benzyl alcohol at respectively 150°C and 210°C. The strategy applied in such cases is beneficial to a grain growth allowing the expression of the tetragonal polymorph of zirconia. The crystallite apparent sizes are respectively about 1.7 nm and 2.3 nm when the solvothermal treatment was performed in benzyl alcohol at 150°C or at 210°C.

Similarly, the addition of sodium hydroxide in the second stage improved greatly the size of crystallites even at a much lower temperature. Indeed, the regeneration of a 0.2 mol.L^{-1} NaOH anisole-based medium permitted to increase the crystallite size from 1.2 nm up to 3.6 nm which is bigger than the size obtained by the increase of temperature from 150°C up to 210°C in the non-alkaline medium. The alkaline parameter seems to prevail over the temperature one in the case of a sample initially prepared in 0.2 mol.L^{-1} NaOH anisole-based medium. This is probably due to the fine nature of the precipitate and the small particles size which confers to the sample a large driving force for ripening and growth mechanisms. However, this assumption needs to be confirmed for selected samples by direct TEM observations.

Two main characteristics emerged from this study:

- Samples synthesized from the alkaline benzyl alcohol route are quite stable towards retreatments at the same temperature. However a growth mechanism via Ostwald ripening can still be activated if the operator regenerates the samples in an alkaline reaction mixture during the second solvothermal stage (alkaline benzyl alcohol combination seems to be an effective mineralizing mixture),
- Samples issued from the alkaline anisole route are highly sensitive towards any retreatment even at lower temperatures as long as the regenerated mixture is composed by benzyl alcohol or alkaline benzyl alcohol.

The dual stage solvothermal synthesis highlights the effects of temperature, benzyl alcohol, and sodium hydroxide content on influencing the size and crystallinity of the zirconia particles. An improvement in crystallinity is clearly seen especially for the smallest zirconia samples. The samples remained to be t-ZrO_2 after the second treatment probably due to the residual NaOH that was not eliminated during the centrifugation of the first stage powder.

3.5 In-depth analysis of selected zirconia samples

Among the results presented until now, two samples appear to be interesting for the understanding of the formation of nanoscale size zirconia particles. In this section, further characterizations are conducted on these samples by various analytical techniques (TEM, FTIR, TGA, ICP and XPS). The synthesis details of the selected samples are listed in Table 11 and their XRD diagrams are recalled in Figure 83.

Table 11: Experimental details for the synthesis of the selected samples

NaOH content ($mol.L^{-1}$)	**Zirconium concentration ($mol.L^{-1}$)**	**Solvent type**	**Solvothermal ageing period at 210°C (days)**	**Zirconia polymorph**	**App. size (nm)**	**Diameter size (nm)**
0.2	0.3	Benzyl alcohol	3.0	Tetragonal	3.0	4.0
0.2	0.3	Anisole	3.0	Broad tetragonal	1.2	1.6

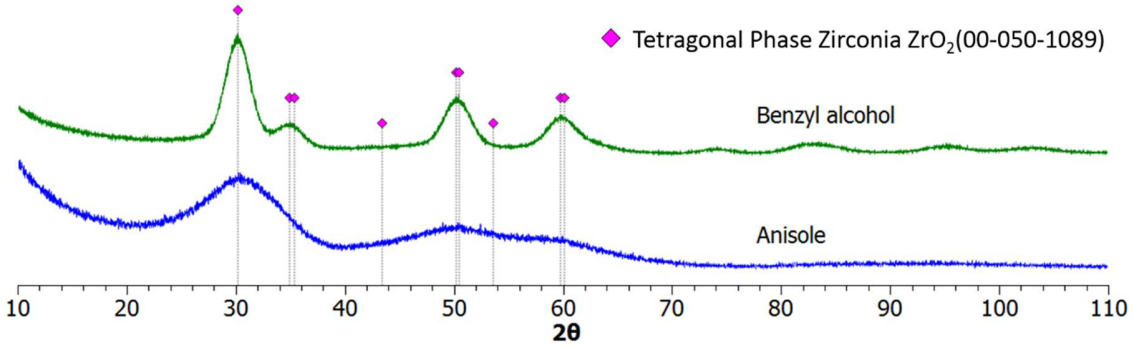

Figure 83: XRD diagrams of the samples obtained via a solvothermal technique at 210°C for 3 days using $[Zr(O^iPr)_4 \cdot HO^iPr]_2$ with 0.2 $mol.L^{-1}$ NaOH in (a) benzyl alcohol and (b) anisole.

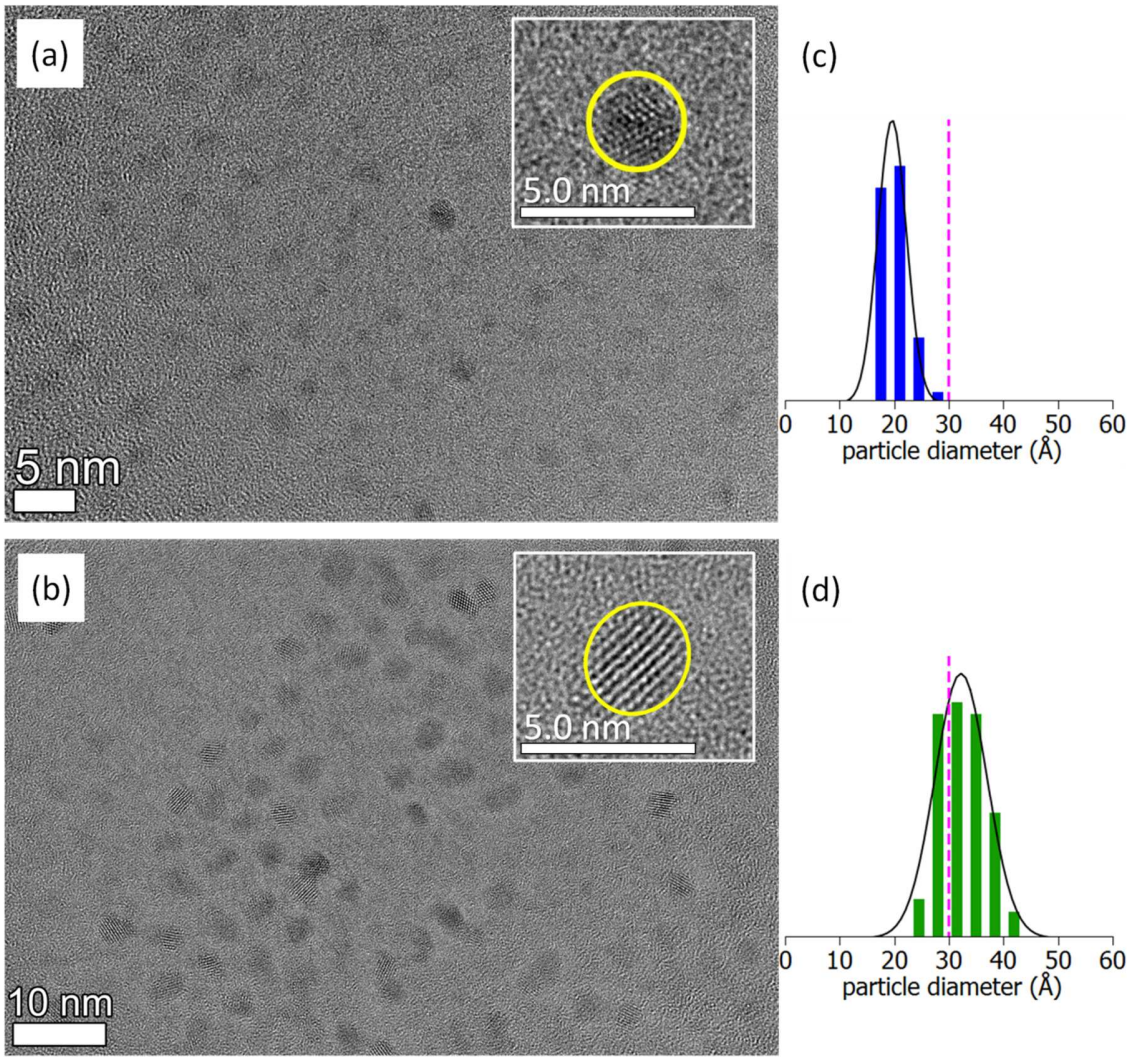

Figure 84: TEM micrographs of the zirconia particles synthesized at 210°C for 3 days in (a) anisole and (b) benzyl alcohol with 0.2 mol.L^{-1} concentration of NaOH. Size dispersion analysis with (c) 49 data points for the anisole sample and (d) 70 data points for the benzyl alcohol sample.

Figure 84 (a) and (b) shows the TEM images of the zirconia nanoparticles synthesized in anisole or benzyl alcohol. Both samples appear to be mostly composed of isolated spherical- and oval-like particles. Such shapes can be attributed to size effect which suggests that if the surface energy is overcomed by the volume free energy then below the critical size a spherical or near spherical shape morphology will be favored [126]. For nanoparticles covered with chemically-bonded ligands the relative volume free energy can become more pronounced than the stabilized surface energy and a slight deviation of the shape can be observed. The well-defined crystal lattice visible

on the particles confirms that the zirconia particles are crystalline whatever the solvent used in the synthesis.

Figure 84 (c) and (d) show the size distribution analyses of the samples using 49 particles and 70 particles data points for the anisole and benzyl alcohol, respectively. Both results can be described by a Gaussian-like distribution function as indicated by the solid black curve fittings. For the anisole prepared sample, it reveals a very narrow and almost symmetrical distribution without tails with an average diameter of 2 nm. The fitting of the results obtained for benzyl alcohol shows a much broader shape but having the same symmetrical distribution with a bit of tails at the edges. The average diameter of the particles in this sample is about 3.2 nm.

The low aggregation state observed for both samples could be related to the presence of the alkoxy groups that act as a capping ligand on the crystals' surface hence reducing the formation of larger crystals during solvothermal ageing and promoting a steric hindrance leading to a physical aggregated sample after drying. The presence of particles larger than 2 nm for the anisole sample and 3.2 nm for the benzyl alcohol sample could be due to the physical aggregation of smaller particles and oriented attachment which favors a particular surface to adhere onto another surface and lead to slight anisotropic growth effects [162]; or this could simply be an overlapping of smaller crystals forming slightly larger particles as observed on the microscope (see Figure 85).

Comparing the average diameter size of the spherical particles obtained via XRD and TEM measurements for both types of samples (Table 11 and Figure 83), there is some difference between the two measurements where the former is comparably larger. The reason for this difference is tackled in detail in the following chapter (Chapter 4).

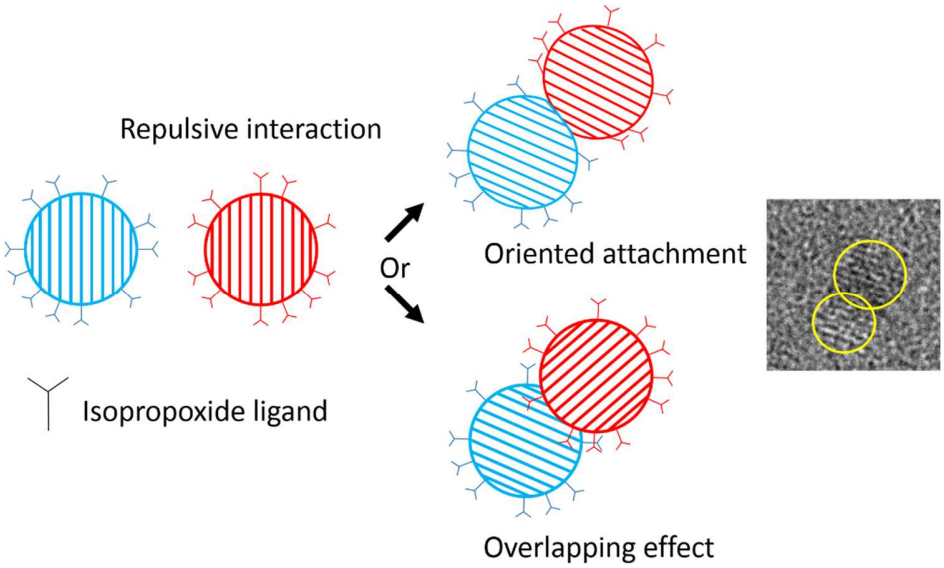

Figure 85: Scheme for the larger particle sizes oriented attachment and overlapping.

The FTIR spectra of the dried zirconia samples are shown in Figure 86 for samples prepared in benzyl alcohol (a) and anisole (b). There appears to be no large difference between the two zirconia samples. The large band from 2800 cm^{-1} to 3700 cm^{-1} with the maximum positioned at 3416 cm^{-1} corresponds to the vibration of hydroxyl groups such as adsorbed water and possible residual hydroxylated group generated from the synthesis [163]. The two distinct peaks at 1574 and 1359 cm^{-1} lie in the region for the carbonate species [164] and possibly alkoxide groups, especially at 1364, 1455 and 2978 cm^{-1} for the C-H vibrations and at 1041 cm^{-1} for the C-O vibration of the residual isopropoxide groups [165].

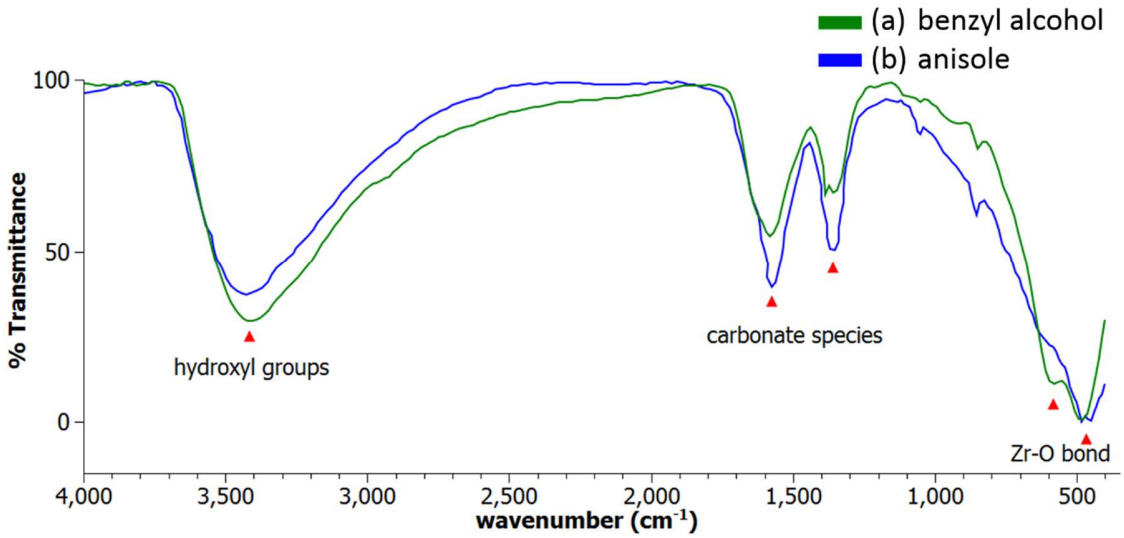

Figure 86: FTIR spectra of the zirconia particles produced at 210°C for three days in (a) benzyl alcohol and (b) anisole with 0.2 mol.L^{-1} of NaOH

Finally, from 400 cm^{-1} to 600 cm^{-1}, the intense bands positioned at 466 cm^{-1} and 583 cm^{-1} are related to the (sym) vibrations of the Zr-O bond for zirconia [166] [167]. These Zr-O bands are more intense for the sample prepared in benzyl alcohol which could be due to the large difference in size and then, crystallite volume.

We recall that the crystalline sodium carbonate peaks were only visible in the samples prepared with a large content of sodium hydroxide superior at 1.0 mol.L^{-1}. The FTIR analysis is more sensitive to impurities compared to XRD analysis. Which means it can detect small quantities of carbonate species which are not easily detected by XRD. These carbonate species are probably lying just surrounding the particles in an individual manner which does not allow the sodium carbonate to crystallize. We believe that the washing step using anhydrous ethanol does not fully eliminate the sodium hydroxide solute from the product, so that carbonation over the zirconia particles can occur during the evaporation of the final rinsing solvent and contamination with carbon dioxide from the ambient atmosphere.

When the amount of sodium hydroxide used in the synthesis is quite small, the carbonation and the precipitation of sodium carbonate are limited but the acidic surface sites neutralized by the Na^+ ions (as it was proposed by Koslowski et al.) can be preferential sites for a reaction with CO_2 and the formation of surface carbonate groups.

The presence of residual alkoxide ligands and carbonate species can be seen by a thermogravimetric analysis (TGA) shown in Figure 87.

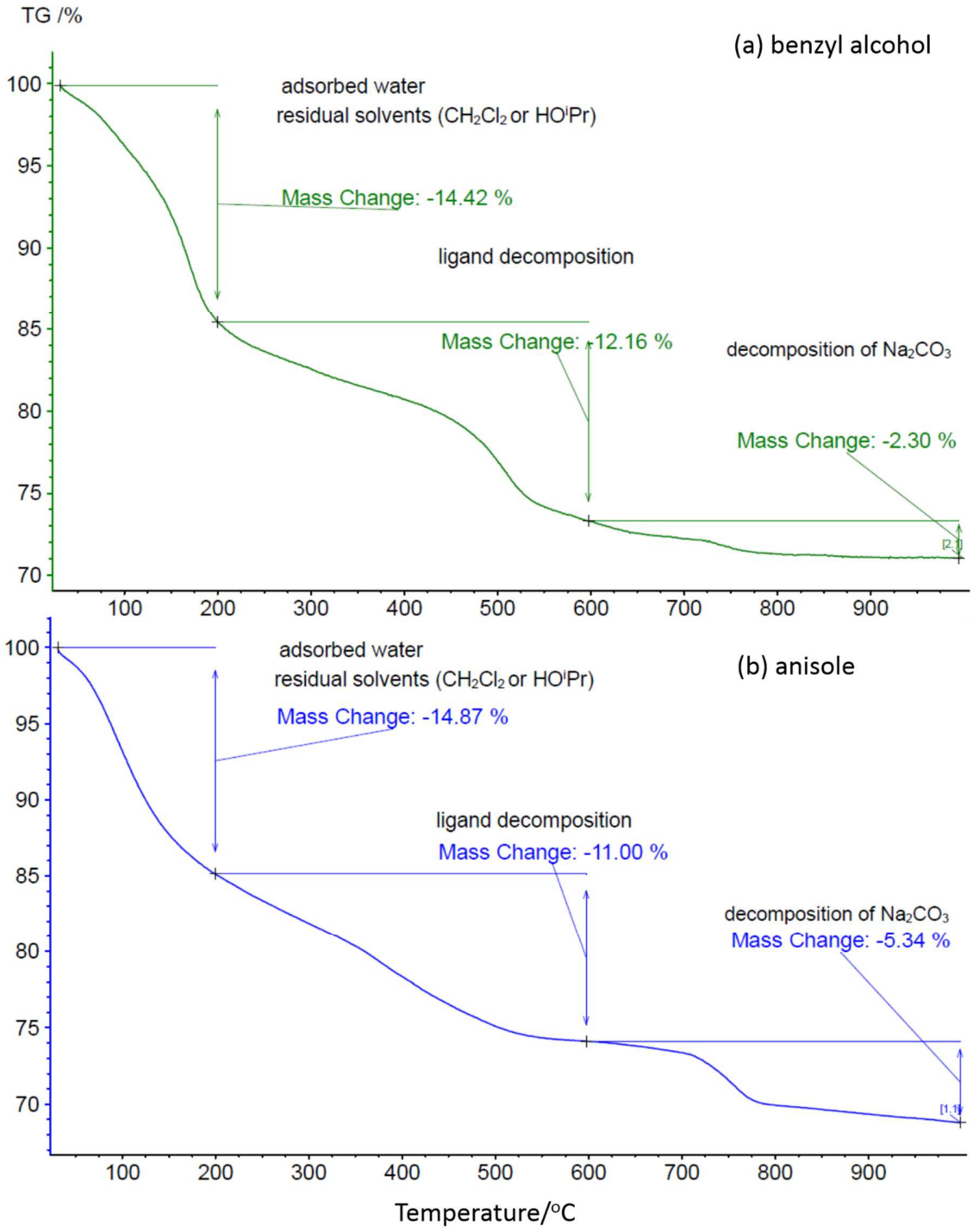

Figure 87: TGA analyses of the zirconia samples produced at 210°C for three days in (a) 0.2 mol.L^{-1} NaOH alkaline benzyl alcohol and (b) 0.2 mol.L^{-1} NaOH alkaline anisole.

The thermogravimetric curves indicate a total mass loss of about 28.88% for the sample prepared in benzyl alcohol and 31.21% for the sample prepared in anisole. Since the global feature of the curves involves three distinct mass losses, we propose to study the thermal decomposition into three temperature regions: 30-200°C, 200-600°C and 600-1000°C:

- The first mass loss corresponds to residual solvents and adsorbed water coming from the post-synthesis operations used to collect the sample (mass loss of 14.42% for the sample prepared in benzyl alcohol and 14.87% for the sample prepared in anisole).
- The second mass loss corresponds to the combustion of strongly bonded organic (residual organic and/or byproducts) like alkoxide groups and chemical hydroxide groups that may have enveloped the zirconia particles (mass loss of 12.16% for the sample prepared in benzyl alcohol and 11.00% for the sample prepared in anisole).
- And lastly, the third mass loss over a quite high range of temperatures could be attributed to the decomposition of sodium carbonate species that were formed during the drying process of the sample (mass loss of 2.30% for the sample prepared in benzyl alcohol and 5.34% for the sample prepared in anisole).

Comparing the three temperature regions for both samples, it seems that the most significant difference in terms of mass loss is in the 600-1000ºC region, i.e. the event associated with the decomposition of sodium carbonate. Indeed, the sample prepared in anisole exhibit almost a twice larger mass loss than the sample prepared in benzyl alcohol. If we take in account the particles size that we have observed by TEM, the larger value for the anisole-based sample could be due to the larger specific surface area (SSA) that is larger for smaller particles and would indicate that the sodium is effectively largely deposited onto the particles surface which is roughly 1.6 times larger in the case of particles measuring 2 nm rather than 3.2 nm (see Table 12).

Table 12: Comparison of specific surface area of the selected samples

	Benzyl alcohol-based synthesis	**anisole-based synthesis**
Average diameter (nm)	3.2	2
Surface area (nm^2)	32.2	12.6
Volume (nm^3)	17.2	4.2
SSA (nm^{-1})	1.9	3

These analyses suggest that the smaller particles prepared in the absence of benzyl alcohol contain a much larger sodium-to-zirconium (*Na/Zr) ratio as compared to the particles prepared in benzyl alcohol and that the sodium is mainly dispersed onto the surface of the particles. The organic content suggested by FTIR was confirmed by TGA and is expected to play a role in the steric hindrance and the poor aggregated state of the particles of the zirconia particles as observed by many research groups.*

The relative quantification of sodium in the samples was determined by (a) ICP and (b) XPS analyses which are gathered in Figure 88. ICP analysis shows that both samples prepared in benzyl alcohol and anisole contains sodium ions. It is also observed that the sodium-to-zirconium molar ratio is 1.56 times higher for the samples prepared in anisole which are significantly smaller in size according their respective average apparent size. Similarly, the XPS analysis confirms the presence of sodium ions on the zirconia samples for both types of solvents and follows a similar increase in the sodium-to-zirconium molar ratio when the size is decreased. The sodium-to-zirconium ratio is also multiplied by 1.55 for samples prepared in anisole. Interestingly, the increase in the sodium-to-zirconium molar ratio is of the same order than the increase in the SSA estimated value when the benzyl alcohol is replaced by anisole in the initial reaction mixture.

Both ICP and XPS give similar trend and the results confirm the large proportion of sodium surrounding the zirconia particles. Even if XPS is a traditional surface analysis method, here in the case of extremely small particles, it becomes a global bulk method. Such results highlight the features of the objects synthesized by the two main routes developed in this work but do not indicate the eventual presence of doping sodium inside the zirconia network. The only proven fact is that the sodium is mainly distributed along the surface of the particles and the largest ratio observed for the anisole-based sample is undoubtedly correlated to the size of the individual zirconia

particles. Whereas Xei et al. claim that the sodium ions were found to play a crucial role in the formation of the stable tetragonal phase zirconia by incorporating into the internal crystal structure of the zirconia during the hydrothermal synthesis [168]*, we think that such hypothesis is not relevant in the light of the exposed results and we propose complementary investigations that will be presented in the last chapter of this work.*

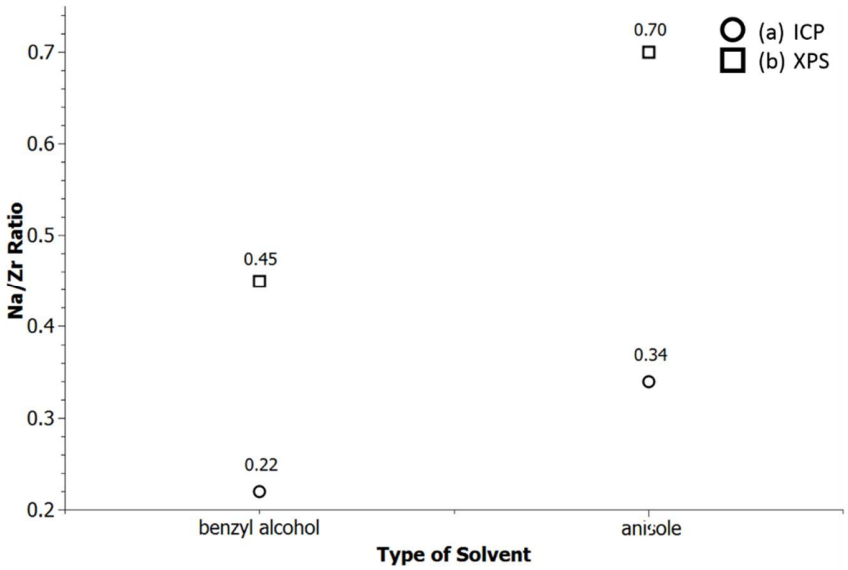

Figure 88: (a) ICP and (b) XPS analyses of the zirconia samples prepared with 0.2 mol.L^{-1} of NaOH for three days at 210°C in benzyl alcohol or in anisole.

3.6 Conclusion

The synthesis of zirconia was successfully achieved via a non-aqueous procedure in a solvent-controlled strategy. Comparing the two types of zirconium precursor, zirconium isopropoxide-isopropanol adduct was chosen over zirconium chloride since it was able to readily form zirconia in various O-donor solvents like ether, alcohol or aldehyde. Such choice inhibits the presence of halide impurities but implies the necessity to heat the reaction mixture to 210°C which is a higher temperature than those generally needed in metal halide-based synthesis.

The addition of an alkali metal in the form of sodium hydroxide proved to be beneficial in order to promote the production of single phase zirconia by inhibiting the dehydration side-reaction presumably responsible for a partial phase conversion t-ZrO_2 to m-ZrO_2. Although the presence of sodium hydroxide influenced the average apparent size of the zirconia particles, the extent of its effect is quite limited within the range of 0.1 to 0.5 mol.L^{-1} with an operating temperature of 210°C. Below or above this its use leads to the formation of phase or organic impurities, respectively. The alkaline conditions generated by the use of 0.2 mol.L^{-1} NaOH have allowed to isolate at 210°C three interesting zirconia samples composed of m-ZrO_2 nanocrystals in benzaldehyde, t-ZrO_2 nanocrystals in benzyl alcohol and finally extremely small t-ZrO_2 nanocrystals in anisole and presenting respectively an average diameter size of 3.6 nm, 4.0 nm and 1.6 nm.

Moreover, the presence of sodium hydroxide has induced an effective size control of the crystallites, whereas the robust and simple benzyl alcohol route is generally claimed by Pinna *et al.* to offer a poor control over the size and shape of the particles [169]. Indeed, the interplay of the NaOH content, the synthesis temperature and the dilution factor of benzyl alcohol allows to vary the size of the zirconia nanoparticles in the range 3-7 nm and even below 2 nm if one achieves *a minima* a 1/10 dilution of benzyl alcohol in anisole:

- the main parameters seem to be both the NaOH content and the synthesis temperature since the temperature can be largely decreased from 210°C to 100°C (even lower at 80°C) by operating in a strongly alkaline (1 mol.L^{-1} NaOH) benzyl alcohol medium, *i.e.* when the thermal budget is then largely balanced by the chemical one guaranteeing a good reaction yield and a large size variability in the range (100°C-210°C *vs.* 0.2-1.0 mol.L^{-1} in NaOH).
- benzyl alcohol-poor (below 10 vol.%) or benzyl alcohol-free syntheses at 210°C in the presence of at least 0.2 mol.L^{-1} NaOH led to zirconia samples characterized by an extremely

small crystallite size (inferior to 2.0 nm) due to the limited presence of alcohol which plays a fundamental role in the reaction mechanism and in the genesis of the nanoparticles.

The last strategy which has been successfully achieved in order to promote a size sampling of the synthesized particles consists of adding a second solvothermal step to the zirconia samples produced by a benzyl alcohol-based or an anisole-based synthesis. The parameters were able to act on the apparent size of the nanoparticles in two ways:

- the use of a regenerated alkaline benzyl alcohol medium for zirconia powder produced initially in benzyl alcohol which permits to induce a grain growth when the applied temperature of the second step is 210°C,
- the single- or joint-use of a benzyl alcohol or an alkaline benzyl alcohol medium for zirconia powder produced initially in anisole which permits to induce a grain growth at moderate temperature and usher in an effective size control.

Many others permutations and tests could be considered but our goal was to propose innovative technological visions in non-aqueous sol-gel route to achieve a good control on the features of metal oxide nanoparticles.

Finally, two main samples were selected and further analyses were carried out before to subject such samples to total X-ray and to get an intimate atomic features of the nanocrystals. These samples were prepared with 0.2 $mol.L^{-1}$ NaOH and 0.3 $mol.L^{-1}$ zirconium isopropoxide-isopropanol adduct at 210°C for three days either in benzyl alcohol or in anisole. These selected samples prepared in benzyl alcohol and anisole have an average apparent sizes of about 4.0 nm and 1.6 nm, respectively. Both samples showed that they are highly crystalline according to their morphological characteristics by TEM analysis. FTIR and TGA have shown that the samples contained a non-negligible fraction of organics and sodium carbonate surrounding the zirconia particles which may play a role in the stabilization of these tiny particles. The Na^+ presence, which was claimed to be responsible for the inhibition of the surface-catalyzed dehydration side-reaction, was quantified by XPS and ICP in both samples and the largest content observed in the case of the anisole-based sample was attributed to the largest SSA value achieved in the case of extremely small nanoparticles.

Chapter 4: Structural Analysis of Selected Samples

4 Structural analysis of selected samples

4.1. Introduction

In this chapter, we present the structural analysis of representative samples of zirconia nanoparticles mainly using X-ray total scattering (TS) and atomic pair distribution functions (PDF) in order to gain insight into the medium-range and short-range regions of the nanoparticles structure which gives invaluable information in identifying the kind of polymorph. Experimental diffraction data are also analyzed using the Rietveld method in order to describe the structure in a more conventional way, *i.e.* in terms of average structure. As mentioned earlier, zirconia exhibits a complex polymorphism with four fluorite-derived structures: the cubic, tetragonal, monoclinic and orthorhombic I. In the following sections, we discuss the structural differences of the different polymorphs thanks to their PDF.

4.1.1 Cubic phase zirconia

The cubic phase has a perfect fluorite-type structure and typically exists at high temperatures, above 2370°C [89]. It is the most symmetric of all zirconia polymorphs, with space group $Fm\bar{3}m$ (No. 225). Each zirconium cation is located in a perfect oxide ions cube and therefore it has an 8 fold-coordination. The cubic unit cell and PDF are presented in Figure 1. We observe various peaks that are characteristics of Zr-O, Zr-Zr and O-O interatomic distances. For this discussion we focus on the eight first peaks visible on the total PDF since at higher positions the peaks begin to be superimposed with large overlaps (Figure 89 (c-d)). The first peak (I) located at 2.21 Å corresponds to the Zr-O distances. It is intense because the eight Zr-O distances are all of the same length and contributes to the same peak. The second peak (II) located at 2.55 Å, corresponds to the O-O distances and it is slightly visible next to the first peak. The peak intensity is less in comparison to zirconium since the oxygen has lesser scattering factor. The third peak (III) is positioned at 3.61 Å and corresponds to the Zr-Zr distance. It is the most intense due to the higher scattering factor contribution in comparison with the other combination of Zr and O atoms. These three peaks are typically the characteristics of the short-range region of a cubic phase zirconia. The next peak position that belongs to the Zr-Zr distance is positioned at (V) 5.10 Å which is in the medium-range region and it is related to the first Zr-Zr distance (III) by $3.6\sqrt{2}$ Å. The last Zr-Zr (VII) peak that is covered within the analyzed region is located 6.31 Å and it is related to the first and second

peaks by $\sqrt{(3.6)^2 + (5.1)^2}$Å. The fourth peak (IV) located at 4.3 Å corresponds to Zr-O correlation and is defined as the distance between O atoms and their second Zr neighbours. The next two Zr-O distances are located (VI) 5.61Å and (VIII) 6.68 Å, respectively.

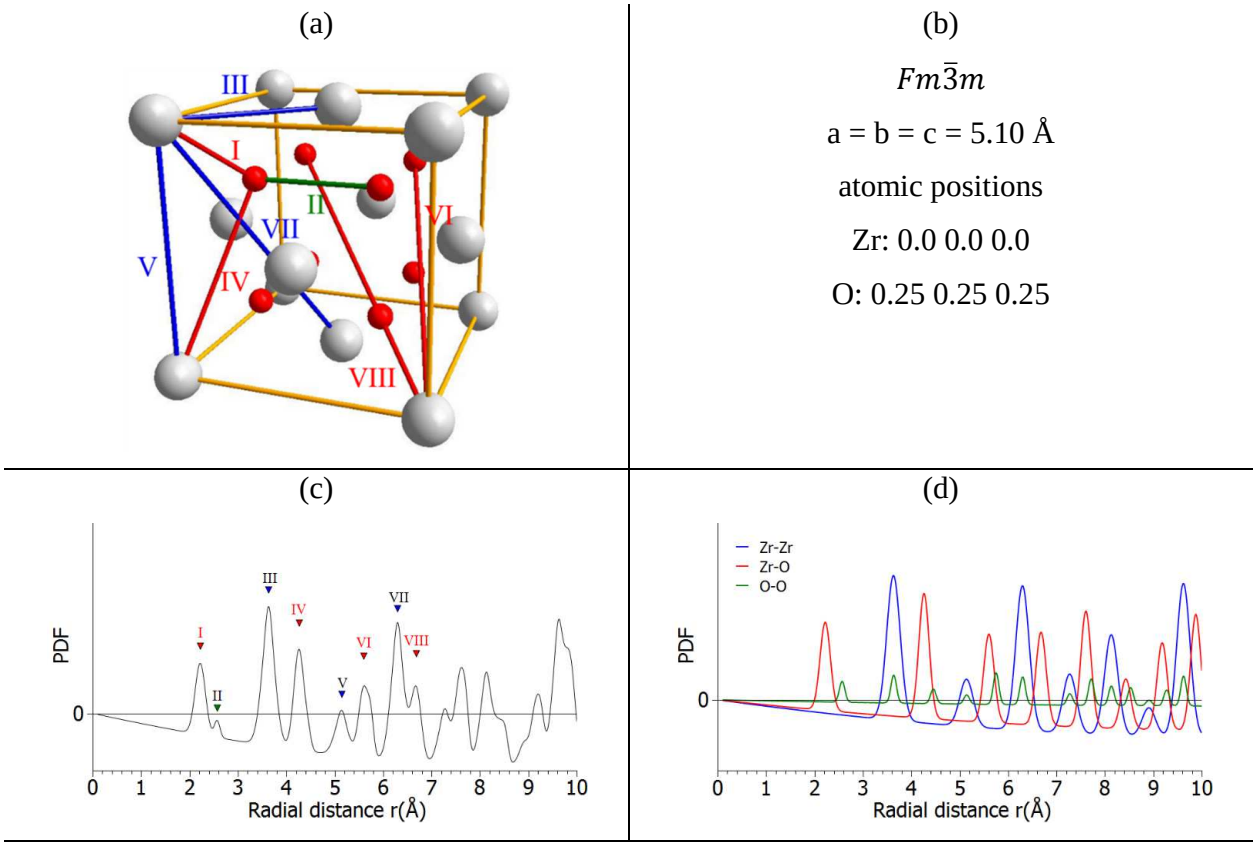

Figure 89: Structural model of the cubic zirconia polymorph: (a) balls representation, (b) structural parameters [89], calculated total (c) and partials (d) PDF.

4.1.2 Tetragonal phase zirconia

The tetragonal zirconia polymorph exists at temperatures between 1270°C and 2370°C [88]. It crystallizes with space group $P4_2/nmc$ (No. 137), which is less symmetrical in comparison with the cubic phase. It is also related to the fluorite structure in such a way that each zirconium cation is surrounded by 8 oxygen anions forming a distorted cube. The tetragonal phase PDF is plotted in Figure 2 (c-d). Again, we observed various peaks corresponding to Zr-O, Zr-Zr and O-O distances. The two first peaks at (I) 2.04 Å and (II) 2.43 Å corresponds to the Zr-O bonds. Comparing this to the cubic phase, the first Zr-O peak is split into two because of the slight shifts of the oxygen atoms along the c-axis. Similar effect is also observed for the peaks that corresponds to the higher Zr-O

distances which are observed at (IV) 3.98 Å,(V) 4.13 Å,(VI) and 4.59 Å (VII) at the medium-range region. The peak that corresponds to O-O distance at 2.6 Å is not easily observed due to low scattering contribution of oxygen atoms and the peak overlaps with the Zr-O (II) peak. The most intense peak which corresponds to the Zr-Zr distances is located around (III) 3.60 Å. In comparison with the cubic phase first Zr-Zr peak, its position is quite similar but it is actually composed of two almost superimposed Zr-Zr peaks (III-1, III-2). The splitting of the two Zr-Zr peaks is more subtle compared with the splitting of the Zr-O peaks (I and II). Other Zr-Zr peaks are also observed at higher distances around (VIII) 5.09 Å and (IX) 5.18 Å within the medium-range order domain.

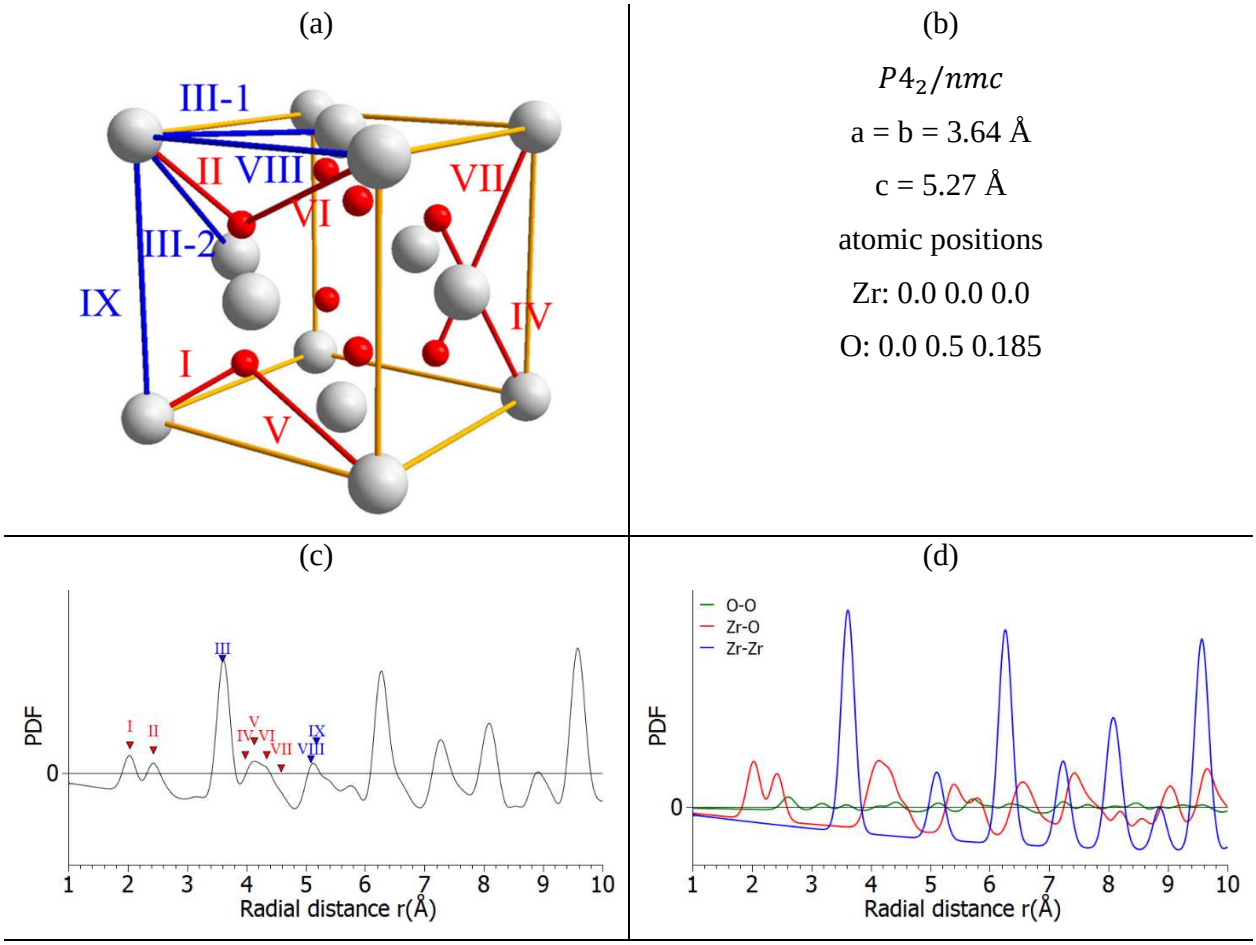

Figure 90: Structural model of the tetragonal phase zirconia (a) balls and stick representation, (b) parameter details of the phase [88], (c) PDF analysis of the phase and (d) interatomic distances of the model.

4.1.3 Monoclinic phase zirconia

The monoclinic phase or baddeleyite zirconia occurs naturally in ambient condition and typically exists at temperatures below 1270°C [87]. It is the least symmetrical in comparison to the other phases mentioned earlier and has space group $P2_1/c$ (No. 14). Its structure and parameters are shown in Figure 91 (a-b).

(a)

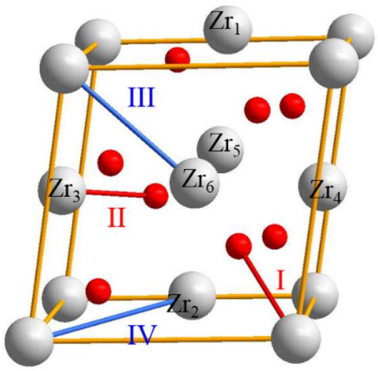

(b)

$P2_1/c$

a = 5.15 Å

b = 5.21 Å

c = 5.32 Å

β = 99.23°

atomic positions

Zr : 0.275 0.039 0.208

O_1 : 0.070 0.332 0.345

O_2 : 0.450 0.757 0.480

(c)

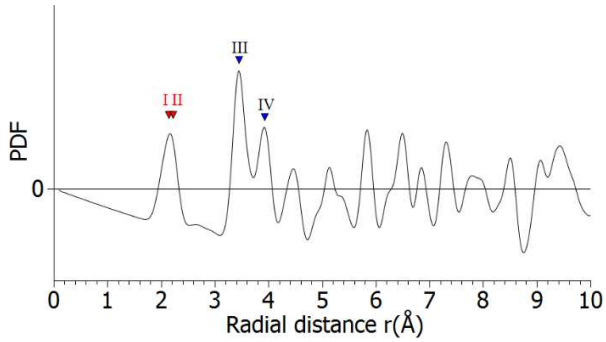

(d)

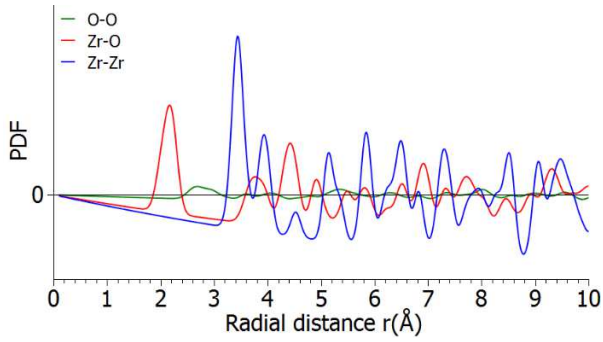

Figure 91: Structural model of the monoclinic phase zirconia (a) balls and stick representation, (b) parameter details of the phase [87], (c) PDF analysis of the phase and (d) interatomic distances of the model.

Comparing the coordination number of the monoclinic towards the previously mentioned polymorphs, each of its zirconium cation is arranged in such way that it is 7 fold coordinated with respect to the oxygen anions, which is one less than the other two polymorphs. This is brought about by the large shift of oxygen atoms that distorts the fluorite oxygen cube immensely and thus reduces the Zr coordination number. Hence, the single peak observed at about 2.16 Å actually

represents 7 Zr-O distances ranging between (I) 2.06 Å to (II) 2.27 Å. The peak that corresponds to the O-O distance is located around 2.54 Å and 2.97 Å and also corresponds to multiple O-O distances. The second and third intense peaks corresponds to Zr-Zr distances at (III) 3.44 Å and 3.93 Å (IV) respectively. These Zr-Zr peaks are quite different in comparison to the cubic and tetragonal phase which usually exists a single peak around 3.60 Å. Similarly, these two Zr-Zr peaks represent 6 Zr-Zr distances ranging from 3.33 Å to 3.93 Å.

4.1.4 Orthorhombic I phase zirconia

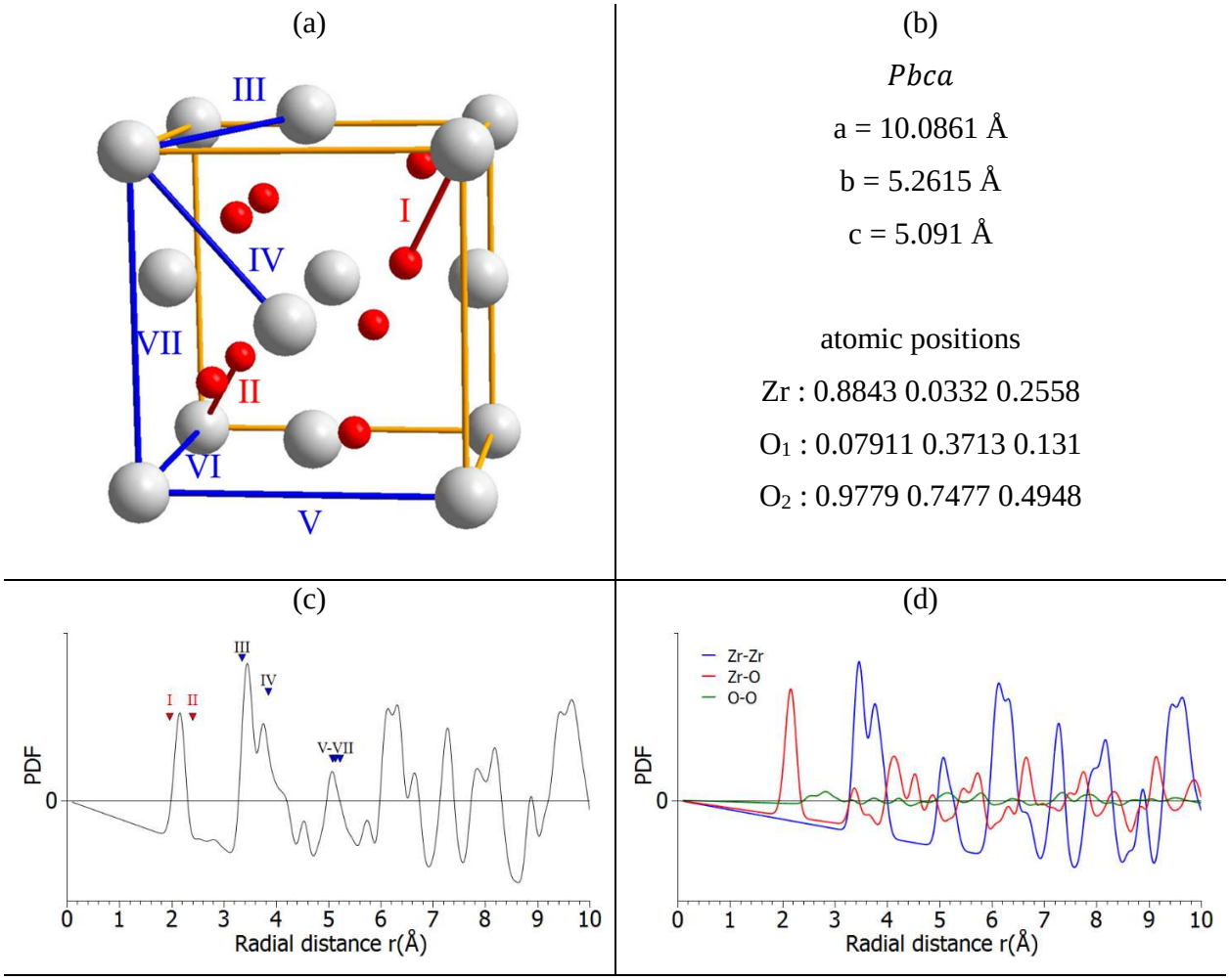

Figure 92: Structural model of the orthorhombic I phase zirconia (a) balls and stick representation, (b) parameter details of the phase [90], (c) PDF analysis of the phase and (d) interatomic distances of the model.

The last fluorite-derived zirconia polymorph is the orthorhombic I phase and typically exists at high atmospheric condition about 3 to 11 GPa [90] and crystallizes with space group $Pbca$ (No. 61). The orthorhombic-I phase PDF is plotted in Figure 92 (c-d). In comparison with the previously mentioned polymorphs, it is less symmetric against tetragonal but more symmetric in comparison with monoclinic. Similar to the monoclinic phase, it has a 7 fold coordinated zirconium cation with respect to the surrounding oxygen anions due to the large distortion of the ideal fluorite structure. Hence, the single peak observed at 2.16 Å actually represents 7 Zr-O distances with positions between (I) 2.06 Å to (II) 2.21 Å. The low lying broad peaks corresponds to the O-O distances which are located at 2.50 Å and 3.1 Å. The second and third peaks that correspond to the Zr-Zr are positioned at (III) 3.45 Å and 3.78 Å (IV), respectively. These Zr-Zr distances are also similar to the monoclinic phase by having two peaks but with the 2nd peak slightly shifted towards the left. These two Zr-Zr distances represent 7 Zr-Zr distances ranging from 3.45 Å to 3.78 Å. The single peak around 5.10 Å which is identified as Zr-Zr distance actually corresponds multiple Zr-Zr distances positioned closely at (V) 5.04 Å, (VI) 5.08 Å, and 5.26 (VII) Å.

4.2. Structural characterization of the sample prepared in alkaline benzyl alcohol

In the last parts of Chapter 3, we have selected the zirconia sample prepared in alkaline benzyl alcohol media with some interesting features such as having a single tetragonal phase, reasonable nanometer scale size (less than 5 nm) and appears to be free from organic or sodium carbonate impurities. Specifically, we have chosen the zirconia sample that was prepared in benzyl alcohol with 0.2 mol.L^{-1} NaOH and 0.3 mol.L^{-1} $Zr(O^iPr)_4(HO^iPr)$ at 210^{o}C for three days. We have decided to investigate further this sample to determine its structural properties which is essential in this work. We analyze the structural details of this sample by Rietveld refinement and by total scattering and pair distribution function analysis.

4.1.5 Rietveld refinement of sample prepared in benzyl alcohol with NaOH

The Rietveld analysis of the sample was done using the program FullProf and the refinement is shown in Figure 93. The peaks located at positions 2θ = 30^o, 35^o, 50^o, and 60^o appears to conform to the tetragonal or cubic phase of zirconia. Normally, the cubic and tetragonal phase zirconia can be differentiated by the presence of the low intensity 102 peak positioned at 2θ = 43^o, which appears with the tetragonal phase. Inspecting the diagram shows a negligible presence of this diffraction peak which suggests that the sample favors a cubic phase. However, the refinement using a cubic

phase zirconia gives a larger difference between the experimental result and calculated model ($\chi^2_{cubic} = 2.488$ and $\chi^2_{tetragonal} = 1.476$). In addition, the refinement done with a tetragonal phase gives a tetragonality ratio (R_t) $= \frac{c}{a\sqrt{2}} = 1.004$ consistent with a tetragonal distortion of the fluorite unit cell. Also, when we look at the internal tetragonality as indicated by the oxygen position (O_z) it gives a value of 0.193 which is closer to the tetragonal phase ($O_z = 0.185$) rather than that of the cubic phase ($O_z = 0.25$). Both metrical (R_t) and internal tetragonality (O_z) lean towards the tetragonal phase of zirconia. Note that the tetragonality is however less than that of the perfect tetragonal phase.

(a)

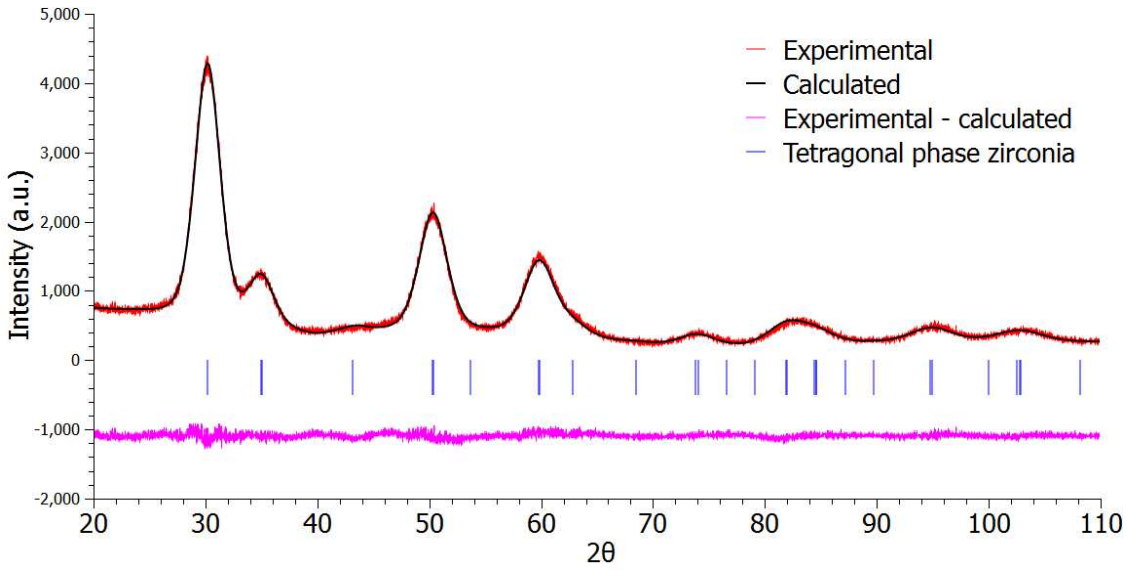

(b)

$\chi^2 = 1.476$	$O_z = 0.1929$	a = b = 3.617(3)Å
$\phi_{Ave.\ App.}$ = 3.003(6) nm		c = 5.136(6) Å
$Strain_{Ave.\ Max.}$ = 0.978(2)%		$R_{tetragonality} = R_t = \frac{c}{a\sqrt{2}} = 1.004$

Figure 93: (a) Rietveld refinement of the XRD diagram and (b) calculation details of the zirconia sample prepared in benzyl alcohol with 0.2 mol.L^{-1} NaOH and 0.3 mol.L^{-1} $Zr(O^iPr)_4(HO^iPr)$ at 210^{o}C for three days.

The refined average apparent size and average strain is around 3 nm and 0.98%, respectively. Based on the TEM image, the samples are dominated by spherical-like particles. With this knowledge, we can get the average crystallite diameter of the sample by using Wilson's formula for spherical

shaped objects [136]. Thus, for an average apparent size of 3.0 nm its equivalent crystallite diameter size is around 4 nm. Comparing to the TEM measurements of the average diameter, 3.2 nm (see Table 3), the XRD crystallite diameter appears to be 20% larger. This discrepancy suggests that the refined model used in Rietveld method may not be accurate which could be due to several factors such as the choice of structural model, microstructural model and background model. It is sensible to think that this is more of a mathematical problem rather than a physical problem since the calculation proceeds without physical discrimination among the background fitting, strain, and size contribution. In other words, it simply proceeds to give the best fitting it can obtain regardless of physical meaning.

4.1.6 Total scattering and PDF analysis of sample prepared in BnOH with NaOH

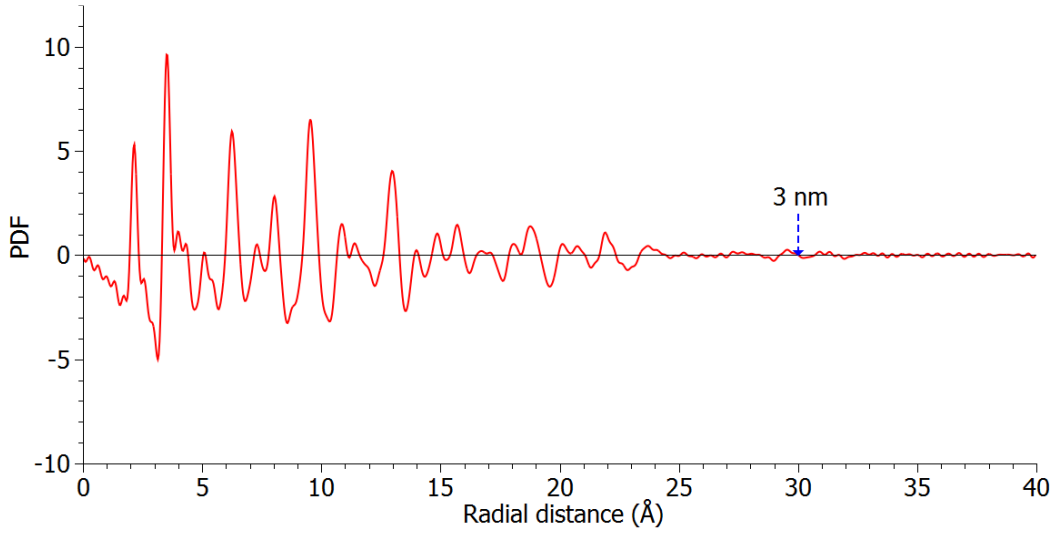

Figure 94: Experimental PDF of the zirconia particles produced at 210°C for three days in benzyl alcohol with 0.2 mol.L^{-1} NaOH.

Shown in Figure 94 is the experimental PDF of the sample. It is characterized by some intense peaks in the short-range order and a decrease of the peak intensities at higher distances, which is mainly due to the finite particle size and possibly structural distortion within the particles. The coherent domain size is measured to be about 3 nm and it is tabulated in Table 13.

Table 13: Average crystallite diameter measurements for zirconia particles produced at 210°C for three days in benzyl alcohol with 0.2 mol.L^{-1} NaOH

Method	Average Diameter
TEM	3.2 nm
XRD (refined)	4.0 nm
PDF	3.0 nm

We observe that both the TEM and PDF qualitative measurement for the crystallite size have similar values. The slight difference between the two measurements could be due to a small presence of structural distortion which would make the PDF appear shorter in comparison with TEM measurement but in this case it is certainly due to the uncertainty of qualitative measurement (estimated as at least 0.1 nm for the PDF measurement). We then proceed to analyze the initial peaks within the range of 1.5 to 5 Å.

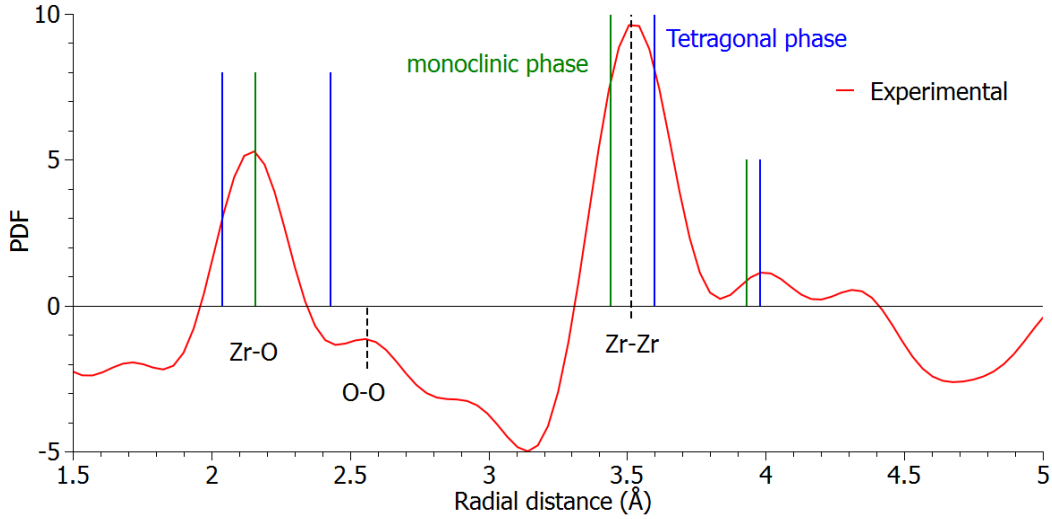

Figure 95: Experimental PDF of the zirconia particles produced at 210°C for three days in benzyl alcohol with 0.2 mol.L^{-1} NaOH compared with well crystallized zirconia tetragonal phase [88] and monoclinic phase [87].

The single peak positioned around 2.15 Å corresponds to the typical Zr-O bond length found in zirconia polymorphs. However, it differs from the tetragonal phase, since instead of a double peak we only have a single peak shown in Figure 95. The weakly intense peak next to the 1st Zr-O distance which is around 2.55 Å could conform to the O-O atomic distance. The 2nd intense peak positioned at 3.52 Å aligns to the typical Zr-Zr distances found in zirconia polymorphs. When we

compare with the Zr-Zr distances in the perfect monoclinic structure (3.44 Å) and tetragonal structure (3.6 Å), it appears to lie in the middle favoring neither phases clearly. The peaks located at 3.98 Å coincide with the peaks for the Zr-O bond lengths for the tetragonal phase but it is also relatively close to the Zr-Zr distance for monoclinic which is around 3.93Å. We then proceed by comparing the experimental PDF to the calculated PDF from the four polymorphs. The calculated PDF of polymorphs were done by using the PDFfit2 [170] program where the cell parameters were allowed to be refined. Two r-ranges were used, one favoring the medium-range region (5-25 Å) and the other favoring the short-range region (0-5Å). These comparisons are illustrated in Figure 96, Figure 97 and Figure 98 and the parameters are listed in Table 14, Table 15, Table 16, and Table 17.

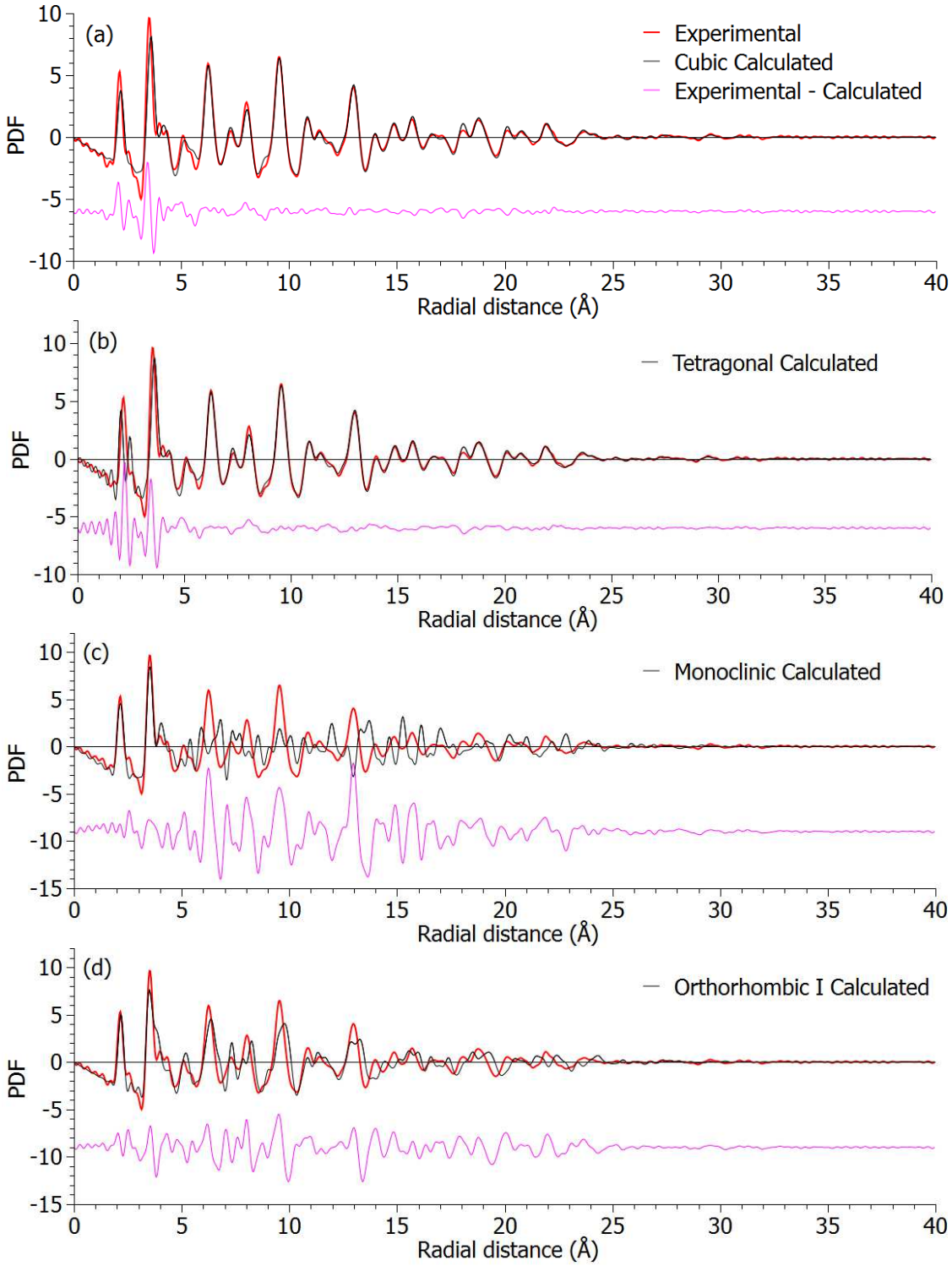

Figure 96: Experimental PDF of the zirconia particles produced at 210°C for 3 days in benzyl alcohol with 0.2 mol.L^{-1} NaOH with the (a) cubic model, (b) tetragonal model, (c) monoclinic model, and (d) orthorhombic I model of zirconia.

Table 14: Refined PDF parameters for sample in benzyl alcohol with NaOH using cubic model

parameters	**Reference** [89]	**Refined cubic**
Range (Å)	NA	5-25
R_w	NA	0.146
a(Å)	5.10	5.11

Table 15: Refined PDF parameters for sample in benzyl alcohol with NaOH using tetragonal model

parameters	**Reference** [88]	**Refined tetragonal**
Range (Å)	NA	5-25
R_w	NA	0.142
a(Å)	3.64	3.60
c(Å)	5.27	5.13
$R_t = \frac{c}{a\sqrt{2}}$	1.023	1.008

Table 16: Refined PDF parameters for sample in benzyl alcohol with NaOH using monoclinic model (*fixed)

parameters	**Reference** [87]	**Refined monoclinic**
Range (Å)	NA	0-5
R_w	NA	0.293
a(Å)	5.15	5.06
b(Å)	5.21	5.39
c(Å)	5.32	5.36
β(°)	99.23	99.23*

Table 17: Refined PDF parameters for sample in benzyl alcohol with NaOH using ortho-I model

parameters	**Reference** [90]	**Refined Ortho-I**
Range (Å)	NA	0-5
R_w	NA	0.332
a(Å)	10.0861	10.084
b(Å)	5.2615	5.2579
c(Å)	5.0910	5.2565

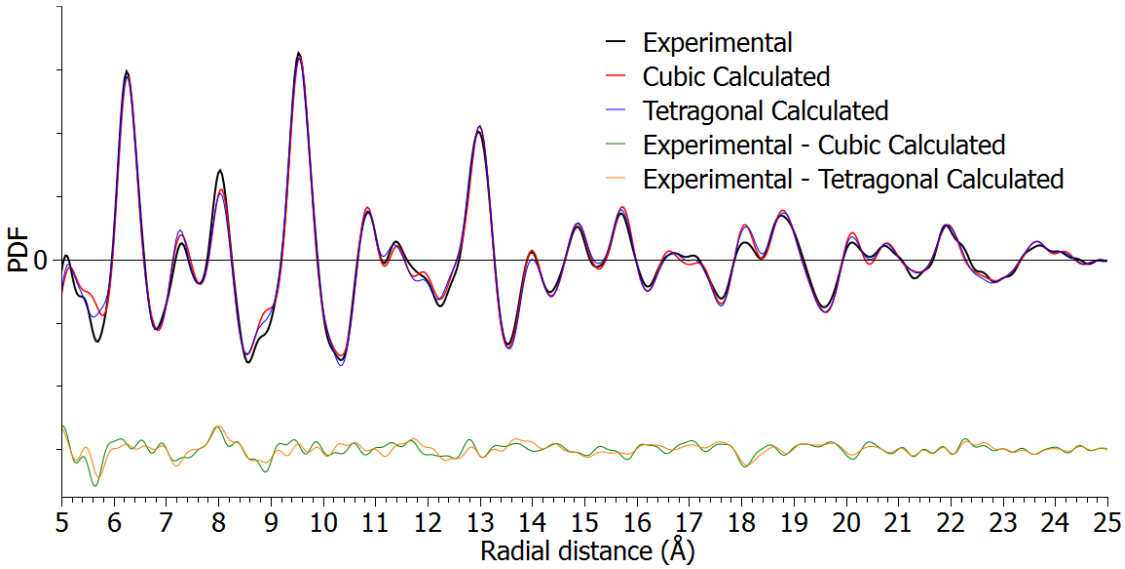

Figure 97: Experimental PDF of the zirconia particles produced at 210°C for three days in benzyl alcohol with 0.2 mol.L^{-1} NaOH compared with a refined tetragonal and cubic models within the range of 5 to 25 Å.

The cubic and tetragonal models appear to agree well with the experimental PDF in the medium-range order and "long-range order" regions as shown in Figure 96 (a & b). If we examine in detail the PDF within the range of 5-25 Å, we observe that the tetragonal and cubic models are quite similar but the former gives a slightly smaller difference between the experimental and calculated PDF as indicated by their R_w values (see Table 14, Table 15 and Figure 97). The tetragonal parameters a and c are slightly smaller compared to the reference standard, but nonetheless they are within reasonable difference and the R_t is consistent with a tetragonal distortion of the fluorite unit cell.

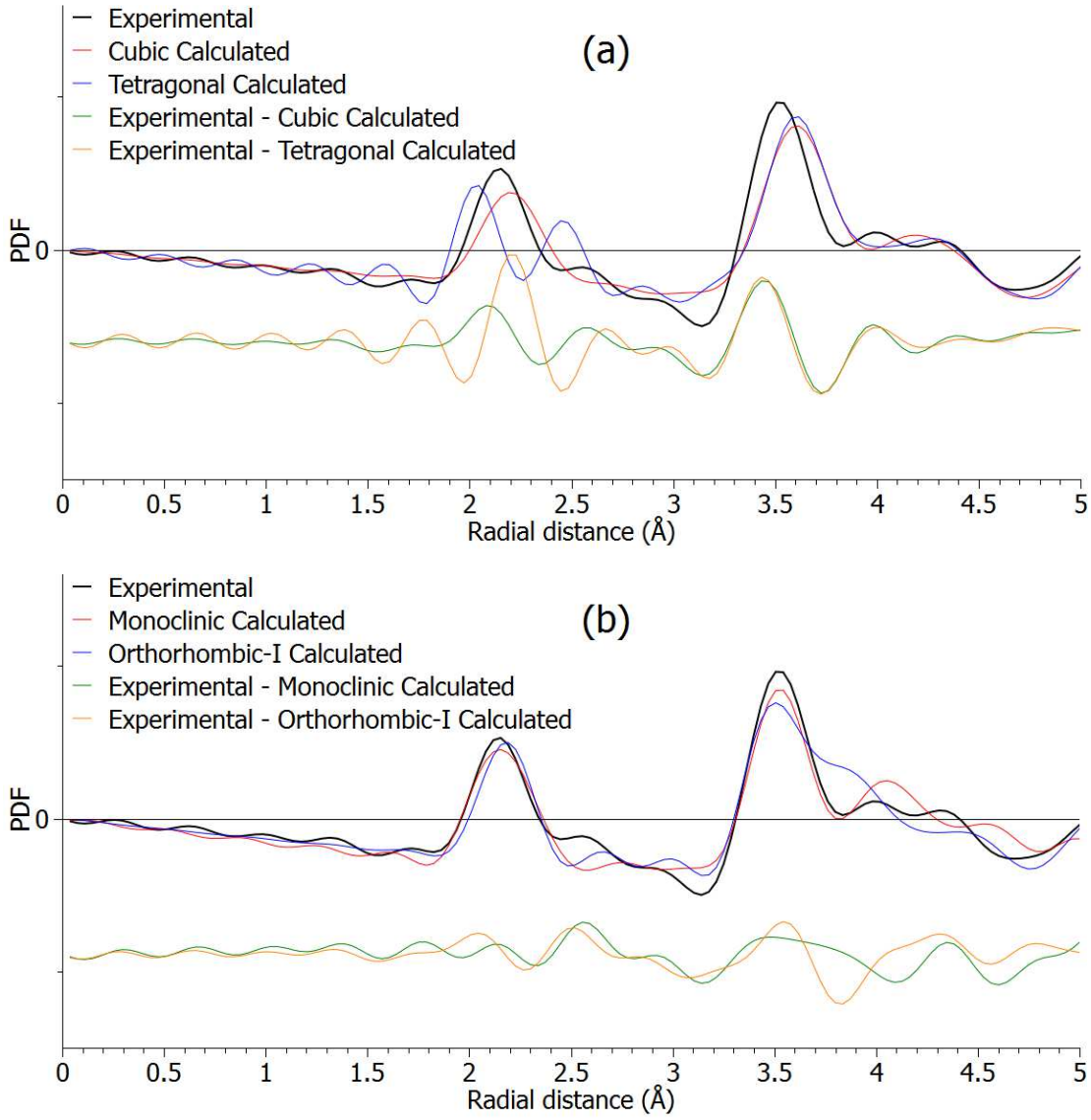

Figure 98: Experimental PDF of the zirconia particles produced at 210°C for three days in benzyl alcohol with 0.2 mol.L^{-1} NaOH compared with a refined (a) cubic and tetragonal and (b) monoclinic and orthorhombic I models within the range of 0 to 5 Å.

Regarding the short-range region, we observe that the peaks positioned at 2.15 Å and 3.52 Å does not conform to the cubic or tetragonal models but aligns better with the monoclinic and orthorhombic models as shown in Figure 96 (c & d). If we look closer, the monoclinic model seems to fit better as indicated by its lower R_w values (see Table 16, Table 17 and Figure 98 (a & b)). The lattice parameters of the refined monoclinic model are slightly altered such that a is smaller and both b and c are bigger in comparison with the reference values of the monoclinic phase.

It is tempting to say that the sample may be a mixture of tetragonal and monoclinic phase, but the absence of peaks in both the short-range and medium-range regions that would correspond to a mixture of phases suggests the opposite. Rather, it implies that the sample presents a structure with a medium-range order similar to the tetragonal phase and a local structure closer to the monoclinic phase. The tetragonal characteristics at the medium- and long-range order of the sample explain why its XRD patterns looks like that of a tetragonal phase. However, the actual structure is clearly neither tetragonal nor monoclinic. For convenience we will call this sample as tetragonal-like sample.

4.3. Structural characterization of the sample prepared in alkaline benzaldehyde

The next zirconia sample that we decided to study is the sample prepared in benzaldehyde. The sample has interesting features such as a single monoclinic phase, limited size (less than 5 nm) and appears to be free of impurities. Specifically, we analyze the sample prepared in benzaldehyde with 0.2 mol.L^{-1} NaOH and 0.3 mol.L^{-1} $Zr(O^iPr)_4(HO^iPr)$ at 210ºC for three days. Similarly, we look into the structural details of the sample by Rietveld refinement and by total scattering and PDF analysis.

4.1.7 Rietveld refinement of sample prepared in benzaldehyde with NaOH

The Rietveld refinement of the sample using a monoclinic structure model is shown in Figure 93. The model appears to show good correlation with the experimental diagram. The lattice parameters (see Table 16) also compare well with the monoclinic zirconia [87]. However, there are some minor discrepancies in the fitting particularly in the line broadening which does not completely envelop the experimental diagram as shown in Figure 100. This could suggest that there may be some size anisotropic effect as observed for other sample with monoclinic phase presented at later sections of this chapter. However, when we utilized an anisotropic size model for this sample there appears to have little improvement on the difference between the calculated and experimental diagrams. Thus, these small discrepancies have probably another origin.

(a)

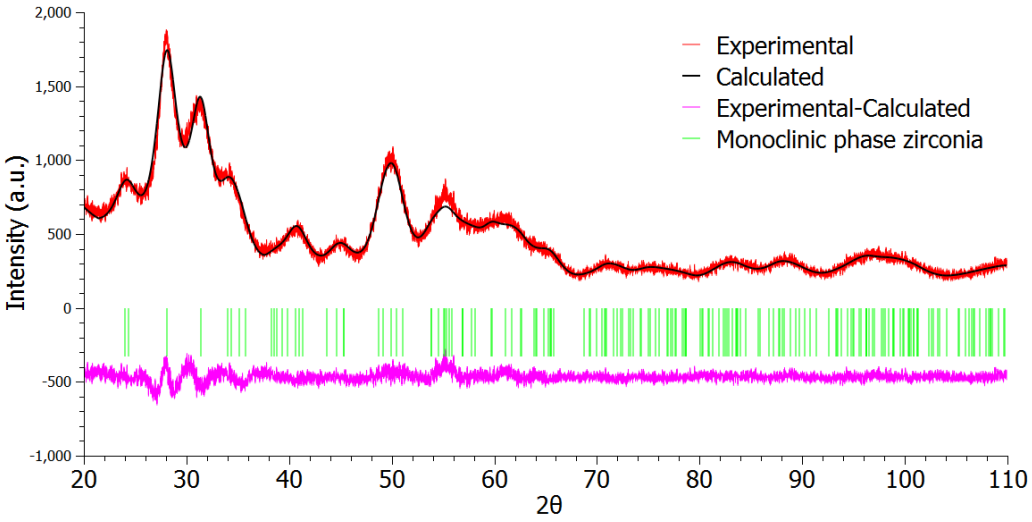

(b)

$\chi^2 = 1.589$	a = 5.168(3)Å
$\phi_{Ave.\ App.} = 2.755(1)$ nm	b = 5.214(3) Å
Strain = 0 or too small to calculate	c = 5.337(3)Å
	β = 99.20(3)°

Figure 99: (a) Rietveld refinement of the XRD diagram and (b) calculation details of the zirconia sample prepared in benzaldehyde with 0.2 mol.L^{-1} NaOH and 0.3 mol.L^{-1} Zr(O^{i}Pr)$_4$(HO^{i}Pr) at 210°C for three days.

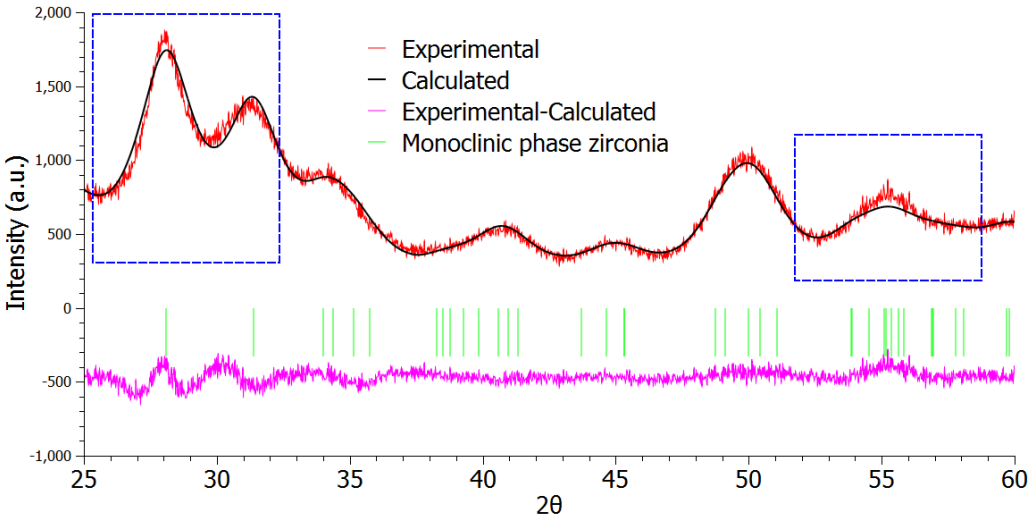

Figure 100: Rietveld refinement of the XRD diagram of the ZrO_2 sample examined at closer range.

The refined microstructural parameters indicate that the average apparent size of the sample is around 2.7 nm with zero average strain. If we assume that the particles have a spherical shape, then its average crystallite diameter size is about 3.7 nm, which is smaller (30%) compared to the tetragonal-like sample prepared in benzyl alcohol. Note that we were not able to successfully characterize the morphology of the sample via TEM due to complications brought about by the characteristics of the synthesized solution which was highly organic and very difficult to wash. Hence, we were not able to compare the diameter sizes between TEM and XRD.

4.1.8 Total scattering and PDF analysis of sample prepared in benzaldehyde with NaOH

As shown in Figure 101, the PDF is characterized by some intense peaks in the short-range region and less intense peaks in the medium-range region. Its coherent domain size is measured to be around 3.0 nm. We observe that the XRD's average crystallite diameter is 19% larger compared to the PDF measurement (see Table 18). This may be due to deficiencies of the XRD Rietveld refinement as explained earlier.

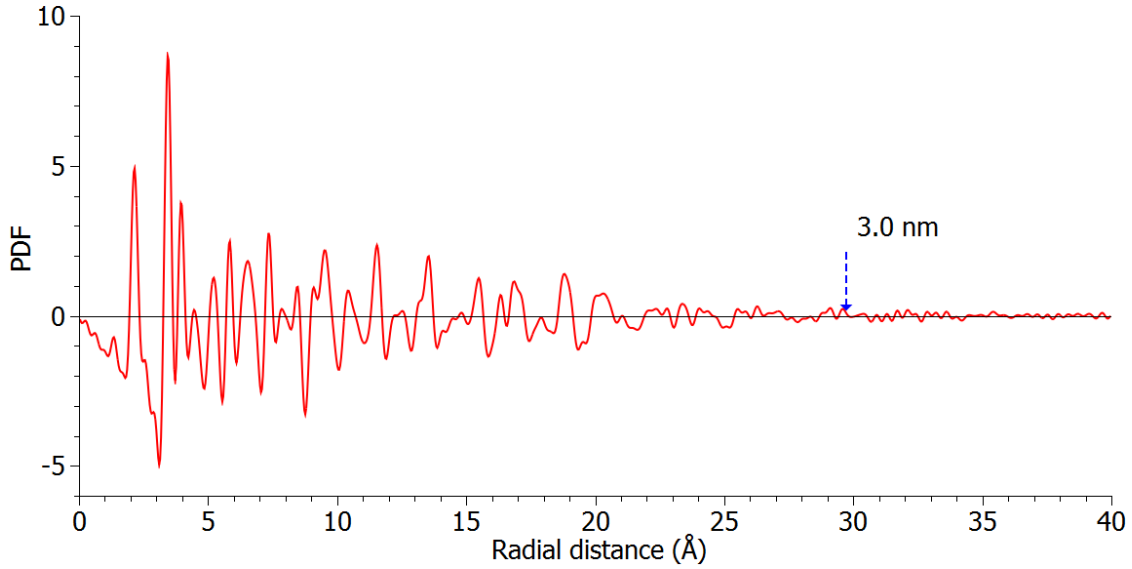

Figure 101: Experimental PDF of the zirconia particles produced at 210°C for three days in benzaldehyde with 0.2 mol.L^{-1} NaOH.

All the PDF peaks observed at 2.16 Å, 3.44 Å and 3.95 Å coincide with the monoclinic Zr-O, Zr-Zr (III) and Zr-Zr (IV) lengths, respectively (see Figure 102). We then proceed to compare the experimental PDF with the refined PDF from a monoclinic structural model. This is shown in Figure 103 (a & b).

Table 18: Average crystallite diameter measurements for ZrO_2 particles using benzaldehyde with NaOH

Method	Ave. Diameter
XRD (refined) PDF	3.7 nm 3.0 nm

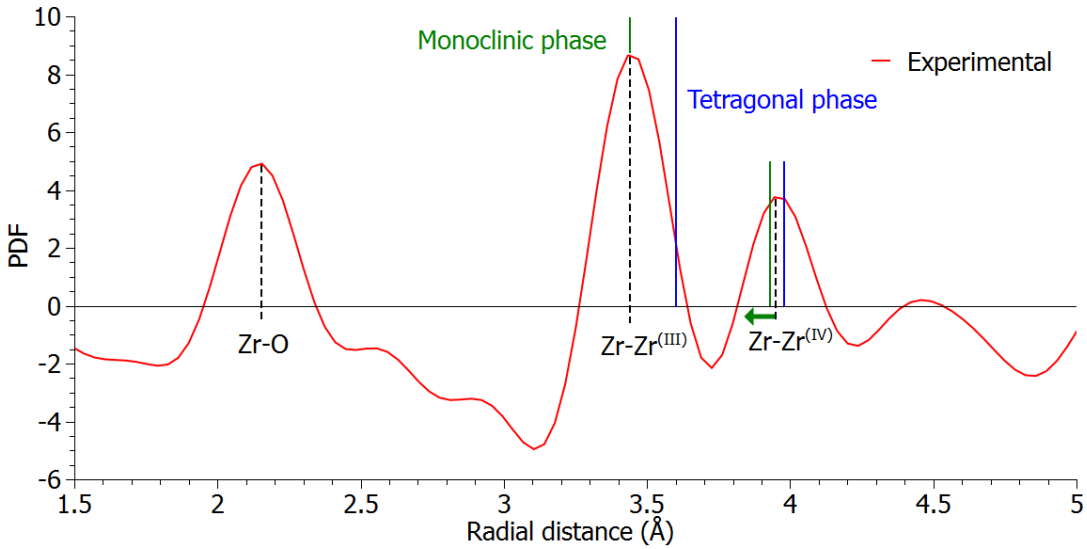

Figure 102: Experimental PDF of the zirconia particles produced at 210°C for three days in benzaldehyde with 0.2 mol.L^{-1} NaOH compared with well crystallized zirconia tetragonal phase [88] and monoclinic phase [87].

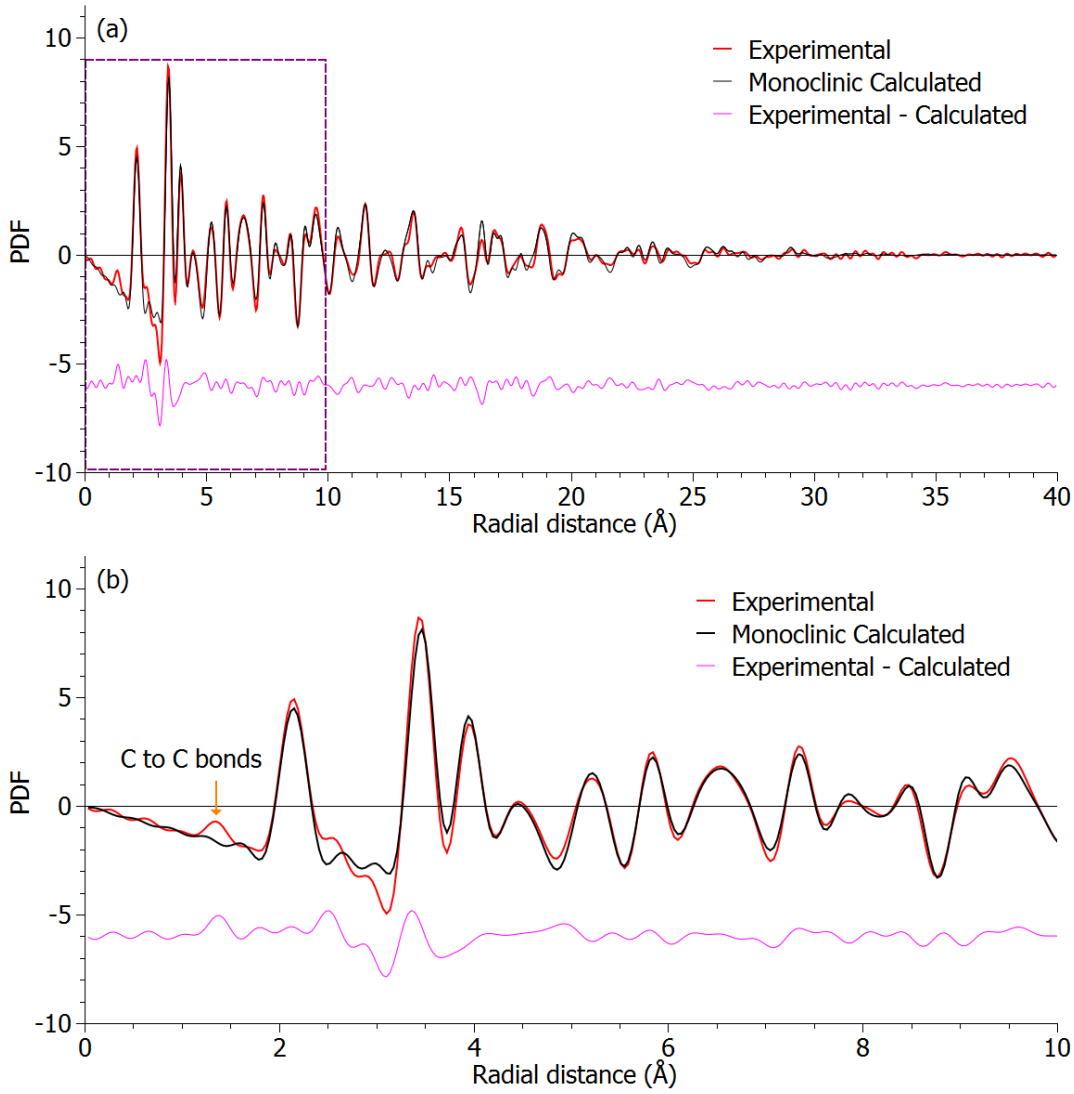

Figure 103: Experimental PDF of the zirconia particles produced at 210°C for three days in benzaldehyde with 0.2 mol.L^{-1} NaOH fitted with the monoclinic model zirconia viewed in (a) large scale and (b) local region.

Table 19: Refined parameters for the sample in benzaldehyde with NaOH using monoclinic model (* fixed)

Lattice parameters	**Reference** [87]	**Refined XRD (3.7 nm)**	**Refined PDF (3 nm)**
Range (Å)	NA	NA	0-40
R_w	NA	NA	0.231
a (Å)	5.15	5.17	5.14
b (Å)	5.21	5.21	5.19
c (Å)	5.32	5.34	5.32
β (°)	99.23	99.20	99.28

The refinement is good and the refined structural parameters listed in Table 19 conform well to the monoclinic structure. This result further supports the result obtained from Rietveld refinement. The lattice parameters are quite similar and within reasonable difference with respect to the reference values and the refined XRD values.

Note that we observe a small intensity peak around 1.34 Å which does not correspond to atomic pairs in zirconia but could correspond to C-C, C-O or O-O bonds (ranging from 1.20 to 1.54 Å) due to organic compounds impurities in our sample. These impurities are certainly due to ineffective washing process that failed to remove completely them from our sample. It is worth noting that the color of this sample is not the typical white feature but rather it is dark yellowish which is consistent with residual organic compound. However, the presence of the impurity does not affect the structural integrity of our sample since the peak corresponding to the impurity is limited only within the short-range region from 1.2 to 1.54 Å.

In summary, we can say that the sample is typical of the monoclinic polymorph with very small crystallite size. The implication of such small size for the monoclinic structure that is far below the critical size (10 nm) was discussed in Chapter 2.

4.4. Structural characterization of the samples prepared in alkaline anisole

In this section we again selected an interesting sample with very broad peaks whose sizes are estimated to be less than 2 nm. We call this sample the ultrasmall zirconia due to its inherent small size. The synthesis specifications of the ultrasmall zirconia is that it was prepared in anisole with 0.2 mol.L^{-1} NaOH and 0.3 mol.L^{-1} $Zr(O^iPr)_4(HO^iPr)$ at 210°C for three days. As usual we analyzed the structure of the sample via Rietveld refinement and by total scattering and pair distribution function analysis.

4.1.9 Rietveld refinement of sample prepared in anisole with NaOH

So far, we have analyzed two kinds of samples having a tetragonal-like structure (prepared in benzyl alcohol) and monoclinic structure (prepared in benzaldehyde). Here, we characterized using the Rietveld method the XRD pattern of the ultrasmall particles using the four fluorite-derived zirconia polymorphs as shown in Figure 104. The pattern lacks any distinguishable features to attribute to one particular polymorph. All models give a reasonable difference between the experimental and calculated diagrams, which makes it difficult to determine what type of zirconia phase is the sample. For this particular sample, the modelling of the line profile was mainly done with Gaussian shape parameters for the size and strain. No Lorentzian contribution was found to cause significant improvement.

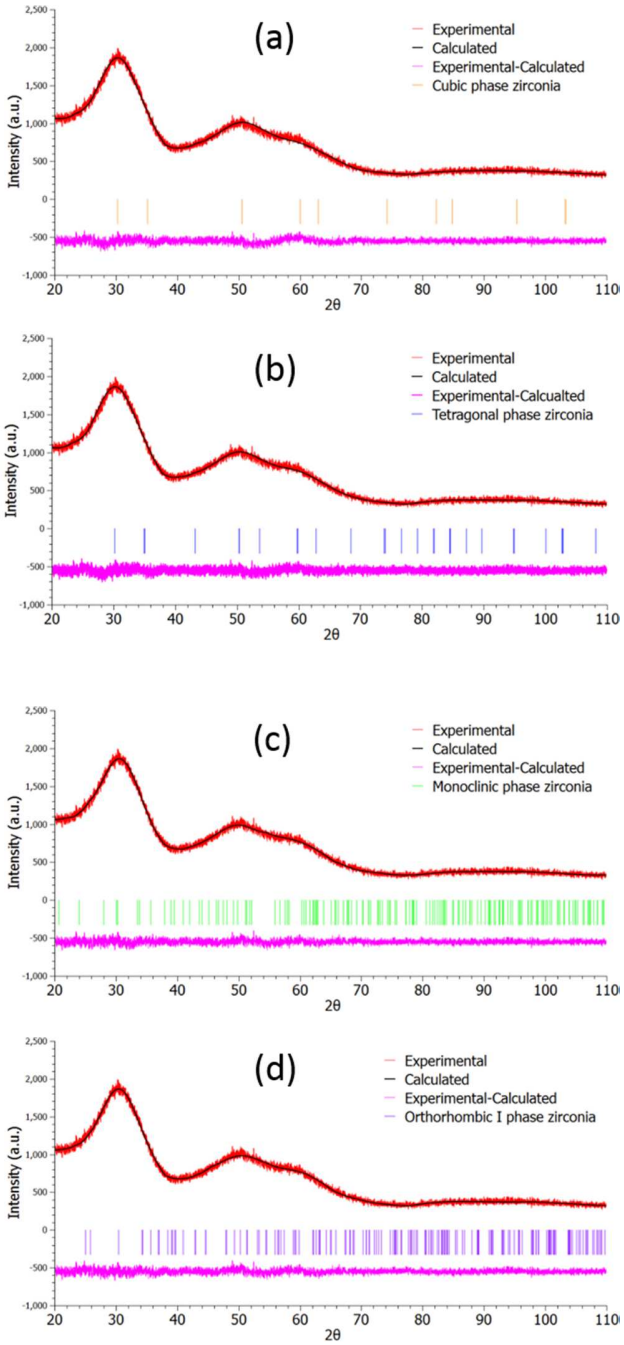

χ^2 = 1.151
a = 5.104*Å
$\phi_{Ave.\ App.}$ = 1.290(3)nm
$Strain_{Ave.\ Max.}$ = 8.17(1)%

χ^2 = 1.092
O_z = 0.195*
a = b = 3.619* Å
c = 5.126*Å
$R_{tetragonality=\frac{c}{a\sqrt{2}}}$=1.001
$\phi_{Ave.\ App.}$ = 1.238(3)nm
$Strain_{Ave.\ Max.}$ =7.09(1) %

χ^2 = 1.050
a = 4.35(1) Å
b = 4.73(1)Å
c = 6.02(2)Å
β = 99.1(2)°
$\phi_{Ave.\ App.}$ = 1.416(9) nm
$Strain_{Ave.\ Max.}$ = 2.760(6)%

χ^2 = 1.087
a =9.70(6)Å
b =5.2(2) Å
c = 5.2(2)Å
$\phi_{Ave.\ App.}$ = 1.418(6) nm
$Strain_{Ave.\ Max.}$ = 5.14(2)%

Figure 104: Experimental, calculated and difference plots for the XRD Rietveld refinement of the ultrasmall particles synthesized at 210°C for 3 days in anisole with 0.2 mol.L^{-1} NaOH using (a) cubic, (b) tetragonal, (c) monoclinic, and (d) orthorhombic I models. (* fixed parameter).

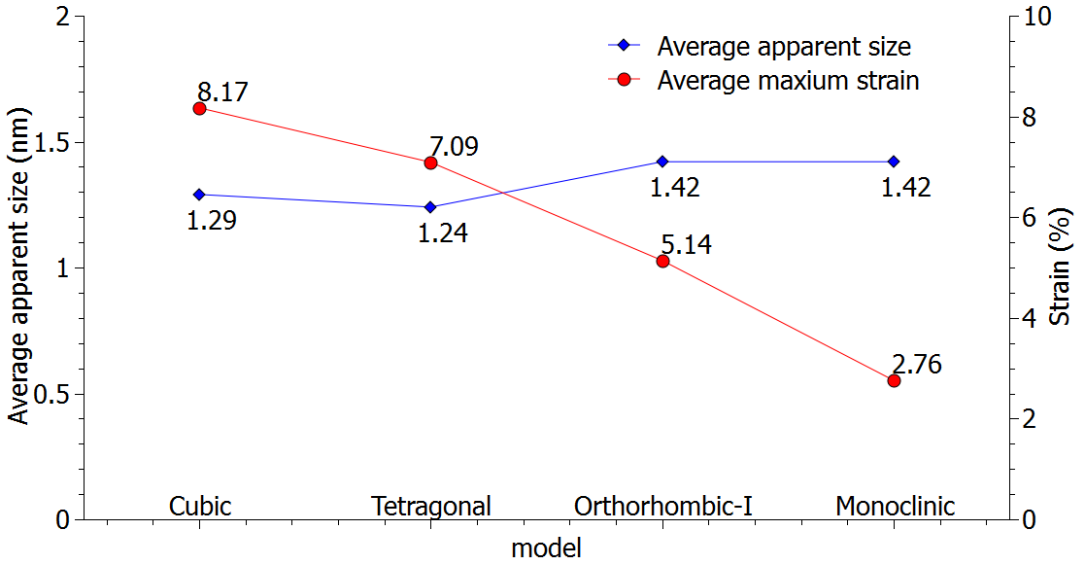

Figure 105: Strain and size calculation for the four polymorphs models of zirconia with a fluorite-derived structure.

We then compare, in Figure 105, the average apparent size and strain obtained with each model. We observe that as the model moves from the highest to lowest symmetry, (Cubic - Tetragonal - Orthorhombic-I - Monoclinic) the size becomes slightly larger and the strain clearly decreases. It is clear that Rietveld refinement of such highly broad sample gives an inconclusive result in determining what type of zirconia phase is present. Thus, we cannot utilize any of the refined values as the real ones. Instead, we determined their average apparent size which is about 1.34 nm and in turn gave an average crystallite diameter size of about 1.8 nm. The amount of microstrains varies from ~3% to 8% which is considered to be large and reflect that the particles have large structural distortions.

4.1.10 Total scattering and PDF analysis of sample prepared in anisole with NaOH

The experimental PDF in Figure 106 reveals that the sample have a very limited structural coherency as indicated by the very rapid signal damping. The estimated coherent domain size is of about 1.1 nm. Clearly, this coherent size is much smaller than the XRD and TEM (see Table 20) values, which suggests the presence of large structural distortions and agrees with the large strain values obtained from XRD analysis.

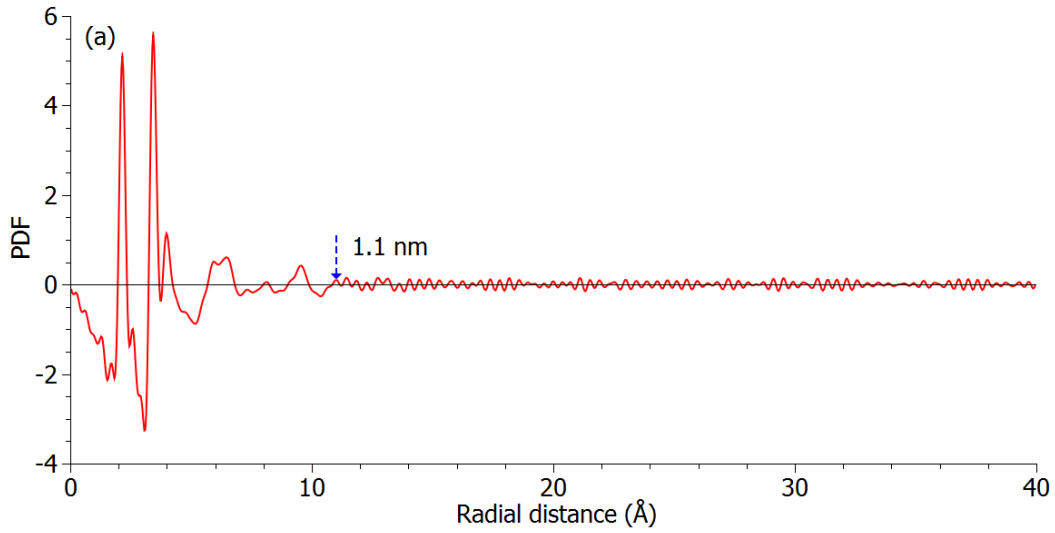

Figure 106: Experimental PDF of the zirconia particles produced at 210ºC for three days in anisole with 0.2 mol.L^{-1} NaOH.

Table 20: Average crystallite diameter measurements for samples produced in anisole with NaOH

Method	Average Size
TEM	2 nm
XRD (refined)	1.8 nm
PDF	1.1 nm

The low r-region of the experimental (see Figure 107) exhibits two intense peaks out of four peaks. The first peak positioned at 2.16 Å appears to conform to the typical Zr-O bond lengths but the absence of a second Zr-O peak suggests that it does not conform to the tetragonal phase.

The second peak observed at 2.59 Å, that appears less intense, is aligned with usual O-O distance. The third intense peak and fourth peak positioned 3.43 Å and 3.98 Å appears to favor the Zr-Zr (III) and Zr-Zr (IV) lengths, respectively. The Zr-Zr distances are quite similar with those of the sample prepared in benzaldehyde and 0.2 mol.L^{-1} NaOH having a monoclinic structure (Figure 102). These results suggests that the sample aligns more to the monoclinic phase in the short-range region. We now compare the experimental data with the four calculated PDF from the zirconia polymorphs shown in Figure 108 and the refined parameters are shown in Table 21, Table 22, Table 23, and Table 24.

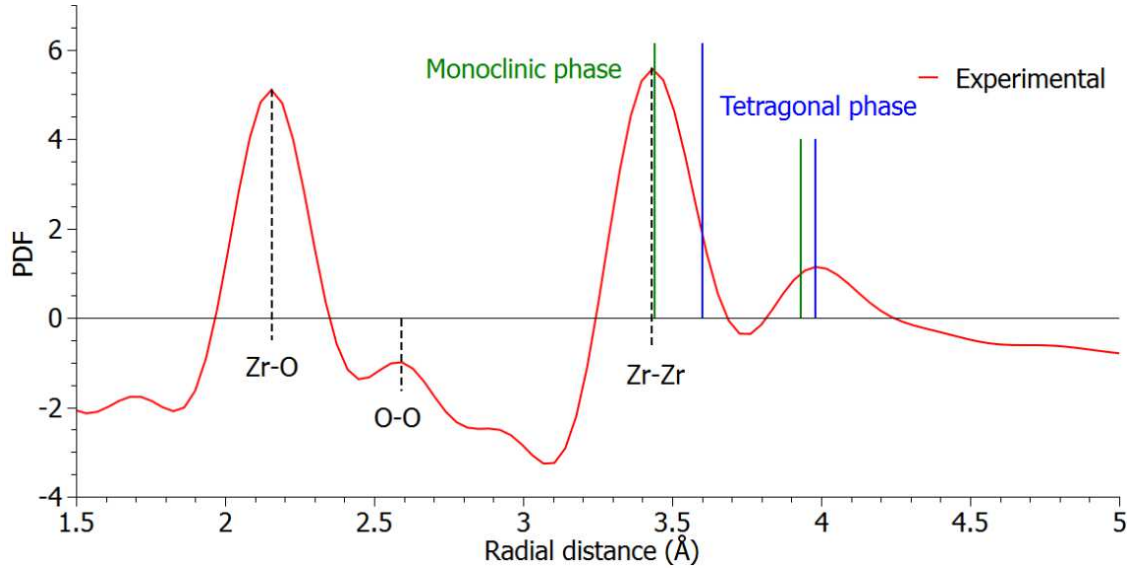

Figure 107: Experimental PDF of the zirconia particles produced at 210°C for three days in anisole with 0.2 mol.L^{-1} NaOH compared with well crystallized zirconia tetragonal phase [88] and monoclinic phase [87].

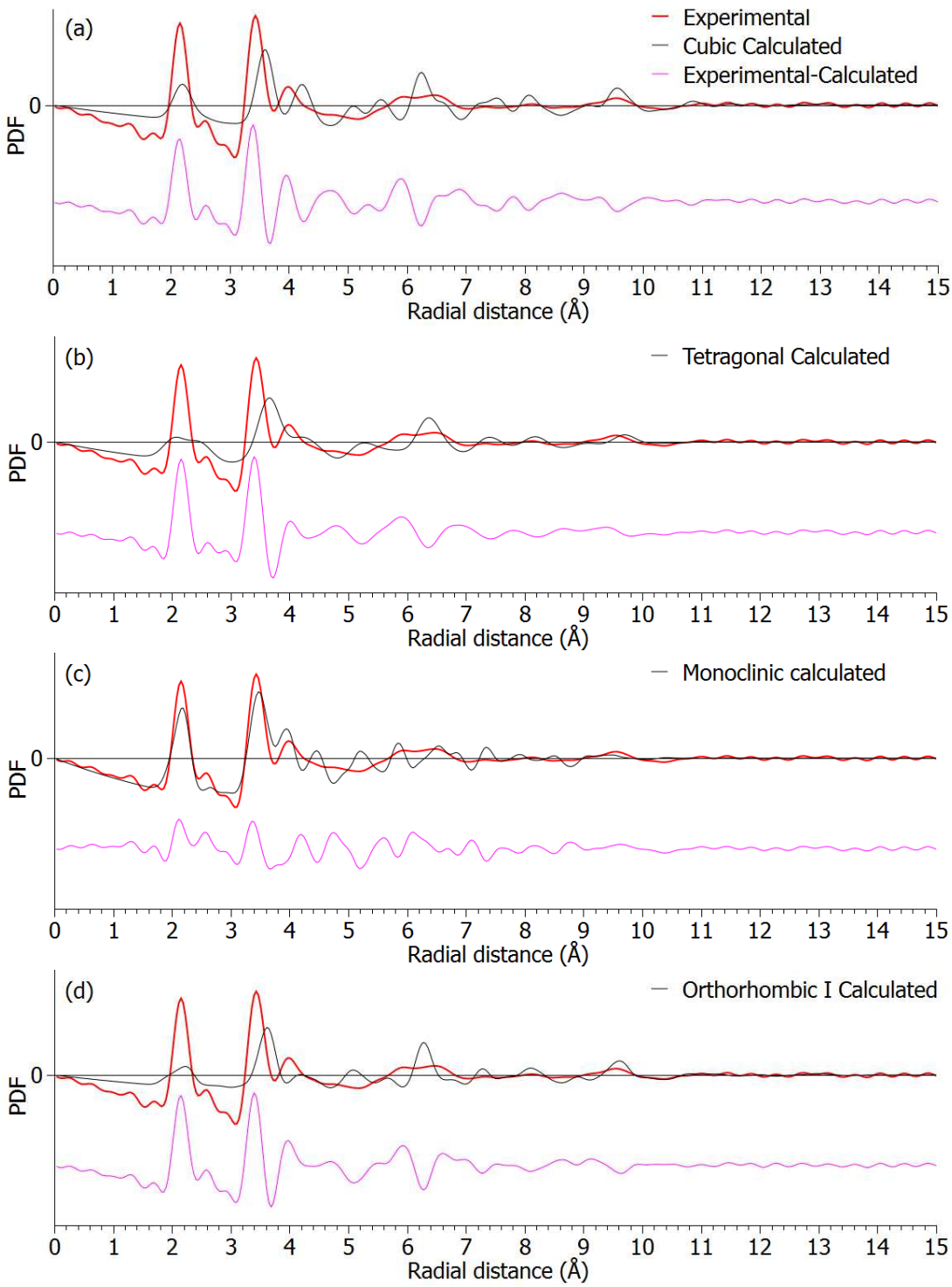

Figure 108: (a) Experimental PDF of the zirconia particles produced at 210°C for three days in anisole with 0.2 mol.L^{-1} NaOH compared with the unrefined (a) cubic model, (b) tetragonal model, (c) monoclinic model, and (d) orthorhombic I model of zirconia.

Table 21: Refined PDF parameters of sample in anisole with NaOH using cubic model

parameters	**Reference** [89]	**Refined cubic**
Range (Å)	NA	0-5
R_w	NA	0.278
a(Å)	5.10	4.92

Table 22: Refined PDF parameters for sample in anisole with NaOH using tetragonal model

parameters	**Reference** [88]	**Refined tetragonal**
Range (Å)	NA	0-5
R_w	NA	0.346
a(Å)	3.64	3.94
c(Å)	5.27	4.12
$R_t \frac{c}{a\sqrt{2}}$	1.023	0.74

Table 23: Refined PDF parameters for sample in anisole with NaOH using monoclinic model

parameters	**Reference** [87]	**Refined monoclinic**
Range (Å)	NA	0-5
R_w	NA	0.231
a(Å)	5.15	5.10
b(Å)	5.21	5.18
c(Å)	5.32	5.32
β(º)	99.23	99.41

Table 24: Refined PDF parameters for sample in anisole using with NaOH orthorhombic-I model

parameters	**Reference** [90]	**Refined Ortho-I**
Range (Å)	NA	0-5
R_w	NA	0.493
a(Å)	10.0861	9.8144
b(Å)	5.2615	4.9453
c(Å)	5.091	4.9327

The analysis reveals that the experimental PDF does not correspond perfectly to any of the PDF calculated from the four polymorphs. However it appears much closer to the monoclinic model in the short-range region. This is also reflected on the R_w values where the monoclinic model gives the smallest. The lattice parameters a, b, c, and β are also observed to be comparable to the reference monoclinic structure. If we focus on the medium range order, it appears that the experimental PDF exhibits much broader peaks, which mostly envelop the PDF peaks of the monoclinic model. This large broadening of the experimental PDF peaks both with the rapid damping of the PDF suggest that the particles lose structural coherency because of high atomic positional disorder. According to TEM observation (see Chapter 3), particles appears with resolved atomic planes thus they are not amorphous. Consequently, these ultrasmall particles seems to have a local monoclinic structure and a rapid loss of the medium-range order.

4.5. Structural characterization of the samples prepared in anisole

In the previous section, we have selected several samples prepared in alkaline media. Here, we present a zirconia sample prepared in anisole alone. Specifically, the synthesis specifications of this sample is that it was prepared in anisole and 0.3 mol.L^{-1} $Zr(O^iPr)_4(HO^iPr)$ at 210°C for three days.

4.1.11 XRD of the sample prepared in anisole

The XRD pattern of the sample is shown in Figure 109. There are three very broad peaks centered on 2θ = 30, 50 and 60°. The two peaks at higher position are so overlapped that it is quite difficult to distinguish one peak from the other. In comparison to the ultrasmall sample, the structural features are far less reliable to assign to any of the four polymorphs. Because of this, we did not proceed to perform Rietveld calculations on this sample but proceeded directly to characterize its interatomic distances using total scattering.

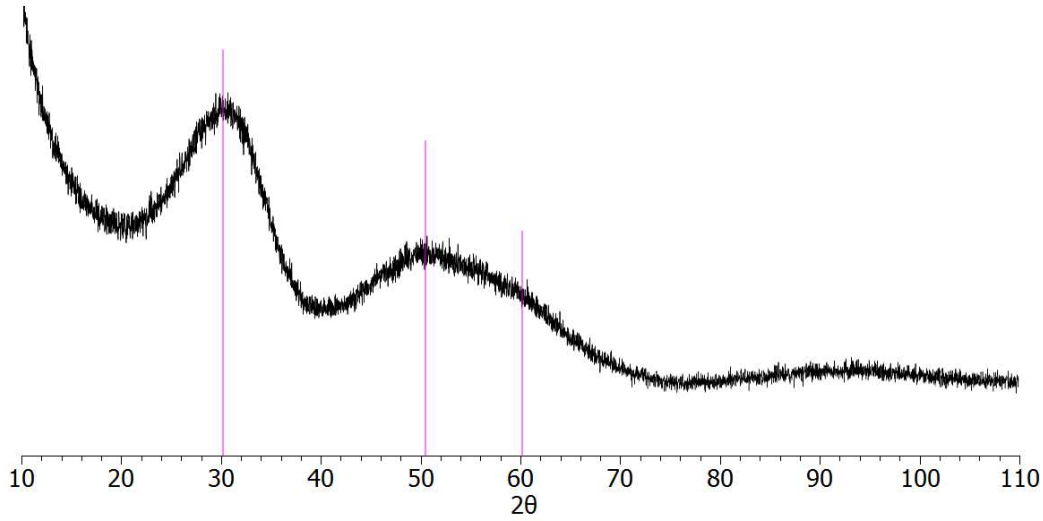

Figure 109: XRD diagram and (b) calculation details of the zirconia sample prepared in anisole and 0.3 mol.L^{-1} Zr(O^{i}Pr)$_4$(HO^{i}Pr) at 210°C for three days.

4.1.12 Total scattering and PDF analysis of sample prepared in anisole

The experimental PDF of the sample prepared in anisole is shown in Figure 110. It appears similar to that of the ultrasmall sample but with peaks in the medium-range region far more damped, which indicate a more rapid loss of structural coherency. Examining the size of the coherent domain of the sample, we estimate that the size is 0.8 nm.

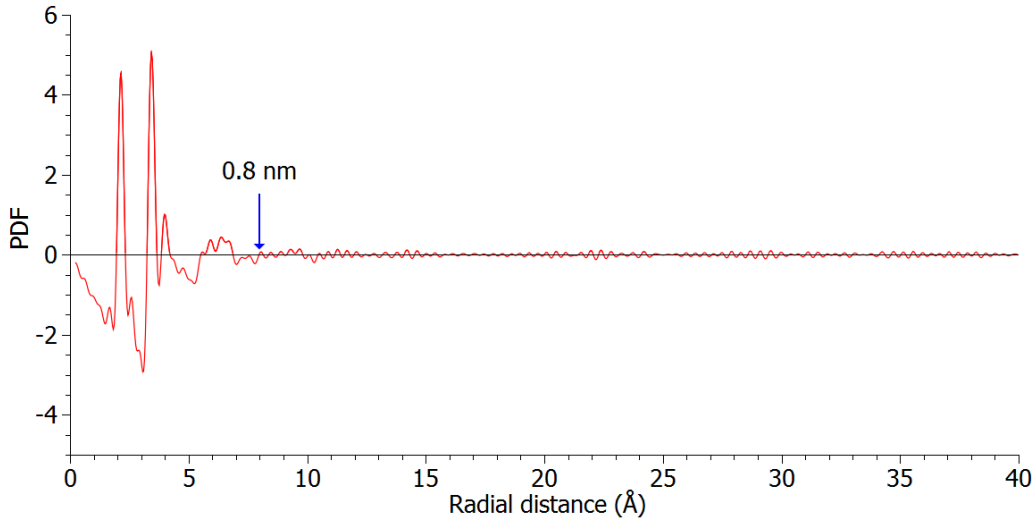

Figure 110: Experimental PDF of the zirconia particles produced at 210°C for three days in anisole.

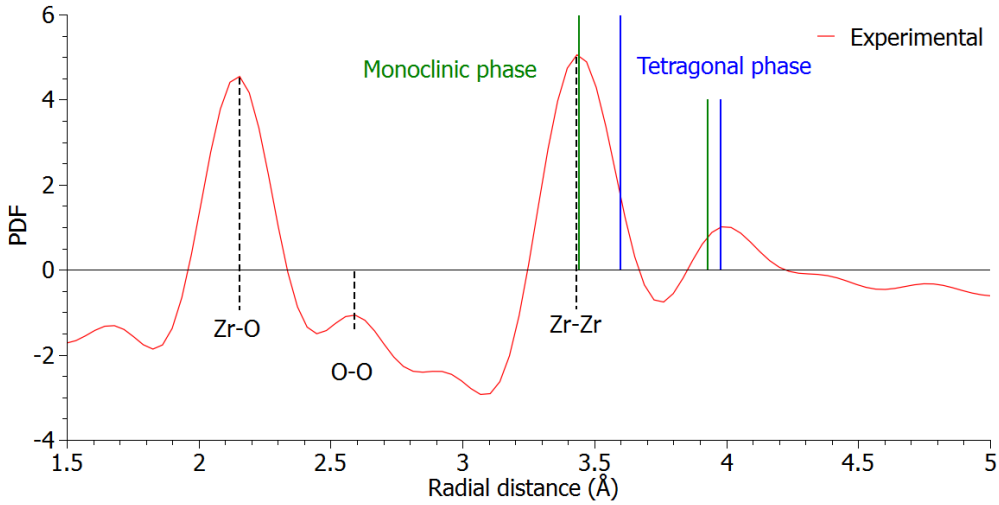

Figure 111: Experimental PDF of the zirconia particles produced at 210°C for three days in anisole compared with well crystallized zirconia tetragonal phase [88] and monoclinic phase [87].

We then examine the low r-region peaks (Figure 111). It is clear that these peaks are quite similar to the ultrasmall sample shown in Figure 107, suggesting that the sample aligns more with the monoclinic structure than with the tetragonal structure. We now then compare the experimental PDF with the calculated PDF using the monoclinic model shown in Figure 112 and Table 25. Note that there is no need to compare this sample with the other models because it is clearly more related to the monoclinic phase.

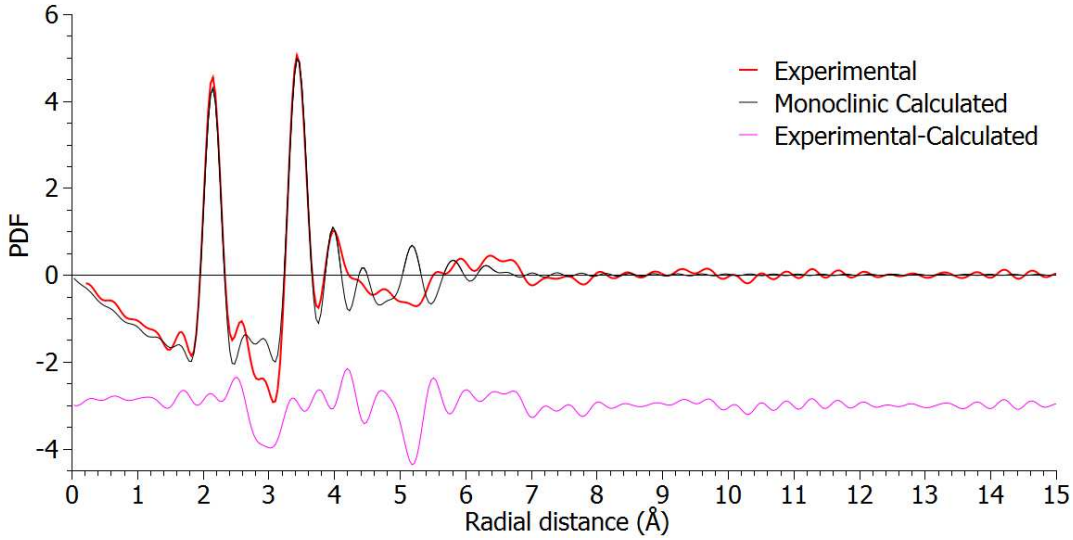

Figure 112: Experimental PDF of the zirconia particles produced at 210°C for three days in anisole with compared with the monoclinic model of zirconia.

Table 25: Refined PDF parameters for the sample in anisole without NaOH using monoclinic model

parameters	**Reference** [87]	**Refined monoclinic**
Range (Å)	NA	0-5
R_w	NA	0.205
a(Å)	5.15	5.11
b(Å)	5.21	5.20
c(Å)	5.32	5.31
β(°)	99.23	99.39

The lattice parameters a, b, c, and β are observed to be within reasonable difference with the reference and the ultrasmall sample see Table 25 and Table 23, respectively. It is clear that this sample is similar with the ultrasmall sample in the local region but with a much larger distortion in the medium-range region suggesting that the structural disorder is higher. Because of its unique structural characteristics, we will call this sample as amorphous-like zirconia.

4.6. Influence of solvothermal ageing and presence of water on the samples prepared in anisole with and without NaOH

In this section, we analyze how the how the ultra-small zirconia and the amorphous-like zirconia develop with ageing time. For this, we investigate the structure of the samples by varying the ageing period from 3 to 24 days (3, 6, 12 and 24 days) at 210°C.

In addition, we investigate the effects of the presence of *ex-situ* water in the reaction mixture on the structure of particles, which was shown (in Chapter 3) to have a large effect on the tetragonal to monoclinic transformation. The effect of water is analyzed for samples with and without sodium hydroxide. Specifically, the amount of *ex-situ* water was varied from 0 to 5% (0, 0.3, 2, 4, and 5% volume content).

4.1.13 Influence of varied solvothermal ageing time for the samples prepared in anisole with and without NaOH

The XRD diagrams of the samples prepared in anisole with and without NaOH with various solvothermal ageing time are given in Figure 113. For both type of samples, increasing the period of solvothermal ageing up to 24 days improved the crystallinity. For the sample with NaOH, the

evolution of the diagrams is progressive. This is not the case for the sample without NaOH, which retains its amorphous-like features after 6 days of ageing and seems to start crystallizing, slightly after 12 days and much more after 24 days. The broad experimental XRD peaks are mainly centered on those of the tetragonal or cubic polymorphs. Aside from these three peaks we can notice for the sample without NaOH small intensity bumps at $2\theta = 24.4^{o}$ and 28.1^{o} which corresponds more to those of monoclinic zirconia. In the following sections we look closer to the interatomic distances of the two types of samples.

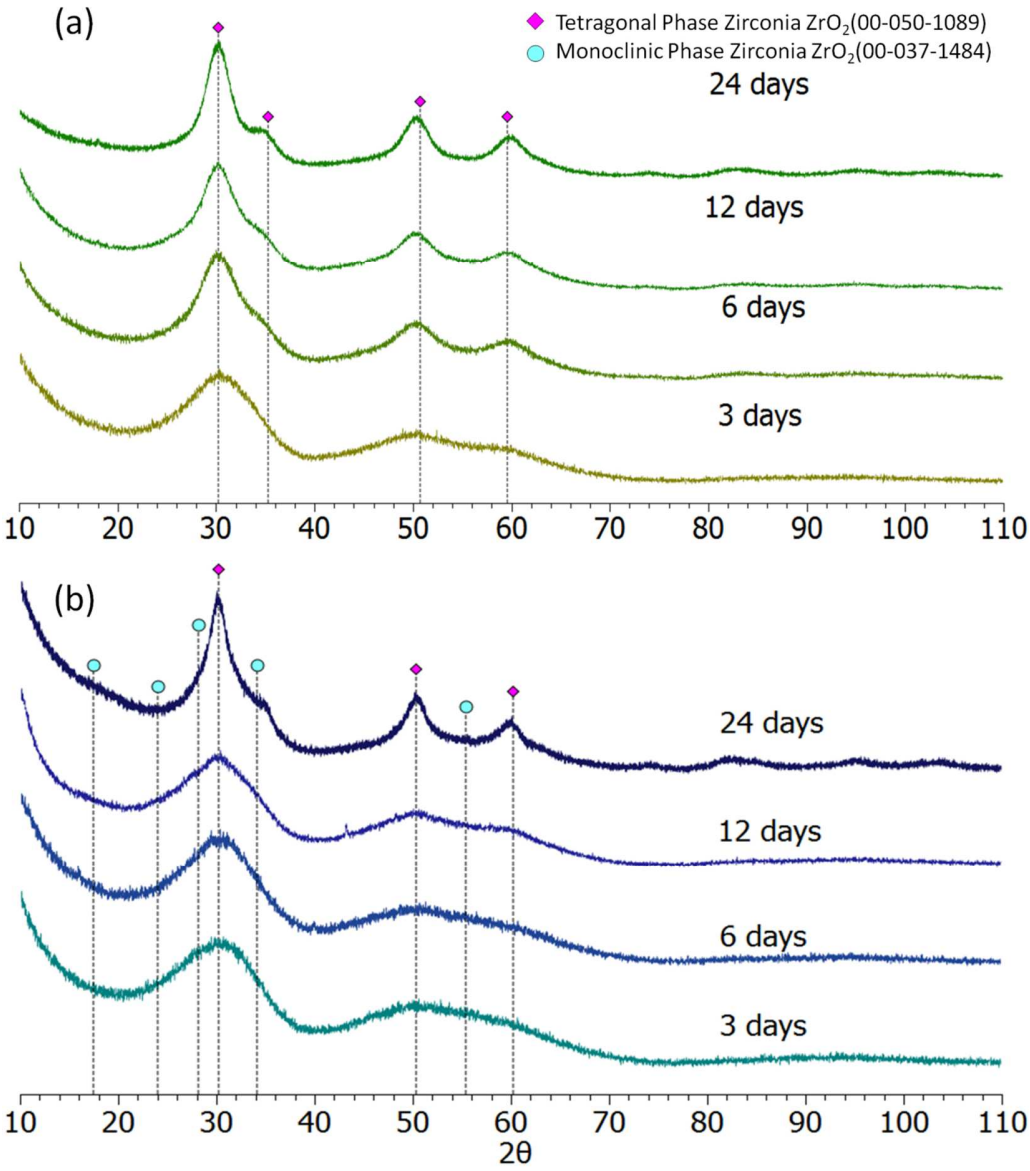

Figure 113: XRD patterns of the samples synthesized at 210°C with different of thermally assisted ageing times (a) with and (b) without 0.2 mol.L^{-1} NaOH.

4.1.13.1 Total scattering and PDF analysis of the selected samples under varied solvothermal ageing period with NaOH

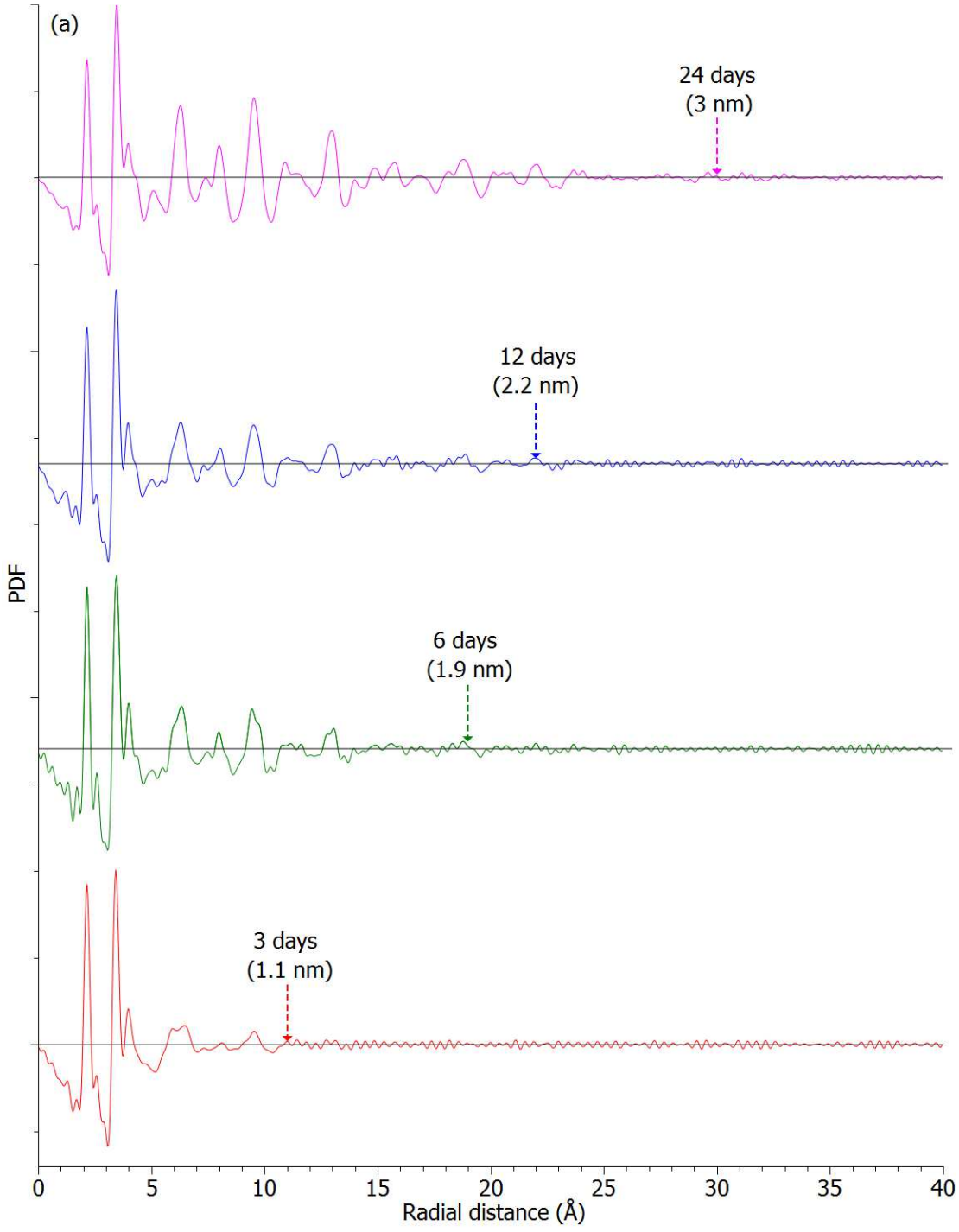

Figure 114: Experimental PDF of the zirconia particles prepared at 210°C in anisole with 0.2 mol.L^{-1} NaOH for varied solvothermal ageing period (3 days, 6 days, 12 days and 24 days).

Shown in Figure 114 are the experimental PDF of the samples prepared with varied ageing period (3 days, 6 days, 12 days, and 24 days) at 210°C in anisole with NaOH. We observe that the samples have varying structural characteristics. Measuring the coherent domain sizes, they appear to have increasing values with 1.1 nm for 3 days, 1.9 nm for 6 days, 2.2 nm for 12 days, and 3 nm for 24 days.

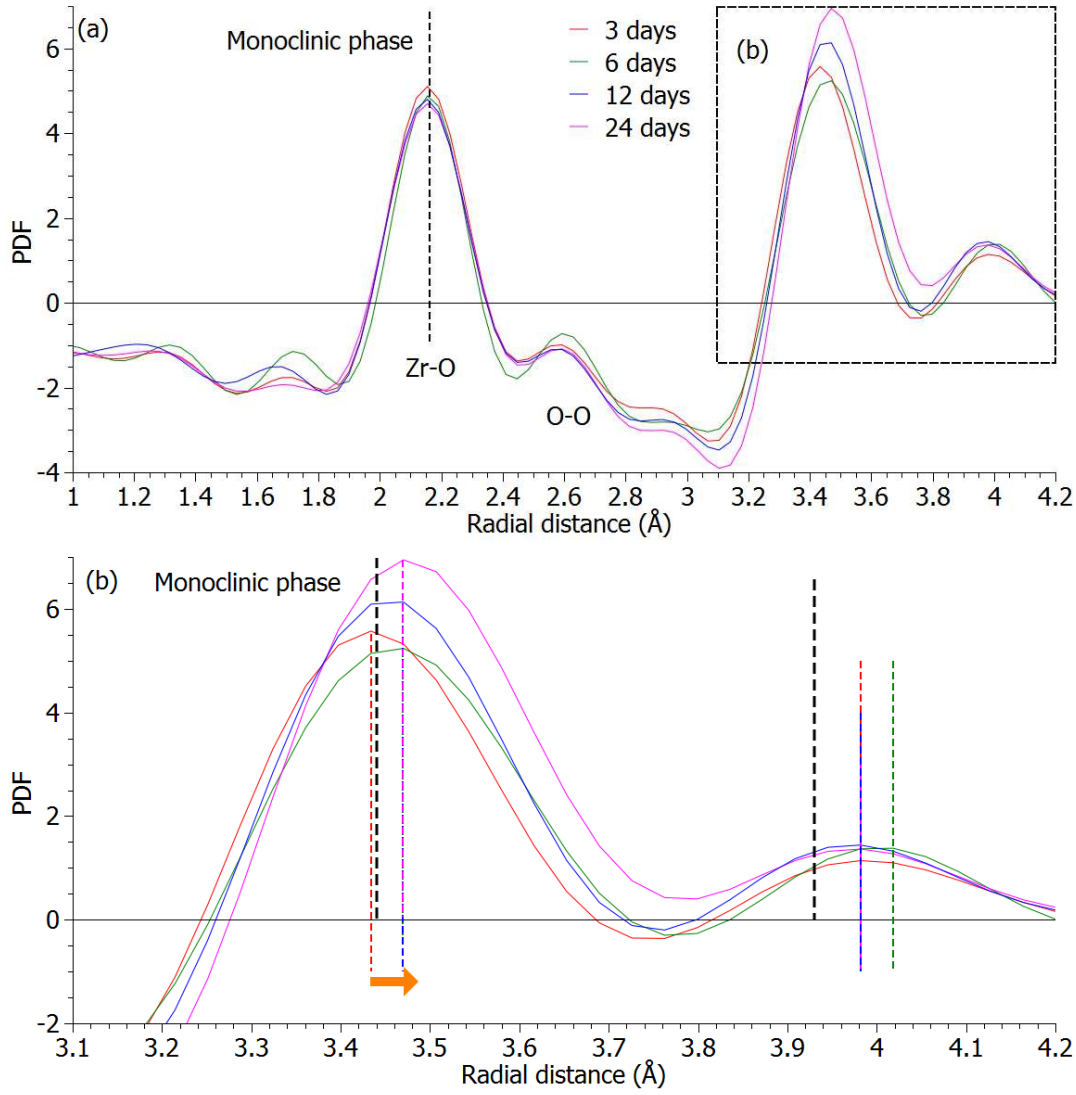

Figure 115: Experimental PDF of the zirconia particles for varied solvothermal ageing prepared at 210°C in anisole with 0.2 mol.L^{-1} NaOH compared with well crystallized zirconia monoclinic phase [87].

We then examine the peaks located in the short-range region from 1 to 4 Å as shown in Figure 115(a). For all the samples, the PDF appear to conform to that of a monoclinic phase. The first (Zr-

O bond length) and second peaks (O-O first distances) located about 2.15 Å and 2.6 Å do not change with ageing process. On the contrary, the third peak (Figure 115(b)) corresponding to Zr-Zr distances (3.6 Å) exhibits a shift towards the right for the samples aged 3, 6, 12 and 24 days. Recall that the fourth peak represents a superposition of various atomic distances for both tetragonal (Zr-O (IV) at 3.98 Å) and monoclinic (Zr-Zr (IV) at 3.93 Å) models. It seems that all the fourth peaks remains unchanged except for the 6 days which is slightly shifted towards the right. Within the selected medium-range region, (Figure 116), the peaks evolved from a less intense to well-defined peaks with increasing ageing time. As early as 6 days we observe some improvements of the peaks, which become more prominent after 12 days. The structural improvement is most observed when the ageing period is 24 days. For this sample, the experimental PDF compares well with the calculated from a tetragonal model (see Figure 117 and Figure 118 (a)). The refined lattice parameters using the tetragonal model within the 5 to 25 Å range (Table 26) appear to be slightly different with the reference but identical with the tetragonal-like sample (see Table 15). Thus, the structure of the samples evolves toward a tetragonal medium-range order with ageing time. The comparison of the PDFs with the monoclinic model in the 0-5 Å region (Figure 118 (b) and Table 27) confirms that local structure of the sample conforms to the monoclinic structure.

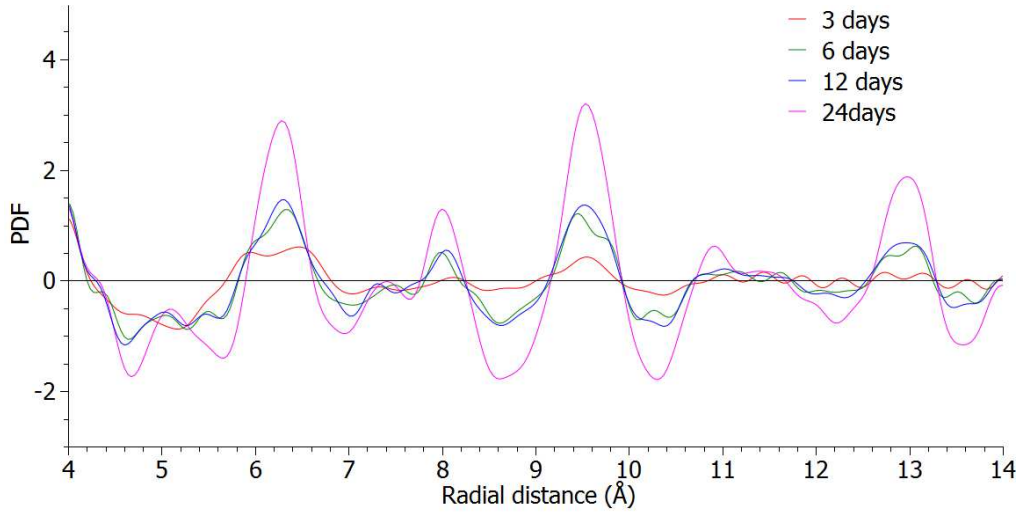

Figure 116: Experimental PDF for varied solvothermal ageing period samples prepared at 210°C in anisole with 0.2 mol.L^{-1} NaOH examining the structural improvements at the selected medium-range region.

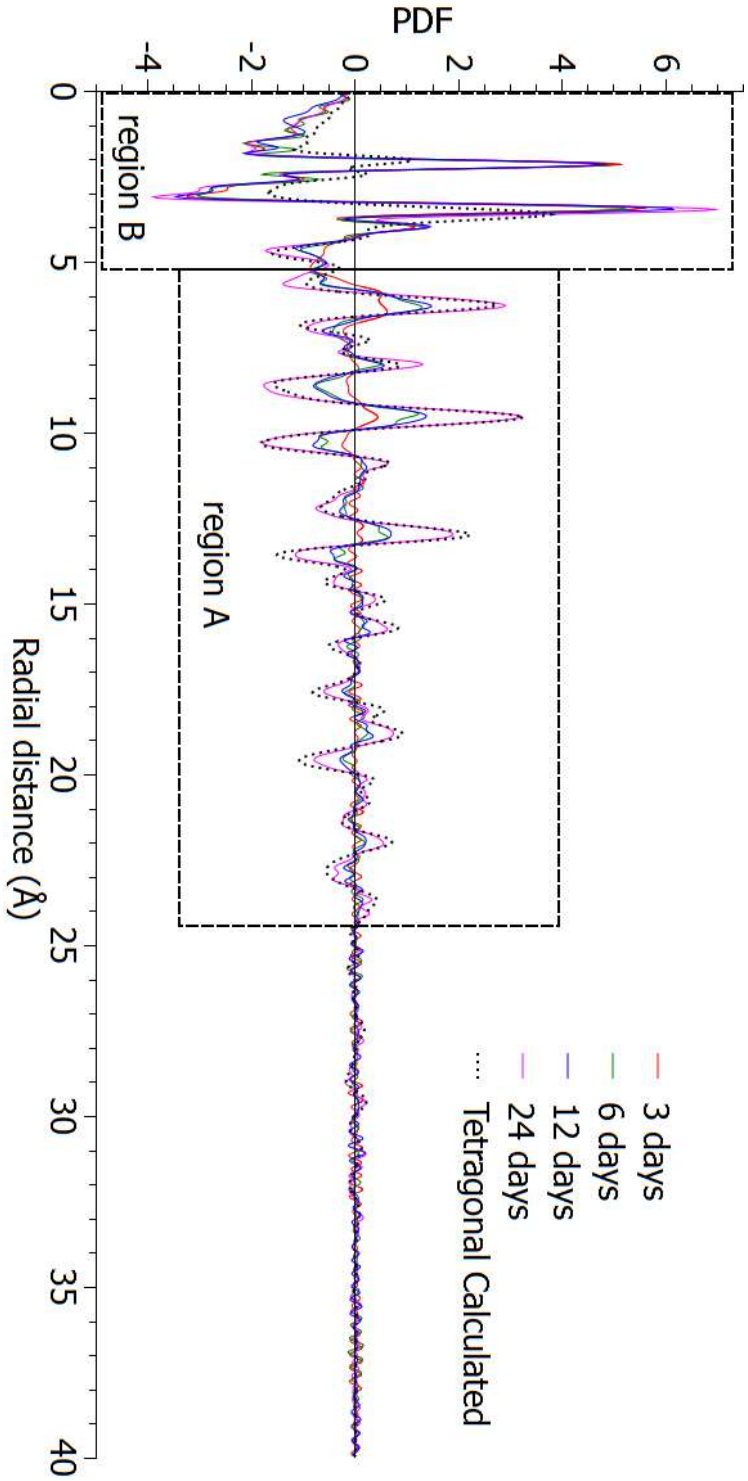

Figure 117: Experimental PDF for varied solvothermal ageing period samples prepared at 210°C in anisole with 0.2 mol.L^{-1} NaOH compared with the tetragonal model.

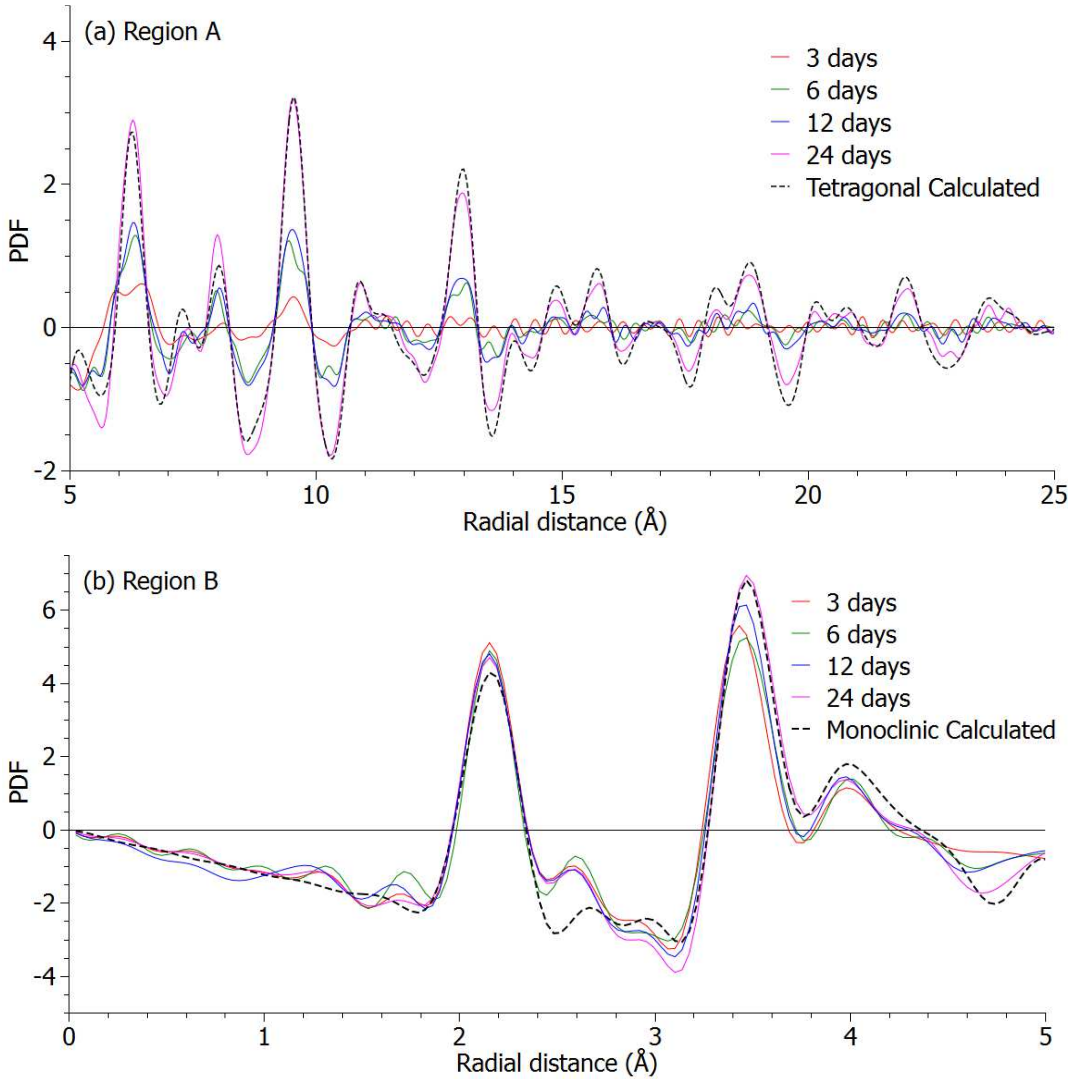

Figure 118: Detailed images of (a) Region A and (b) Region B for samples with NaOH under varied ageing period.

Table 26: Refined PDF parameters for sample with 24 days ageing and with NaOH using tetragonal model

parameters	**Reference** [88]	**Refined tetragonal**
Range (Å)	NA	5-25
R_w	NA	0.157
a(Å)	3.64	3.61
c(Å)	5.27	5.12*
$R_t \frac{c}{a\sqrt{2}}$	1.023	1.002

Table 27: Refined PDF parameters for sample with 24 days ageing with NaOH using monoclinic model

parameters	**Reference** [87]	**Refined monoclinic**
Range (Å)	NA	0-5
R_w	NA	0.188
a(Å)	5.15	5.00
b(Å)	5.21	5.35
c(Å)	5.32	5.29
β(º)	99.23	96.87

4.1.13.2 Total scattering and PDF analysis of the selected samples under varied solvothermal ageing period without NaOH

Shown in Figure 119 are the experimental PDF of the samples prepared with varied ageing period without the presence of NaOH. Similar to the previous set of samples (with the presence of NaOH), the samples appear to have some structural improvement but not as fast and requires longer ageing period in order to observe some distinguishable difference. Measuring the coherent sizes of the sample gives an increasing value with 0.8 nm for 3 days, 1.1 nm for 6 days, 1.4nm for 12 days, and 3 nm for 24 days.

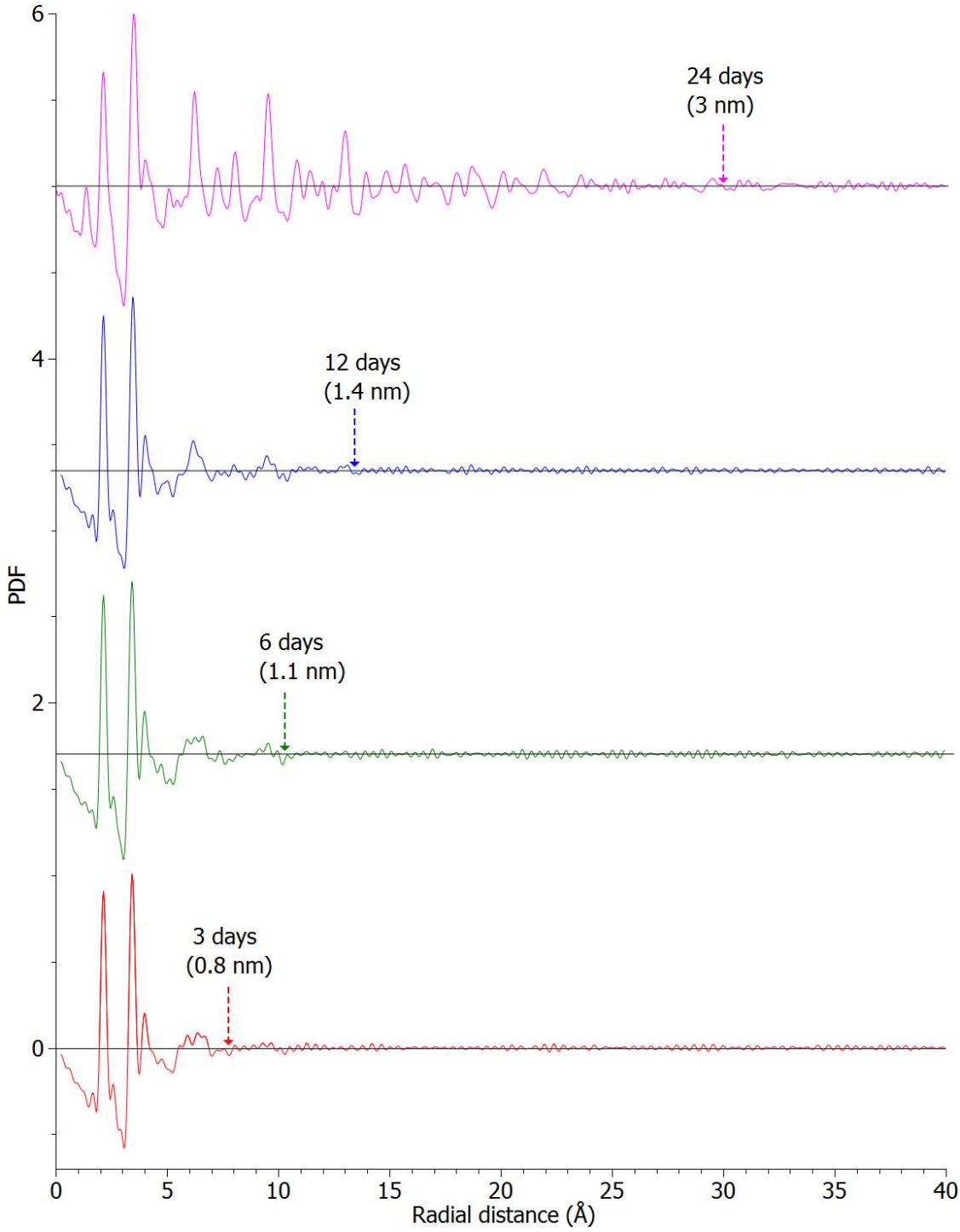

Figure 119: Experimental PDF of the zirconia particles prepared at 210°C in anisole without NaOH for varied solvothermal ageing period (3 days, 6 days, 12 days, and 24 days).

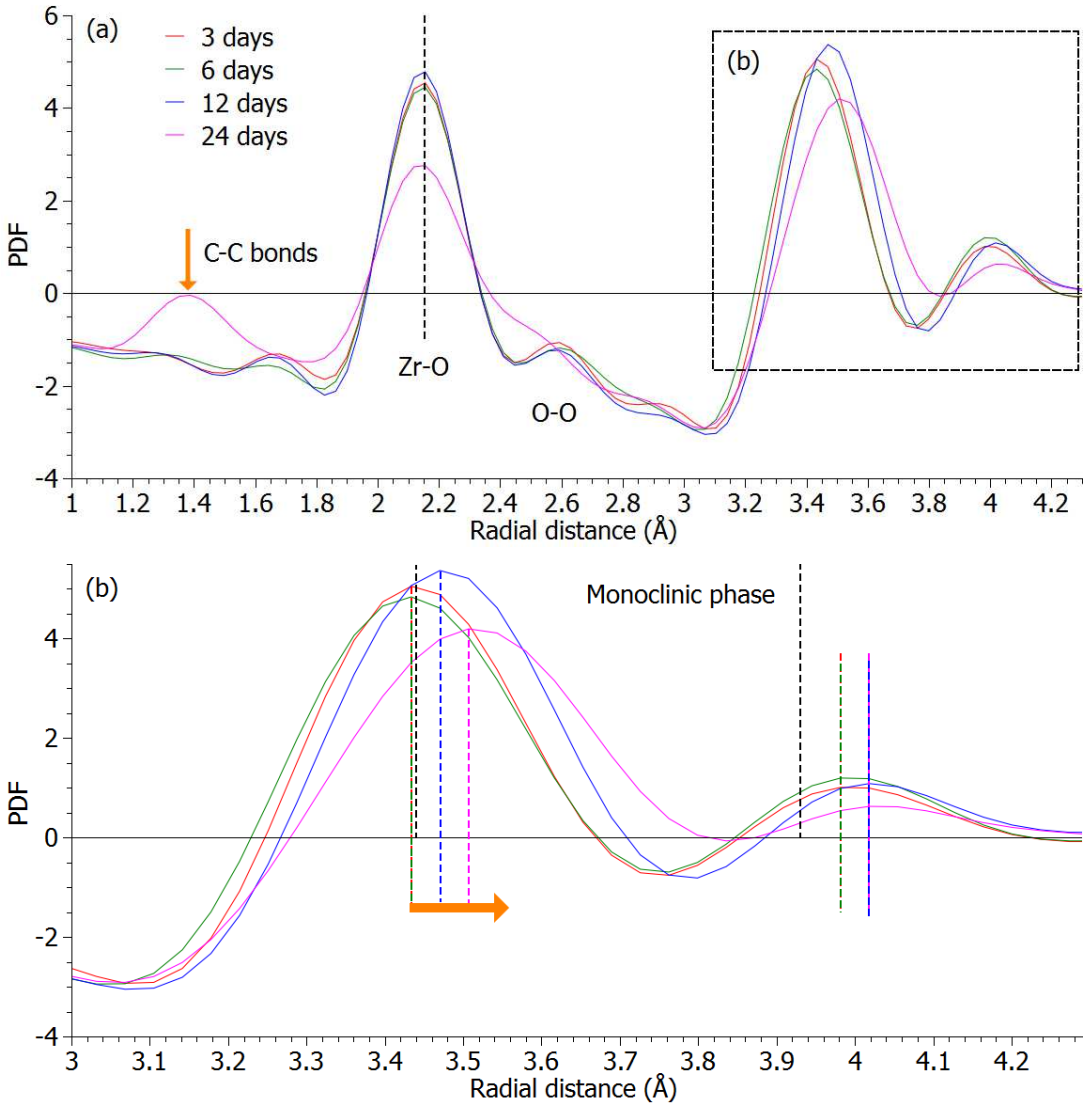

Figure 120: Experimental PDF of the zirconia particles for varied solvothermal ageing period prepared at 210°C in anisole without NaOH compared with well crystallized zirconia monoclinic phase [87].

As we focus on the selected short-range region (1 to 4 Å) of the samples, we observe that the first two peaks positioned at 2.15 Å and 2.59 Å coincide with the monoclinic phase, similarly to the samples prepared with NaOH. Again, the peaks position does not evolve with ageing time but we can notice that they are broader for the 24 days sample. We also observe a peak around 1.37 Å that could correspond to C-C, C-O or O-O bonds (ranging from 1.20 to 1.54 Å) due to organic compounds impurities in our sample (as already noticed in the sample prepared in benzaldehyde with NaOH in section 4.3.2). Aside from the similarities of peak positions, the shifts around the

Zr-Zr peak are also similar to those of the samples prepared with NaOH but with its oldest aged sample (24 days) shifted a bit farther to the right. The last two peaks are positioned at 3.50 Å and 4.0 Å.

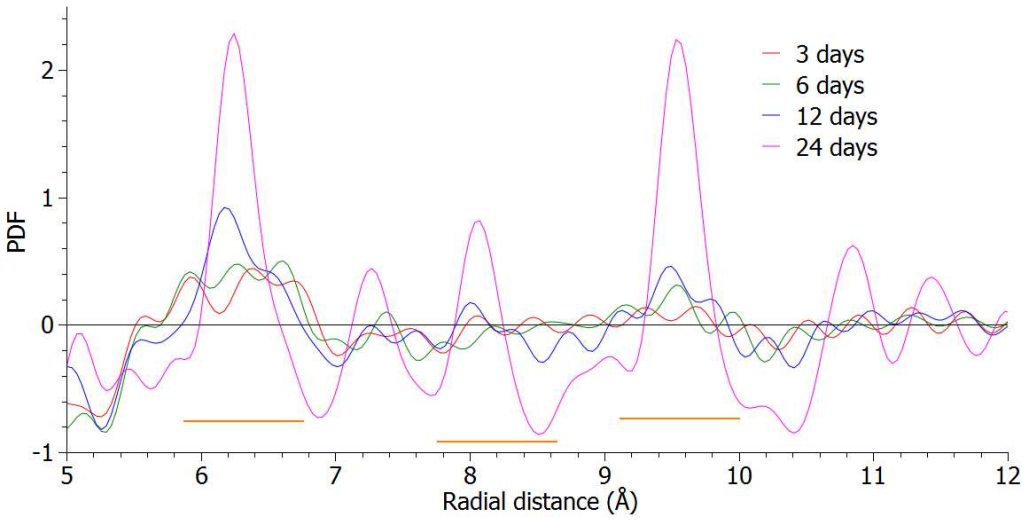

Figure 121: Experimental PDF of samples with varied solvothermal ageing period prepared at 210°C in anisole without NaOH at the selected medium-range region (5 to 12 Å).

At the selected medium-range region shown in Figure 121, we observe some structural improvements at positions 6.24, 8.09 and 9.55 Å. In comparison with the samples aged with NaOH, similar trend is observed with respect to the length of ageing. Specifically, for the 3 and 6 days samples they appear to be similar and less intense compared to the 12 days sample. These structural changes are improved significantly after 24 days as indicated by the narrow peaks. We then fit the samples with tetragonal and monoclinic models as shown in Figure 122 and Figure 123 and their refined PDF parameters in Table 28 and Table 29.

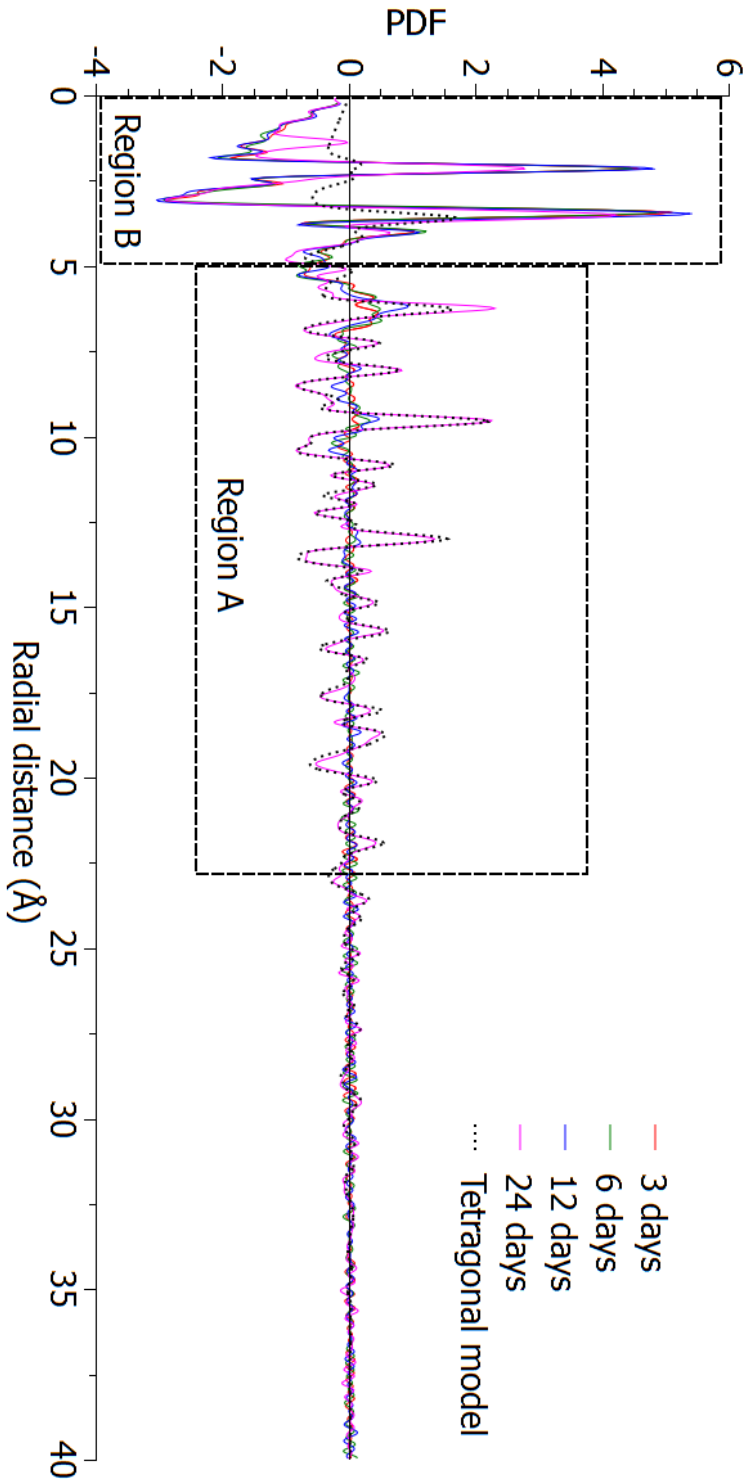

Figure 122: Experimental PDF for varied solvothermal ageing period samples prepared at 210°C in anisole without NaOH compared with tetragonal model.

Generally, the same observation is made from the experimental PDF of the samples without NaOH with the samples with NaOH when compared to the PDF of the tetragonal model (see Figure 122). Again, only the sample aged at 24 days coincides well with a tetragonal model in comparison with the other samples but limited mostly in the medium-range region as shown in Figure 123 (a). Likewise, the peaks at the short-range region corresponds to the monoclinic phase shown in Figure 123 (b). The refined PDF parameters for the tetragonal and monoclinic models are comparable to the reference and samples with NaOH.

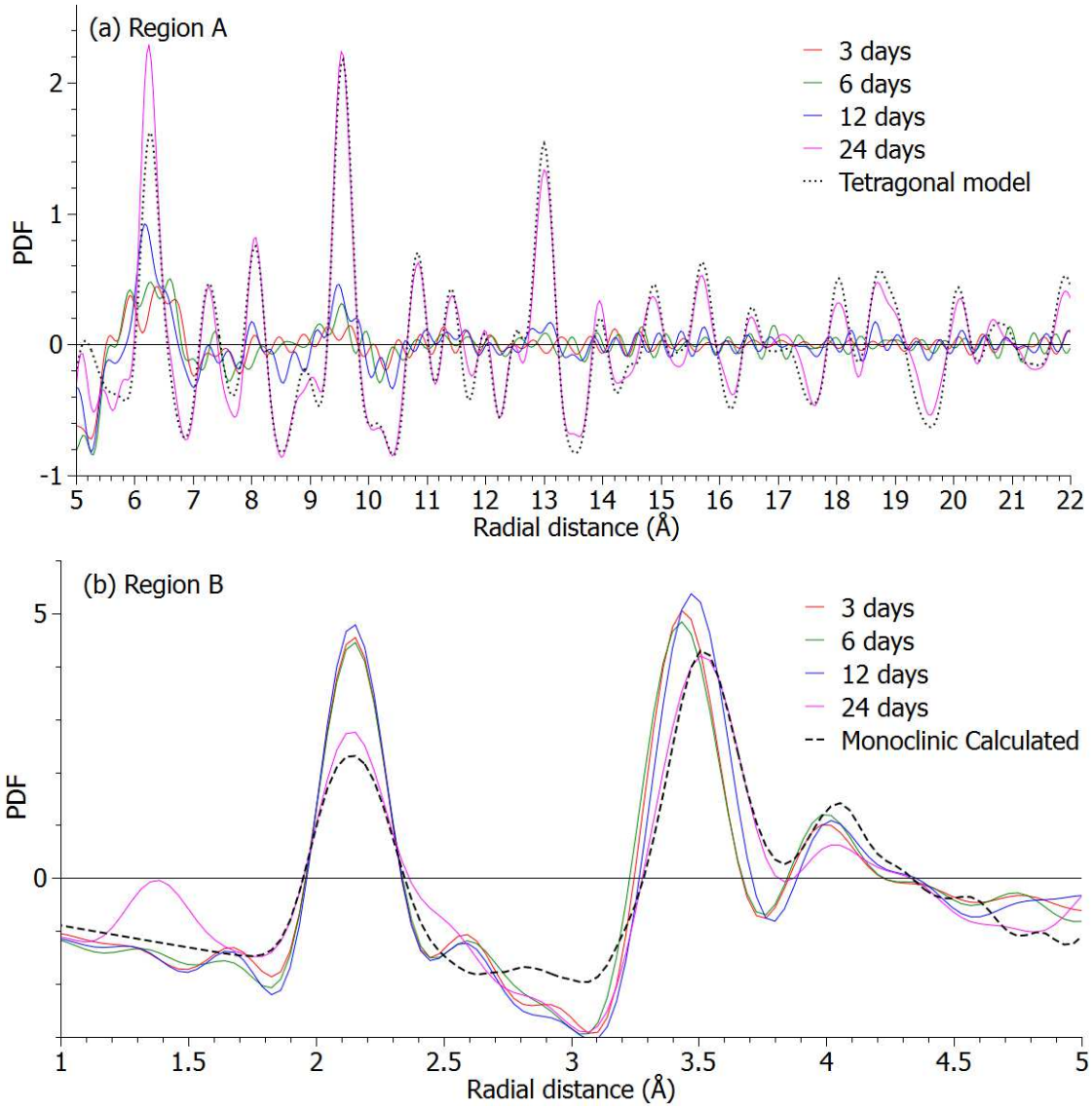

Figure 123: Detailed images of (a) Region A and (b) Region B for samples without NaOH under varied ageing period.

Table 28: Refined PDF parameters for sample with 24 days ageing without NaOH using tetragonal model

parameters	**Reference** [88]	**Refined tetragonal**
Range (Å)	NA	5-25
R_w	NA	0.200
a(Å)	3.64	3.60
c(Å)	5.27	5.13
$R_t \frac{c}{a\sqrt{2}}$	1.023	1.009

Table 29: Refined PDF parameters for sample with 24 days ageing without NaOH using monoclinic model

parameters	**Reference** [87]	**Refined monoclinic (3nm)**
Range (Å)	NA	0.0365-5
R_w	NA	0.285
a(Å)	5.15	5.03
b(Å)	5.21	5.40
c(Å)	5.32	5.31
β(º)	99.23	97.46

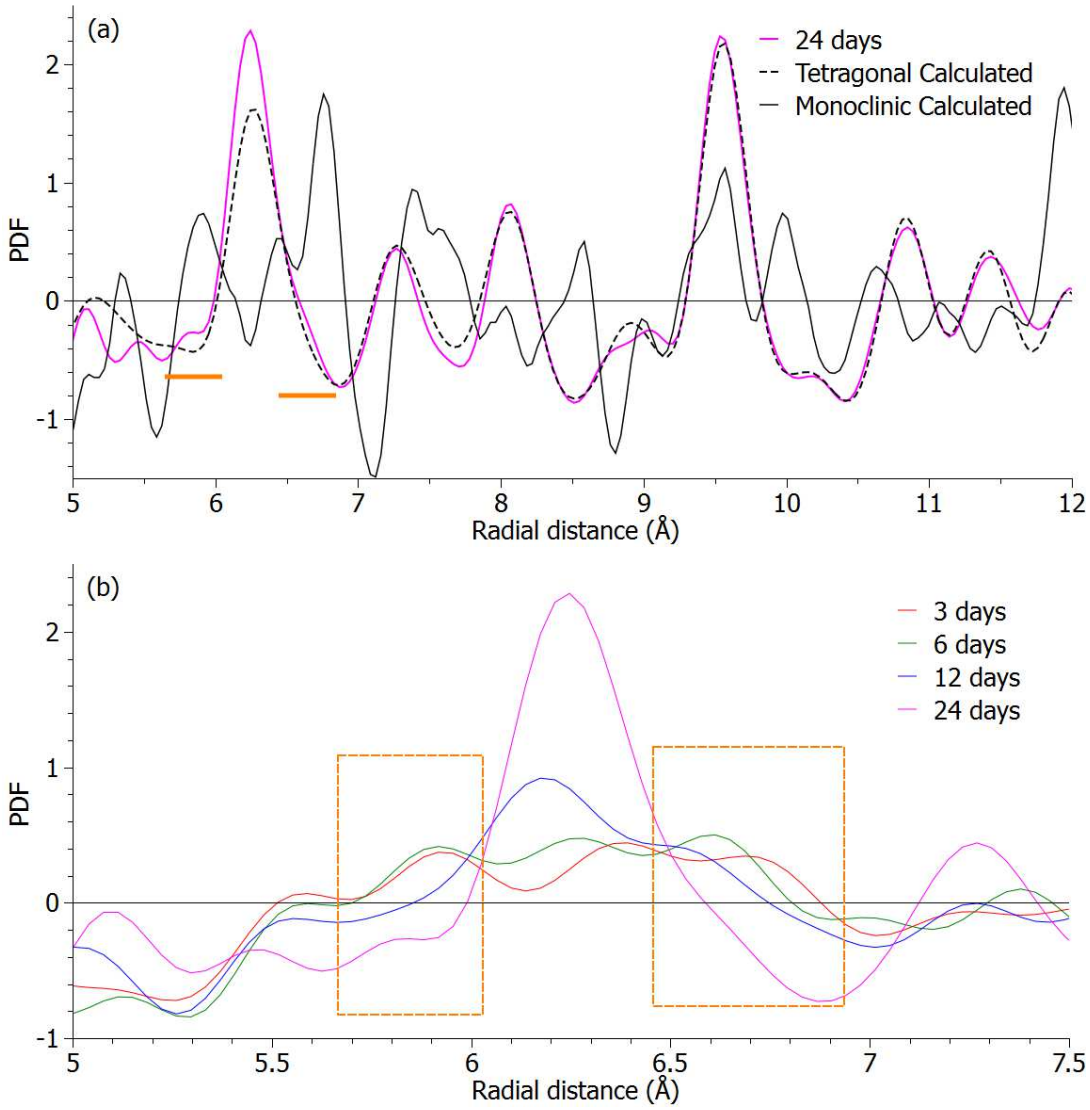

Figure 124: Experimental PDF of samples with 24 days solvothermal ageing period prepared at 210ºC in anisole without NaOH at the selected medium-range regions (a) 5-12 Å and (b) 5-7 Å.

Examining further the sample aged for 24 days, we observe a tiny peak positioned at around 5.8 Å and a slight deformation around 6.59 Å which conforms to the monoclinic phase zirconia (see Figure 124). It appears that the local monoclinic features has extended towards the medium-range region mixing with the tetragonal peaks in that same region. This result suggests that the tiny bumps observed in the XRD pattern for the sample with 24 days ageing period in Figure 113 (b) could be due to the extension of the monoclinic features and restructuring of the tetragonal-like phase zirconia.

However, we observe that along the selected regions for the monoclinic peaks indicated by the rectangular boxes, they seem to correlate with the development for both tetragonal and monoclinic phases as shown in Figure 124 (b). Which suggests that the formation of monoclinic and tetragonal-like phase could also occur together at an earlier stage. This correlation of peaks in these selected regions seems to be exclusive for samples without NaOH. Hence, we can say that the effects of *in-situ* water may have influenced amorphous-like at an earlier stage.It is also possible that the onset of monoclinic phase occurs at an earlier time than the tetragonal-like phase since at the local region we always observe a monoclinic feature.

In summary, it is arguably difficult to isolate the effects of *in-situ* water on the structural evolution of the zirconia samples without NaOH. But it is clear that trend of restructuring is different for with and without NaOH as indicated by the presence of monoclinic feature at the medium-range region.

4.1.13.3 Comparison of the zirconia samples with varied ageing period

In this section we compare in parallel the samples synthesized in various ageing periods with and without 0.2 mol.L^{-1} NaOH. We briefly summarize the results for the samples with varied ageing periods for both with and without NaOH.

If we examine the samples prepared at 3 days ageing period for both types of samples, we observe that the addition of an alkali source promotes an earlier restructuring (see Figure 125 (a)). The structural changes are improved for samples prepared at 6, 12 and 24 days (see Figure 125 (b, c, & d)). We also observe that the restructuring lean towards the tetragonal-like from an amorphous-like structure with a local monoclinic feature for all samples. Here we notice that the onset of tetragonal-like occurs earlier for samples with NaOH as shown in Figure 125 (b & c).

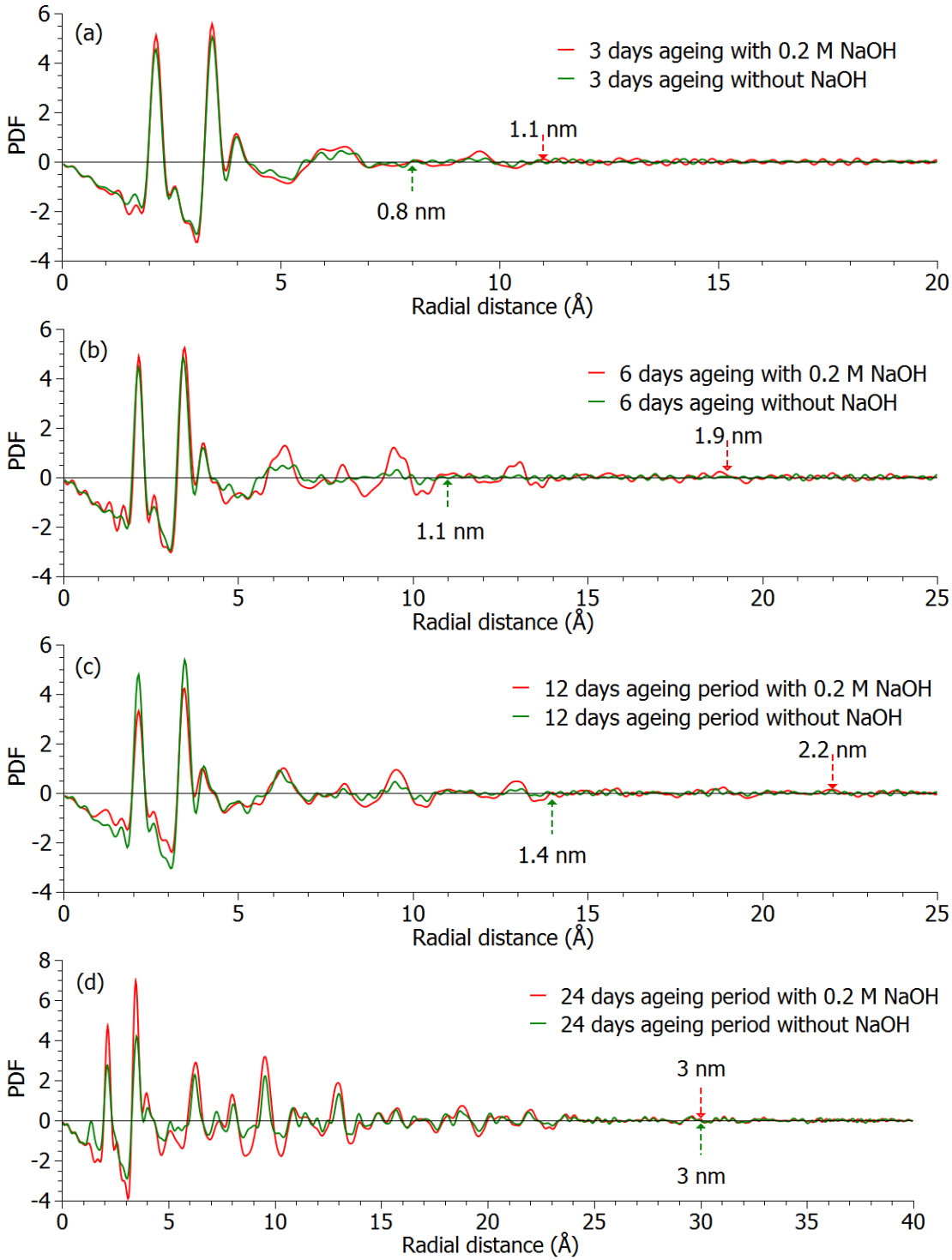

Figure 125: Experimental PDF of the zirconia particles produced at 210°C in anisole with and without 0.2 mol.L^{-1} NaOH for (a) 3 days ageing, (b) 6 days ageing, (c) 12 days ageing, and (d) 24 days ageing assisted thermally.

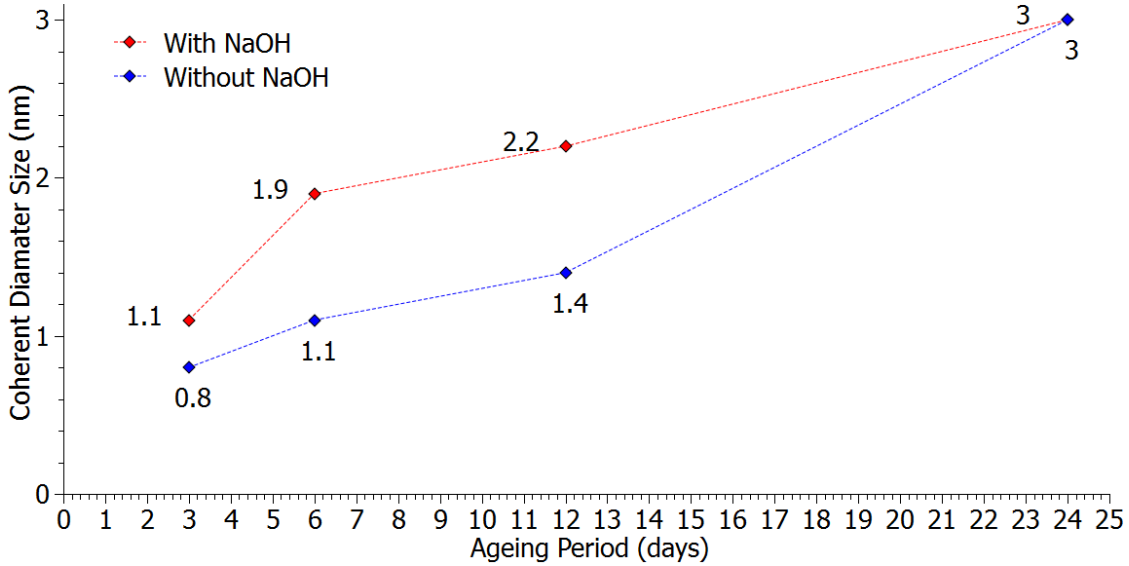

Figure 126: Comparison of coherent diameter sizes of the samples prepared with varied ageing period for samples with and without NaOH.

The trends of the coherent size for both types of samples are quite similar as shown in Figure 126. However, the sizes obtained for the samples with NaOH are much bigger except for the samples prepared at 24 days where both types converge to the same size. It is clear that thermally assisted ageing improved the structural features of all the samples from an amorphous-like structure and the presence of NaOH is invaluable in inducing a much better and shorter crystallization with good phase purity.

4.1.14 Influence of varied ex-situ water for samples synthesized in anisole with and without NaOH

Shown in Figure 127(a) are the XRD patterns of the samples obtained with 0.2 mol.L^{-1} NaOH with varied amounts of water. The addition of water onto the reaction mixture drastically changed the crystallinity and phase purity of the nanoparticles. As observed the sample without any water transformed progressively into a narrow peaked tetragonal phase with the addition of water (volume percentage of 0.33% and 2%) suggesting an increase in the average size. Looking at the sample with a water volume percentage of 2%, the pattern suggests that the presence of sodium hydroxide exhibits a shielding effect in the transformation of the tetragonal phase towards monoclinic phase as indicated by the peaks that correspond solely to the tetragonal phase. However, increasing the amount of water (volume percentage of 4% and 5%) completely transformed the

tetragonal phase into pure monoclinic phase composed of large crystallites. The transformation to a monoclinic phase appears to be gradual as indicated by the presence of an intermediate dual phases of the sample at volume percentage of 4%.

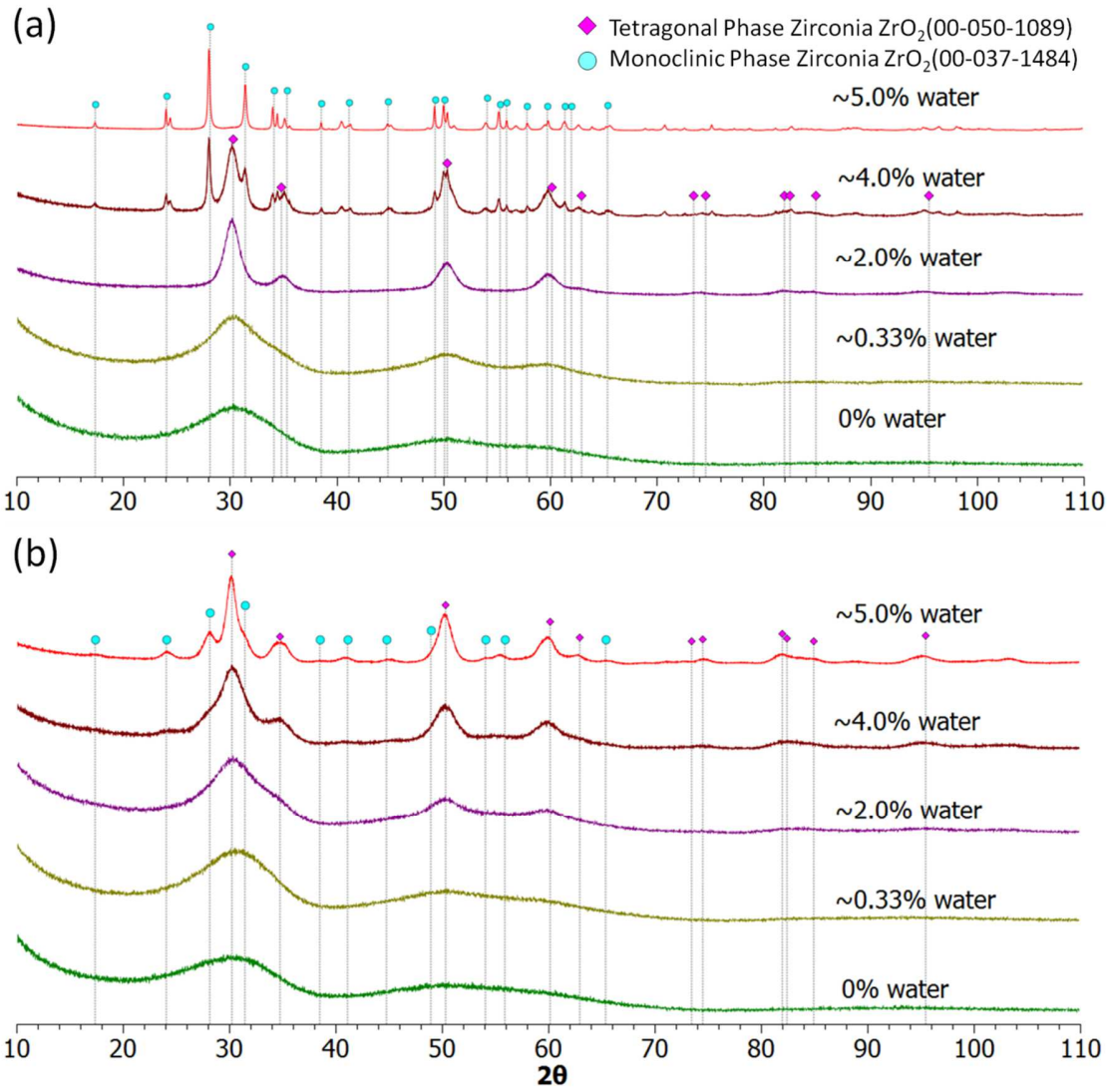

Figure 127: XRD patterns of the samples synthesized at 210°C for 3 days with varied volume ratio of anisole and water (a) with and (b) without 0.2 mol.L^{-1} NaOH.

In the absence of NaOH shown in Figure 127 (b), the addition of water (volume percentage of 0.33% and 2%) into the starting reagents improved the crystallinity of the particles from amorphous-like to crystalline as indicated by the three broad accented peaks at positions $2\theta = 30.3^{o}$, 49.9^{o}, and 58.5^{o}. A bigger addition of water (volume percentage of 4% and 5%) into the starting reagents led to the crystallization of a mixture of tetragonal/cubic and monoclinic phases while

favoring the former for the most intense peaks. Also, in these cases the peaks appear to be much narrower as compared to the previous samples suggesting that the presence of water affects both crystallization and growth processes. In this case it is possible that no phase selection occurred and there is a strong possibility that the broad peaks that were initially observed at lower amount of water were actually an overlap of monoclinic and tetragonal/cubic contributions from very small particles.

Comparing the same samples (volume percentage of 4%) with and without sodium hydroxide, the former shows a quick transformation from a dual phase to single phase with very large crystallite size. These results suggest that the addition of water induces a significant improvement in its crystallinity but is detrimental to the phase purity.

4.1.14.1 Rietveld refinement of the selected sample under varied amounts of ex-situ water

Here we analyze some samples synthesized with the addition of water via Rietveld refinement. The samples' selection process is based on the quality of their XRD diagram. This process simply chooses samples with distinguishable peaks that can easily be assigned to a particular zirconia phase. If we compare the samples in Figure 127 (a) with varied water content, the samples with NaOH and with water volume percentage of 2%, 4% and 5% looks suitable for characterization. Similarly, for the samples without NaOH and with water volume percentage of 4% and 5% seems reasonable for characterization (see Figure 127 (b)).

The average apparent sizes, refined lattice parameters, strain and relative weight fraction of phases for the samples with 0.2 mol.L^{-1} NaOH are shown in Figure 128 (a), Table 30 (a) and Table 31 (a).The average apparent sizes of the samples show a significant increase to 36.7 nm. Unlike the sample without NaOH, the dual phase sample (w = 6.5 or 4%) shows that the monoclinic phase is larger (22.7 nm) than the tetragonal phase (5 nm). Similarly, the samples are under structural strain which eventually decreases when the size increases.

Shown in Figure 128 (b), Table 30 (b) and Table 31 (b) are the average apparent sizes, refined lattice parameters, strain, and relative weight fraction of phases for the samples without NaOH. The average apparent sizes of the monoclinic crystallites are systematically lower than the ones of the tetragonal phase. Also, the strain seems higher in the tetragonal phase particles than in the monoclinic ones. As observed the structural strain decreases when the size of the particles increases which allows the structure to be relieved.

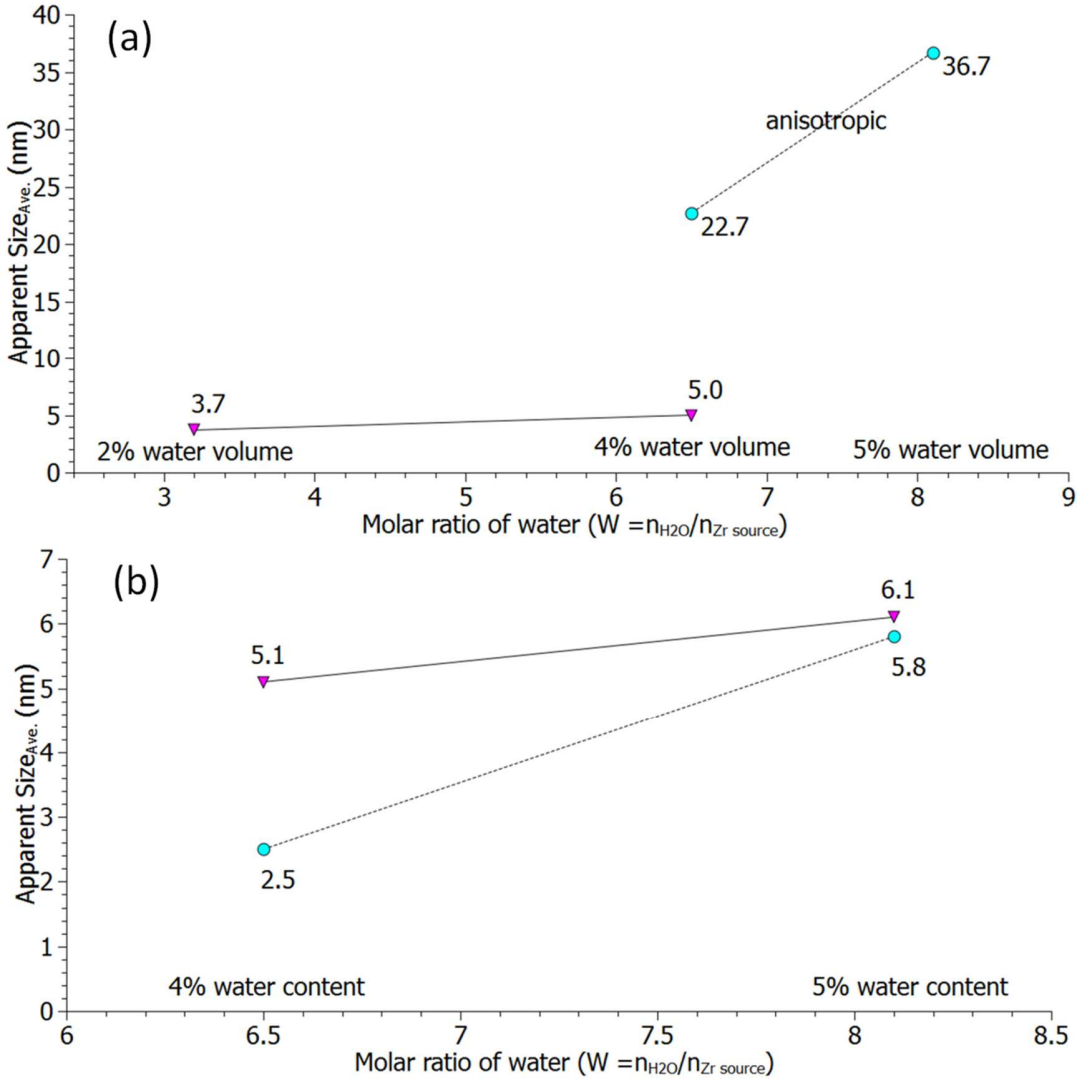

Figure 128: Average apparent sizes of the samples synthesized at 210°C for 3 days with varied volume ratio of anisole and water (a) with and (b) without 0.2 mol.L^{-1} NaOH

Table 30: Refined lattice parameters for samples (a) with and (b) without 0.2 mol.L^{-1} NaOH

(a) Samples with NaOH				
	2% water	**4% water**		**5% water**
	Tetragonal	Tetragonal	Monoclinic	Monoclinic
χ^2	1.361	1.718		6.010
a (nm)	3.614	3.610	5.179	5.177
b (nm)	-	-	5.203	5.205
c (nm)	5.147	5.155	5.345	5.344
β (°)	-	-	99.64	99.64
R_t	1.007	1.009	-	-
O_z	0.181	0.182	-	-
(b) Samples without NaOH				
	4% water		**5% water**	
	Tetragonal	Monoclinic	Tetragonal	Monoclinic
χ^2	2.218		1.430	
a (nm)	3.597	5.064	3.599	5.152
b (nm)	-	5.203	-	5.211
c (nm)	5.173	5.415	5.183	5.320
β (°)	-	101.05	-	99.36
R_t	1.02	-	1.02	-
O_z	0.153	-	0.199	-

Table 31: Strain and relative weight fraction for samples (a) with and (b) without 0.2 mol.L^{-1} NaOH synthesized at 210°C for 3 days with varied volume ratio of anisole and water (* too small to calculate)

(a) Samples with NaOH				
Molar ratio of water ($w = n_{H20}/n_{Zr\ source}$)	Tetragonal Strain (%)	Monoclinic Strain (%)	Tetragonal phase (%)	Monoclinic phase (%)
3.2 (2% water)	0.09		100	0
6.5 (4% water)	*	0.13	64.10	35.90
8.1 (5% water)		0.07	0	100
(b) Samples without NaOH				
Molar ratio of water ($w = n_{H20}/n_{Zr\ source}$)	Tetragonal Strain (%)	Monoclinic Strain (%)	Tetragonal phase (%)	Monoclinic phase (%)
6.5 (4% water)	0.85	0.64	49.11	50.89
8.1 (5% water)	0.15	*	61.34	38.66

4.1.14.2 Total scattering and PDF analysis of the selected samples under varied amounts of *ex-situ* water with NaOH

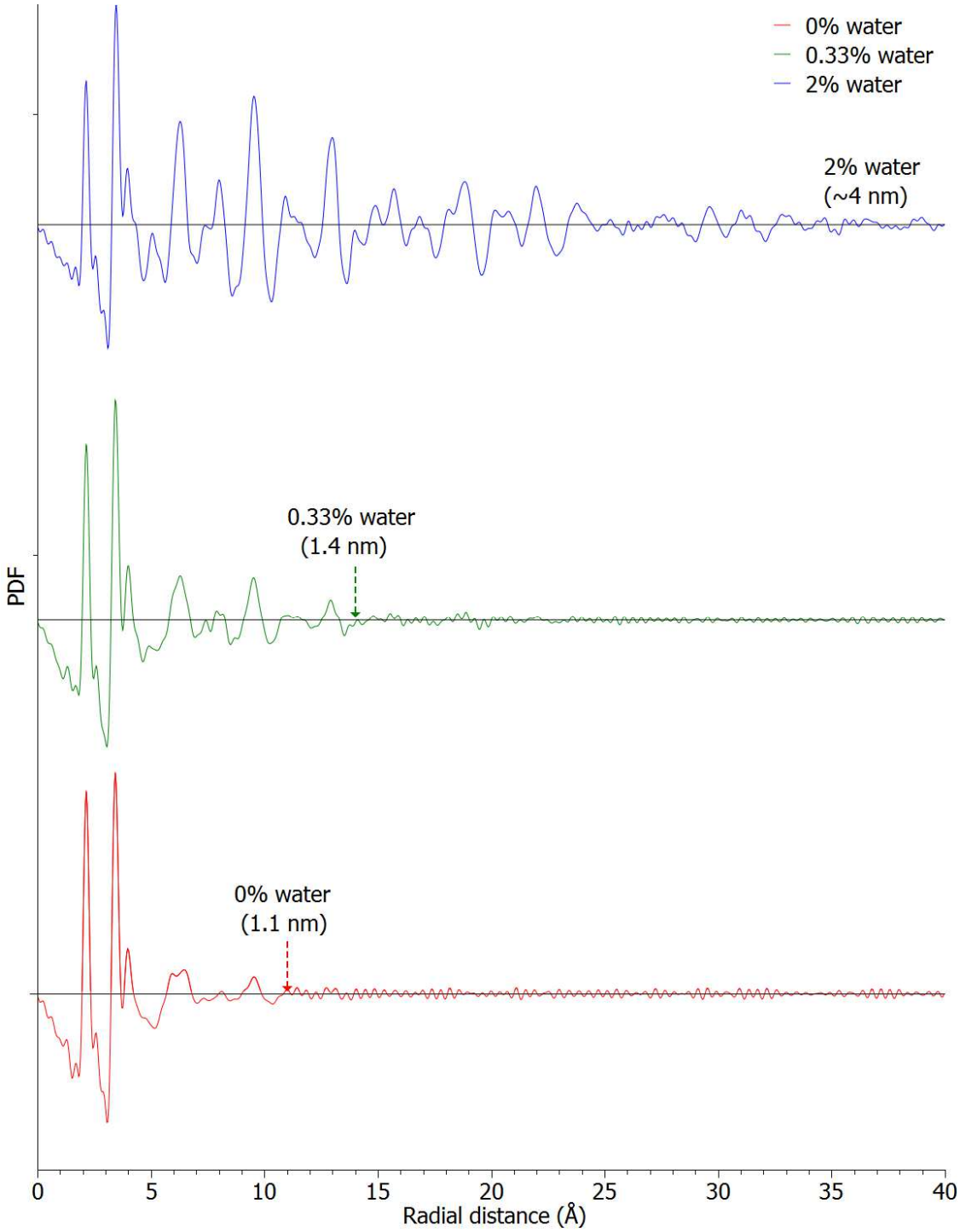

Figure 129: Experimental PDF of the zirconia particles with varied amounts of water 0%, 0.33%, and 2.0% volume, produced at 210°C for three days in anisole with 0.2 mol.L^{-1} NaOH.

Shown in Figure 129 are the experimental PDF for the samples with varied water volume percentage of 0%, 0.33% and 2% prepared in anisole with 0.2 mol.L^{-1} NaOH at 210°C. The effect of *ex-situ* water is clearly evident as indicated by the structural changes. As small as 0.33% volume content or approximately 1 drop of water is enough to induce modifcations and becomes more apparent when the water amount is increased to 2%. In comparison to the aged samples with and without NaOH, the presence of water seems to promote a much earlier crystallization. Measuring the samples' coherent domain lengths show different values with 1.1 nm for 0% water content, 1.4 nm for 0.33% water content and around 4 nm for the 2% water content.

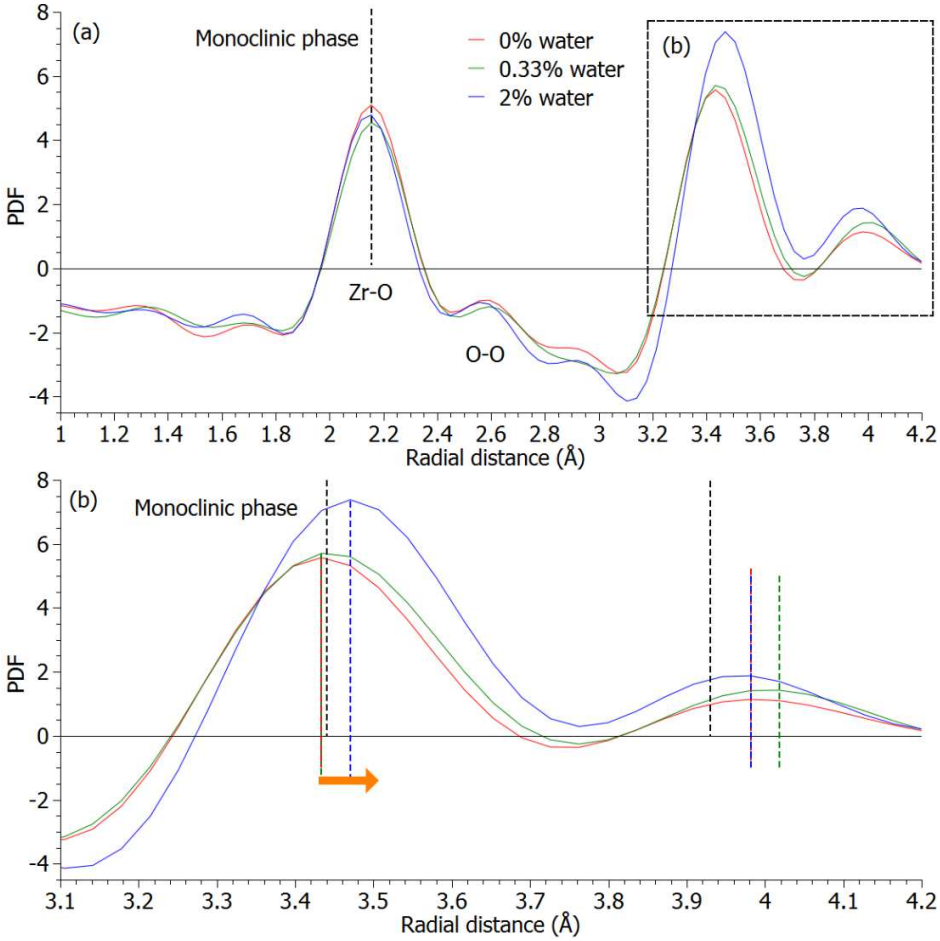

Figure 130: Experimental PDF of the zirconia particles with varied amounts of water produced at 210°C for three days in anisole with 0.2 mol.L^{-1} NaOH compared with well crystallized zirconia monoclinic phase [87].

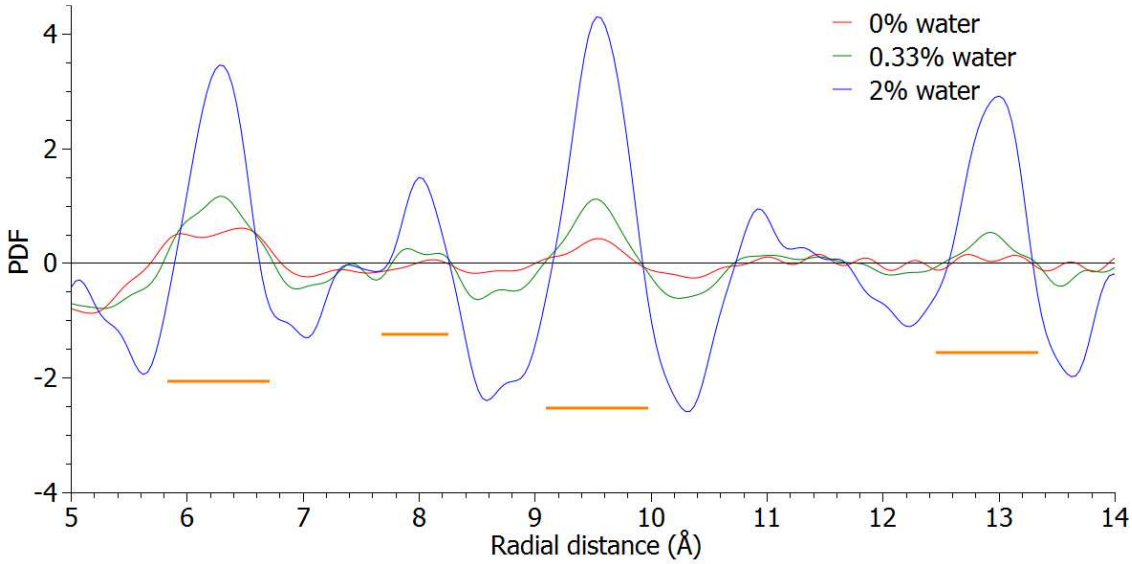

Figure 131: Experimental PDF of the zirconia particles with varied amounts of water produced at 210°C for three days in anisole with 0.2 mol.L^{-1} NaOH at the selected medium-range region

As we examine the peaks at the selected short-range region (1-4.2 Å), the peaks also conform to the monoclinic model with a shift towards to the right as the amount of added water increases. These shifts seem to be the trend for all types of samples as the crystallization of progresses (see Figure 130 (a) & (b)). Similarly, the peaks at the selected medium-range region (5-14 Å) also exhibits similar structural improvements and are most visible at positions 6.27, 8.01, 9.55, and 13.0 Å as seen in Figure 131.

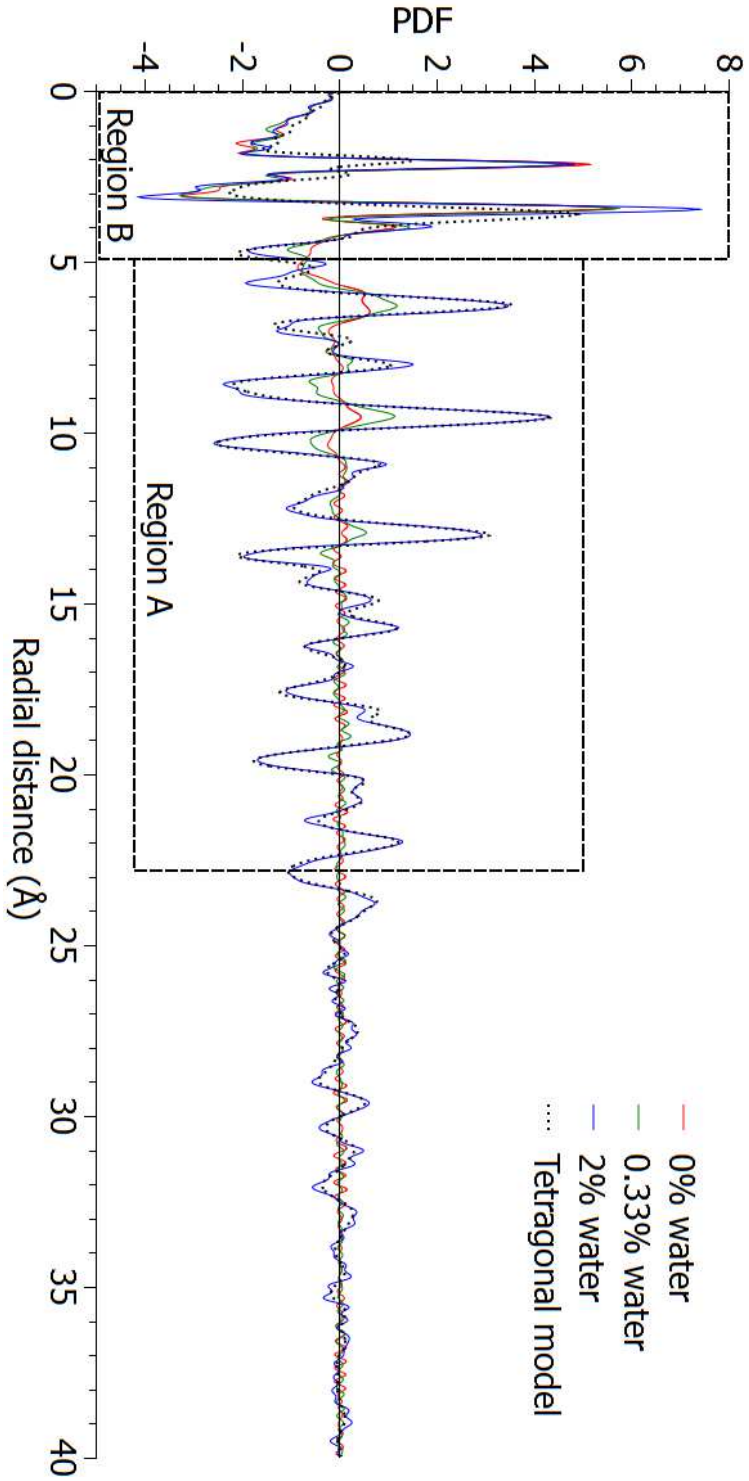

Figure 132: Experimental PDF of the zirconia particles with varied amounts of water produced at 210°C for three days in anisole with 0.2 mol.L^{-1} NaOH compared with tetragonal model.

We then compare the samples with tetragonal and monoclinic models as shown in Figure 132 and Figure 133 with its refined lattice parameters listed in Table 32 and Table 33. Similar observations are seen with the samples' structural characteristics in both the selected short-range and medium-range region in comparison with the aged samples with and without NaOH.

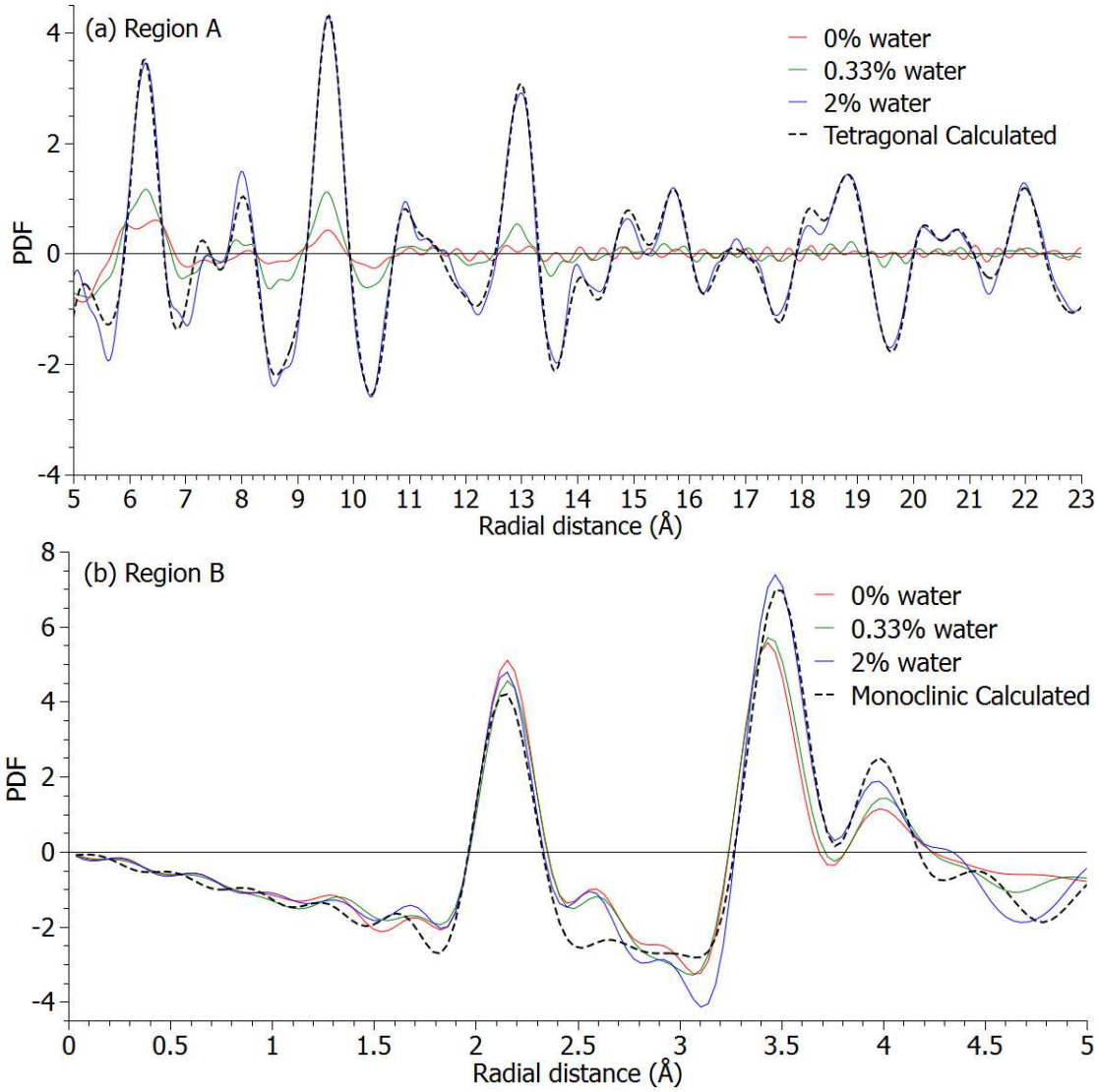

Figure 133: Detailed images of (a) Region A and (b) Region B for samples with NaOH under varied amounts of water.

Table 32: Refined PDF parameters for sample with 2% water and with NaOH using tetragonal model (* fixed)

parameters	**Reference** [88]	**Refined tetragonal**
Range (Å)	NA	5-25
R_w	NA	0.162
a(Å)	3.64	3.60
c(Å)	5.27	5.16*
$R_t \frac{c}{a\sqrt{2}}$	1.023	1.014

Table 33: Refined PDF parameters for sample with 2% water and with NaOH using monoclinic model

parameters	**Reference** [87]	**Refined monoclinic**
Range (Å)	NA	0.0365-5
R_w	NA	0.179
a(Å)	5.15	5.01
b(Å)	5.21	5.36
c(Å)	5.32	5.27
β(°)	99.23	96.60

4.1.14.3 Total scattering and PDF analysis of the selected samples under varied amounts of ex-situ water without NaOH

Shown in Figure 134 are the experimental PDF of the samples for with varied water volume percentage of 0%, 0.33%, and 2% prepared at 210°C in anisole without NaOH. In the absence of NaOH, the samples' structural development is not as substantial with that of the samples with NaOH, but nonetheless its effect is still observable. Measuring the samples' coherent domain lengths show different values with 0.8 nm for 0% water content, 1.1 nm for 0.33% water content, and 2.4 nm for 2% water content. The samples selected short-range and medium-range regions also shows similar structural trend as shown in Figure 135 and Figure 136 with the samples prepared with varied ageing periods. However, the difference between the sample without water and with 0.33% water is comparably small and requires more water to effectively observe significant changes. Clearly, the effectiveness of water alone is not the same as the samples synthesized with both water and NaOH.

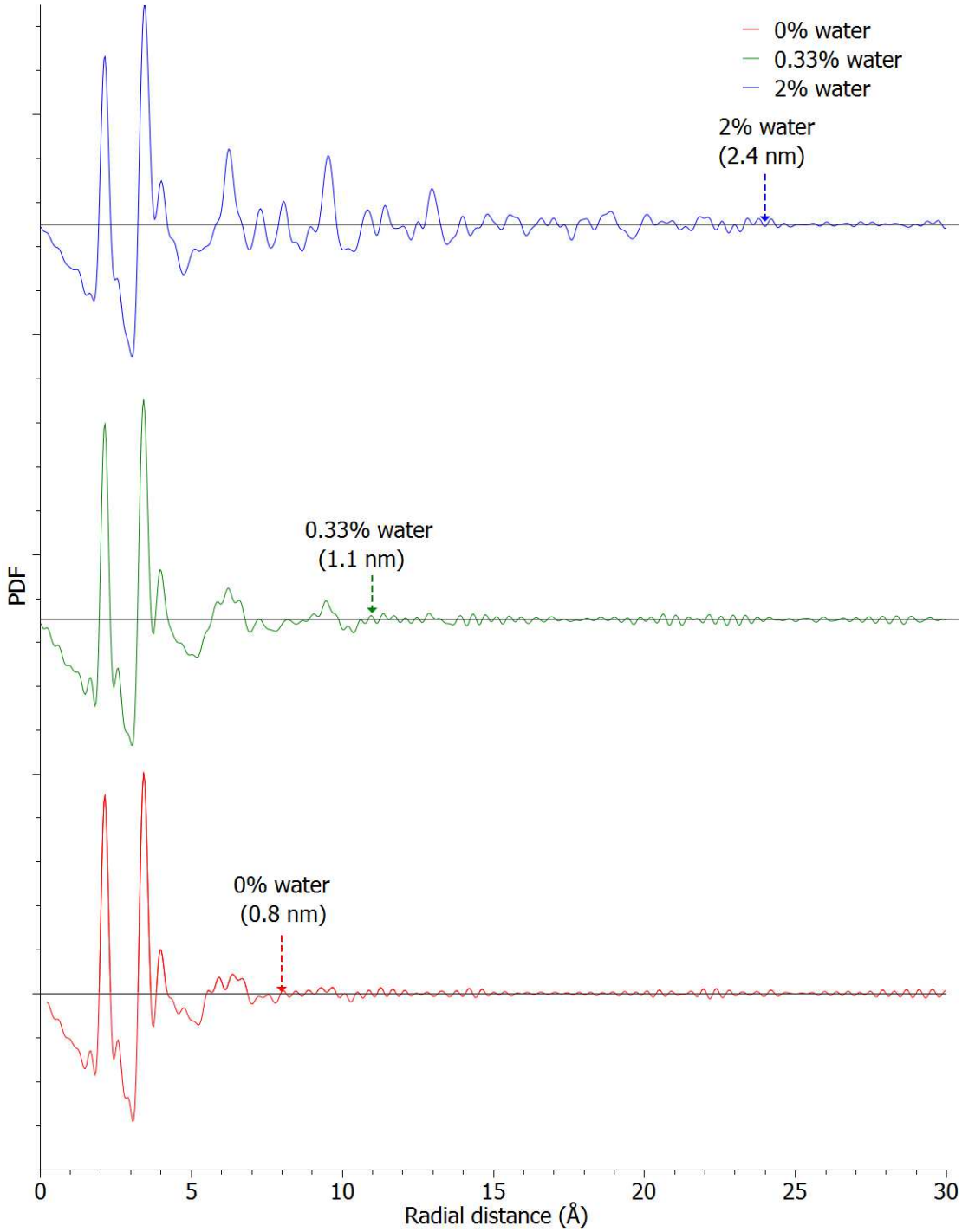

Figure 134: Experimental PDF of the zirconia particles with varied amounts of water percentage 0%, 0.33%, and 2.0% volume, produced at 210°C for three days in anisole without NaOH.

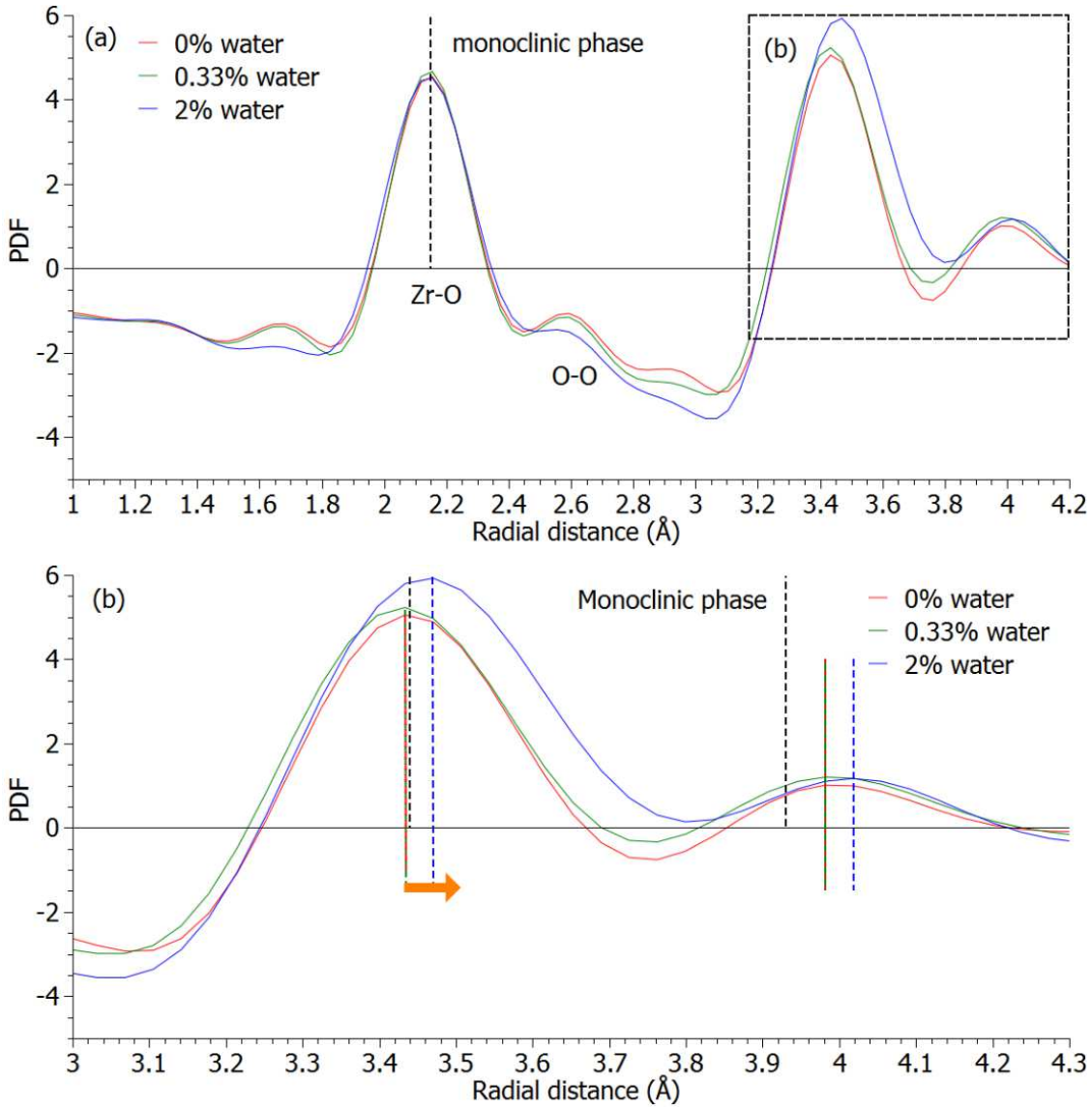

Figure 135: Experimental PDF of the zirconia particles with varied amounts of water produced at 210°C for three days in anisole without NaOH compared with well crystallized zirconia monoclinic phase [87].

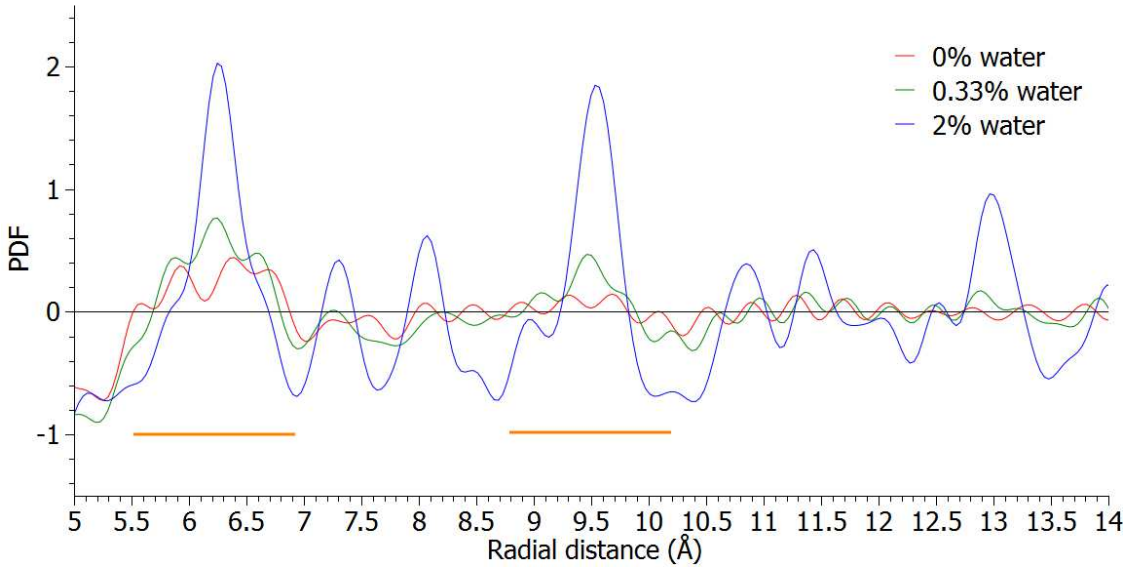

Figure 136: Experimental PDF of the zirconia particles with varied amounts of water produced at 210°C for three days in anisole without NaOH at the selected medium-range region.

Similarly, we compared the samples by fitting them with the tetragonal and monoclinic PDF models as shown in Figure 137 and Figure 138 and their refined lattice parameters in Table 34 and Table 35. Similar observations can also be drawn from the comparison of the experimental and calculated PDF models. However, for the selected medium-range region, it appears that there are some peaks (positioned at 5.8, 6.59 and 8.49 Å) that do not conform to tetragonal model but conform more to the monoclinic model as shown in Figure 139. This suggests that the sample with 2% water volume content has some similar condition as the samples aged for 24 days without NaOH but with much larger monoclinic feature at the medium-range region.

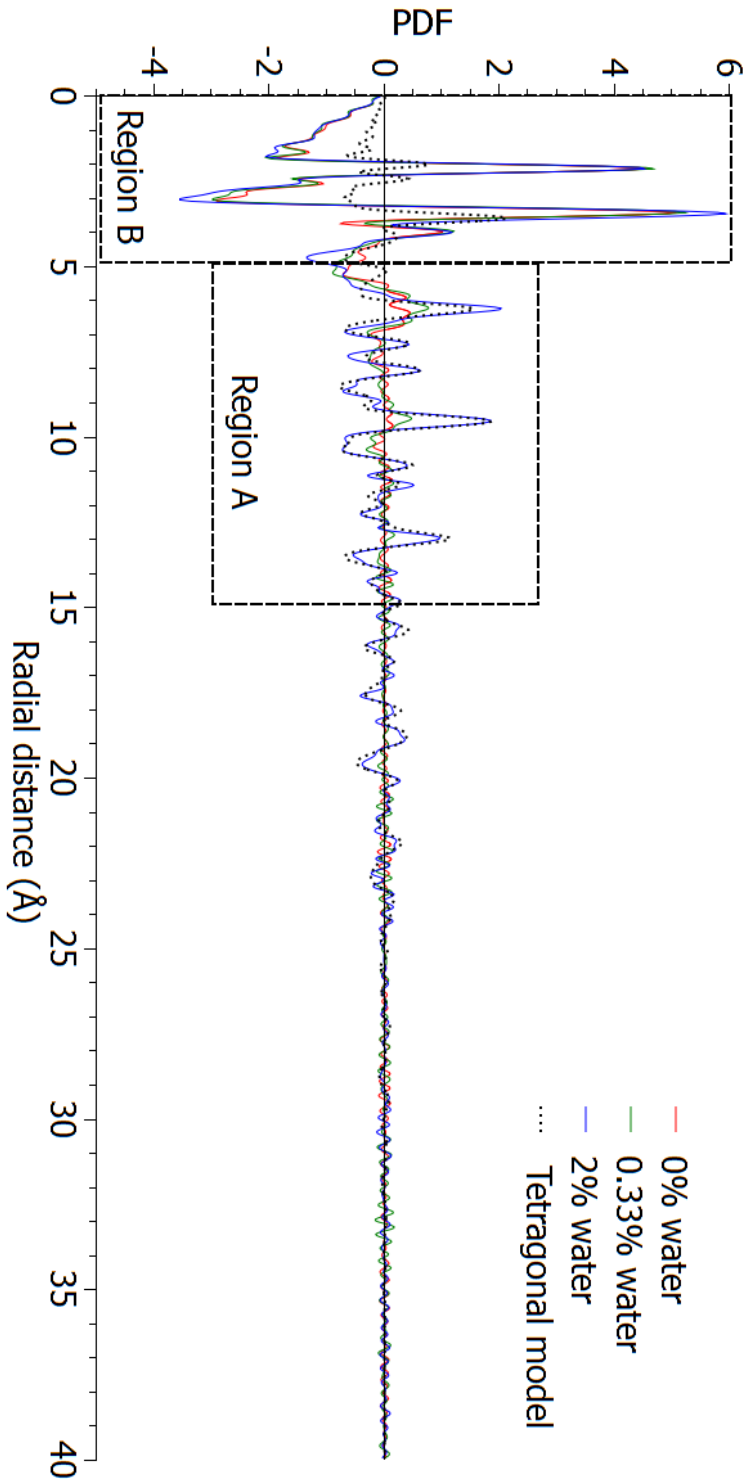

Figure 137: Experimental PDF of the zirconia particles with varied amounts of water produced at 210°C for three days in anisole without NaOH compared with tetragonal model.

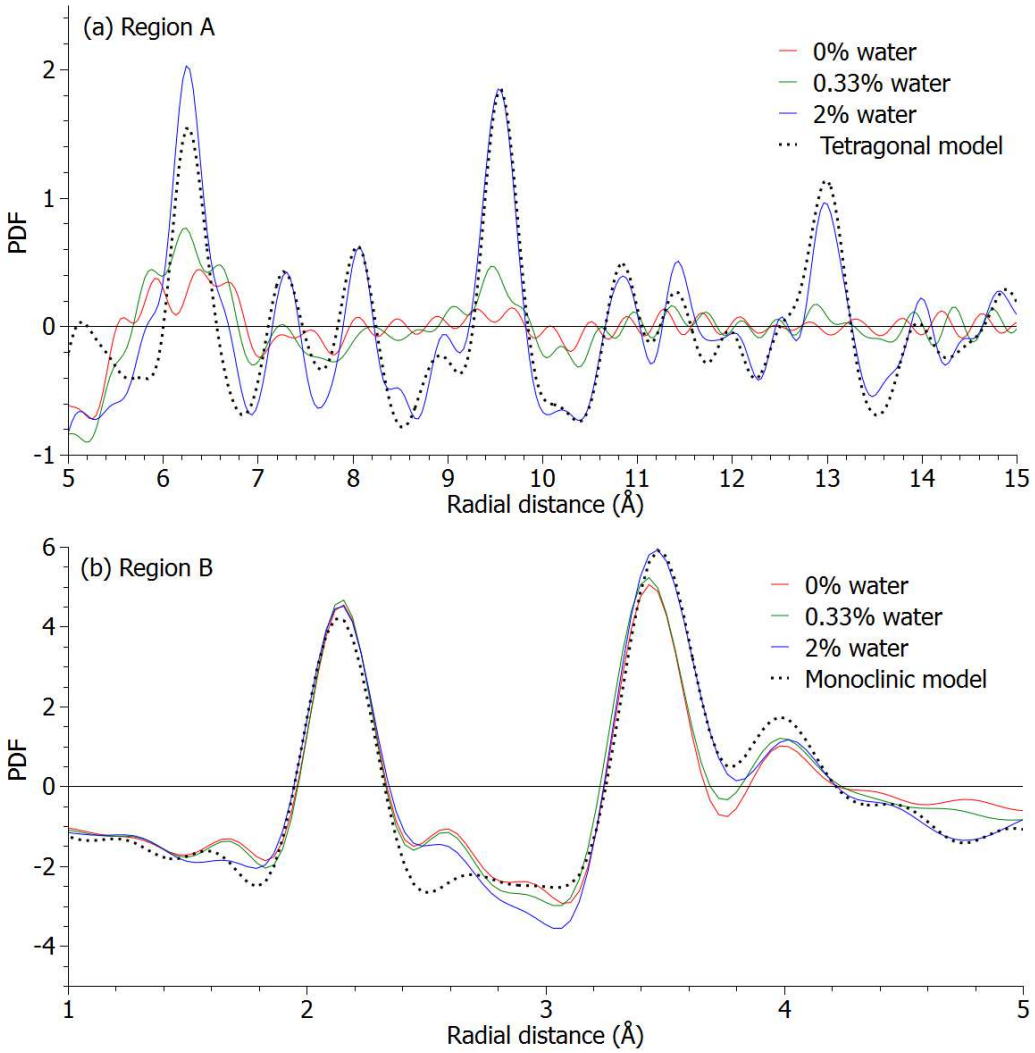

Figure 138: Detailed images of (a) Region A and (b) Region B for samples without NaOH under varied amounts of water.

Table 34: Refined PDF parameters for sample with 2% water and without NaOH using tetragonal model

parameters	**Reference** [88]	**Refined tetragonal**
Range (Å)	NA	5-25
R_w	NA	0.375
a(Å)	3.64	3.59
c(Å)	5.27	5.15
$R_t \frac{c}{a\sqrt{2}}$	1.023	1.014

Table 35: Refined PDF parameters for sample with 2% water and without NaOH using monoclinic model

parameters	**Reference** [87]	**Refined monoclinic**
Range (Å)	NA	0-5
R_w	NA	0.178
a(Å)	5.15	4.98
b(Å)	5.21	5.37
c(Å)	5.32	5.27
β(º)	99.23	97.47

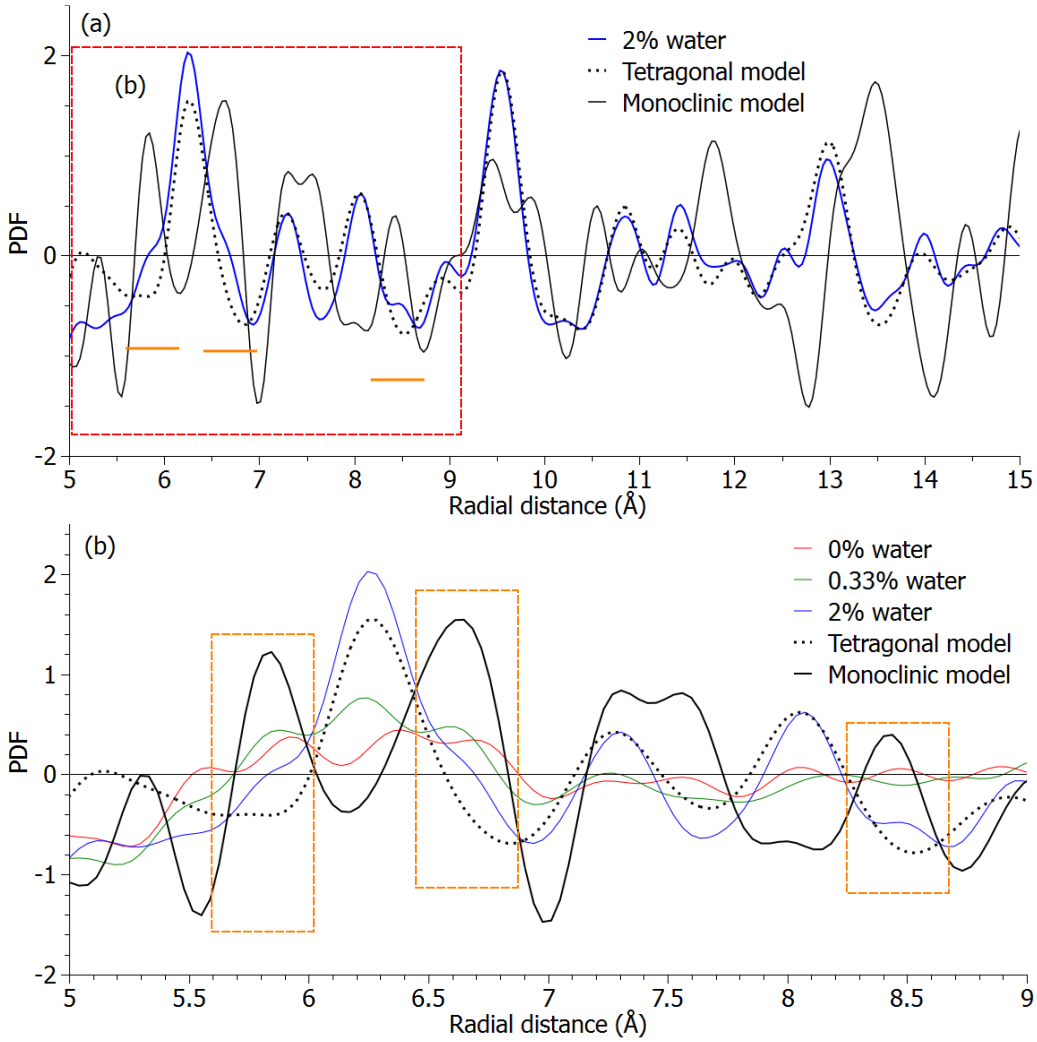

Figure 139: Experimental PDF of samples with 2% water volume content prepared at 210ºC in anisole without NaOH at the selected medium-range regions (a) 5 to 15 Å and (b) 5 to 9 Å.

4.1.14.4 Comparison of the zirconia samples with varied amounts of ex-situ water

Shown in Figure 140 are all the samples with and without the presence of sodium hydroxide. The addition of minute amounts of water appears to have consequential effects as indicated by the structural improvements. Although all the samples have a monoclinic phase feature at the short-range region, the structural changes appear to favor the transformation towards the tetragonal phase zirconia as shown in the medium-range region. Comparing these samples with the aged samples as shown in Figure 125, we observe that the presence of an alkali source promotes a much active restructuring effect in comparison to the samples without and it is evidenced by the samples' rapid transformation from an amorphous-like phase.

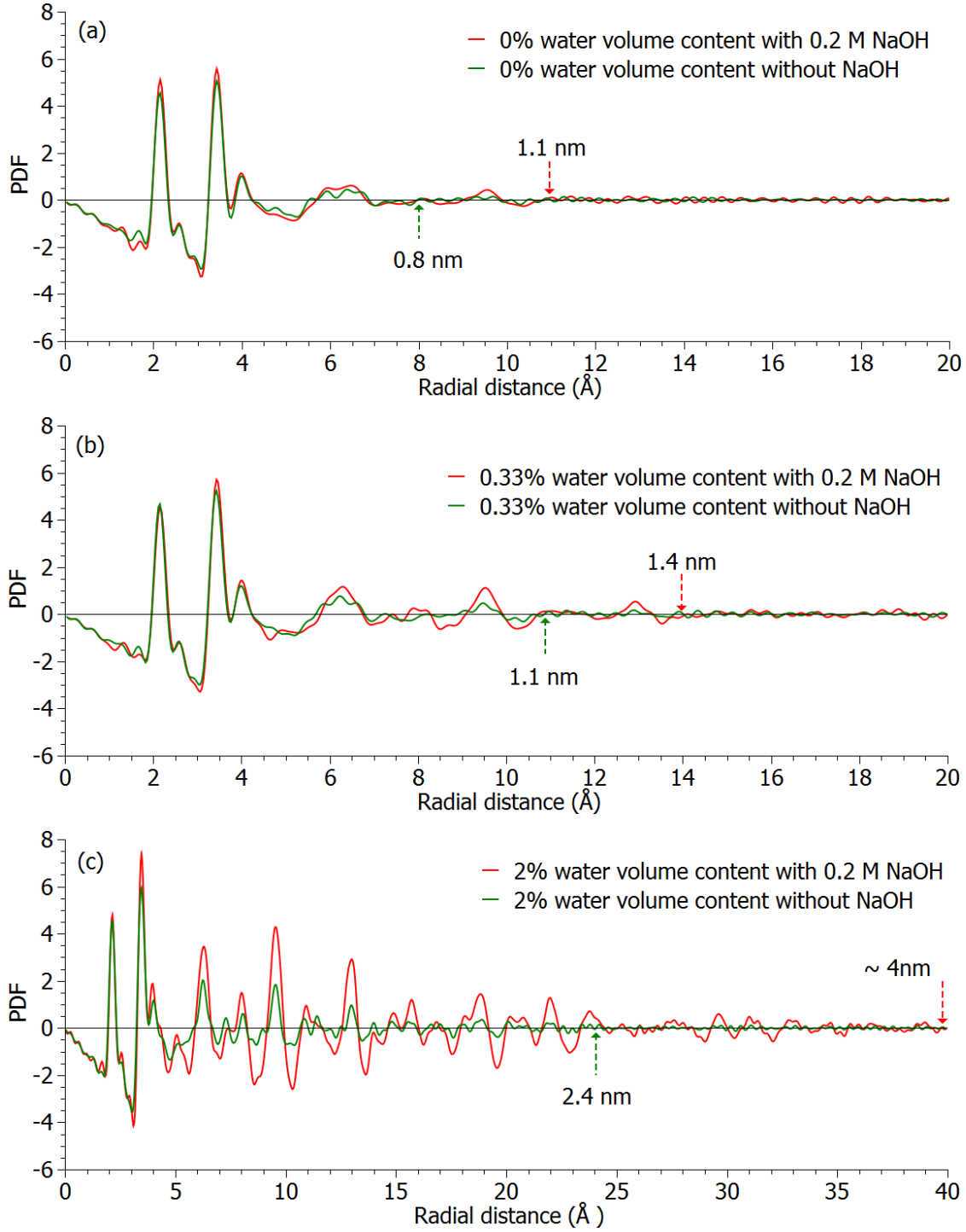

Figure 140: (a) Experimental PDF of the zirconia particles produced at 210°C in anisole without and with 0.2 mol.L^{-1} NaOH for (a) 0% water volume content, (b) 0.33% water volume content, and (c) 2% water volume content.

Shown in Figure 141, are the crystallite diameter sizes measured from XRD and PDF for both types of samples with and without NaOH. With the coherent diameter size measurements obtained via PDF, we are able to get a much better view of the trend of the crystallite sizes as the amount of added water is increased. Both types of samples show an increasing size and eventual formation of large monoclinic crystallites.

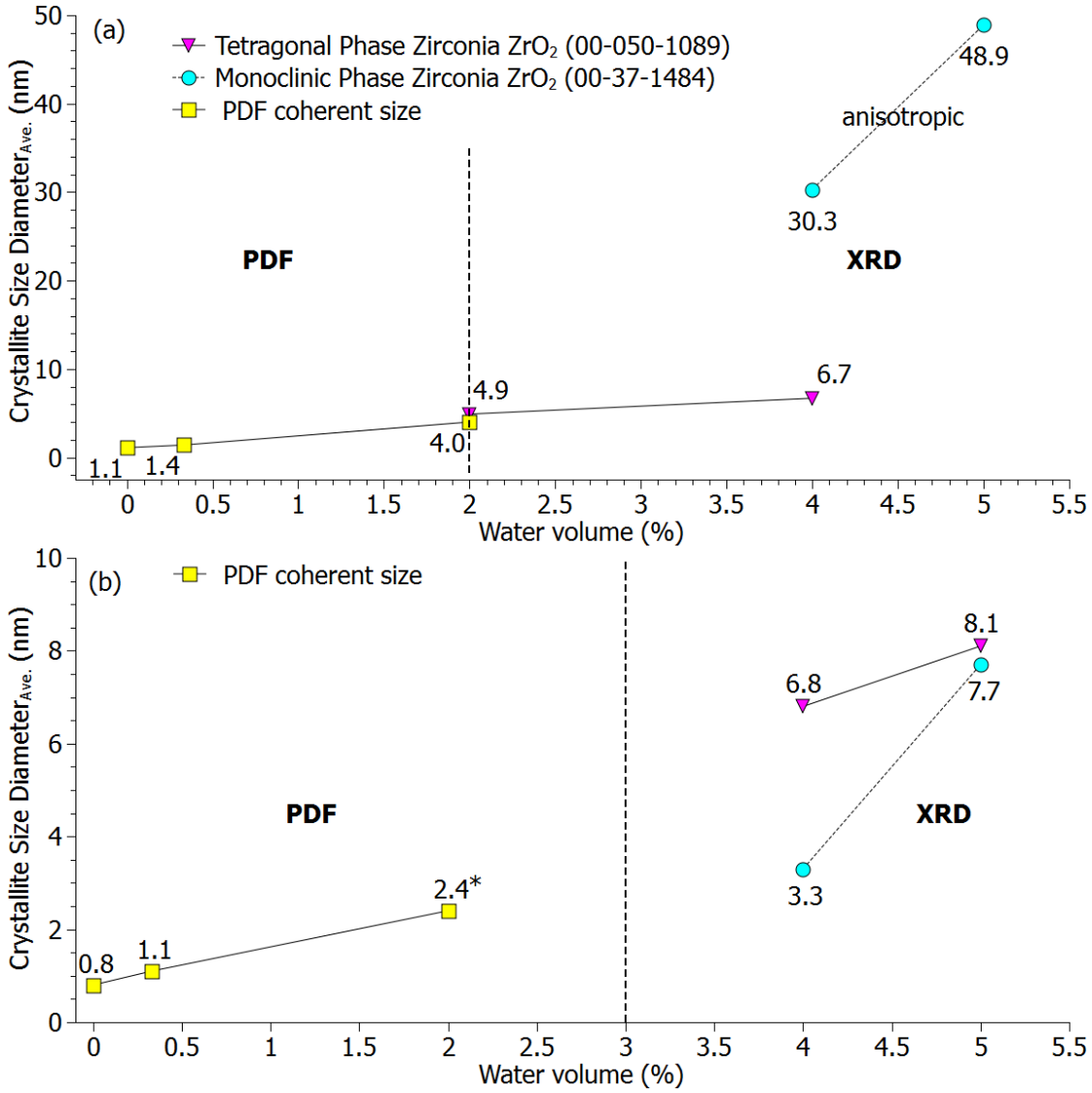

Figure 141: Average crystallite diameter sizes of the samples synthesized at 210°C for 3 days with varied volume percentage of water (a) with and (b) without 0.2 mol.L^{-1} NaOH (* minute presence of monoclinic phase)

For the samples with the presence of NaOH shown in Figure 141 (a), the absence of monoclinic phase within the average-range supports the idea that the presence of NaOH is able to inhibit the formation of monoclinic phase but limited to a critical amount of water (2% volume content). In contrast, the absence of NaOH showed in Figure 141 (b) promoted the expansion of the monoclinic phase in the medium-range region with added water as low as 2% volume content. This suggests that the broad peaks at 2% water volume content that were observed in XRD are evidence of monoclinic feature expanding towards the medium-range region and restructuring the tetragonal-like phase to accommodate the formation of the monoclinic phase.

4.7. Conclusion

Structural characterization via Rietveld and PDF of the selected zirconia samples prepared in benzyl alcohol, benzaldehyde and anisole with 0.2 mol.L^{-1} NaOH at 210^{o}C provided an important insight into their structural properties. Rietveld analysis of the zirconia powders prepared in benzyl alcohol that appears to have a tetragonal or cubic phase appearance, reveals that it is closely related to the former despite the ambiguous presence of the 102 peak. However, experimental PDF reveals that the sample has monoclinic feature at the short-range region while a tetragonal-like structure at the medium-range region. This kind of phase maybe limited only to nano-sized zirconia with diameter size around 5 nm.

The sample prepared in benzaldehyde with NaOH is confirmed to have a monoclinic structure according to its Rietveld and PDF results. The detailed analysis on the atomic structure by PDF reveal that its crystallite diameter size is less than the critical size as defined by Garvie. The implications of such case is discussed in the previous chapter (see Chapter 3).

Considering ultrasmall zirconia prepared in anisole with broad XRD peaks, it does not seem to conform to any of the known polymorphs of zirconia having a fluorite-derived structure. However, the PDF shows that the sample has a monoclinic feature at the short-range region and a large structural disorder in the medium-range region. When the samples were given a substantial amount of time to age under thermal condition the samples transformed into a familiar phase that is similar to the sample prepared in benzyl alcohol having a tetragonal-like structure at the medium-range region. This suggests that the sample may be an intermediate phase between an amorphous-like and tetragonal-like zirconia.

Thermally assisted ageing of the zirconia samples without the presence of NaOH induced the expansion of the monoclinic feature in the medium-range region. This result supports the idea that the presence of *in-situ* water that was formed via the dehydration of the tiny amounts of ispropanol is able to promote the formation of monoclinic phase zirconia. The addition of minute amounts of water induced phase transformation as shown by their XRD and PDF results. It is clear that for both types of sample, with and without the presence of NaOH, the presence of water has consequential effects even if it is only in minute amounts (0.33% and 2% water volume content). The inhibition of formation of monoclinic phase is observed for samples with the presence of NaOH but limited to about 2% volume content of *in-situ* water and higher than this amount leads to the formation of large particles with monoclinic phase.

Chapter 5: Discussion on the Factors Governing the Formation of Zirconia NPs

5 Discussion on the factors governing the formation of zirconia NPs

5.1 Chemistry of the phase selection

An alkaline-catalyzed non-aqueous route to the formation of zirconia nanoparticles has been presented and detailed in chapter 3. Pure tetragonal t-ZrO_2 or monoclinic m-ZrO_2 nanoparticles have successfully been achieved by the addition of at least 0.2 mol.L^{-1} NaOH respectively in benzyl alcohol or in benzaldehyde. We have seen that the alkalinity of the alcoholic medium allowed the activation of the sol-gel condensation. Indeed, such a pathway insured the formation of pure nanoparticles with desired average crystallite size whereas no trace of water was detected in the alcoholic supernatant. Conversely, the absence of NaOH in the case of benzyl alcohol medium lead to the formation of biphasic samples beside the presence of an aqueous phase. The presence of m-ZrO_2 nanocrystals in the samples prepared in pure benzyl alcohol or in alkalinized benzaldehyde was related to the generation of this aqueous phase. Indeed, the low temperature degradation (LTD) of doped or undoped t-ZrO_2 is well-known and seems to be active even at low temperature when the presence of a liquid or gaseous water phase is ensured. The appearance of water in the benzyl alcohol route was attributed to the dehydration of HO^iPr mediated by the growing surface of the zirconia nanoparticle acting like a catalyst whereas in the benzaldehyde route, such a presence was mainly attributed to the mechanism pathway itself due to the generation of hydroxide group during the aldol-condensation of organic molecules.

In the same chapter, relative sodium-to-zirconium molar ratios measured by ICP or XPS have shown a similar trend insuring that the majority of Na^+ lied on the surface of the particles inhibiting the possible dehydration of HO^iPr and limiting consequently the risk of water production. Moreover, we strongly believe that the presence of minute amount of sodium could not dope and stabilize the tetragonal phase of zirconia. Hence, we propose to investigate in this chapter the use of different alkali sources, namely sodium salts and various other alkaline salts, in order to precise whether the stabilization of the metastable phase in the NaOH-based alcohol route finds or not its origin in a doping mechanism involving the substitution for Zr^{4+} by Na^+ and the creation of oxygen vacancies or rather in the surface disruption of Lewis acid-base sites of the growing nanocrystals inhibiting isopropanol dehydration jointly to the Brønsted acid-base neutralization of any trace of water.

5.1.1 Effect of alkali cation-type on the formation of tetragonal zirconia nanoparticles

In order to investigate the ability for other alkali cations to direct the phase selection by doping zirconia network or by inhibiting the Lewis catalytic sites responsible for alcohol dehydration and LTD-like phase conversion, we decided to use different alkali hydroxides in replacement of NaOH. The XRD patterns of the samples produced in the case of LiOH, NaOH and KOH are presented in Figure 142.

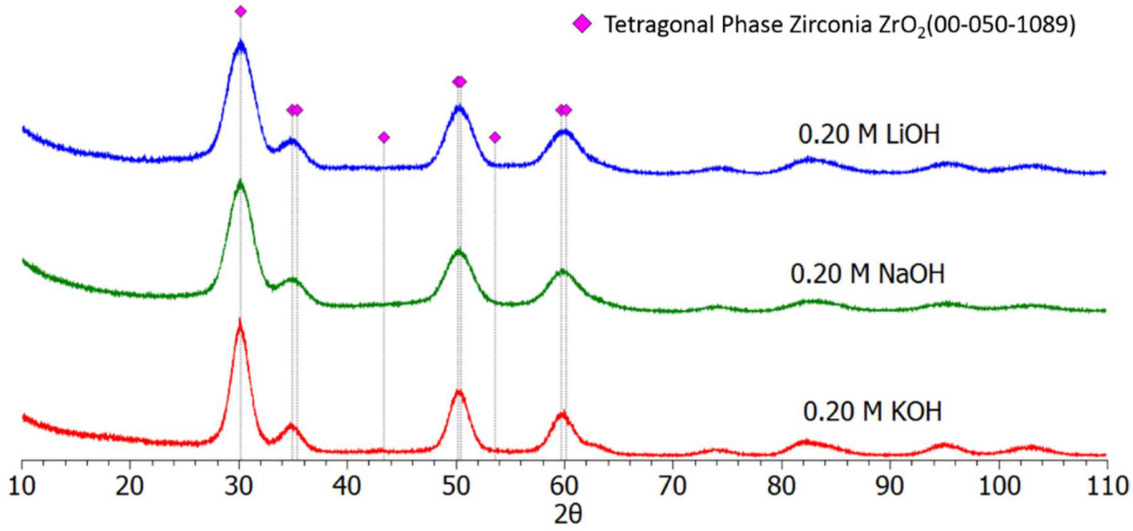

Figure 142: XRD patterns of samples obtained using $[Zr(O^iPr)_4 \cdot HO^iPr]_2$ in benzyl alcohol under varied types of alkali hydroxides *via* solvothermal technique at 210°C for 3 days.

The samples are exclusively composed of t-ZrO_2 nanoparticles and the phase selection process seems to be effective not only in the case of Na^+ but also with Li^+ or K^+. We cannot give a preference to one or another mechanism responsible for the phase selection, namely doping or inhibiting processes. Nevertheless, we can notice in Table 36 that the refined cell parameters are approximately the same whatever the type of cations and such feature does not fit well with a doping mechanism in a large extent. Indeed, the ionic radius of Zr^{4+} is 0.072 nm close to 0.076 nm the radius of Li^+, but Na^+ and K^+ are clearly larger with ionic radius of respectively 0.102 and 0.138 nm (K^+ is almost twice bigger than Zr^{4+}) and such substitution in a large extent should alter the average cell parameters to adapt the dissolution of such alkali cations into the network. Evidently, this is not a direct proof for a non-doping mechanism since the solubility of alkali cations into the

zirconia network can be rather small but allows anyway an effective phase stabilization due to the large generation of oxygen vacancies ($Na'''_{Zr} + \frac{3}{2}V_O^{\cdot\cdot}$).

If we consider the different apparent crystallite sizes which are reported in Table 37, we clearly see that the crystallites size is influenced by the type of alkali cation. The trend for the crystalline growth is monotonous and the larger crystallites are obtained in the case of the alkali with the larger atomic period. The main difference among the IA family group can be gathered in their ionic potential which represents the charge density of the cation, *i.e.* the global charge of the ion divided by its radius. Ionic potential gives a sense of how strongly or weakly the ion will be electrostatically attracted to ions of opposite charge. This scale is very useful in understanding the behavior of relatively hard cations like alkali cation Li^+, Na^+, K^+ or even Zr^{4+} following the HSAB principle (hard-soft acid-base).

By calculating the ionic potential for the cations of the IA group using ionic radius in nm (Li^+=13.2; Na^+=9.8; K^+=7.2), we can see that the Li^+ possesses the largest potential among the alkali cations. If we consider the ability for the alkali cation to bind onto the surface, the largest interaction will be obtained in the case of Li^+ and this could be the reason why the average apparent size is the smallest in the LiOH-system compared to the KOH-one. From the point of view of the sol-gel condensation, the addition of a new monomer, *i.e.* highly nucleophile zirconate group $(RO)_3Zr\text{-}O^-$, requires the displacement of the cation which acts as a terminal blocking agent. The displacement will be much easier than the electrostatic interaction between the cation and the zirconia network is weaker. In other words, the growth of the particle will be promoted in the case of the cation exhibiting the weakest interaction with the particles and then the lowest ionic potential.

Table 36: Refined parameters for the different cations from group IA

parameter	Reference [88]	LiOH	NaOH	KOH
a	3.64 Å	3.611(3) Å	3.617(3) Å	3.613(1)
c	5.27 Å	5.144(6) Å	5.136(6) Å	5.161(3)
$R_t \ \frac{c}{a\sqrt{2}}$	1.024	1.007	1.004	1.011
O_z	0.185	0.1931	0.1929	0.1969
χ^2	NA	2.035	1.476	1.976

Table 37: Ionic radius of cations from group IA

Cation	Ionic radius (nm)	Crystallite apparent size of ZrO_2 (nm)
Lithium (Li^+)	0.076	2.73
Sodium (Na^+)	0.102	3.03
Potassium (K^+)	0.138	3.74

The results of this section have shown that the selection process is not exclusively restricted to the use of NaOH and could be extended to other alkali hydroxide. The origin for the phase selection is not unambiguously solved but another argument for the alkali cations to inhibit isopropanol dehydration has been evidenced by the significant increase of the crystallite size by varying the alkali source from LiOH to NaOH and finally KOH. An interpretation of this fact was done using the ionic potential of the alkali cation in electrostatic interaction with the growing nanoparticle.

5.1.2 Effect of the nature of different bases on the formation of zirconia nanoparticles

So far, we have only used NaOH or other alkali hydroxides for the synthesis of zirconia nanoparticles. Nevertheless, Portal *et al.* has shown that the use of sodium metal generating sodium benzoxide base was also effective in the phase selection process. In this section, we have used distinct type of base precursors and observed their effects on the phase purity of the zirconia

samples. The XRD patterns of the samples prepared in benzyl alcohol using different types of base are gathered in Figure 143. All samples are roughly estimated to be composed of t-ZrO_2 nanoparticles. Comparing Figure 143 (a) and (b), it appears that NaOMe is as effective as NaOH in avoiding the presence of m-ZrO_2 nanocrystals into the samples since the XRD patterns exhibit similar features specifically a comparable broadness of the peaks. When Na^+ cation is replaced by tetra-n-butylammonium $(TBA)^+$ keeping jointly the methoxide group as shown in the comparison of Figure 143 (b) and (c), we observe that the sample appears to be also composed by t-ZrO_2 nanocrystals in the absence of Na^+. This implies that the proposition for a Na+ doping of the zirconia network is not the reason for the phase selection to occur since voluminous tetra-n-butylammonium $(TBA)^+$ cations could not substitute for Zr^{4+} inside the oxidic network. The large broadness of the XRD peaks observed for the sample (c) could be explained by the steric hindrance effect induced by the $(TBA)^+$ cations capping onto the surface. Such a capping effect is known to be responsible for limited growth of nanoparticles in the case of a surfactant-controlled synthesis route and we can expect that the t-ZrO_2 nanocrystals of sample (c) are comparably smaller with the ones prepared with sodium-based alkaline precursors (a) and (b).

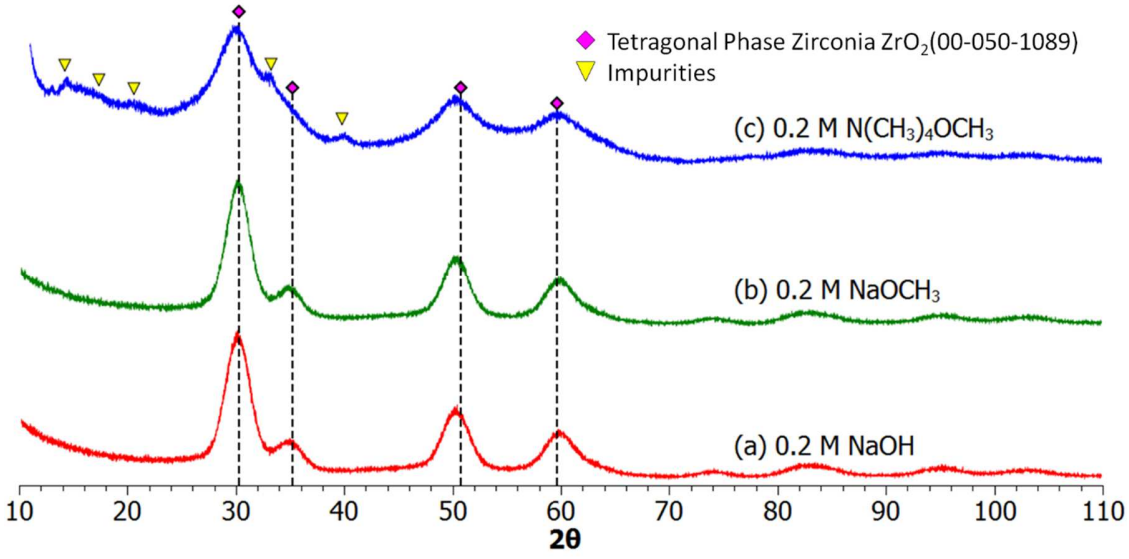

Figure 143: XRD patterns of samples prepared via a solvothermal technique at 210°C for 3 days using $[Zr(O^iPr)_4 \cdot HO^iPr]_2$ in benzyl alcohol with 0.2 mol.L^{-1} (a) NaOH, (b) $NaOCH_3$ and (c) $N(C_4H_9)_4OCH_3$ or TBAOMe (tetra-n-butylammonium methoxide solution 20% in methanol).

By analyzing these three samples we can now assume that the presence of $(TBA)^+$ cations would act like in the case of Na^+ by capping the acidic sites of ZrO_2 nanocrystals and then inhibiting the

dehydration of HO^{i}Pr. It is interesting to note that such a large cation can effectively confer more steric hindrance to the surrounding of the nanoparticles surface and then reduce the size of the particle by limiting effectively the growth. The effect of TBAOMe base will be investigated in the near future in our group especially the imaging of the obtained nanoparticles by cryo-TEM. Finally, the possibility of using either NaOH or NaOMe raises the question whether the role of NaOH is attributed to a direct interaction between the Lewis acid-base sites of the nanoparticles at the surface or to a the desiccation of the reaction medium due to the Brønsted acid-base neutralization between NaOR (issued from the basic catalysis of the non-aqueous sol-gel route) and traces H_2O regenerating NaOH reagent or simply to a combination of both strategies.

5.1.3 Effect of sodium counter-ions on the formation of zirconia nanoparticles

In this section we investigate whether the presence of the phase selection towards tetragonal polymorph of zirconia is exclusively limited to the use of sodium base namely whether the counter-ions type is playing a role in the selection process. The different sodium salts used in this study are listed in Table 3.

Table 38: Sodium salts used in the synthesis of modified benzyl alcohol route (0.2 mol.L^{-1})

(a) Halides	**(b) Nitrate & (c) sulfate**	**(d) Alkoxides**	**(e) amide**
sodium fluoride (NaF) sodium chloride (NaCl) sodium bromide (NaBr)	sodium nitrate ($NaNO_3$) sodium sulfate (Na_2SO_4)	sodium methoxide ($NaOCH_3$) sodium ethoxide ($NaOC_2H_5$) sodium isopropoxide ($NaOCH(CH_3)_2$)	sodium amide ($NaNH_2$)

The XRD patterns for the halide-based precursors are gathered in Figure 144 (a_1-a_3). Sodium halides (a_1 and a_2) except for sodium fluoride (a_3) exhibited no effect on the phase selection of the ZrO_2 nanoparticles. We also observe in the patterns of the samples (a_1 and a_3) the presence of extra thin diffraction peaks which are undoubtedly attributed to some remaining sodium halide precursors. These impurities could be due to an incomplete washing process. Considering the bi-phasic samples, the appearance of monoclinic phase suggests that *in-situ* water was formed and able to promote the tetragonal to monoclinic transformation *via* LTD process. Sodium fluoride is

definitively an exception to this trend since a phase selection process is clearly promoted in this specific case. Indeed, the XRD pattern of sample (a_1) only exhibits the diffraction peaks of t-ZrO_2 nanoparticles together with those of a remaining fraction of sodium fluoride.

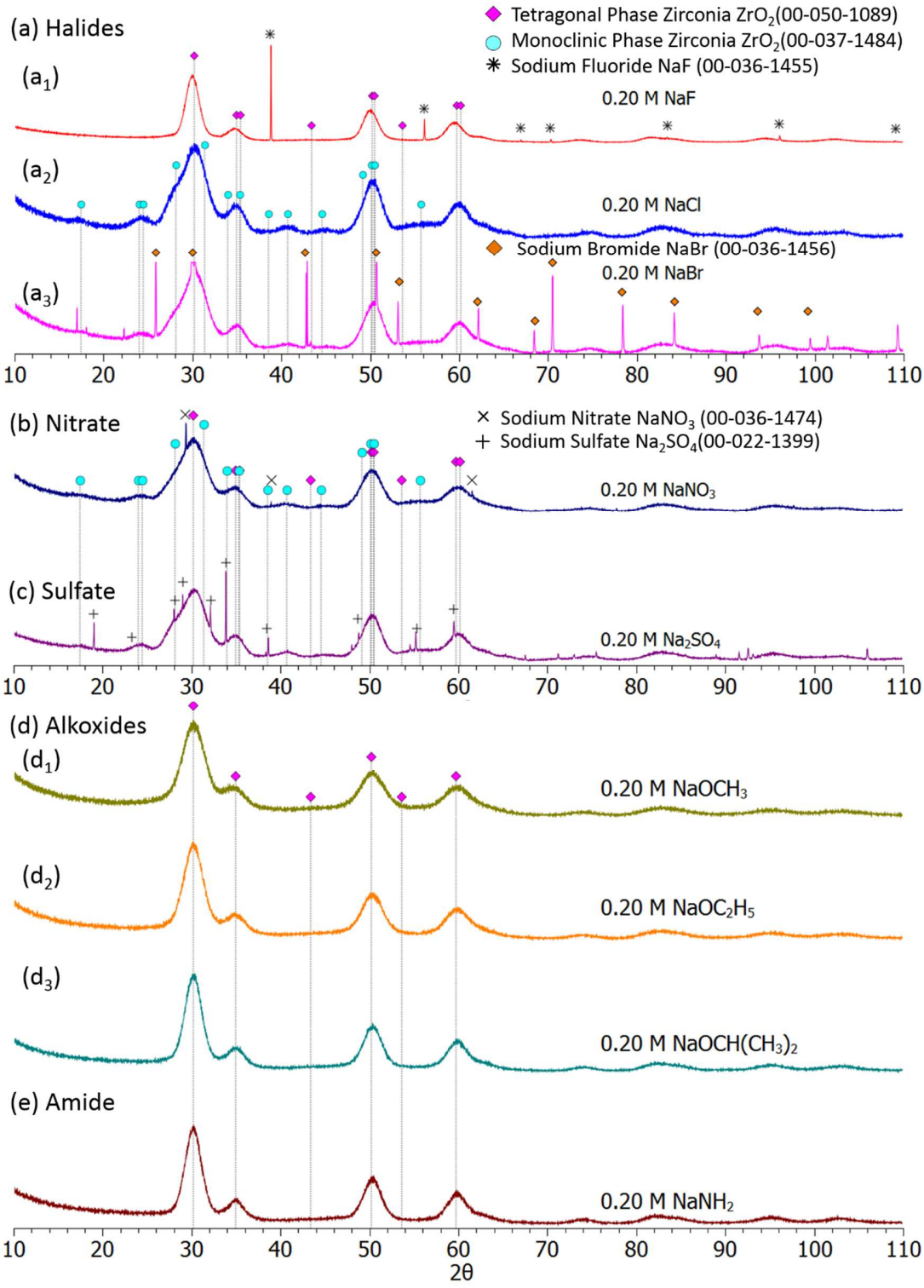

Figure 144: XRD patterns of samples obtained via a solvothermal technique at 210°C for 3 days using $[Zr(O^iPr)_4 \cdot HO^iPr]_2$ in benzyl alcohol and varied Na sources: (a_1-a_3) halides, (b) nitrate, (c) sulfate, (d_1-d_4) alkoxides, and (e) amide.

This fact is not surprising since fluoride anion is a highly active reagent in sol-gel routes and its action is as comparable to the effect of HO^- as Corriu *et al.* has evidenced in his work [171]. The F^- which is about the same size of OH^-, has the ability to increase the coordination and to activate the metal center as shown in Figure 145. Moreover, fluoride ion is a weak Brønsted base in water and alcohols and fluoride salts are well-known to be some excellent mineralizers in hydro- or solvothermal treatments. For all these reasons we can reasonably think that NaF has the same behavior and effective power than NaOH in the phase selection process.

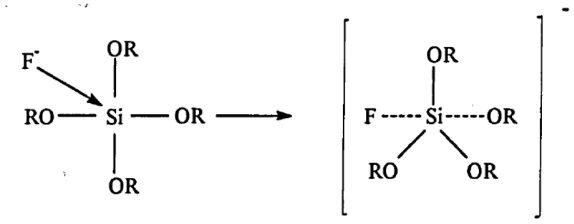

Figure 145: Fast reversible formation of a pentavalent intermediate by the presence of F^- [171].

For the sodium nitrate and sodium sulfate cases, no phase selection was promoted as shown in Figure 144 (b & c). This suggests that the use of any sodium-based salt in the reaction mixture is not enough to prevail the LTD conversion process to occur. At first view, the sodium presence seems to be accompanied with a Brønsted base but this assumption is not totally relevant since chloride ion reveals a basic activity in alcohol, a less dissociative solvent than water.

Like in the cases of the sodium halide samples, it appears that the samples also contain some remaining traces of sodium salt which were not fully removed during the washing process but the procedure can easily be improved.

For all the sodium alkoxide-based samples, the XRD patterns exhibit a t-ZrO_2 single phase as shown in Figure 144 (d_1 - d_3). This suggests that the action of the alkoxides is comparable to the hydroxides. This fact completes the idea of Portal *et al.* that the non-aqueous sol-gel route was promoted by a larger metal-ligand exchange of isopropoxide groups by benzoxide ones and a benzoxide-activated ether-elimination. Indeed, not only benzoxide species are needed to operate the phase selection of the t-ZrO_2 nanoparticles. We have evidenced up to now that the formation of pure t-ZrO_2 samples could be achieved using alternatively either sodium hydroxide, sodium

alkoxides or sodium fluoride. We have to notice that the length and the ramification of the alkyl seems to play a role on the apparent crystallites size achieved in each cases since the broadness of the diffraction peaks are not systematically the same in the cited samples.

The last type of sodium source which has been used is the sodium amide and the obtained XRD pattern of the sample is shown in Figure 144 (e). It is observed that the pattern exhibits a single t-ZrO_2 feature similar to that obtained with the use of the various sodium alkoxides. We wanted to investigate with this last compound the effectiveness of a stronger base than alkoxides. Nevertheless, we have to keep in mind that amide ions can finally acting like alkoxide groups by deprotonating protic hydrogen of alcohol, metal precursor, or even water to generate respectively alkoxide, highly nucleophilic zirconate function or sodium hydroxide together with anhydrous ammonia, a basic catalyst frequently used in sol-gel processing (see Equations (56), (57) and (58)). So finally this last situation due to these acid-base-like reactions goes back to the cases of a sodium alkoxide-catalyzed system.

$$NaNH_2 + ROH \rightleftarrows NaOR + NH_3 \quad (56)$$

$$NaNH_2 + Zr\text{-}OH \rightleftarrows Zr\text{-}ONa + NH_3 \quad (57)$$

$$NaNH_2 + H_2O \rightleftarrows NaOH + NH_3 \quad (58)$$

The average apparent sizes of the nanoparticles synthesized with various sodium sources are plotted in Figure 146.

Because of the presence of sodium salts impurities some of the results are less reliable compared to the others but for the sake of this discussion we consider their approximate values with same reliability as the refined ones.

(i) The crystallites sizes of the bi-phasic sodium halide samples are comparably smaller with respect to the average size measured in the sodium fluoride sample as shown in Figure 146 (halides). However, both bi-phasic halides have similar sizes of their tetragonal and monoclinic particles.

(ii) For the nitrate and sulfate samples, the latter have larger apparent size in comparison with the former as shown in Figure 146 (nitrate and sulfate). But both are within the same range as the other bi-phasic samples prepared using sodium halides.

(iii) For the samples prepared with sodium alkoxides (Figure 146 (alkoxides)), we have found an important effect of the length and ramification of the alkyl chain on the final apparent size. The rationalization of the effect is difficult to extract since the inductive effects and the steric effects depend on the ramification degree of the chain, they are not necessary equivalent and can sometimes be antagonistic. For the ethoxide groups, we could say that the catalytic power and nucleophilicity are moderated whereas for the isopropoxide groups, we observe a good catalytic power but finally a poor steric effect since the apparent size of the nanoparticles is larger.

(iv) Lastly, for the sample prepared with sodium amide, its size appears to be larger compared to the samples prepared using sodium alkoxides and this could be attributed to the generation of ammonia during the acid-base neutralization of the amide ion since ammonia is an effective simultaneous Brønsted and Lewis base.

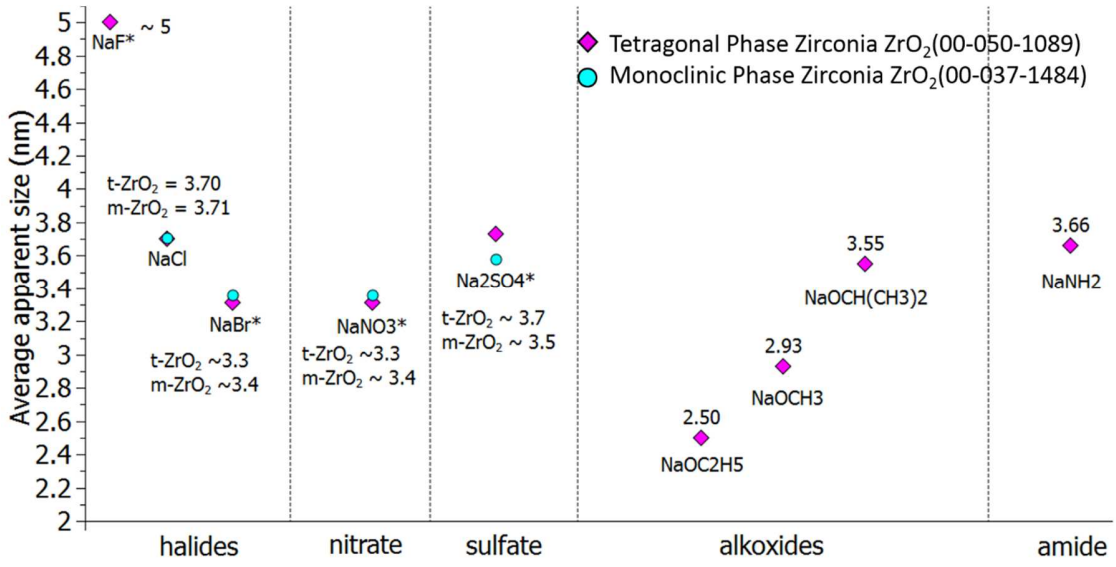

Figure 146: Phases and crystallites sizes for the different cases of sodium precursors. * low reliability due to remaining sodium salt.

If we examine the results obtained in the different cases of sodium precursors in terms of hard and soft Lewis acid and base (HSAB) concept, only hard Lewis bases seem to promote effectively the phase selection process. Indeed, final bi-phasic samples are obtained in the case of sodium borderline base (Cl^- , Br^- , NO_3^-, and SO_4^{2-}) salts. The disruption of the Lewis acid-base sites of

zirconia seems to be limited to the cases where hard acidity and hard basicity are conjugated and only the interplay of both features is effective in the selection phase process. The Figure 147 show the comparison of properties of the different counter-ions used in this study.

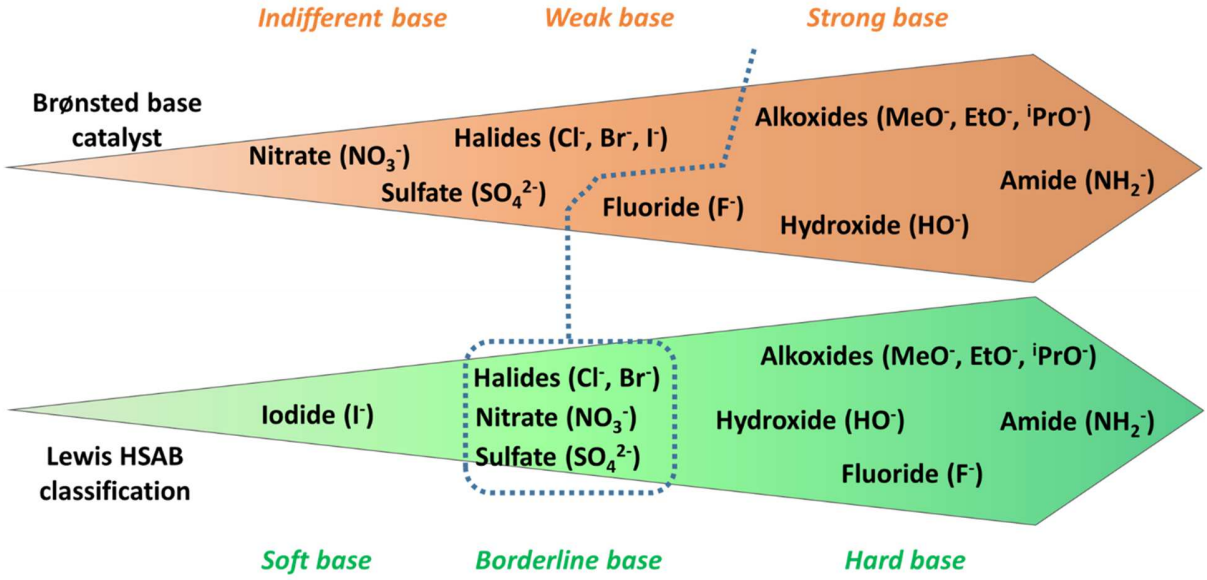

Figure 147: Classification of the sodium counter-ions used in the study: first scale respecting the Brønsted acid-base tendency, second scale respecting Lewis acid-base tendency and hard-soft acid-base principle (HSAB).

5.1.4 Conclusion on the phase selection process

The investigation of this first part based on the use of different types of alkali-salts provided an insight regarding the stabilization of the nanosized metastable t-ZrO_2 and the absence of m-ZrO_2. By replacing the NaOH with an organic base or other alkali bases, we have ruled out the possibility of the doping process as the mechanism in the stabilization of the tetragonal phase.

The different types of result obtained using different varieties of sodium sources suggests that the governing rule for an acid-base salt to be able to promote a phase selection process is related to the HSAB principle. Regarding the absence of water, two possible scenarios schematically represented in the Figure 148 could explain why in the final supernatant there is no presence of water:

- First, the presence of the hard Na^+ (also other alkali cations or even tetrabutylammonium cation) caps the surface of the growing particles and disrupts the Lewis acid-base surface sites which are necessary for the low thermal dehydration of isopropanol.
- Second, the water is simply neutralized by its interaction with the alkoxides acting like a desiccating side-reaction.
- Also, we cannot dismiss the possibility that both types of reactions occurred during the synthesis in order to effectively prevent the action of *in-situ* water.

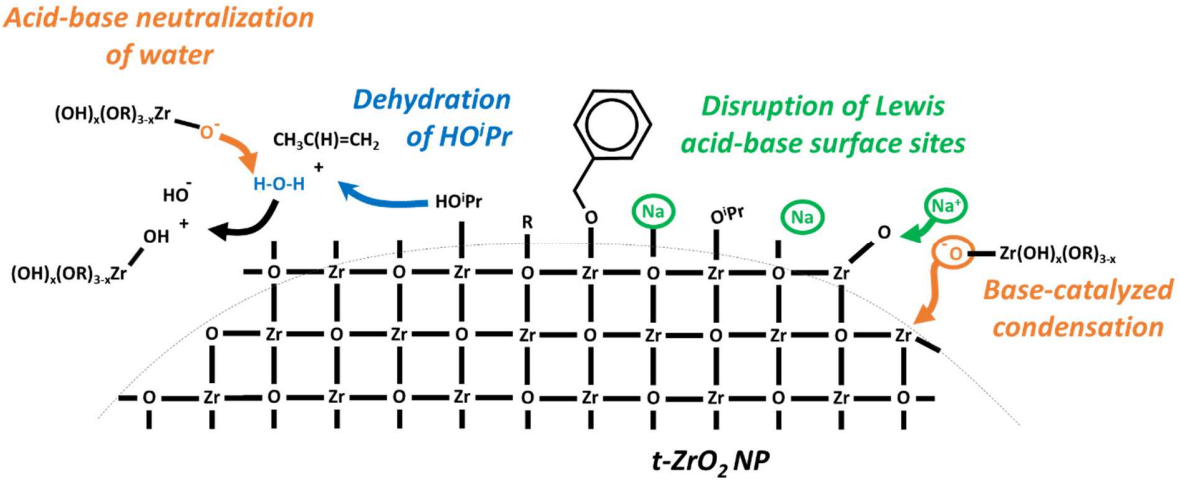

Figure 148: Schematic representation of the two types of inhibition or neutralization of water.

Finally, we propose a new lecture of the phase selection process in the presence or not of an effective hard-hard acid-base salt:

- *The only way to reconcile the effects of both hard acid Na^+ and hard base X^- is to consider that the surface interaction of sodium on the nanoparticle is not sufficient to completely inhibit the dehydration of isopropanol. However, the hard base generates reactive species capable of neutralizing traces of water during the sol-gel process and avoids any risk of LTD-like mechanism for the metastable t-ZrO_2 nanocrystals.*
- *In the case of the borderline bases which have not generated some alkoxide groups able to neutralize water, the dehydration of the isopropanol is only partially inhibited and the appearance of water ends up inducing strong structural modifications on the nanoparticles. It is legitimate to consider that the released water will first hydrolyze the surface Na^+ ions*

and release more and more active Lewis surface sites so that the dehydration of the alcohol intensifies. During the ageing of the reaction mixture, the aqueous phase thus produced will not only be sufficient to leach the surface of the particles but will also cause a hydrolysis of the zirconia network initiating the LTD-like process and lead to the formation of m-ZrO_2 nanocrystals.

The effectiveness of the sodium hydroxide addition has been shown to be the key for the production of zirconia NPs sample in either an alcohol-rich or an alcohol-limited environment. By allowing a phase selection process to occur and jointly by promoting the condensation of the sol-gel process, NaOH has exhibited to play two fundamental roles in the formation of pure and well-crystallized nanoparticles. In the case of an alcohol-limited environment, NaOH was essential to insure the base-catalyzed condensation supplanting the conventional ether-elimination mechanism. The second and last part of the chapter 5 will deal with effect of the reaction medium in the ageing of the nanoparticles.

5.2 Restructuring effect

5.2.1 Introduction

Firstly, we have to recall the possible chemical reactions involved during the synthesis as supported by the experimental results and analysis from Chapters 3 and 4 (Table 39). Three main samples were selected and obtained by using zirconium isopropoxide-isopropanol adduct as the zirconium source and either benzyl alcohol with or without 0.2 $mol.L^{-1}$ sodium hydroxide or anisole with 0.2 $mol.L^{-1}$ sodium hydroxide as solvent. The principal reactions are summarized in the Figure 149 and discussed briefly.

Table 40: Different possible reactions involved during the non-aqueous sol-gel route synthesis

DIRECT REACTION		REVERSE REACTION
Ether elimination	$Zr-OR+R'O-Zr \rightleftarrows Zr-O-Zr+ROR'$ $R, R' = Bn \text{ or } {}^{i}Pr$	Etherolysis
Non-hydrolytic hydroxylation	$NaOH+RO-Zr \rightleftarrows Zr-OH+NaOR$	Esterification
Base-activation of hydroxide group	$Zr-OH+NaOR \rightleftarrows Zr-ONa+ROH$	Protonation of oxide group
Base-catalyzed condensation	$Zr-ONa+XO-Zr \rightleftarrows Zr-O-Zr+NaOX$ $X = R \text{ or } H$	Alkaline depolymerization of the oxidic network
Olation	$Zr-OH+Zr \leftrightarrow (ROH) \rightleftarrows Zr-O(H)-Zr+ROH$	μ_2-OH, $2\mu_2$-OH, $3\mu_2$-OH or μ_3-OH
Oxolation	$Zr-OH+HO-Zr \rightleftarrows Zr-O-Zr+H_2O$	Hydrolysis of the oxidic network
Water neutralization	$H_2O+NaOR \rightleftarrows NaOH+ROH$	Alcohol dehydration
Alcoxolation	$Zr-OH+RO-Zr \rightleftarrows Zr-O-Zr+ROH$	Alcoholysis of the oxidic network

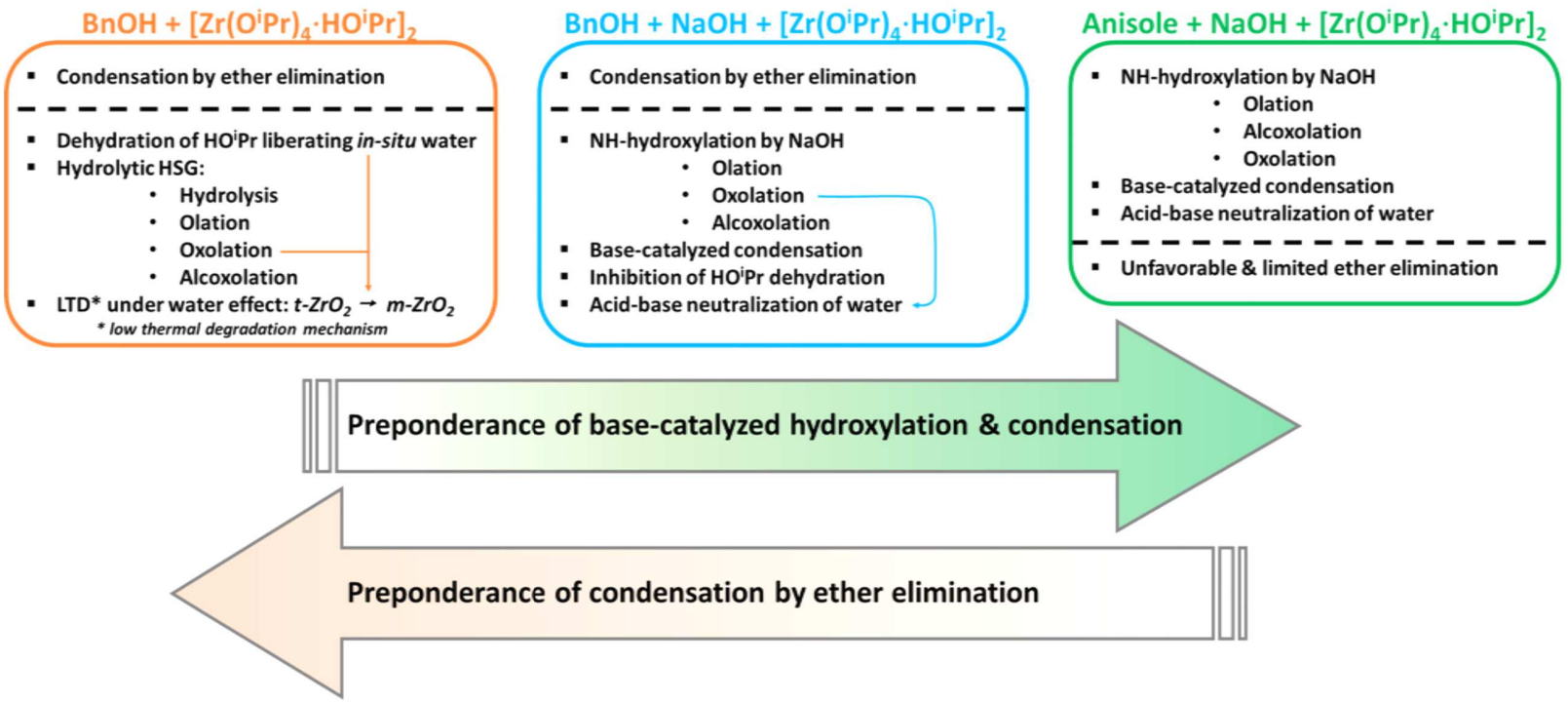

Figure 149: Schematic summary of the three main systems based on the permutation of solvent and sodium hydroxide.

For the sample prepared without the presence of sodium hydroxide, the resulting product was a bi-phasic (tetragonal-like and monoclinic phase zirconia) whereas for the sample prepared with NaOH the resulting product was essentially pure tetragonal-like zirconia.

(1) Under benzyl alcohol without NaOH, the major reactions towards the formation of the metal oxide bonds are the ether elimination and the hydrolytic sol-gel reactions. Indeed, the dehydration of isopropanol produces *in-situ* water accompanied with propene and promotes hydrolytic sol-gel reactions such as olation, oxolation, and alcoxolation. Aside from promoting hydrolytic sol-gel reactions, the presence of *in-situ* water also induces the tetragonal to monoclinic transformation which gives reason to the bi-phasic characteristic of the zirconia samples prepared in benzyl alcohol without NaOH.

(2) Considering the zirconia samples prepared using benzyl alcohol with the presence of sodium hydroxide. As what we have discussed in Chapter 3, the dominant reaction remains to be ether elimination but with the presence of an alkali source it is accompanied by other reactions such as base-activated non-hydrolytic hydroxylation and condensation. Other minor reactions such as olation, oxolation, and alcoxolation are also possible. The absence of m-ZrO_2 nanoparticles could be brought about by the inhibition of the dehydration of isopropanol jointly to the acid-base neutralization of any traces of water by sodium alkoxide and then the prevention of any LTD-like process.

(3) For the sample with sodium hydroxide but without the presence of abundant benzyl alcohol, the dominant reactions are now the base-catalyzed reactions which are the base-activated non-hydrolytic hydroxylation and condensation. The ether elimination is still possible but as a minor reaction due to the limited presence of isopropanol and benzyl alcohol.

The crystallization process involves the good interplay of the forward and reverse reactions allowing an effective restructuring process. If we compare the samples with alkalinized benzyl alcohol or anisole, we note that the zirconia sample prepared in benzyl alcohol exhibits a much better crystallization according to its XRD, TEM, and PDF analyses. This suggests that the etherolysis for the sample prepared in abundant ether (anisole) is less efficient compared to the alcoholysis for the sample prepared in abundant alcohol (benzyl alcohol) in achieving a larger ordering of the oxidic network. In the following sections, we will guide the discussion on the effects of restructuration occurring during the formation and the thermal ageing of the nanoparticles.

5.2.2 Restructuring effect under varied ageing periods

In Chapter 4, we have studied finely the samples prepared with or without NaOH and aged for various durations. We have observed that in an alcohol-deficient environment the building and the restructuring of the oxidic network required a longer ageing period in order to observe any significant changes. The catalytic role of NaOH has been clearly evidenced but the capability for the nanoparticles to undergo a progressive change is strongly limited by the reaction medium due to the progressive release of various active organic molecule occurring throughout the process and finally the classic dissolution-reprecipitation process currently involved in Ostwald ripening. Indeed, over time the presence of active ether and isopropanol becomes step by step more abundant, possibly due to alcoxolation or ether elimination even the non-hydrolytic hydroxylation, which supports the restructuring effect. Indeed, these effects become more observable after 12 and 24 days ageing period for the non-alkaline system and already after 3 days of solvothermal treatment for the alkaline-catalyzed system. It was clear and it is schematically represented in Figure 150 that thermally-assisted ageing improved the structural features of all the samples from an amorphous-like structure to a tetragonal-like structure with only minor reminiscence of local monoclinic distortion and the presence of NaOH is invaluable in inducing a much better and shorter crystallization with good phase purity.

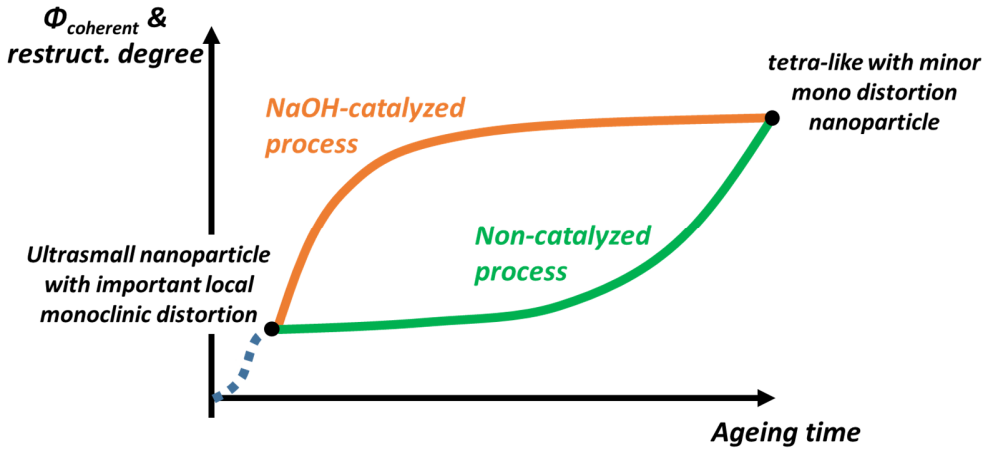

Figure 150: Schematic representation of the two types of restructuring and Ostwald ripening under alkaline or non-alkaline medium from amorphous-like to tetragonal-like zirconia nanoparticles.

5.2.3 Restructuring effect under varied solvents

In this section we have decided to investigate whether the restructuring effect is exclusively limited to benzyl alcohol route. The details for the syntheses performed with 0.2 mol.L^{-1} NaOH and 3 days of solvothermal treatment at 210°C for varied types of solvent are given in Table 9.

Table 41: Synthesis details for the chemical treatment with varied solvent content

NaOH (mol.L^{-1})	Zirconium (mol.L^{-1})	Type of solvent	Ageing time (days)
0.2	0.3	Anisole	3.0
0.2	0.3	Diisopropyl ether	3.0
0.2	0.3	Dibenzyl ether	3.0
0.2	0.3	Ethanol	3.0
0.2	0.3	Isopropanol	3.0
0.2	0.3	Benzyl alcohol	3.0

The XRD patterns corresponding to the different solvents are shown in Figure 151. Ignoring the presence of some inorganic impurities, the samples prepared under various types of alcohol were composed of t-ZrO_2 nanoparticles. This suggests that the restructuring effect is not limited to benzyl alcohol or alcohols having an aromatic and primary alcohol class but also works well with aliphatic or ramified primary and secondary alcohols.

For the samples prepared under varied ethers, we observe only some minor differences in their characteristic peaks but remain to have a large broadening of the peaks profile. Only the sample prepared in dibenzyl ether seems to be more evaluated since the profile expresses more distinctly the feature of t-ZrO_2 with large peak broadening. Compared to alcohols, ethers are definitively less effective and lead to a lowest degree of restructuring giving the idea that alcoholysis is more competitive than etherolysis in the process. Finally, we can distinguish some slight difference in the efficiency of the ether. Anisole is ineffective to promote restructuring since etherolysis is not possible. Only diisopropyl ether and dibenzyl ether can cleave and promote etherolysis and it seems that dibenzyl ether is more effective than diisopropyl ether probably due to the strong mesomeric effect promoted by the aromatic ring.

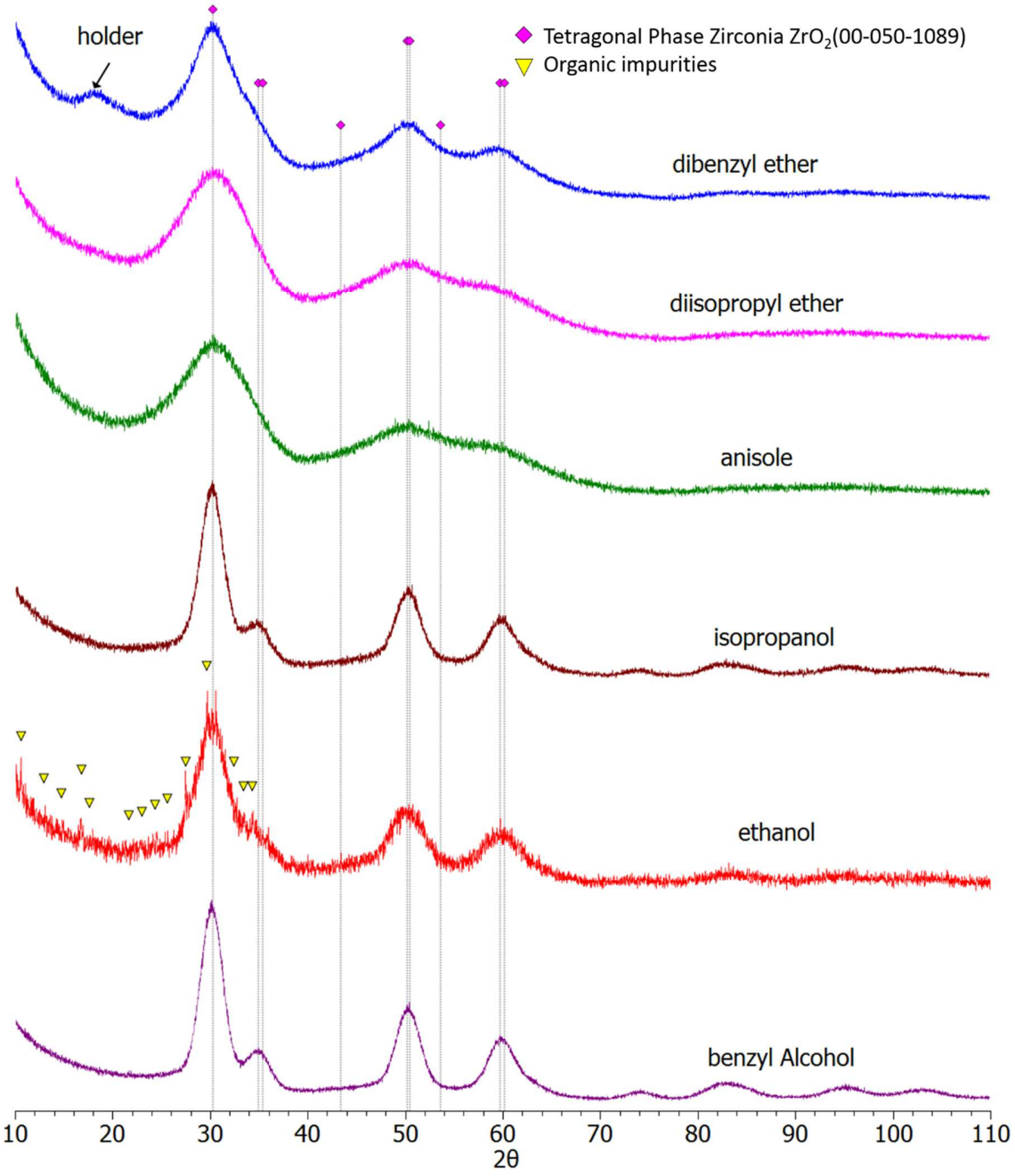

Figure 151: XRD patterns of zirconia samples prepared via a solvothermal technique at 210°C for 3 days using $[Zr(O^iPr)_4 \cdot HO^iPr]_2$ and 0.2 mol.L^{-1} NaOH under various solvents.

If we use the sample prepared in anisole (containing at least 1 equivalent of isopropanol for 1 equivalent of zirconium precursor) as a standard we can establish the relative scale of efficiency for the restructuring process promoted by the reaction medium as it is schematically represented in Figure 152.

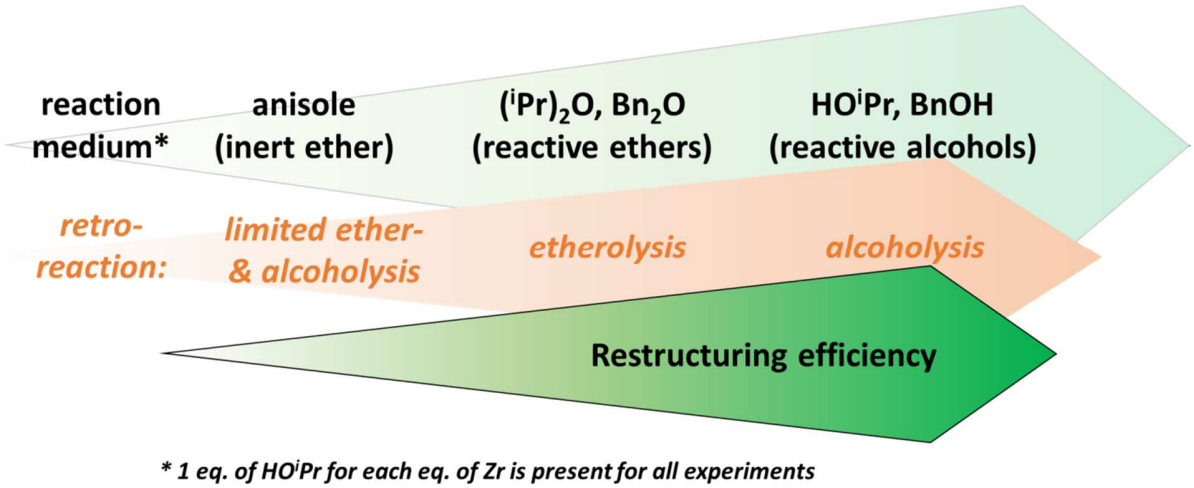

Figure 152: Restructuring efficiency for selected alcohols and ethers.

As what we have discovered with the ageing experiments in Chapter 4, the restructuring can eventually transform the ultrasmall zirconia having large structural distortion towards a more crystallized zirconia having a tetragonal-like phase with a local monoclinic distortion. The usage of other types of alcohols and ethers suggests that the effects brought about by the benzyl alcohol is not exclusive. This provides the possibility of alternative precursors for the synthesis of zirconia nanoparticles.

5.2.4 Restructuring effect under single or dual phase with the presence of *ex-situ* water

In Chapter 4, the direct addition of *ex-situ* water for the zirconia synthesis prepared using anisole with and without presence of NaOH showed some interesting behavior. The presence of *ex-situ* water and sodium hydroxide showed a more effective restructuring effect leading towards the formation of a tetragonal-like phase with minor local monoclinic distortion. In this section we pursue a similar methodology with the addition of water but at the secondary stage. The dual stage experiments with addition of *ex-situ* water onto the second stage are gathered in Table 42.

Table 42: Dual stage syntheses details for studying the effects of water onto the samples restructuration.

Stages	NaOH (mol.L^{-1})	Zirconia source (mol.L^{-1})	Solvent (% volume)		Solvothermal ageing time (days)	Temperature (^{o}C)
			Anisole	water		
Stage 1	0.2	0.3	100	0	3.0	210
Stage 2 (a)	0.0	0.0	95	5	3.0	210
	0.0	0.0	80	20	3.0	210
	0.0	0.0	50	50	3.0	210
Stage 2 (b)	0.2	0.0	100	0	3.0	210
	0.2	0.0	95	5	3.0	210

The XRD patterns of the zirconia samples synthesized via dual-stage strategy using the zirconia sample prepared in anisole with 0.2 mol.L^{-1} NaOH at 210°C for 3 days are shown in Figure 153. In the second stage, we investigate the effects of the presence of *ex-situ* water and/or sodium hydroxide by adding them in the mixture before the second solvothermal stage. For the samples without NaOH in the second stage, we detect some structural improvements with the presence of monoclinic phase together with the tetragonal phase zirconia for 5% water volume. The proportion of monoclinic phase continues to increase while the tetragonal phase fraction diminishes as the amount of water increases. In contrast, with the addition of sodium hydroxide and water onto the second stage some drastic structural improvements are evidenced. With only 5% water volume content and 0.2 mol.L^{-1} NaOH, the ultrasmall nanoparticles appear to have been transformed completely into monoclinic m-ZrO_2. In summary, the restructuring process occurs efficiently for the samples prepared with sodium hydroxide and *ex-situ* water in the second stage by including parallel to the grain growth a drastic LTD-like phase conversion.

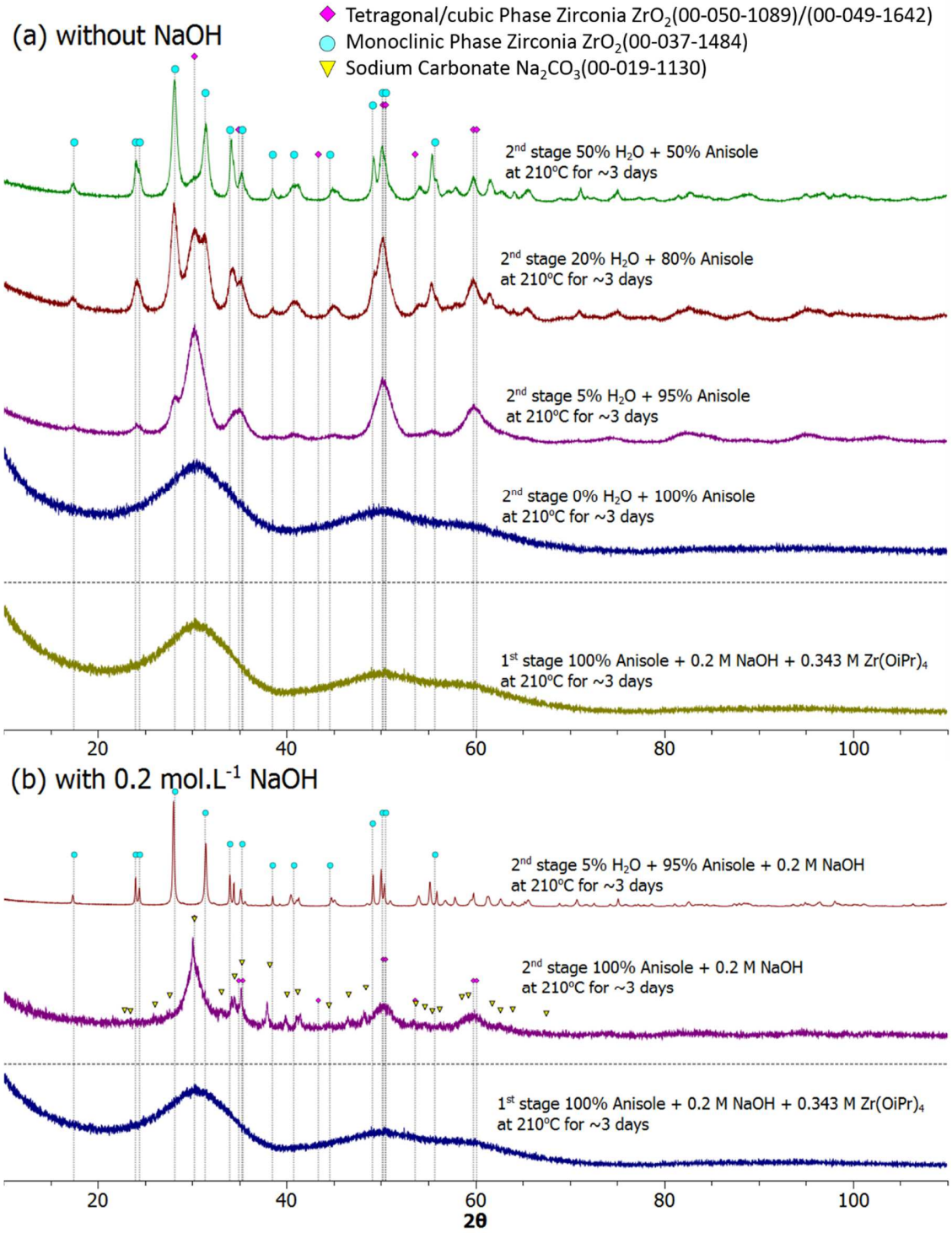

Figure 153: XRD patterns of zirconia samples prepared via dual-stage strategy at 210°C for (3+3) days using $[Zr(O^iPr)_4 \cdot HO^iPr]_2$ (a) without and (b) with 0.2 mol.L^{-1} NaOH in anisole prepared using solvothermal technique with varied amounts of water.

5.2.5 Crystallization towards tetragonal-like and monoclinic zirconia

The schemes for the formation of the tetragonal-like and monoclinic phase zirconia under various solvents are represented in Figure 154 (a) and (b). The scale of the pyramid is set such that at the top you have samples composed by well-crystallized zirconia particles jointly to a well-coherent structure due to the use of the high reactivity of selected medium. For the formation of a well-crystallized tetragonal-like zirconia, we start from the formation of an amorphous-like phase. With the addition of NaOH, we initiate the formation of ultrasmall zirconia which eventually leads into the formation of a tetragonal-like phase when aged for a long period. The ageing process to form the tetragonal-like phase can be shortened by simply adding some minute amounts of water together with the presence of NaOH.

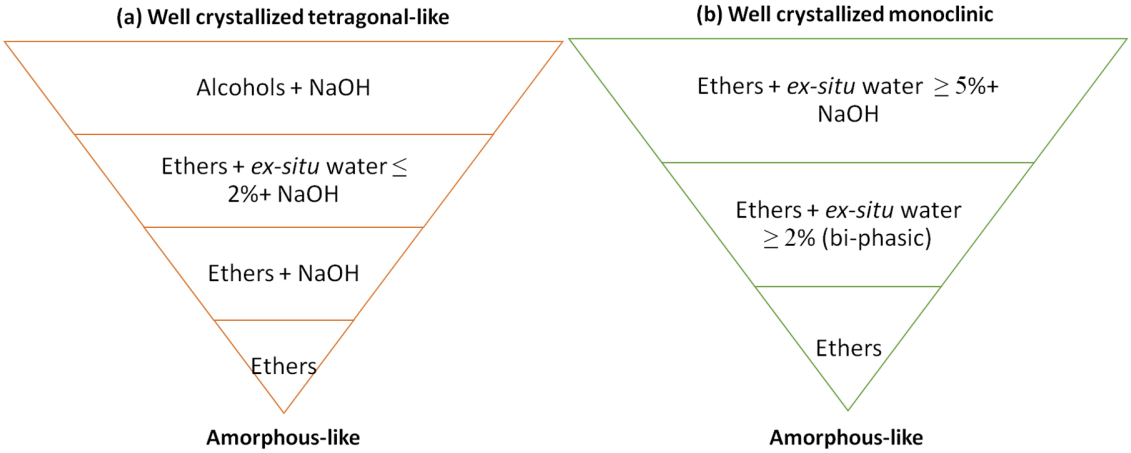

Figure 154: Formation of (a) tetragonal-like and (b) monoclinic zirconia nanoparticles using the restructuring effect of the various proposed reaction medium.

We note that for the samples prepared with *ex-situ* water, we only consider the samples up to 2% water volume content where there is some shielding effect brought about by the presence of sodium hydroxide which effectively inhibits the formation of monoclinic m-ZrO_2 nanoparticles. Finally with alkalinized benzyl alcohol, the restructuring towards the formation of well-crystallized tetragonal-like phase zirconia is most active.

For the formation the monoclinic phase zirconia, we initiate again with the amorphous-like phase under an ether. Rough restructuring of the amorphous-like can be achieved by allowing the reaction mixture to thermally age longer. This ageing process induces the formation of the tetragonal-like phase with some possible presence of monoclinic phase. Similarly, the process of restructuring can be hastened by the addition of *ex-situ* water which promotes the formation of a bi-phasic sample.

Finally, in order to promote the crystallization of a single monoclinic phase, the combination of NaOH and at least 5% volume percentage of water is needed but lead also to a large grain growth.

5.3 Conclusion

The respective roles of the solvent/reaction medium and alkali source are eminently important in the crystallization of the zirconia nanoparticles obtained by a non-aqueous sol-gel route. From the experiments using various types of base precursors, we have been able to conclude that the stabilization of the tetragonal-like phase is not due to a doping process of the sodium cations but rather it more driven by the inhibition of the apparition of *in-situ* water. However, it is not yet clear which of the two possible reaction mechanism leads to the absence of water on the final synthesized solution since inhibition and acid-base neutralization of water can occur simultaneously. On the second part of this work, we have found out that the use of alcohol is not necessarily restricted to alcohols having an aromatic ring and primary level since similar samples have been produced using ethanol or isopropanol. Finally, the effectiveness of the reaction medium governing the restructuring effect has shown to possess a hierarchal order which is based on how well the reverse sol-gel reactions, namely etherolysis, alcoholysis, and hydrolysis, are implemented.

General conclusion

The synthesis and characterization (chemical, morphological and structural) of nano-sized zirconia particles with adjustable phase and tunable size were presented in this manuscript. The production and study of such particles (size less than 5 nm) are essential for the understanding of their formation and structure. The syntheses were conducted via non-hydrolytic solvothermal and kinetically-controlled strategy in an adapted environment. X-ray total scattering was used for the fine structural analysis of the disorder in these very small particles.
The presentation of this work was divided into three parts:

1. The synthesis of ZrO_2 nanoparticles with adjustable phase and tunable size;
2. The in-depth structural characterization by pair distribution function analysis of selected samples;
3. The presentation of potential roles of the solvent and alkali sources in the formation of the zirconia nanoparticles.

First, the synthesis of zirconia nanoparticles was successfully achieved via non-aqueous procedures in a solvent-controlled strategy. The experiments using two types of zirconium precursor (zirconium chloride and zirconium isopropoxide-isopropanol adduct) led us to conclude that a zirconium alkoxide source is far more beneficial in terms of chemical reactivity and avoidance of halide impurity coming from the zirconium chloride. Moreover it is able to form zirconia polymorphs under various solvents (aldehydes, alcohols and ethers).
The addition of NaOH as the alkali source promotes the formation of a single phase zirconia by inhibiting the dehydration side-reaction presumably responsible for a partial phase conversion t-ZrO_2 to m-ZrO_2. Aside from the phase control, the role of NaOH also extends towards the fine tuning of the size. However, the extent of its effect is quite limited within the range from 0.1 to 0.5 $mol.L^{-1}$ of NaOH with an operating temperature of 210°C. Outside of this range unwarranted phase or inorganic impurities are formed. Interestingly, we have obtained three peculiar types of single phased zirconia samples under a fixed amount of NaOH (0.2 $mol.L^{-1}$ NaOH) at 210°C by using different solvents. These are: m-ZrO_2 nanocrystals in benzaldehyde, t-ZrO_2 nanocrystals in benzyl

alcohol and finally extremely small t-ZrO_2 nanocrystals in anisole. They present respectively average crystallite diameters of 3.7 nm, 4.0 nm and 1.6 nm.

The fine tuning of the size was addressed by considering an orchestrated interplay of the precursors. We formulated three ways to influence the size on the nanoparticles: first by varying the temperature and amount of alkali source, second by decreasing the amount of benzyl alcohol while maintaining an alkali environment and third by adding a second solvothermal step with regenerated alcohol, with or without the addition of an alkali source. In all cases it is clear that the presence of sodium hydroxide warranties the ability to condense the precursor whereas these three strategies have induced an effective size reduction of the crystallites and allowed it to vary from 3-5 nm and even reach below 2 nm if one achieves *a minima* of 1/10 dilution of benzyl alcohol in anisole, although the robust and simple benzyl alcohol route is generally claimed by Pinna *et al.* to offer a poor control over the size and shape of the particles [169].

Out of the previous zirconia particles we have chosen two samples that were prepared with 0.2 $mol.L^{-1}$ NaOH and 0.3 $mol.L^{-1}$ zirconium isopropoxide-isopropanol adduct at 210°C for three days, synthesized either in benzyl alcohol or in anisole. These selected samples have an average diameter sizes of about 4.0 nm and 1.6 nm, respectively. Both samples exhibit highly crystalline characteristics according to their TEM analysis. Both their FTIR and TGA have shown that the samples contain a non-negligible fraction of organics and sodium carbonate surrounding the zirconia particles which may play a role in the stabilization of these tiny particles. The Na^+ presence, which was claimed to be responsible for the inhibition of the surface-catalyzed dehydration side-reaction, was quantified by XPS and ICP in both samples and the largest content observed in the case of the anisole-based sample was related to the largest specific surface area characteristic of extremely small nanoparticles.

The second part of the work presents the in-depth structural characterization of selected samples by Rietveld refinement and atomic pair distribution function (PDF) analysis. Structural characterization of the zirconia samples prepared in benzyl alcohol, benzaldehyde and anisole with 0.2 $mol.L^{-1}$ NaOH at 210°C provided an important insight into their structural properties.

- Experimental PDF of the sample prepared in benzyl alcohol that appears tetragonal by conventional X-ray diffraction reveals a monoclinic feature at the short-range region while a

exhibiting a tetragonal feature at the medium-range region. The measured coherent size of the particle is 3 nm.

- The sample synthesized using benzaldehyde with NaOH is confirmed to have a monoclinic structure with a coherent size of 3 nm which is less than the critical size as defined by Garvie. This implies that the stabilization of the monoclinic phase in this system is not directly governed by size effect.
- For the ultrasmall zirconia sample prepared in anisole and NaOH, and characterized by three broad accented peaks in XRD, it does not seem to conform to any of the known polymorphs of zirconia having a fluorite-derived structure. However, the PDF shows that the sample has a monoclinic feature at the short-range region and a large structural disorder in the medium-range region. Its coherent size is 1.1 nm.

When the ultrasmall sample was subjected to thermally-assisted ageing, it transformed into a phase similar to the one prepared in benzyl alcohol, *i.e.* a monoclinic feature at the short-range region and a tetragonal feature at the medium-range one. This suggests that the original sample may be an intermediate phase between an amorphous and tetragonal-like zirconia.

To confirm this assumption we prepared a sample with similar synthesis conditions to the ultrasmall preparation except the presence of NaOH and labeled it as the amorphous-like sample. This sample appeared to have a monoclinic feature at the local-range region with a much higher distorted medium-range region compared to the ultrasmall sample and a very small coherent size of 0.8 nm. Thermally-assisted ageing of this amorphous-like sample induced the expansion of the monoclinic distorted zone in the medium-range region. This last result supports the idea that the presence of *in-situ* water formed by partial dehydration of isopropanol was able to promote the formation of monoclinic phase zirconia possibly by a low-thermal degradation-like (LTD) process in the presence of traces of an aqueous phase. The addition of minute amounts of *ex-situ* water induced a similar phase transformation. It is evident that for both types of samples the presence of water has consequential effects even at very low amounts (0.33% and 2% water volume content). The introduction of more than 2% volume of water led to the formation of larger particles dominated by a monoclinic structure rather than a tetragonal one.

Finally, the third part of the work deals with the respective roles of the alkali sources, the solvent or reaction medium and on the synthesis of nanoparticles. It is evident that the roles of these reagents are vital to the kinetically-driven formation of zirconia particles with tunable size and phase. The use of various types of base precursors led us to conclude that the stabilization of the tetragonal-like phase was not caused by a sodium cations doping in the structure, but was rather driven by its ability to inhibit the formation of *in-situ* water which can promote the LTD-like phase transformation. By varying the class and nature of the solvent, we found out that its effectiveness was not limited to the benzyl alcohol since similar samples have been produced using ethanol or isopropanol.
Finally, the effectiveness of the reaction medium governing the restructuring effect has been observed. It shows a hierarchical reactivity order which is based on how well the reverse sol-gel reactions (etherolysis, alcoholysis, and hydrolysis) are implemented.

As a recommendation for future studies related to this work, the chemical characterization of the supernatant would provide additional insights to the absence of *in-situ* water. Indeed, it is not yet clear which of the two possible reaction mechanisms leads to the absence of water on the final synthesized solution since inhibition and acid-base neutralization of water can occur simultaneously. Since we are able to influence the size of the particles at very low temperatures, we also recommend an *in-situ* structural characterization of the evolution of amorphous-like or ultrasmall zirconia by thermally-assisted ageing to obtain a more detailed description of the transformation from a highly disordered to a well-defined structure. Finally, construction of theoretical models would provide an invaluable insight regarding the formation of these tiny zirconia particles.

References

[1] L. E. Brus, "Electron–electron and electron-hole interactions in small semiconductor crystallites: The size dependence of the lowest excited electronic state," *The Journal of Chemical Physics*, vol. 80, no. 9, p. 4403–4409, 1984.

[2] P. E. Lippens and M. Lannoo, "Calculation of the band gap for small CdS and ZnS crystallites," *physical review B*, vol. 39, no. 15, pp. 10935-10942, 1989.

[3] A. P. Alivisatos, ""Semiconductor Clusters, Nanocrystals, and Quantum Dots," *Science*, vol. 271, no. 5251, pp. 933-937, 1996.

[4] H. Dosch, "Some General Aspects of Confinement in Nanomaterials," *Applied Surface Science*, vol. 182, no. 3-4, pp. 192-195, 2001.

[5] B. Gilbert, F. Huang, H. Zhang, G. A. Waychunas and J. F. Banfield, "Nanoparticles: Strained and Stiff," *Science*, vol. 305, no. 5684, pp. 651-654, 2004.

[6] T. Egami and S. J. Billinge, underneath the Bragg peaks: structural analysis of complex materials, Oxford: Elsevier Ltd, 2003.

[7] F. Conchon, "Elaboration et étude structurale et microstructurale d'un aérogel de zircone dopée à l'oxyde d'yttrium," Ecole Nationale Supérieure de Céramique Industrielle, Limoges, 2004.

[8] L. Portal, *Thesis: Syntheses et caracterisation de nancristaux d'oxydes metalliques*, Limoges, 2013.

[9] T. Yamaguchi, "Application of ZrO2 as a catalyst and catalyst support," *catalysis today Elsevier*, vol. 20, no. 2, pp. 199-218, 1994.

[10] J. Kašpar and P. Fornasiero, "Nanostructured materials for advanced automotive de-pollution catalysts," *Journal of solid state chemistry*, vol. 171, no. 1, pp. 19-29, 2003.

[11] W. C. Maskell, "Progress in the development of zirconia gas sensors," *Solid State Ionics,* vol. 134, no. 1-2, p. 43–50, 2000.

[12] J. Riegel, H. Neumann and H.-M. Wiedenmann, "Exhaust gas sensors for automotive emission control," *Solid State Ionics,* Vols. 152-153, p. 783–800, 2002.

[13] Y. Mizutania, K. Hisadaa, K. Ukaia, H. Sumia, M. Yokoyamaa, Y. Nakamuraa and O. Yamamotob, "From rare earth doped zirconia to 1 kW solid oxide fuel cell system," *Journal of Alloys and Compounds,* Vols. 408-412, no. 9, p. 518–524, 2006.

[14] J. M. Ralph, A. C. Schoeler and M. Krumpelt, "Materials for lower temperature solid oxide fuel cells," *Journal of Materials Science,* vol. 36, no. 5, pp. 1161-1172, 2001.

[15] M. H. Bocanegra-Bernal and S. D. d. l. Torre, "Phase transitions in zirconium dioxide and related materials for high performance engineering ceramics," *Journal of Materials Science,* vol. 37, no. 33, pp. 4947-4971, 2002.

[16] U. Leonhardt, "Optical Metamarials: Invisibilty cup," *Nature photonics,* vol. 1, pp. 207-208, 2007.

[17] R. Feynman, "There's plenty of room at the bottom," *Journal of microeletromechanical systems,* vol. 1, no. 1, pp. 60-66, 1959.

[18] N. Taniguchi, "On the basic concept of "Nano Technology"," *Proceedings of the International Conference on Production Engineering: Tokyo part 2,* pp. 18-23, 1974.

[19] G. Binnig and H. Rohrer, "Scanning tunneling microscopy," *IBM Journal of Research and Development,* vol. 30, no. 4, pp. 355-369, 1986.

[20] A. R. G. Ledesma and M. F. L. d. Almeida, "Nanometrology, Standardization and Regulation of Nanomaterials in Brazil: a Proposal for an Analytical-Prospective Model," *Journal of technology management and innovation,* vol. 8, pp. 39-52, 2013.

[21] Statnano, "Statnano 2015," Statnano, 2015.

[22] M. Steigerwald and L. Brus, "Synthesis, Stabilization, and Electronic Structure of Quantum Semiconductor Nanoclusters," *Annual Review of Materials Research,* vol. 19, pp. 471-495, 1989.

[23] L. V. Interrante and M. J. Hampden-Smith, Chemistry of Advanced Materials: An Overview, New York: WILEY-VCH, 1998.

[24] A. P. Alivisatos, "Perspectives on the Physical Chemistry of Semiconductor Nanocrystals," *The journal of physical cheimstry* , vol. 100, no. 31, p. 13226–13239, 1996.

[25] S. Morup, Nanomagnetism: Studies of Superparamagnetism in Samples of Ultrafine Particles, Boston: Kluwer Academic Publishers,, 1993.

[26] K. O'Grady and R. Chantrell, Magnetic properties: Theory and experiments, Amsterdam: Elsevier, 1992.

[27] H. Gleiter, "Nanostructured materials: basic concepts and microstructure," *Acta Materialia,* vol. 48, no. 1, p. 1–29, 2000.

[28] M. Grätzel, "photoelectrochemical cells," *nature,* vol. 414, pp. 338-344 , 2001.

[29] M. Fernandez-Garcia, A. Martinez-Arias, J. Hanson and J. Rodriguez, "Nanostructured oxides in chemistry: Characterization and properties," *Chemical reviews,* vol. 104, no. 9, p. 4063–4104, 2004.

[30] J. M. Taylor, "New dimensions for manufacturing: A UK starategy for nanotechnology," London, 2002.

[31] D. D. Ebbing, General Chemistry, 3rd ed., Houghton Mifflin, 1990.

[32] M. Gutowski, J. E. Jaffe, C.-L. Liu, M. Stoker, R. I. Hegde, R. S. Rai and P. J. Tobin, "Thermodynamic Stability of High-K Dielectric Metal Oxides ZrO 2 and HfO 2 in Contact with Si and SiO2," *MRS Proceedings,* vol. 716, p. B3. 2, 2002.

[33] J. Robertson, "High dielectric constant gate oxides for metal oxide Si transistors," *Reports on Progress in Physics,* vol. 69, no. 2, pp. 327-396, 2006.

[34] K. Chen, A. T. Bell and E. Iglesia, "The Relationship between the Electronic and Redox Properties of Dispersed Metal Oxides and Their Turnover Rates in oxidative dehydrogenation reactions," *Journal of Catalysis,* vol. 209, pp. 35-42, 2002.

[35] V. V. Sysoev, B. K. .. Button, K. Wepsiec, S. Dmitriev and A. Kolmakov, "Toward the nanoscopic “electronic nose”: Hydrogen vs carbon monoxide discrimination with an array of individual metal oxide nano-and mesowire sensors," *Nano letters,* vol. 6, no. 8, pp. 1584-1588, 2006.

[36] M. Lee, S. Han, S. Jeon, B. Park, B. Kang, S. Ahn, K. Kim, C. Lee, C. Kim, I. Yoo, D. Seo, X. Li, J. Park, J. Lee and Y. Park, "Electrical manipulation of nanofilaments in transition-metal oxides for resistance-based memory," *Nano letters,* vol. 9, no. 4, pp. 1476-1481, 2009.

[37] G. Mavrou, S. Galata, P. Tsipas, A. Sotiropoulos, Y. Panayiotatos, A. Dimoulas, E. Evangelou, J. W. Seo and C. Dieker, "Electrical properties of La2O3 and HfO2/La2O3 gate dielectrics for germanium metal-oxide-semiconductor devices," *Journal of applied physics,* vol. 103, no. 1, p. 4506, 2008.

[38] A. V. Emeline, G. V. Kataeva, A. V. Panasuk, V. K. Ryabchuk, N. V. Sheremetyeva and N. Serpone, "Effect of Surface Photoreactions on the Photocoloration of a Wide Band Gap Metal Oxide: Probing Whether Surface Reactions Are Photocatalytic," *The journal of physical chemistry B,* vol. 109, no. 11, p. 5175–5185, 2005.

[39] M. Kröger, S. Hamwi, J. Meyer, T. Riedl, W. Kowalsky and A. Kahn, "Role of the deep-lying electronic states of MoO3 in the enhancement of hole-injection in organic thin films," *Applied physics letters,* vol. 12, p. 95, 2009.

[40] U. S. Schubert and D. Wouters, "Nanolithography and Nanochemistry: Probe-Related Patterning Techniques and Chemical Modification for Nanometer-Sized Devices," *Angewandte Chemie international edition,* vol. 43, pp. 2480-2495, 2004.

[41] M. Niederberger and N. Pinna, Metal oxide nanoparticles in organic solvent, Verlag London: Springer , 2009.

[42] J. C. Brinker and G. W. Scherer, Sol-Gel Science: The Physics and Chemistry of of Sol-Gel Processing, San Diego: Academic Press, Inc., 1990.

[43] R. K. Iler, The Chemistry of Silica: Solubility, Polymerization, Colloid and Surface Properties and Biochemistry of Silica, New york: Wiley, 1979.

[44] J. Elbem, *Compte-Rendu de l'Académie des Sciences,* vol. 25, p. 854, 1847.

[45] R. Mayet, *Propriétés structurales de nanocristaux d'oxydes métalliques: utilisation de la diffusion total des rayon X et des calculs quantiques, PhD dissertation,* Limoges: Université de Limoges, 2008.

[46] M. Chatry, M. Henry and J. Livage, "Synthesis of non-aggregated nanometric crystalline zirconia particles," *Materials Research Bulletin,* vol. 29, no. 5, pp. 517-522, 1994.

[47] A. Vioux and P. H. Mutin, "Nonhydrolytic Processing of Oxide-Based Materials: Simple Routesto Control Homogeneity, Morphology, and Nanostructure," *Chemistry of Materials,* vol. XXI, no. 4, p. 582–596, 2009.

[48] C. B. Murray, D. J. Norris and M. G. Bawendi, "Synthesis and characterization of nearly monodisperse CdE (E = sulfur,selenium, tellurium) semiconductor nanocrystallites," *journal of the american chemical society,* vol. 115, no. 19, pp. 8706-8715, 1993.

[49] J. Joo, T. Yu, Y. W. Kim, H. M. Park, F. Wu, J. Z. Zhang and T. Hyeon, "Multigram scale synthesis and characterization of monodisperse tetragonal zirconia nanocrystals," *Journal of the american chemistry society,* vol. 125, no. 21, p. 6553–6557, 2003.

[50] T. J. Trentler, T. E. Denler, J. F. Bertone, A. Agrawal and V. L. Colvin, "Synthesis of TiO2 Nanocrystals by Nonhydrolytic Solution-Based Reactions," *Journal of the american chemical society,* vol. 121, no. 7, pp. 1613-1614, 1999.

[51] M. Niederberger, "Nonaqueous Sol–Gel Routes to Metal Oxide Nanoparticles," *Accounts of Chemical Research,* vol. 40, no. 9, pp. 793-800, 2007.

[52] X. Ji, N. Zhao, D. Pan and W. Nie, "Two-Phase Synthesis of Shape-Controlled Colloidal Zirconia," *Journal of the American Chemical Society,* vol. 128, no. 31, pp. 10118-10124, 2006.

[53] X. Xu and X. Wang, "Fine tuning of the sizes and phases of ZrO2 nanocrystals," *Nano Research,* vol. 2, pp. 891-902, 2009.

[54] M. Niederberger, N. Pinna, J. Polleux and M. Antonietti, "A General Soft-Chemistry Route to Perovskites and Related Materials: Synthesis of BaTiO3, BaZrO3, and LiNbO3 Nanoparticles," *Angewandte Chemie International Edition,* vol. XLIII, no. 17, p. 2270–2273 , 2004.

[55] G. Garnweitner, *Thesis: Nonaqueous synthesis of transition-metal oxide nanoparticles and their formation mechanism,* 2005.

[56] A. Pucci and N. Pinna, "Non-aqueous Sol-Gel Routes ti Metal Oxides Nanocrystals under Solvothermal Conditions: Review and Case study on the Doped IV Metal Oxides," *Verlag der Zeitschrift fur Naturfirschung,* pp. 1015-1023, 2010.

[57] G. Garnweitner, L. Goldenberg, O. Sakhno, M. Antonietti, M. Niederberger and J. Stumpe, "Large-Scale Synthesis of Organophilic Zirconia Nanoparticles and their Application in Organic–Inorganic Nanocomposites for Efficient Volume Holography," *Small - Wiley-VCH Verlag,* vol. III, no. 9, pp. 1626-1632, 2007.

[58] M. Niederberger, M. H. Bartl and G. D. Stucky, "Benzyl Alcohol and Titanium TetrachlorideA Versatile Reaction System for the Nonaqueous and Low-Temperature Preparation of Crystalline and Luminescent Titania Nanoparticles," *American Chemical Society,* vol. XIV, no. 10, p. 4364–4370, 2002.

[59] J. Ba, J. Polleux, M. Antonietti and M. Niederberger, "Non-aqueous Synthesis of Tin Oxide Nanocrystals and Their Assembly into Ordered Porous Mesostructures," *advanced materials,* vol. XVII, no. 20, pp. 2509-2512, 2005.

[60] K. D. Keukeleere, J. D. L. P. Roo, J. C. Martins, P. V. D. Voort and I. V. Driessche, "Fast and Tunable Synthesis of ZrO2 Nanocrystals: Mechanistic Insights into Precursor Dependence," *Inorganic chemistry,* vol. 54, no. 7, p. 3469–3476, 2015.

[61] B. Cushing, V. Kolesnichenko and C. O'Connor, "Recent advances in the liquid-phase," *Chemical Reviews,* vol. 104, no. 9, pp. 3893-3946, 2004.

[62] E. R. Leite and C. Ribeiro, Crystallization and growth of colloidal nanocrystals, New York: Springer, 2012.

[63] J. Baumgartner, A. Dey, P. H. H. Bomans, C. Le Coadou, P. Fratzl, N. A. J. M. Sommerdijk and D. Faivre, "Nucleation and growth of magnetite from solution," *Nature materials,* vol. 12, pp. 310-314, 2013.

[64] T. H. Zhang and X. Y. Liu, "How Does a Transient Amorphous Precursor Template Crystallization," *Journal of the american chemical society,* vol. 129, no. 44, pp. 13520-13526, 2007.

[65] S. Kwon and T. Hyeon, "Formation mechanisms of uniform nanocrystals via hot-injection and heat-up methods," *Small,* vol. 7, no. 19, pp. 2685-2702, 2011.

[66] N. T. K. Thanh, N. Maclean and S. Mahiddine, "Mechanisms of Nucleation and Growth of Nanoparticles in Solution," *Chemical reviews,* vol. 114, no. 15, pp. 7610-7630, 2014.

[67] V. K. La Mer, "Nucleation in phase transition," *Industrial and Engineering Chemistry,* vol. 44, no. 6, pp. 1270-1277, 1952.

[68] C. Burda, X. Chen, R. Narayanan and M. A. El-Sayed, "Chemistry and Properties of Nanocrystals of Different Shapes," *Chemical reviews,* vol. 105, no. 4, p. 1025–1102, 2005.

[69] I. Lifshitz and V. Slyozov, "The kinetics of precipitation from supersaturated solid solutions," *the journal of physical chemistry solids,* vol. 22, no. 1/2, pp. 35-50, 1961.

[70] M. A. v. Huis, L. T. .. Kunneman, K. Overgaag, Q. Xu, G. Pandraud, H. W. Zandbergen and D. Vanmaekelbergh, "Low-temperature nanocrystal unification through rotations and relaxations probed by in situ transmission electron microscopy," *Nano letters,* vol. 8, no. 11, pp. 3959-3963, 2008.

[71] M. H. Bocanegra-Bernal and S. D. d. l. Torre, "Phase transitions in zirconium dioxide and related materials for high performance engineering ceramics," *Journal of Materials Science,* vol. XXXVII, no. 33, pp. 4947-4971, 2002.

[72] Y. Mizutania, K. Hisadaa, K. Ukaia, H. Sumia, M. Yokoyamaa, Y. Nakamuraa and O. Yamamotob, "From rare earth doped zirconia to 1 kW solid oxide fuel cell system," *Journal of Alloys and Compounds,* Vols. CDVIII-CDXII, no. 9, p. 518–524, 2006.

[73] J. M. Ralph, A. C. Schoeler and M. Krumpelt, "Materials for lower temperature solid oxide fuel cells," *Journal of Materials Science,* vol. XXXVI, no. 5, pp. 1161-1172, 2001.

[74] W. C. Maskell, "Progress in the development of zirconia gas sensors," *Solid State Ionics,* vol. CXXXIV, no. 1-2, p. 43–50, 2000.

[75] J. Riegel, H. Neumann and H.-M. Wiedenmann, "Exhaust gas sensors for automotive emission control," *Solid State Ionics,* Vols. CLII-CLIII, p. 783–800, 2002.

[76] S. Das, C. Yang and C. Lu, "Structural and Optical Properties of Tunable Warm-White Light-Emitting ZrO2: Dy3+–Eu3+ Nanocrystals," *journal of the american ceramic society,* vol. 96, no. 5, pp. 1602-1609, 2013.

[77] T. Yamaguchi, "Application of ZrO2 as a catalyst and catalyst support," *catalysis today Elsevier,* vol. XX, no. 2, pp. 199-218, 1994.

[78] J. Kašpar and P. Fornasiero, "Nanostructured materials for advanced automotive de-pollution catalysts," *Journal of solid state chemistry,* vol. CLXXI, no. 1, pp. 19-29, 2003.

[79] K. Tanabe, "Surface and catalytic properties of ZrO2," *Materials Chemistry and Physics,* vol. 13, no. 3-4, pp. 347-364, 1985.

[80] G. Zhang, H. Hattori and K. Tanabe, "Aldol addition of acetone, catalyzed by solid base catalysts: magnesium oxide,calcium oxide, strontium oxide, barium oxide, lanthanum oxide and zirconium oxide," *applied catalysis,* vol. 36, pp. 189-197, 1988.

[81] C. Morterra, E. Giamello, L. Orio and M. Volante, "Formation and reactivity of zirconium(3+) centers at the surface of vacuum-activated monoclinic zirconia," *the journal of the physical chemistry : pre 1997,* vol. 94, no. 7, pp. 3111-3116, 1990.

[82] M. A. Aramendía, V. Boráu, C. Jiménez, J. M. Marinas, A. Porras and F. J. Urbano, "Synthesis and characterization of ZrO2 as an acid–base catalyst Dehydration–dehydrogenation of propan-2-ol," *Journal of the Chemical Society, Faraday Transactions,* vol. 93, pp. 1431-1438, 1997.

[83] P. Kostestkyy, J. Yu, R. J. Gorte and G. Mpourmpakis, "Structure–activity relationships on metal-oxides: alcohol dehydration," *The Royal Society of Chemistry 2014: Catalysis Science & Technology,* vol. 4, no. 11, pp. 3861-3869, 2014.

[84] J. Nawrocki, C. J. Dunlap, P. W. Carr and J. A. Blackwell, "New Materials for Biotechnology: Chromatographic Stationary Phases Based on Zirconia," *Biotechnology progress,* vol. 10, no. 6, pp. 561-573, 1994.

[85] J. A. Blackwell and P. W. Carr, "The role of Lewis acid-base processes in ligand-exchange chromatography of benzoic acid derivatives on zirconium oxide," *analytical chemistry,* vol. 64, no. 8, pp. 853-862, 1992.

[86] P. T. Chung, C. T. Yang, S. H. Wang, C. W. Chen, A. S. Chiang and C.-Y. Liu, "ZrO2/epoxy nanocomposite for LED encapsulation," *Materials chemistry and physics,* vol. 136, no. 2-3, pp. 868-876, 2012.

[87] C. J. Howard, R. J. Hill and B. E. Reichert, "Structures of ZrO2 polymorphs at room temperature by high-resolution neutron powder diffraction," *Acta Crystallographica Section B Structural Science,* vol. 44, no. 2, p. 116–120, 1988.

[88] G. Teufer, "The crystal structure of tetragonal ZrO2," *Acta Crystallographica,* vol. 15, no. 11, p. 1187–1187, 1962.

[89] G. Katz, "X-Ray Diffraction Powder Pattern of Metastable Cubic ZrO2," *Journal of the American Ceramic Society,* vol. 54, no. 10, p. 531–531, 1971.

[90] O. Ohtaka, T. Yamanaka and S. Kume, "Structural analysis of orthorhombic ZrO2 by high resolution neutron powder diffraction," *Proceedings of the Japan Academy. Ser. B: Physical and Biological Sciences,* vol. 66, no. 10, pp. 193-196, 1990.

[91] J. Haines, J. M. Léger and A. Atouf, "Crystal Structure and Equation of State of Cotunnite-Type Zirconia," *Journal of the American Ceramic Society,* vol. 78, no. 2, pp. 445-448, 1995.

[92] E. G. Rauh and S. P. Garg, "The ZrO2-x (cubic)-ZrO2-x (cubic+tetragonal) Phase Boundary," *Journal of the american ceramic society,* vol. 63, no. 3-4, p. 239–240, 1980.

[93] M. Hillert, "Thermodynamic Model of the Cubic → Tetragonal Transition in Nonstoichiometric Zirconia," *Journal of the american ceramic society,* vol. 74, no. 8, pp. 2005-2006, 1991.

[94] N. Mommer, T. Lee and J. A. Gardner, "Stability of monoclinic and tetragonal zirconia at low oxygen partial pressure," *Journal of materials research,* vol. 15, no. 2, pp. 377-381, 2000.

[95] P. Li, I.-W. Chen and J. E. Penner-Hahn, "Effect of dopants on zirconia stabilization – An x-ray-absorption study: I. Trivalent dopants," *Journal of the American ceramic society,* vol. 77, no. 1, pp. 118-128, 1994.

[96] P. Li, I.-W. Chen and J. E. Penner-Hahn, "Effect of Dopants on Zirconia Stabilization—An X-ray Absorption Study: II, Tetravalent Dopants," *Journal of the American ceramic society,* vol. 77, no. 5, pp. 1281-1288, 1994.

[97] P. Li, I.-W. Chen and J. E. Penner-Hahn, "Effect of Dopants on Zirconia Stabilization—An X-ray Absorption Study: III, Charge-Compensating Dopants," *Journal of the American Ceramic society,* vol. 77, no. 5, pp. 1289-1295, 1994.

[98] R. C. Garvie, "The Occurence of Metastable Tetragonal Zirconia as Crystallite Size Effect," *The Journal of Physical Chemistry,* vol. LXIX, no. 4, pp. 1238-1243, 1964.

[99] T. Chraska, A. H. .. King and C. C. .. Berndt, "on the size-dependent phase transformation in nanoparticulate zirconia," *Materials science and engineering: A,* vol. 286, no. 1, pp. 169-178, 2000.

[100] T. Mitsuhashi, M. Ichihara and U. Tatsuke, "Characterization and stabilization of metastable tetragonal ZrO2," *Journal of the American ceramic society ,* vol. 57, no. 2, pp. 97-101, 1974.

[101] H.-C. Wang and K.-L. Lin, "Characterization and metastability of alkoxy-derived tetragonal zirconia powder," *Journal of materials science,* vol. 26, no. 9, pp. 2501-2506, 1991.

[102] R. Ramamoorthy, D. Sundararaman and S. Ramasamy, "X-ray Diffraction Study of Phase Transformation in Hydrolyzed Zirconia Nanoparticles," *journal of the European ceramic society ,* vol. 19, no. 10, pp. 1827-1833, 1999.

[103] R. C. Garvie, "Stabilization of the tetragonal structure in zirconia microcrystals," *The journal of physical chemistry,* vol. 82, no. 2, p. 218–224, 1978.

[104] P. Li, I.-W. Chen and J. E. Penner-Hahn, "X-ray-absorption studies of zirconia polymorphs. I. Characteristic local structures," *Physical review: B,* vol. 48, no. 14, pp. 10063-10073, 1993.

[105] G. Skandan, H. Hahn, M. Roddy and W. R. Cannon, "ultrafine-grained dense monoclinic and tetragonal zirconia," *Journal of the American ceramic society,* vol. 77, no. 7, pp. 1706-1710, 1994.

[106] M. Winterer, R. Nitsche, S. Redfern, W. W. Schmahl and H. Hahn, "Phase Stability in Nanostructured and Coarse Grained Zirconia at High Pressures," *Nanostructured Materials,* vol. 5, no. 6, pp. 679-688, 1995.

[107] G. Skandan, H. Hahn and J. Parker, "Nanostructured Y2O3: synthesis and realation to microstructure and properties," *Scripta metallurgica et materialia,* vol. 25, no. 10, pp. 2389-2393, 1991.

[108] J. Livage, K. Doi and G. Mazieres, "Nature and thermal evolution of amorphous hydrated zirconium oxide," *Journal of the American ceramic society,* vol. 51, no. 6, pp. 349-353, 1968.

[109] V. G. Keramidas and W. B. White, "Raman Scattering Study of the Crystallization and Phase Transformations of ZrO2," *Journal of the American ceramic society,* vol. 57, no. 1, pp. 22-24, 1974.

[110] E. Tani, M. Yoshimura and S. Somiya, "formation of ultrafine tetragonal ZrO2 powder under hydrothermal conditions," *Journal of the American ceramic society,* vol. 66, no. 1, pp. 11-14, 1983.

[111] S. Gutzov, J. Ponahlo, C. L. Lengauer and A. Beran, "Phase characterization of precipitated zirconia," *Journal of the American ceramic society,* vol. 77, no. 6, pp. 1649-1652, 1994.

[112] Z. Yanwei, G. Fagherazzi and S. Polizzi, "The local structure characterization and resulting phase-transition mechanism of amorphous ZrO2," *Journal of materials science,* vol. 30, no. 8, pp. 2153-2158, 1995.

[113] O. Stachs, T. Gerber and V. Petkov, "Atomic-scale structure of ZrO2 xerogels by X-ray diffraction and reverse Monte Carlo simulations," *Journal of non-crystalline solids,* vol. 210, no. 1, pp. 14-22, 1997.

[114] M. Z. Hu, R. D. Hunt, E. A. Payzant and C. R. Hubbard, "Nanocrystallization and phase transformation in monodispersed ultrafine zirconia particles from various homogeneous precipitation methods," *Journal of the American ceramic society,* vol. 82, no. 9, pp. 2313-2320, 1999.

[115] F. Bondioli, A. M. Ferrari, C. Leonelli, C. Siligardi and G. C. Pellacani, "Microwave-Hydrothermal Synthesis of Nanocrystalline Zirconia Powders," *Journal of the American ceramic society,* vol. 84, no. 11, pp. 2728-2730, 2001.

[116] Y. Murase and E. Kato, "phase transformation of zirconia by ball-milling," *Journal of the American ceramic society,* vol. 62, no. 9-10, p. 527, 1979.

[117] R. Cypres, R. Wollast and J. Raucq, "Contribution to the knowledge of the polymorphic transformations of pure zirconium oxide," *Berichte der Deutschen Keramischen Gesellschaft,* vol. 40, no. 9, p. 527–532, 1963.

[118] X. Bokhimi, A. Morales, O. Novaro, T. Lopez, R. Gomez, T. Xiao and P. Strutt, "Nanocrystalline Tetragonal Zirconia Stabilized with Yttrium and Hydroxyls," *nanostructured materials,* vol. 12, no. 1-4, pp. 593-596, 1999.

[119] M. A. Blesa, A. J. G. Maroto, S. I. Passaggio, N. E. Figliolia and G. Rigotti, "Hydrous zirconium dioxide: interfactial properties, the formation of monodisperse spherical particles, and its crystallization at high temperatures," *Journal of materials science,* vol. 20, no. 12, pp. 4601-4609, 1985.

[120] A. C. Geiculescu and H. G. Spencer, "Thermal Decomposition and Crystallization of Aqueous Sol-Gel Derived Zirconium Acetate Gels: Effects of the Additive Anions," *Journal of sol-gel science and technology,* vol. 17, no. 1, pp. 25-35, 2000.

[121] X. Bokhimi, A. Morales, O. Novaro, M. Portilla, T. Lopez, F. Tzompantzi and R. Gomez, "The Effect of sulfating on the Crystalline Structure of Sol-Gel Zirconia Nanophases," *Materials research society proceedings* , vol. 457, pp. 51-56, 1996.

[122] C. J. Normair, P. A. Goulding and I. McAlpine, "Role of anions in the surface area stabilisation of zirconia," *Catalysis today,* vol. 20, no. 2, pp. 313-321, 1994.

[123] S. Chokkaram, R. Srinivasan, D. R. Milburn and B. H. Davis, "Ion Exchange and Thermal Studies of Sulfated Zirconia," *Journal of colloid and interface science,* vol. 165, no. 1, pp. 160-168, 1994.

[124] F.-C. Wu and S.-C. Yu, "Effects of H2SO4 on the crystallization and phase transformation of zirconia powder in the precipitation processes," *Journal of materials science,* vol. 25, no. 2, pp. 970-976, 1990.

[125] K. Parida and P. Pattnayak, "Studies on PO3−4/ZrO2: I. Effect of H3PO4on Textural and Acidic Properties of ZrO2," *Journal of colloid and interface science,* vol. 182, no. 2, pp. 381-387, 1996.

[126] S. Seal and S. Shukla, "Mechanisms of Room Temperature Metastable Tetragonal Phase Stabilisation in zirconia," *International Materials Reviews,* vol. 50, no. 1, pp. 45-64, 2005.

[127] N. Igawa, Y. Ishii, T. Nagasaki, Y. Morii, F. S. and H. Ohno, "Crystal structure of metastable tetragonal zirconia by neutron powder diffraction study," *Journal of the American ceramic society,* vol. 76, no. 10, pp. 2673-2676 , 1993.

[128] H. Liu, L. Feng, X. Zhang and Q. Xue, "ESR Characterization of ZrO2 Nanopowder," *The journal of physical chemistry* , vol. 99, no. 1, pp. 332-334, 1995.

[129] M. Che and J. C. Ve´drine, Characterization of Solid Materials and Heterogeneous Catalysts- from Structure to Surface Reactivity, Boschstr. 12, 69469 Weinheim, Germany: Wiley-VCH Verlag GmbH & Co. KGaA., 2012.

[130] R. Brundle, C. A. J. Evans and S. Wilson, Encyclopedia of Materials Characterization; Surfaces, interfaces and thin films, Greenwich: Manning Publications Co., 1992.

[131] C. Giacovazzo, H. Monaco, G. Artioli, D. Viterbo, G. Ferraris, G. Gilli, G. Zanotti and M. Catti, Fundamentals of Crystallography, 2e ed., Great Clarendon Street, Oxford: OXFORD University Press, 2002.

[132] webmaster@icdd.com, "The International Centre for Diffraction Data," 2015. [Online]. Available: http://www.icdd.com/. [Accessed 11 September 2015].

[133] admin@ccdc.cam.ac.uk, "The Cambridge Crystallographic Data Centre," 2015. [Online]. Available: http://www.ccdc.cam.ac.uk/. [Accessed 11 September 2015].

[134] P. Scherrer, "Bestimmung der Grösse und der inneren Struktur von Kolloidteilchen mittels Röntgenstrahlen," *Nachrichten von der Gesellschaft der Wissenschaften zu Göttingen,* vol. XXVI, pp. 98-100, 1918.

[135] J. I. Langford and A. J. C. Wilson, "Scherrer after sixty years: A survey and some new results in the determination of crystallite size," *Journal of Applied Crystallography,* vol. XI, pp. 102-113, 1978.

[136] A. J. C. Wilson, X-ray Optics: the diffraction of X-rays by finite and imperfect crystals, 2e ed., London: Methuen, 1962.

[137] B. E. Warren, X-ray diffraction, New york: Dover publications, Inc., 1920.

[138] J. Rodriguez-Carvajal and R. T., "Computer program FULLPROF (LLB-LCSIM)," may 2003.

[139] R. A. Young, The Rietveld Method, Walton Street, Oxford OX2 6 DP: Oxford University Press, 1993.

[140] Masson, *XTSScan : X ray total scattering acquisition program,* 2008.

[141] Masson, *pyReduWaxs,* 2012.

[142] P. Arnal, R. J. P. Corriu, D. Leclercq, P. H. Mutin and A. Vioux, "Preparation of anatase, brookite and rutile at low temperature by non-hydrolytic sol–gel methods," *Journal of materials chemistry*, vol. 6, no. 12, pp. 1925-1932, 1996.

[143] A. Cimino, D. Gazzoli, G. Minelli and M. Valigi, "Effect of Na+ ions on some properties of hydrous and thermally decomposed zirconium oxide," *Journal of materials chemistry*, vol. 2, pp. 75-82, 1992.

[144] A. Adamski, P. Jakubus and Z. Sojka, "Synthesis of nanostructured tetragonal ZrO2 of enhanced thermal stability," *Nukleonika*, vol. 51, no. 1, pp. 27-33, 2006.

[145] W. Gerrard and A. H. Woodhead, "Interaction of Alcohols with Silicon Tetrachloride," *Journal of the chemical society (Resumed)*, no. 0, pp. 519-522, 1951.

[146] R. Corriu, D. Leclercq, P. Lefevre, P. H. Mutin and A. Vioux, "Preparation of monolithic binary oxide gels by a nonhydrolytic sol-gel process," *Chemistry of materials*, vol. 4, no. 5, pp. 961-963, 1992.

[147] R. J. P. Corriu, D. Leclercq, P. Lefèvre and A. Vioux, "Preparation of Monolithic Metal-Oxide Gels by a Non-Hydrolytic Sol-Gel Process," *Journal of Materials Chemistry* , vol. 2, no. 6, pp. 673-674, 1992.

[148] M. Niederberger, M. H. Bartl and G. D. Stucky, "Benzyl Alcohol and Titanium Tetrachloride-A Versatile Reaction System for the Nonaqueous and Low-Temperature Preparation of Crystalline and Luminescent Titania Nanoparticles," *Chemistry materials*, vol. 14, no. 10, p. 4364–4370, 2002.

[149] A. Vioux and P. H. Mutin, "Nonhydrolytic Processing of Oxide-Based Materials: Simple Routesto Control Homogeneity, Morphology, and Nanostructure," *Chemistry of Materials*, vol. 21, no. 4, p. 582–596, 2009.

[150] G. Garnweitner, L. Goldenberg, O. Sakhno, M. Antonietti, M. Niederberger and J. Stumpe, "Large-Scale Synthesis of Organophilic Zirconia Nanoparticles and their Application in Organic–Inorganic Nanocomposites for Efficient Volume Holography," *Small - Wiley-VCH Verlag,* vol. 3, no. 9, pp. 1626-1632, 2007.

[151] M. Niederberger and N. Pinna, Metal oxide nanoparticlesin organic solvents: synthesis, formation, assembly, and application, London: Springer, 2009.

[152] W. Li, H. Huang, H. Li, W. Zhang and H. Liu, "Facile Synthesis of Pure Monoclinic and Tetragonal Zirconia Nanoparticles and Their Phase Effects on the Behavior of Supported Molybdena Catalysts for Methanol-Selective Oxidation," *Langmuir,* vol. 24, no. 15, p. 8358–8366, 2008.

[153] Y.-D. Li, Z.-X. Deng and C. Wang, "New Hydrolytic Process for Producing Zirconium Dioxide,Tin Dioxide, and Titanium Dioxide Nanoparticles," *Journal of the American Ceramic Society,* vol. LXXXV, no. 11, p. 2837–2839, 2002.

[154] M. Taguchi, T. Nakane, A. Matsushita, Y. Sakka, T. Uchikoshi, T. Funazukuri and T. Naka, "One-pot synthesis of monoclinic ZrO2 nanocrystals under subcritical hydrothermal conditions," *Journal of supercritical fluids,* vol. 85, pp. 57-61, 2014.

[155] M. Taguchi, S. Takami, T. Adschiri, T. Nakane, K. Sato and T. Naka, "Simple and rapid synthesis of ZrO2 nanoparticles from Zr(OEt)4 and Zr(OH)4 using a hydrothermal method," *crystal engineering communications,* vol. 14, pp. 2117-2123, 2012.

[156] G. Stefanic, S. Music and K. Molcanov, "The crystallization process of HfO2 and ZrO2 under hydrothermal conditions," *Journal of alloys and compounds,* vol. 387, pp. 300-307, 2005.

[157] R. C. Garvie, "The Occurrence of Metastable Tetragonal Zirconia as a Crystallite Size Effect," *the journal of physical chemistry,* vol. 69, no. 4, p. 1238–1243, 1965.

[158] R. C. Garvie and M. F. Goss, "Intrinsic size dependence of the phase transformation temperature in zirconia microcrystals," *Journal of materials science,* vol. 21, no. 4, p. 1253–1257, 1986.

[159] L. Zhang, G. Garnweitner, I. Djerdj and M. N. M. Antonietti, "Generalized Nonaqueous Sol–Gel Synthesis of Different Transition-Metal Niobate Nanocrystals and Analysis ofthe Growth Mechanism," *Chemistry, an Asian Journal,* vol. 3, no. 4, pp. 746-752, 2008.

[160] L. Zhang, I. Djerdj, M. Cao, M. Antonietti and M. Niederberger, "Nonaqueous Sol–Gel Synthesis of a Nanocrystalline InNbO4 Visible-Light Photocatalyst," *Advanced materials,* vol. 19, no. 16, pp. 2083-2086, 2007.

[161] J. T. Kozlowski and R. J. Davis, "Sodium Modification of Zirconia Catalysts for Ethanol Coupling to 1-Butanol," *Journal of Energy Chemistry,* vol. 22, no. 1, p. 58–64, 2013.

[162] M. Niederberger and G. Garnweitner, "Organic Reaction Pathways in the Nonaqueous Synthesis of Metal Oxide Nanoparticles," *Chemistry - A European Journal,* vol. 12, no. 28, p. 7282–7302, 2006.

[163] G. Socrates, Infrared and Raman Characteristiccs Group Frequencies : Tables and Charts, 3e ed., Baffins Lane, Chichester, West Sussex PO19 1UD, England: John Wiley &Sons Ltd, 2001.

[164] E.-M. Köck, M. Kogler, T. Bielz, B. Klötzer and S. Penner, "In Situ FT-IR Spectroscopic Study of CO2 and CO Adsorption on Y2O3,ZrO2, and Yttria-Stabilized ZrO2," *The journal of physical chemistry,* vol. 117, p. 17666−17673, 2013.

[165] A. Aboulaich, B. Boury and P. H. Mutin, "Reactive and Organosoluble SnO2 Nanoparticles by a Surfactant-Free Non-Hydrolytic Sol–Gel Route," *European Journal of Inorganic Chemistry,* vol. 2011, no. 24, p. 3644–3649, 2011.

[166] V. Santos, M. Zeni, C. Bergmann and J. Hohemberger, "Correlation Between Thermal Treatment and Tetragonal/Monoclinic Nanostructured Zirconia Powder Obtained by Sol-Gel Process," *Reviews on Advanced Materials Science,* vol. XVII, no. 1, pp. 62-70, 2008.

[167] S. Jayakumara, P. Ananthapadmanabhan, K. Perumal, T. Thiyagarajan, S. Mishra, L. Su, A. Tok and J. Guo, "Characterization of nano-crystalline ZrO2 synthesized via reactive plasma processing," *Materials science and engineering: B,* vol. 176, no. 12, p. 894–899, 2011.

[168] H. Xie, J. Lu, M. Shekhar, J. W. Elam, W. N. Delgass, F. H. Ribeiro, E. Weitz and K. R. Poeppelmeier, "Synthesis of Na-Stabilized Nonporous t-ZrO2 Supports and Pt/t-ZrO2 Catalysts and Application to Water-Gas-Shift Reaction," *American Chemical Society,* vol. III, no. 1, pp. 61-73, 2013.

[169] N. Pinna and M. Niederberger, "Surfactant-Free Nonaqueous Synthesis of Metal Oxide Nanostructures," *angewandte chemie international edition,* vol. 47, no. 29, p. 5292–5304, 2008.

[170] C. L. Farrow, P. Juhás, J. W. Liu, D. Bryndin, E. S. Božin, J. Bloch, T. Proffen and S. J. L. Billinge, "PDFfit2 and PDFgui: computer programs for studying nanostructure in crystals," *Journal of Physics: Condensed Matter,* vol. 19, no. 23, pp. 1-7, 2007.

[171] R. J. Corriu, D. LeClerq, A. Vioux, M. Pauthe and J. Phalippou, "Utrastructure processing of advanced ceramics," J. D. Mackenzie and D. R. Ulrich, Eds., New York, Wiley, 1988, pp. 113-126.

Titre : Synthèse non-hydrolytique et structure de nanoparticules de ZrO_2

Les matériaux nanocristallins sont devenus la pierre angulaire de plusieurs avancées technologiques en raison de leurs propriétés intrinsèques qui sont différentes par rapport à leurs homologues micrométriques classiques. Ces propriétés sont principalement causées par des effets de confinement quantiques provoqués par la réduction de la taille des particules, qui sont largement étudiés et relativement bien compris.

La taille des particules a également un fort effet sur leur structure inhabituelle qui n'est pas identique à la structure monocristalline dite parfaite. En outre, la compréhension des propriétés de ces matériaux est assez limitée en raison de la complexité actuelle dans la synthèse et la caractérisation des objets stables qui sont inférieurs à 5 nm.

Ce travail est donc consacré à la détermination d'une manière reproductible de synthétiser des nanoparticules à phase sélectionnable et taille réglable. Ensuite, après avoir contrôlé ces paramètres, nous avons étudié leurs caractéristiques structurales par rapport à leur échelle, ce qui est conséquent pour une meilleure compréhension de ces matériaux, y compris leurs propriétés.

Une des procédures typiques utilisées pour synthétiser des particules de taille nanométrique appartient aux voies de solution chimique. En effet, ces itinéraires offrent une manière polyvalente de former des particules en suivant une approche "ascendante". En principe, ce type d'approche élimine la limite inférieure de taille qui peut être formée. Cependant, la stabilisation de ces petites particules avec une cristallinité et une pureté chimique acceptables nécessite une compréhension plus complète du comportement chimique des précurseurs individuels pendant la synthèse. En général, ces itinéraires peuvent être divisés en deux catégories: les processus hydrolytique et non hydrolytique. Chaque processus offre la possibilité de former des particules de taille nano avec une grande variété de propriétés désignables mais aussi avec ses limitations correspondantes. Par exemple, on peut citer la synthèse hydrolytique sol-gel de ZrO2 qui est capable de produire des nanoparticules de tailles inférieures à 2 nm. Malheureusement, ils possèdent une distribution de grande taille et présentent à leur surface de grandes quantités d'impuretés carbonées. En revanche, la synthèse sol-gel non hydrolytique de ZrO2 réalisée par des voies solvothermales a également produit des particules de taille nanométrique mais avec des caractéristiques plus satisfaisantes en termes de distribution de taille et d'absence d'impuretés. Il est clair que pour ce travail particulier la décision de suivre une procédure non hydrolytique offre une meilleure stratégie pour obtenir des objets de taille minuscule.

Le choix du ZrO2 comme matériau à étudier a été dicté par ses propriétés intrinsèques remarquables et son potentiel pour un grand progrès technologique, comme dans la catalyse, la détection des gaz, la technologie des piles à combustible, et les céramiques. De plus, il présente un polymorphisme complexe et a la particularité d'être stabilisé à l'échelle nanométrique sous des formes cristallines qui ne sont pas stables à la pression normale et à la température ambiante.

Dans ce travail, la stratégie solvothermale a été utilisée et a servi de base expérimentale pour la synthèse des nanoparticules de zircone. Les principaux réactifs choisis sont l'adduit d'isopropoxyde de zirconium-isopropanol, l'alcool benzylique et l'hydroxyde de sodium comme le zirconium, le solvant et les sources alcalines, respectivement. Les préparations pour toutes les synthèses ont été réalisées à l'intérieur d'une boîte à gants contenant de l'air sec pour assurer une exposition minimale à l'humidité.

Pour les caractérisations chimiques, morphologiques et structurales, nous avons combiné différentes techniques afin d'obtenir une meilleure compréhension de la nature de ces particules. La caractérisation structurale a reçu une attention particulière et a été réalisée en utilisant la diffusion totale des rayons X (TS) et l'analyse de la fonction de distribution des paires atomiques (PDF). Cet outil se spécialise dans l'analyse des régions à moyenne et à courte portée de la structure nanoparticules qui donne des informations précieuses pour identifier le type de polymorphe. Des échantillons sélectionnés présentant des caractéristiques structurelles particulières ont été étudiés et ont permis une meilleure compréhension de la nature de sa cristallisation et de sa stabilisation.

Le manuscrit est divisé en cinq chapitres.

Dans le premier chapitre qui est l'état de la technique, nous discutons brièvement les travaux pertinents réalisés dans la synthèse et la caractérisation des nanocristaux. Ici, nous abordons plus sur les questions actuelles liées à la stabilisation de l'oxyde métallique en utilisant une voie non-hydrolytique sol-gel.

Les caractéristiques des techniques de synthèse et de caractérisation sont présentées dans le chapitre 2. Les caractéristiques sont classées en trois types: chimique (analyse thermogravimétrique, spectrométrie de masse à plasma inductif, spectroscopie de photoélectrons aux rayons X, spectroscopie de résonance magnétique nucléaire de protons , Spectroscopie infrarouge à transformée de Fourier), morphologiques (microscopie électronique à transmission) et structuraux (diffraction des rayons X et diffusion totale des rayons X). Dans cette section, nous discutons brièvement les principes et les mécanismes derrière les outils de caractérisation mentionnés.

Le chapitre 3 présente les résultats initiaux sur la synthèse de zircone nanométrique dans une voie sol-gel non hydrolytique utilisant deux types de précurseurs de zirconium. De produire avec succès des nanoparticules de zircone, nous démontrons alors le réglage fin de la taille des particules et la pureté de phase en faisant varier sa température de fonctionnement, la quantité de contenu d'alcool et la synthèse à deux étages. Nous avons sélectionné ici quelques échantillons présentant des caractéristiques intéressantes pour une caractérisation approfondie qui s'est avérée indispensable pour comprendre leurs caractéristiques structurelles.

Dans le chapitre 4, nous nous sommes concentrés plus sur les propriétés structurales des échantillons présentant des caractéristiques structurales intéressantes et les avons comparés aux quatre polymorphes de zircone ayant une structure dérivée de fluorite. Cela a été fait en générant

des modèles théoriques de ces polymorphes et en les comparant avec les résultats expérimentaux. Parmi ces échantillons choisis de zircone, nous avons choisi l'un d'entre eux ayant une taille finie inférieure à 2 nm et une bonne cristallinité et mené deux types d'expériences: le premier était l'étude des effets du vieillissement assisté thermiquement et le second était le Effets de l'eau ex-situ sur les caractéristiques structurelles de l'échantillon.

Enfin, dans le cinquième et dernier chapitre, nous avons effectué des expériences complémentaires pour étudier les effets des contraintes cationiques et anioniques de l'hydroxyde de sodium et d'autres sels inertes ou acides et du type solvant en substituant l'alcool benzylique par d'autres alcools ou éthers. Combinés aux résultats obtenus à partir d'autres chapitres, nous avons proposé des schémas qui décrivent la formation de divers types de nanoparticules de zircone et les recommandations futures dérivées des travaux expérimentaux.

La synthèse et la caractérisation (chimique, morphologique et structurelle) des particules de zircone de taille nanométrique à phase réglable et taille réglable ont été présentées dans ce manuscrit. La production et l'étude de ces particules (taille inférieure à 5 nm) sont essentielles pour comprendre leur formation et leur structure. Les synthèses ont été réalisées via une stratégie non hydrolytique solvothermale et cinétiquement contrôlée dans un environnement adapté. La diffusion totale des rayons X a été utilisée pour l'analyse structurale fine du trouble dans ces très petites particules. Les conclusions apportées par ce travail concernent les trois points suivants:

1. La synthèse de nanoparticules de ZrO2 à phase ajustable et taille accordable;

2. La caractérisation structurale approfondie par analyse de la fonction de répartition des paires d'échantillons sélectionnés;

3. La présentation des rôles potentiels du solvant et des sources alcalines dans la formation des nanoparticules de zircone.

Premièrement, la synthèse des nanoparticules de zircone a été réalisée avec succès par des procédures non aqueuses dans une stratégie contrôlée par solvant. Les expériences utilisant deux types de précurseurs de zirconium (chlorure de zirconium et adduit d'isopropoxyde de zirconium-isopropanol) nous ont amené à conclure qu'une source d'alcoxyde de zirconium est beaucoup plus bénéfique en termes de réactivité chimique et d'évitement de l'impureté d'halogénure provenant du chlorure de zirconium. En outre, il est capable de former des polymorphes de zircone sous divers solvants (aldéhydes, alcools et éthers).

L'addition de NaOH en tant que source alcaline favorise la formation d'une zircone monophasique en inhibant la réaction secondaire de déshydratation vraisemblablement responsable d'une conversion de phase partielle t ZrO2 en m-ZrO2. Mis à part le contrôle de phase, le rôle de NaOH s'étend également vers le réglage fin de la taille. Cependant, l'étendue de son effet est très limitée dans la plage de 0,1 à 0,5 mol.L-1 de NaOH avec une température de fonctionnement de 210 ° C. En dehors de cette plage, on forme une phase non justifiée ou des impuretés inorganiques. De

façon intéressante, nous avons obtenu trois types particuliers d'échantillons de zircone à phase unique sous une quantité fixe de NaOH (NaOH 0,2 mol.L-1) à 210 ° C en utilisant différents solvants. Ce sont: les nanocristaux m-ZrO2 dans le benzaldéhyde, les nanocristaux t-ZrO2 dans l'alcool benzylique et enfin les nanocristaux t-ZrO2 extrêmement petits dans l'anisole. Ils présentent respectivement des diamètres de cristallites moyens de 3,7 nm, 4,0 nm et 1,6 nm.

Le réglage fin de la taille a été abordé en considérant un jeu orchestré des précurseurs. Nous avons formulé trois façons d'influencer la taille des nanoparticules: d'abord en faisant varier la température et la quantité de source alcaline, d'autre part en diminuant la quantité d'alcool benzylique tout en maintenant un environnement alcalin et en ajoutant une deuxième étape solvothermale avec de l'alcool régénéré avec ou Sans ajout d'une source alcaline. Dans tous les cas, il est clair que la présence d'hydroxyde de sodium garantit la capacité de condenser le précurseur, alors que ces trois stratégies ont induit une réduction de taille efficace des cristallites et lui ont permis de varier de 3 à 5 nm et même d'atteindre moins de 2 nm si une Atteint un minimum de dilution 1/10 d'alcool benzylique dans l'anisole, bien que la voie robuste et simple d'alcool benzylique soit généralement revendiquée par Pinna et al. Pour offrir un mauvais contrôle sur la taille et la forme des particules.

Sur les particules de zircone précédentes, nous avons choisi deux échantillons qui ont été préparés avec 0,2 mol.L-1 NaOH et 0,3 mol.L 1 d'isopropoxyde de zirconium-isopropanol adduct à 210 ° C pendant trois jours, synthétisés soit dans l'alcool benzylique soit dans l'anisole. Ces échantillons choisis ont des diamètres de diamètre moyen d'environ 4,0 nm et 1,6 nm, respectivement. Les deux échantillons présentent des caractéristiques très cristallines selon leur analyse TEM. Tant leur FTIR que leur TGA ont montré que les échantillons contiennent une fraction non négligeable d'organiques et de carbonate de sodium entourant les particules de zircone qui peuvent jouer un rôle dans la stabilisation de ces minuscules particules. La présence de Na +, qui était revendiquée responsable de l'inhibition de la réaction secondaire de déshydratation catalysée en surface, a été quantifiée par XPS et ICP dans les deux échantillons et la plus grande teneur observée dans le cas de l'échantillon à base d'anisole était liée à la La plus grande surface spécifique spécifique des nanoparticules extrêmement petites.

La deuxième partie du travail présente la caractérisation structurale en profondeur des échantillons sélectionnés par l'analyse du raffinement de Rietveld et de la fonction de distribution de paires atomiques (PDF). La caractérisation structurale des échantillons de zircone préparés dans l'alcool benzylique, le benzaldéhyde et l'anisole avec 0,2 mol.L-1 de NaOH à 210 ° C a fourni un aperçu important de leurs propriétés structurales.

Le PDF expérimental de l'échantillon préparé dans de l'alcool benzylique qui apparaît tetragonal par diffraction de rayons X conventionnelle révèle une caractéristique monoclinique dans la région à courte distance alors que présente une caractéristique tétragonale dans la région à moyenne portée. La taille cohérente mesurée de la particule est de 3 nm.

L'échantillon synthétisé à l'aide de benzaldéhyde avec NaOH est confirmé avoir une structure monoclinique avec une taille cohérente de 3 nm qui est inférieure à la taille critique telle que définie par Garvie. Ceci implique que la stabilisation de la phase monoclinique dans ce système n'est pas directement régie par l'effet de taille.

Pour l'échantillon de zircone “ultra-petit” préparé dans l'anisole et NaOH, et caractérisé par trois pics larges accentués dans XRD, il ne semble pas se conformer à l'un quelconque des polymorphes connus de zircone ayant une structure dérivée de fluorite. Cependant, le PDF montre que l'échantillon a une caractéristique monoclinique dans la région à courte portée et un grand désordre structurel dans la région à moyenne portée. Sa taille cohérente est de 1,1 nm.

Lorsque l'échantillon “ultra-petit” a été soumis à un vieillissement assisté thermiquement, il a été transformé en une phase similaire à celle préparée dans l'alcool benzylique, c'est-à-dire une caractéristique monoclinique dans la région à courte distance et une caractéristique tétragonale à moyenne portée. Ceci suggère que l'échantillon d'origine peut être une phase intermédiaire entre une zircone amorphe et de type tétragonale.

Pour confirmer cette hypothèse, nous avons préparé un échantillon avec des conditions de synthèse semblables à la préparation “ultra-petite”, à l'exception de la présence de NaOH, et on l'a marqué comme échantillon amorphe. Cet échantillon semblait avoir une caractéristique monoclinique dans la région de portée locale avec une région de milieu de gamme distordue beaucoup plus élevée par rapport à l'échantillon ultrasmall et une très petite taille cohérente de 0,8 nm. Le vieillissement assisté thermiquement de cet échantillon de type amorphe a induit l'expansion de la zone déformée monoclinique dans la région à moyenne portée. Ce dernier résultat confirme l'idée que la présence d'eau in situ formée par déshydratation partielle de l'isopropanol a été capable de favoriser la formation de zircone de phase monoclinique, éventuellement par un procédé à faible dégradation thermique (LTD) en présence de traces d'un phase aqueuse. L'addition de quantités infimes d'eau ex situ a induit une transformation de phase similaire. Il est évident que pour les deux types d'échantillons, la présence d'eau a des effets consécutifs même à des quantités très faibles (teneur en volume d'eau de 0,33% et 2%). L'introduction de plus de 2% de volume d'eau a conduit à la formation de particules plus grandes dominées par une structure monoclinique plutôt que par une structure tétragonale.

Enfin, la troisième partie traite des rôles respectifs des sources alcalines, du solvant ou du milieu réactionnel et de la synthèse des nanoparticules. Il est évident que les rôles de ces réactifs sont vitaux pour la formation cinétique de particules de zircone à taille et phase ajustables. L'utilisation de divers types de précurseurs de base nous a amenés à conclure que la stabilisation de la phase de type tétragonale n'était pas provoquée par un dopage de cations sodium dans la structure, mais plutôt par sa capacité à inhiber la formation d'eau in situ Peuvent favoriser la transformation de phase de type LTD. En variant la classe et la nature du solvant, on a découvert que son efficacité

n'était pas limitée à l'alcool benzylique puisque des échantillons similaires ont été produits en utilisant de l'éthanol ou de l'isopropanol.

Enfin, l'efficacité du milieu réactionnel régissant l'effet de restructuration a été observée. Il montre un ordre de réactivité hiérarchique qui est basé sur la façon dont les réactions sol-gel inverse (étherolyse, alcoolyse et hydrolyse) sont mises en œuvre.

En guise de recommandation pour les futures études liées à ce travail, la caractérisation chimique du surnageant permettrait de mieux comprendre l'absence d'eau in situ. En effet, il n'est pas encore clair lequel des deux mécanismes réactionnels possibles conduit à l'absence d'eau sur la solution synthétisée finale puisque l'inhibition et la neutralisation acide-base de l'eau peuvent se produire simultanément. Puisque nous sommes capables d'influencer la taille des particules à des températures très basses, nous recommandons également une caractérisation structurale in situ de l'évolution de la zircone amorphe ou ultra-mince par le vieillissement assisté thermiquement pour obtenir une description plus détaillée de la transformation de Un très désordonné à une structure bien définie. Enfin, la construction de modèles théoriques fournirait un aperçu inestimable concernant la formation de ces minuscules particules de zircone.